Transactions of the ASME

Journal of Fluids Engineering

Published Quarterly by The American Society of Mechanical Engineers

VOLUME 103 • NUMBER 3 • SEPTEMBER 1981

EDITORIAL STAFF
Editor, **J. J. JAKLITSCH, JR.**
Production Editor, **CORNELIA MONAHAN**
Editorial Production Assistant,
BETH DARCHI

FLUIDS ENGINEERING DIVISION
Technical Editor
FRANK M. WHITE (1981)
Executive Secretary
L. T. NELSON (1981)
Calendar Editor
M. F. ACKERSON

Associate Editors
Fluid Machinery
H. JAMES HERRING (1981)
BUDUGUR LAKSHMINARAYANA (1982)
Fluid Measurements
BHARATAN R. PATEL (1982)
Fluid Mechanics
CHARLES DALTON (1983)
OWEN M. GRIFFIN (1981)
BRIAN E. LAUNDER (1981)
WILLIAM G. TIEDERMAN (1981)
Fluid Transients
M. HANIF CHAUDHRY (1983)
Polyphase Flow
PAUL H. ROTHE (1983)
ROBERT L. STREET (1981)
Review Articles
KENNETH E. HICKMAN (1981)

FOREIGN CORRESPONDENTS
Europe and Russia
JACQUES CHAUVIN
Europe and Russia
JOHN H. HORLOCK
India and Middle East
ARUN PRASAD
Japan and China
YASUTOSHI SENOO

BOARD ON COMMUNICATIONS
Chairman and Vice President
MICHAEL J. RABINS

Members-at-Large
W. BEGELL, J. CALLAHAN, D. KOENIG,
M. KUTZ, F. LANDIS, J. W. LOCKE,
J. ORTLOFF, C. PHILLIPS, K. REID

Business Staff
345 East 47th St.
New York, N. Y. 10017
(212) 644-7789
Mng. Dir., Publ., **J. J. FREY**

OFFICERS OF THE ASME
President, **ROBERT B. GAITHER**
Secretary and Treasurer,
ROBERT A. BENNETT

The Journal of FLUIDS ENGINEERING (USPS 278-480) is edited and published quarterly at the offices of The American Society of Mechanical Engineers, United Engineering Center, 345 E. 47th St., New York, N. Y. 10017. Cable Address, "Mechaneer," New York. **Second-class** postage paid at New York, **CHANGES OF ADDRESS** must be received at Society headquarters seven weeks before they are to be effective. Please send old label and new address. **PRICES:** To members, $30.00, annually: to nonmembers, $60.00. Single copies, $20.00 each. Add $5.00 for postage to countries outside the United States and Canada.

STATEMENT from By-Laws. The Society shall not be responsible for statements or opinions advanced in papers or . . . printed in its publications (B7.1, Par. 3), **COPYRIGHT © 1981** by The American Society of Mechanical Engineers. Reprints from this publication may be made on condition that full credit be given the TRANSACTIONS OF THE ASME, JOURNAL OF FLUIDS ENGINEERING and the author, and date of publication be stated.

INDEXED by the Engineering Index, Inc.

Downloaded 03 Jun 2010 to 171.66.16.159. Redistribution subject to ASME license or copyright; see http://www.asme.org/terms/Terms_Use.cfm

Journal of Fluids Engineering

Editorial

The Spring 1981 Fluids Engineering Meeting was held June 22–24 at the University of Colorado in Boulder, Co. It was a very large meeting, labelled Joint Mechanics Conference, and was co-sponsored by the ASME Divisions of Fluids Engineering, Applied Mechanics, and Biomechanics, the ASCE Engineering Mechanics Division, and the Committee on Structures of the AIAA. Of the 400 papers presented, 185 were directly related to fluids engineering. The Technical Editor managed to miss all 185 of these, June 22 being the day set for the abortive air controllers' strike. When informed by the airlines that his flight was to be cancelled, the Technical Editor—decisive as ever—cancelled out. Shortly thereafter, the air traffic controllers, equally decisive, cancelled the strike. The remaining 800 attendees ignored the strike and had a good time at the meeting.

Our division offered three symposia at the Boulder meeting: Fluid Mechanics of Combustion, with 40 papers, Cavitation Erosion in Fluid Systems (16 papers), and 6 papers on Transient Fluid-Structure Interaction in Liquid Handling Systems. In addition, there were 20 papers on modelling of environmental systems, 30 papers on general fluid mechanics, 8 papers on vortex flows, 8 on hydrodynamic loading, 8 on computational fluid mechanics, 6 on rough surface boundary layers, 8 on turbulence modelling, and 15 on turbulent flows and statistical techniques. Finally, there were 20 papers in the Cavitation and Polyphase Flow Forum. If you missed them as we did, they are now available from ASME in New York, and many will no doubt make their way into the JFE eventually.

The Fluids Engineering Executive Committee has now approved a number of upcoming FED symposia extending to spring of 1983. The list is as follows:

A. Winter Annual Meeting, 1981, Washington, D.C.:
   1. Fluid-Structural Interactions in Turbomachinery
   2. Computers in Flow Predictions and Fluid Dynamic Experiments
   3. Materials of Construction of Fluid Machinery and Their Relation to Design and Performance

B. Spring 1982 Meeting, St. Louis, Mo:
   1. Measurements in Polyphase Flows
   2. Particulate Laden Gas Flows in Turbomachinery
   3. Three-Dimensional Turbulent Shear Flows
   4. Multiphase Heat and Mass Transfer Processes in Fluid Transients
   5. Fluid Flow and Heat Transfer in Tube Bundles

C. Winter Annual Meeting, 1982, Phoenix, Ariz:
   1. Engineering Applications of Laser Velocimetry
   2. Cavitation Noise
   3. Fluid Mechanics of Mechanical Seals

D. Spring 1983 Meeting, Houston, Texas:
   1. Return Passages of Multistage Turbomachinery

For further details and contact persons for these symposia, consult the JFE Calendar and the JFE Calls for Papers. At least 15 additional symposia are planned for 1983–1985.

Finally, on a very serious note, budget pressures and the increasing costs and sizes of *Transactions Journals* have caused the ASME Publications Committee to formulate a new policy on excess-page charges, shown below. All papers received in the JFE office after July 1, 1981 will be assessed a mandatory charge of $125 for each page in excess of six pages when printed in the JFE. From now on, prospective JFE authors should do their very best to hold their manuscripts to the 24-typed-page maximum to avoid these excess charges, which are payable before the paper is printed. We, of course, regret these charges but have no other way to balance our printing budget without greatly increasing subscription fees.

FRANK M. WHITE
TECHNICAL EDITOR

Effects of Free-Stream Turbulence on Diffuser Performance[1]

J. A. Hoffmann
Professor,
Aeronautical and Mechanical Engineering
Department,
California Polytechnic State University,
San Luis Obispo, Calif. 93407
Mem. ASME

An experimental evaluation of the effects of free-stream turbulence on the performance of a subsonic two-dimensional diffuser has been made. Increases of the diffuser's static pressure recovery coefficient of 11.3 and 23.9 percent at total included divergence angles of 12 and 20 degrees respectively were obtained when the value of the inlet integral free-stream scale of turbulence in the flow direction was at least 7.2 times larger than the inlet boundary layer displacement thickness, when the inlet total free-stream turbulence intensity was at least 3.5 percent, and when the axes of upstream rods used to generate turbulence were perpendicular to the flow and parallel to the diverging walls of the diffuser. It is hypothesized that a larger scale of turbulence with the specified eddy axis orientation transmits the free-stream energy to the walls more effectively and, when coupled with large turbulence intensities, are mechanisms which act to decrease the distortion and delay separation within the diffuser.

Introduction

A diffuser, one of the basic components of systems utilizing fluid flow, is a device in which the inlet dynamic pressure of a fluid is converted to a static pressure rise. For subsonic flow, this is done by decelerating the fluid by means of a gradual increase of the cross sectional flow area. An understanding of basic mechanisms which control diffuser performance will lead to the design of systems which employ techniques to utilize these mechanisms in improving the efficiency of fluid machines.

The literature contains many studies of diffuser performance such as those presented by Cockrell [1], McDonald [2), Sovran [3], and Fox and Kline [4]. When Moore and Kline [5] placed one rod ($D/W_1 = 1.25$) at the lip of a diffuser entrance with $2\Theta = 45$ deg, the existing stall was eliminated, and the pressure recovery coefficient increased from 0.3 to 0.575. Also, Waitman [6] placed a rod upstream of a diffuser and obtained a 21.5 percent increase in the peak pressure recovery of the diffuser and a 38 percent increase in the pressure recovery at $2\Theta = 20$ deg. More recently, Sajben [7] eliminated separation and increased the pressure recovery of a conical diffuser as much as 16 percent by mounting a cylinder near the entrance to the diffuser.

Vortex generators, normally used in flows with adverse pressure gradients, such as in diffusers and on airfoils, mix high energy air from outside the boundary layer, thereby delaying separation. The trailing vortex of the generators is the mixing mechanism. Vortex generator designs used to delay separation are described by Lachmann [8], Brown [9], Woolard [10], Taylor [11], Gadetskiy [12], and Senoo and Nishi [13].

In this investigation, experimentally determined free-stream turbulence parameters measured at the diffuser inlet will be correlated with diffuser performance in an attempt to obtain an understanding of basic mechanisms which improve diffuser performance.

Experimental Apparatus and Procedure

Experimental Apparatus. The experimental system used for the investigation is described by Hoffmann [14]. Air is drawn through the straight channel and two-dimensional straight-walled diffuser shown in Fig. 1. The channel width dimension, W_1, is 1.024 in. (2.60 cm). The channel height/inlet width ratio (b/W_1) is 5.86, the channel length/inlet width ratio (c/W_1) is 4.88, and the wall length ratio of the diffuser (L/W_1) is 14.7.

Equally spaced rods used for turbulence generation were placed between a baseplate and topplate upstream of the throat as illustrated in Fig. 2. The rod length/channel height ratio (b_o/b) was 1.71. Geometrical information about all upstream rod sets is presented in Table 1. The axes of the rods in rod sets GH, JH, and KH are parallel to the y axis, while the axes of all other rod sets are parallel to the z axis.

Velocity and turbulence measurements were obtained using constant temperature hot wire anemometers and associated instrumentation described by Hoffmann [14]. Inclined manometers were used for all pressure measurements.

Procedure. All data were taken with an inlet Reynolds number of 7.83×10^4; hot wire measurements were obtained at the diffuser inlet (section 1) with the diffuser walls removed and with the probe body aligned parallel to the flow.

Values of boundary layer displacement thickness (δ^*), momentum thickness (δ^{**}), and the shape factor (H), along with turbulence intensity profiles, were obtained using a single

---

[1] Prepared under NASA-ARC Grant #NSG-2391.

Contributed by the Fluids Engineering Division and presented at the Joint Applied Mechanics, Fluids Engineering, and Bioengineering Conference, Boulder, Colo., June 22-24, 1981, of THE AMERICAN SOCIETY OF MECHANICAL ENGINEERS. Manuscript received by the Fluids Engineering Division, June 27, 1980. Paper No. 81-FE-4.

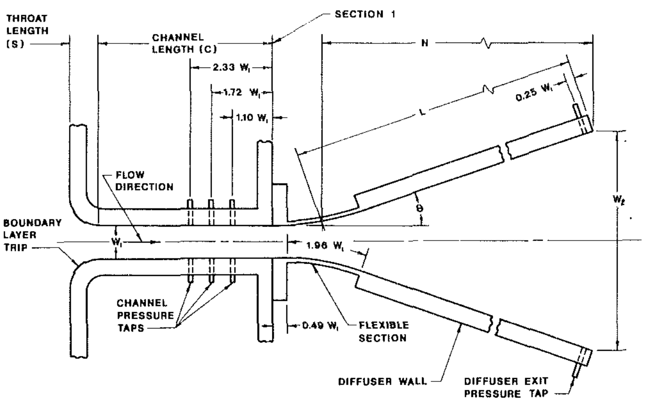

Fig. 1 Inlet, channel, and diffuser

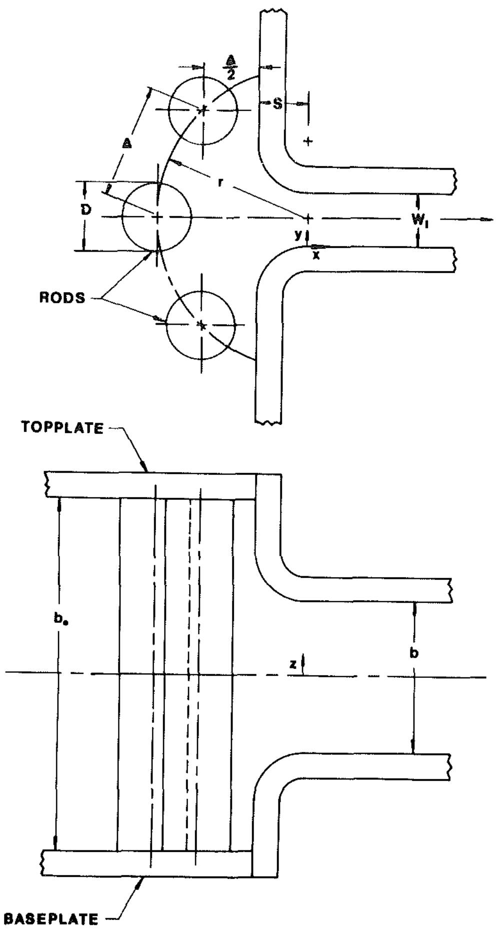

Fig. 2 Rod set geometry nomenclature

hot wire mounted in a micrometer traversing device. Free-stream turbulence intensities in the y and z directions were determined using both an X-wire probe and probes with single wires placed perpendicular and inclined 45 deg to the mean flow direction. Free-stream longitudinal correlation coefficients and spectral density measurements were obtained using a single hot wire placed normal to the flow. Values of the longitudinal integral scale of turbulence (λ_x) were obtained by integration of the area under curves of the longitudinal correlation coefficient (R_x) versus a distance corresponding to the time delay of the hot wire signal (Taylor's hypothesis [15]).

The pressure rise across the diffuser was determined by taking the difference between the pressure from taps at the diffuser exit and the pressure at the exit of the channel (section 1), obtained by extrapolating the static pressures measured in the inlet channel using a power law relationship for boundary layer growth ($\delta^* \sim x^{0.8}$) (16). The correction associated with this extrapolation increased C_p by a maximum of 1.4 percent. A pressure loss coefficient across the rods (C_o) was experimentally obtained for each rod set and was found to have a maximum value of 2.2 percent. This pressure loss, along with a pressure differential between the pressure from taps located in the topplate and baseplate upstream of the rods and the extrapolated pressure at section 1, was used to determine the free-stream channel velocity and corresponding value of inlet mass average velocity.

Nomenclature

AR = diffuser area ratio, W_2/W_1
b = distance between parallel walls of diffuser
b_o = rod length
c = channel length
C_p = static pressure recovery coefficient, $(P_2-P_1)/\rho\overline{U}^2/2$
C_o = pressure loss coefficient across rods, $\Delta P_o/\rho\overline{U}^2/2$
D = rod diameter
H = shape factor, δ^*/δ^{**}
L = diffuser wall length
n = number of rods
N = diffuser axial length
P = static pressure
$\sqrt{\overline{q'^2}}$ = total RMS turbulence quantity, $\sqrt{(\overline{u'^2}+\overline{v'^2}+\overline{w'^2})/3}$
r = radius of rod set geometry
$\mathrm{R_e}$ = Reynolds number, $\overline{U}W_1/\nu$
R_x = free-stream autocorreleation coefficient in flow direction at diffuser inlet, $\overline{u'(x)u'(x-\Delta x)}/\overline{u'^2}$
S = throat section dimension (see Fig. 1)
$\bar{u}$ = average velocity in flow direction at diffuser inlet
u' = turbulence component in flow direction at diffuser inlet
$\overline{U}$ = mass average velocity at diffuser inlet
U_m = average free-stream velocity in flow direction at diffuser inlet
v' = turbulence component in y direction at diffuser inlet
W = diffuser width measured between diverging walls
w' = turbulence component in z direction at diffuser inlet
δ = boundary layer thickness at diffuser inlet
δ^* = boundary layer displacement thickness at diffuser inlet
δ^{**} = boundary layer momentum thickness at diffuser inlet
Θ = divergence angle of diffuser wall
ν = kinematic viscosity
λ_x = free-stream integral scale of turbulence at diffuser inlet in x direction, $\int_0^\infty R_x dx$
ρ = fluid density

Subscripts

0 = location of rods
1 = diffuser inlet ($0.49W_1$ upstream from beginning of diffuser wall curvature)
2 = diffuser exit
x = flow direction
y = direction normal to the flow and parallel to the parallel walls of the diffuser
z = direction normal to the flow and perpendicular to the parallel walls of the diffuser

Table 1

Rod Set	D/W_1	r/W_1	n	$C_p(2\theta = 12^o)$	$C_p(2\theta = 20^o)$	$\sqrt{\overline{u'^2}}/U_m(\%)$	$\sqrt{\overline{v'^2}}/U_m(\%)$	$\lambda x/\delta^*$
None	-	-	0	0.705	0.577	0.57	0.57	-
A	0.18	2.93	19	0.713	0.583	1.75	3.02	4.28
B	0.18	4.39	35	0.709	0.594	1.31	2.89	6.10
C	0.37	2.93	11	0.751	0.658	2.03	4.05	4.35
D	0.37	3.90	11	0.736	0.631	1.58	3.60	6.95
E	1.28	2.93	3	0.765	0.674	3.07	5.49	6.38
F	1.28	4.39	5	0.798	0.703	2.10	4.46	7.53
G	1.28	5.85	7	0.782	0.687	1.28	3.83	8.37
GH	1.28	5.85	7	0.737	0.635	2.53	6.05	9.07
H	1.28	5.51	7	0.773	0.679	1.53	3.89	7.92
I	4.39	8.78	3	0.756	0.616	0.80	2.87	10.55
J	4.39	7.80	3	0.778	0.682	1.14	3.43	11.61
JH	4.39	7.80	3	0.754	0.686	2.76	7.53	9.71
K	4.39	9.76	5	0.793	0.713	2.05	6.32	9.17
KH	4.39	9.76	5	0.773	0.699	2.99	8.91	10.26
L	4.39	6.83	3	0.792	0.702	2.14	5.87	10.27
M	1.83	3.73	3	0.785	0.717	3.02	6.42	7.21
N	2.99	7.32	5	0.788	0.715	1.76	4.51	10.94

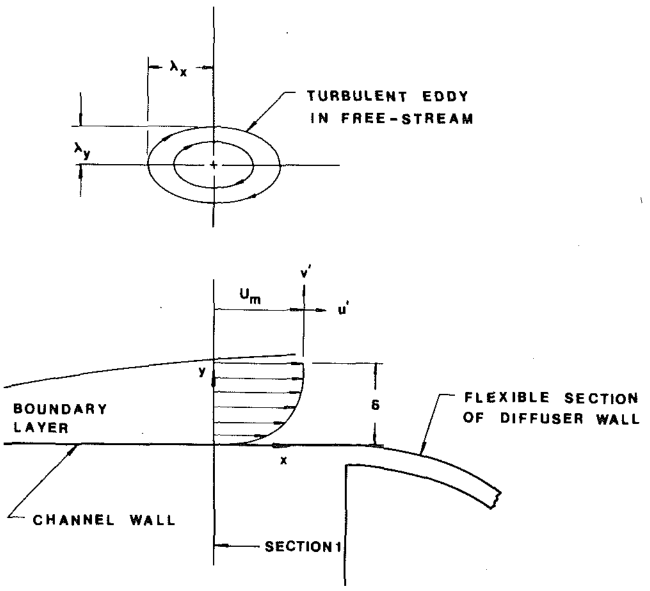

Fig. 3 Two-dimensional schematic of flow characteristics at diffuser inlet

Results and Discussion

Inlet flow characteristics, pressure recovery measurements, and correlations between the pressure recovery and inlet free-stream turbulence parameters are discussed below. A representation of the flow characteristics at the diffuser inlet is presented in Fig. 3.

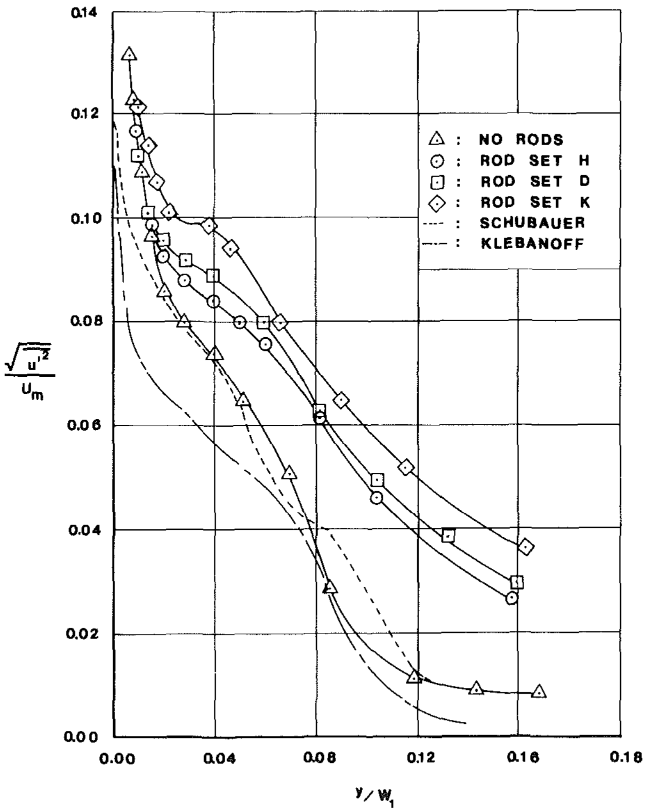

Fig. 4 Inlet boundary layer longitudinal turbulence profiles

Inlet Velocity and Longitudinal Turbulence Profiles. The average dimensionless inlet blockage parameter, $2\delta^*/W_1$, obtained from the velocity profiles was 0.040 for all rod sets except rod sets GH, JH and KH, for which it was 0.034. The average shape factor (H) obtained for all rod sets was 1.56, a reasonable value for a turbulent boundary layer in the final stage of transition. Small changes in the velocity profile of a turbulent boundary layer when free-stream longitudinal turbulence intensities were varied to 4 percent were also observed by Kline [17]. The estimated uncertainties in $2\delta^*/W_1$ and H, obtained using the method of Kline and

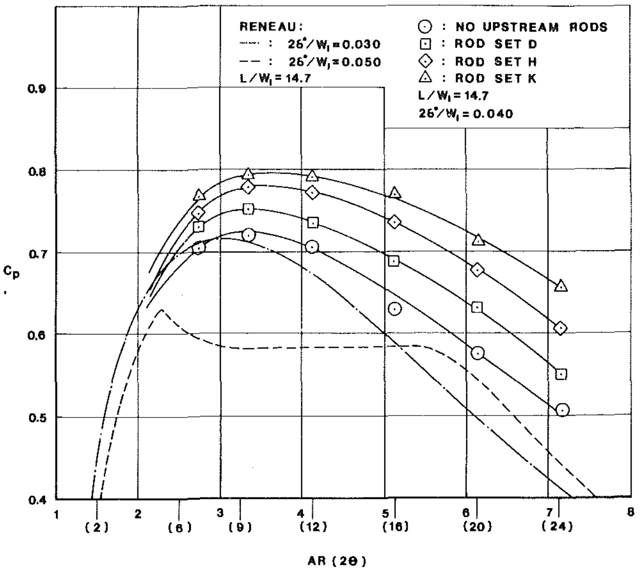

Fig. 5 Comparison of static pressure recovery coefficient versus area ratio curves

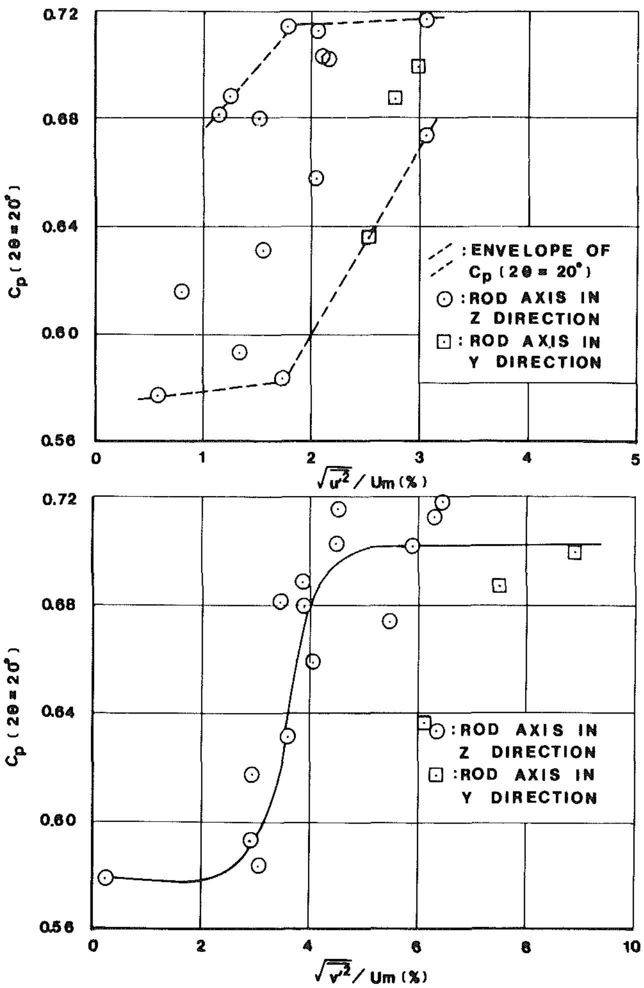

Fig. 6 Static pressure recovery coefficient versus inlet free-stream longitudinal turbulence intensity and inlet free-stream turbulence intensity in *y* direction

McClintock [18] with 20:1 odds, were ±5 percent for the no rod case and rod sets A through D, and were ±10 percent for rod sets E through N.

Longitudinal turbulence intensity profiles within the boundary layer are presented in Fig. 4. The results, which agree with those of Ahmad [19], indicate that the free-stream turbulence significantly affects the turbulent structure of the boundary layer. Turbulence intensity profiles obtained by Klebanoff [20] and Schubauer [21] for low free-stream turbulence levels demonstrate a reasonably good agreement with the results of this study for the case of no upstream rods.

All velocity profiles exhibit a uniform core velocity in the center 75 percent of the channel. The region of uniform turbulence intensities varied from the center 70 percent of the channel for the no rod condition, to the center 30 percent of the channel for rod sets with $D/W_1 = 4.39$.

Free-Stream Turbulence Parameters. Values of the turbulence intensity in the flow direction ($\sqrt{\overline{u'^2}}/U_m$) and in the y direction ($\sqrt{\overline{v'^2}}/U_m$) for all rod sets are presented in Table 1. The estimated uncertainties in the measurements are ±5 percent for rod sets A through H and ±10 percent for the no rod case and rod sets I through N. The free-stream turbulence intensities obtained using the single wire method agree well with those obtained using the X-wire. The average value of $\sqrt{\overline{w'^2}}/\sqrt{\overline{v'^2}}$ was 0.80 for all rod sets. The estimated uncertainties in the total turbulence intensity ($\sqrt{\overline{q'^2}}/U_m$) are ±7 percent for rod sets A through H and ±14 percent for the no rod case and rod sets I through N.

Spectral density and correlation coefficient curves for the longitudinal component of turbulence are presented by Hoffmann [14]. The spectral density curves show a broadband turbulence without peaks of power at any one frequency. Values of the dimensionless integral scale of turbulence (λ_x/δ^*) are presented in Table 1. The estimated uncertainty in this quantity varies from ±10 percent for rod sets A through D to ±15 percent for rod sets E through N.

Diffuser Performance. Data for C_p at $2\Theta = 12$ and 20 deg for all of the rod sets are presented in Table 1; the results have estimated uncertainties of ±5 percent. Typical C_p versus 2Θ curves are presented in Fig. 5. The results of Reneau [22] at a value of $2\delta^*/W_1 = 0.040$ (an average of Reneau's results at values of $2\delta^*/W_1 = 0.030$ and 0.050) compare favorably to those for the case of no upstream rods at $2\Theta \leq 4$ deg, but are as much as 11 percent lower in the region of peak pressure recovery. The agreement seems reasonable considering that the results presented by Reneau are correlations of measurements from a wide variety of data and that geometrical differences (e.g., the length of the flexible section of the diffuser's throat) may exist between various test systems. The results also indicate that increases in C_p of 23.6 percent at $2\Theta = 20$ deg and 12.5 percent at $2\Theta = 12$ deg are obtained for the K rod set as compared to the no rod case. The peak pressure recovery was increased 9.8 percent and the value of 2Θ corresponding to the peak value of C_p increased approximately 1.5 deg. Since all rod geometries produce essentially the same velocity profile at the diffuser inlet, the increase in C_p can be attributed to differences in inlet turbulence quantities.

Values of C_p at $2\Theta = 20$ deg are presented as a function of $\sqrt{\overline{u'^2}}/U_m$, $\sqrt{\overline{v'^2}}/U_m$, $\sqrt{\overline{q'^2}}/U_m$, and λ_x/δ^* in Figures 6 and 7. The values of C_p appear relatively insensitive to $\sqrt{\overline{u'^2}}/U_m$, and λ_x/δ^*. The results show that generally larger values of C_p are obtained as values of $\sqrt{\overline{v'^2}}/U_m$ and $\sqrt{\overline{q'^2}}/U_m$ are increased, but the trend is not consistent (e.g., rod sets E and GH produce relatively high turbulence intensities, but the corresponding values of C_p are lower than those obtained with some rod sets producing lower turbulence intensities). The results show that a threshold turbulence intensity in the y direction of about 3 percent or a total tur-

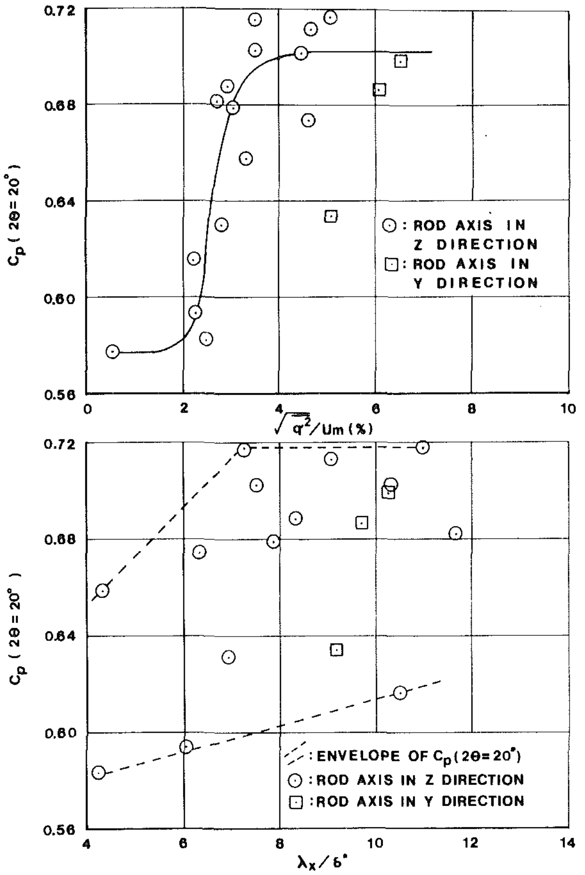

Fig. 7 Static pressure recovery coefficient versus inlet free-stream total turbulence intensity and dimensionless inlet free-stream integral scale of turbulence in flow direction

bulence intensity of about 2 percent is required to obtain increases in C_p. All of the largest values of C_p (C_p ($2\Theta = 20$ deg) ≥ 0.699) were obtained with values of $\sqrt{\overline{v'^2}}/U_m$ and $\sqrt{\overline{q'^2}}/U_m$ equal to or larger than 4.46 and 3.47 percent respectively, and with values of $\lambda_x/\delta^* \geq 7.21$ (or with $\lambda_x \geq 1.2\delta$).

Figure 8 was constructed to examine a possible correlation between C_p, λ_x/δ^* and $\sqrt{\overline{q'^2}}/U_m$. Values of $C_p(2\Theta = 20$ deg) are listed next to each data point along with, in parentheses, values of C_p ($2\Theta = 12$ deg). The implication of this figure is that a larger scale of turbulence more effectively transfers free-stream turbulent energy to the diffuser walls and, when coupled with larger values of total turbulence intensity, apparently results in a decrease of the distortion within the diffuser and delays separation, which correspondingly produces increased pressure recovery. Data for rods with axes in the y direction do not fit the indicated contours. Comparing two rod sets with relatively large values of $\sqrt{\overline{q'^2}}/U_m$ and λ_x/δ^* but different rod axis orientations, a 23.6 percent increase in C_p ($2\Theta = 20$ deg) is obtained for rod set K, whereas a 10.1 percent increase is obtained for rod set GH. The curves of Fig. 8 indicate that in order to obtain increases of $C_p(2\Theta = 20$ deg) of 23.9 percent and increases of $C_p(2\Theta = 12$ deg) of 11.3 percent, minimum values of λ_x/δ^* and $\sqrt{\overline{q'^2}}/U_m$ must be 7.2 and 3.5 percent respectively, and the axes of the rods and corresponding predominant axes of the eddies must be perpendicular to the flow and parallel to the diverging walls of the diffuser. For the range of parameters studied, values of C_p depend only upon $\sqrt{\overline{q'^2}}/U_m$ when $\lambda_x/\delta^* \geq 8$. A study by Arnel [23] of the effect of free-stream turbulence on a boundary layer using free-stream total turbulence intensities of about 5 percent showed a decrease in the shape factor of the boundary layer which would correspondingly delay separation.

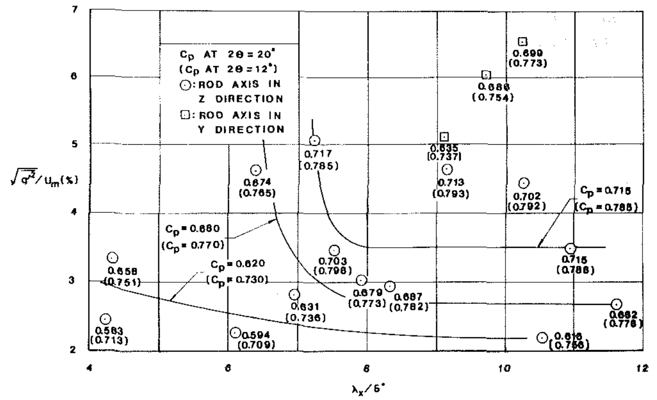

Fig. 8 Inlet free-stream total turbulence intensity versus inlet free-stream dimensionless integral scale of turbulence with static pressure recovery coefficient contours

The results of this preliminary study suggest that the free-stream scale of turbulence, the total turbulence intensity, and the orientation of the axes of the eddies are important parameters, but these may not be the only parameters affecting diffuser performance (or the delay of separation for the case of external flows). In this limited study, values of the integral scale of turbulence in the y and z directions were not measured; also $\sqrt{\overline{v'^2}}/\sqrt{\overline{w'^2}}$ was relatively constant and $\sqrt{\overline{v'^2}}/\sqrt{\overline{u'^2}} \geq 1.73$ for all rod sets. It was observed that the free-stream turbulence altered the turbulence structure of the boundary layer; perhaps other means of altering the turbulence structure of the boundary layer would result in similar improvements in diffuser performance.

Conclusions

An experimental investigation of the influence of free-stream turbulence on the performance of a subsonic two-dimensional diffuser with a wall length/inlet width ratio of 14.7 has been made. The diffuser's pressure recovery coefficient at a total included divergence angle of 20 deg was increased 23.9 percent, the peak pressure recovery coefficient was increased 9.8 percent, and the total included divergence angle corresponding to the peak pressure recovery coefficient was increased approximately 1.5 degrees when values of the inlet free-stream integral scale of turbulence in the flow direction were greater than 7.2 times the inlet boundary layer displacement thickness, and when the inlet total turbulence intensity was greater than 3.5 percent; from the limited data obtained, eddy axis orientation in the direction perpendicular to the flow and parallel to the diverging walls of the diffuser apparently more effectively transmits turbulent energy to the diffuser walls. The free-stream turbulence was found to significantly affect the turbulence intensities within the boundary layer but did not significantly alter the velocity profile of the boundary layer at the diffuser's inlet. The results of the study suggest basic mechanisms that can be used to delay separation. These may be applicable for both internal and external flows for improvement of heat transfer and/or lift, drag, or pressure recovery coefficients when the turbulence is generated with low losses (e.g., near stagnation regions).

Acknowledgments

This project was sponsored by NASA-ARC Grant #NSG-2391. The author gratefully acknowledges the work of graduate students Masao Fukuda, Yu Hang Ho, and James

Ross, and of student assistants Michael Dudley, John McCrillis, Michael Reinath, and Philip Snyder.

References

1 Cockrell, D. J., and Markland, E., "A Review of Incompressible Diffuser Flow," *Aircraft Engineering,* Vol. 35, Oct. 1963, pp. 286-292.

2 McDonald, A. T., and Fox, R. W., "An Experimental Investigation of Incompressible Flow in Conical Diffusers," ASME Paper No. 65-FE-25, 1965.

3 Sovran, G., and Klomp, E. D., "Experimentally Determined Optimum Geometries for Rectilinear Diffusers with Rectangular, Conical, or Annular Cross-Section," from *Fluid Mechanics of Internal Flow,* edited by G. Sovran, Elsevier Publishing Co., Amsterdam, 1967, pp. 270-319.

4 Fox, R. W., and Kline, S. J., "Flow Regime Data and Design Methods for Curved Subsonic Diffusers," ASME, *Journal of Basic Engineering,* Vol. 84, 1962, pp. 303-312.

5 Moore, C. A., Jr., and Kline, S. J., "Some Effects of Vanes and of Turbulence on Two-Dimensional Wide Angle Subsonic Diffusers," Department of Mechanical Engineering, Stanford University, Sept. 1, 1955.

6 Waitman, B. A., Reneau, L. B., and Kline, S. J., "Effects of Inlet Conditions on Performance of Two-Dimensional Diffusers," *Journal of Basic Engineering,* Vol. 83, 1961, pp. 349-360.

7 Sajben, M., Chen, Ç. P., and Kroutel, J. C., "A New Passive Boundary Layer Control Device," *Journal of Aircraft,* Vol. 14, No. 7, July 1977, pp. 654-660.

8 Lachmann, G. V., *Boundary Layer and Flow Control,* Vol. 2, Pergamon Press, New York, 1961.

9 Brown, A. C., Nawrochi, H. F., and Palez, P. N., "Subsonic Diffusers Designed Integrally with Vortex Generators," *Journal of Aircraft,* Vol. 5, No. 3, May/June 1968, pp. 221-229.

10 Woodard, H. W., Benson, J. L., Stroud, J. F., and Drell, H., "Boundary Layer Forced Mixing Investigation—Literature Survey and Progress Report," Lockheed California Co., Report LR 18478, Nov. 1965.

11 Taylor, H. D., "Application of Vortex Generator Mixing Principles to Diffusers," Concluding Report, United Aircraft Corp., Research Dept., Report R-15064-5, Dec. 31, 1948.

12 Gadetskiy, V. M., Serebrizskig, Ya. M., and Fomin, V. M., "Investigation of the Influence of Vortex Generators on Turbulent Boundary Type Separation," NASA Technical Trans., NASA TT-F-16, 056, 1972.

13 Senoo, Y., and Nishi, M., "Improvement of the Performance of Conical Diffuser by Vortex Generators," ASME JOURNAL OF FLUIDS ENGINEERING, Vol. 96, Mar. 1974, pp. 4-10.

14 Hoffmann, Jon A., "Effects of Free-Stream Turbulence on Diffuser Performance," NASA-CR-163194, Jun. 1980.

15 Hinze, J. O., *Turbulence,* 2nd edition, McGraw-Hill, New York, 1975.

16 Schlichting, Hermann, *Boundary Layer Theory,* 6th edition, McGraw-Hill, New York, 1968.

17 Kline, S. J., Lisin, A. V., and Waitman, B. A., "Preliminary Experimental Investigation of Effects of Free Stream Turbulence on Turbulent Boundary Layer Growth," NASA TN D-368, Mar. 1960.

18 Kline, S. J., and McClintock, F. A., "Describing Uncertainties in Single Sample Experiments," *Mechanical Engineering,* Jan. 1953, pp. 3-8.

19 Ahmad, Q. A., Luxton, R. E., and Antonia, R. A., "Characteristics of a Turbulent Boundary Layer with an External Turbulent Uniform Shear Flow." *Journal of Fluid Mechanics,* Vol. 37, Part 2, 1976, pp. 369-396.

20 Klebanoff, P. S., "Characteristics of Turbulence in a Boundary Layer with Zero Pressure Gradient," NACA Rep. No. 1247, 1955.

21 Schubauer, G. B., "Turbulent Processes as Observed in Boundary Layer and Pipe Flow," *Journal of Applied Physics,* Vol. 25, No. 2, Feb. 1954.

22 Reneau, L. R., Johnston, J. P., and Kline, S. J., "Performance and Design of Straight, Two-Dimensional Diffusers," ASME Paper No. 66-FE-10, Apr. 1966.

23 Arnal, D., Cousteix, J., and Michel, R., "Couche Limite se Developpant Avec Gradient de Pression Positif Dans un Ecoulement Exterieur Turbulent," *Resh. Aerospatiale* (Janvier-Fevrie 1976), pp. 13-26.

K. E. Hansen
Mechanical Engineer,
Alpha Diesel A/S,
DK-9900 Frederikshavn, Denmark

P. Jørgensen
Danfoss A/S,
DK-6430 Nordborg, Denmark

P. S. Larsen
Associate Professor,
Fluid Mechanics Department,
Technical University of Denmark,
DK-2800 Lyngby, Denmark

Experimental and Theoretical Study of Surge in a Small Centrifugal Compressor

Experimental results for deep surge in a small single-stage centrifugal compressor are compared to predictions based on the lumped parameter Greitzer model developed for axial compressors. Both negative and positive flow branches of the steady characteristic, being essential for the model, were measured. Predictions are in fair agreement with data when using a relaxation time smaller than the one proposed for axial compressors. The stability limit of the model equations have been studied for finite amplitude disturbances.

Introduction

The occurrence of surge cycles in a compression system is associated with a dynamic instability in which the compressor feeds energy into the oscillations. During the recovery period the system plenum is refilled while the flowrate decreases. As the stall limit is reached strong pressure fluctuations precede eventual breakdown of flow in all channels causing flow reversal. In deep surge the order of magnitude of negative flowrates is comparable to that of positive flowrates. As pressure decreases and flowrate approaches zero with a different kind of breakdown, positive flow is rapidly reestablished, and the cycle repeats itself. The frequency of oscillation depends primarily on plenum volume and ducting of the system and it is on the order of the Helmholtz resonator frequency of the system. The speed of the compressor remains essentially constant during surge.

The overall dynamics of surge and rotating stall in axial flow compression systems has been studied theoretically and experimentally by Greitzer [1, 2]. A nonlinear lumped-parameter model was found to describe a variety of large amplitude oscillations in the real time domain. It also served to identify the stability limit for the stall/surge transition. To predict experimentally observed deep surge cycles by the model it was found to be necessary to supplement the measured steady-state compressor characteristic for positive flow with a negative flow branch extracted from surge data. The model includes a first order relaxation equation which describes phenomenologically the transient compressor response to departures from steady-state operation. In their discussion of this work Bammert and Mobarak [3] reported results of their study of the linearized model equations in regard to system stability. Their experimental study of a highly loaded centrifugal compressor emphasized on detailed pressure measurements used to interpret the various phases of a surge cycle.

Several studies [4 - 6] have pursued further the role played by the diffusor flow in regard to incipient stall and flow breakdown. However, neither a complete picture of mechanisms at play, nor an applicable quantitative flow model describing the rate of flow breakdown appears to be available at this time to assist in the prediction of overall surge behavior. Progress is being made, however, on predicting the performance of multistage axial flow compressors during various degrees of rotating stall [7]. Nevertheless, for an engineering application in system dynamics analyses a lumped parameter model, such as that of Greitzer, remains of considerable interest. The model may be employed, for example, to study staged compressor dynamics of large heat pump systems during start-up and load changes, to establish stable operation procedures.

It has been the purpose of the present study to further explore the Greitzer model and test its applicability to describe surge in a small single-stage centrifugal compressor. Specifically, it was of interest to see if the dynamic behavior could be predicted alone based on measured steady-state branches of the compressor characteristic, supplemented by a simple assumption regarding the relaxation time appearing in the model.

Surge Model

The compressor system comprising a short inlet, the compressor, the discharge line (plenum) and a throttle valve (Figure 1) is modelled by the nonlinear lumped parameter equations derived by Greitzer [1]. Using the same notation we have, in dimensionless form,

$$d\dot{\tilde{m}}_c/d\tilde{t} = (\tilde{C}-\Delta\tilde{P})B \qquad (1a)$$

$$d\dot{\tilde{m}}_T/d\tilde{t} = (\Delta\tilde{P}-\tilde{F})B/G \qquad (1b)$$

$$d\Delta\tilde{P}/d\tilde{t} = (\dot{\tilde{m}}_c-\dot{\tilde{m}}_T)/B \qquad (1c)$$

Contributed by the Fluids Engineering Division and presented at the Joint Applied Mechanics, Fluids Engineering, and Bioengineering Conference, Boulder, Colo., June 22-24, 1981, of THE AMERICAN SOCIETY OF MECHANICAL ENGINEERS. Manuscript received by the Fluids Engineering Division, July 21, 1980. Paper No. 81-FE-1.

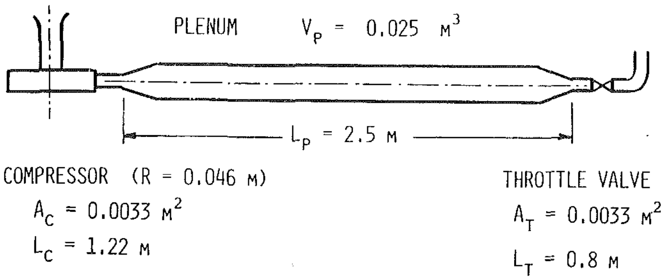

Fig. 1 Compression system geometry

$$d\tilde{C}/d\tilde{t} = (\tilde{C}_{ss} - \tilde{C})/\tilde{\tau}, \qquad (1d)$$

where system parameters are given by

$$B = [U/(2a)][V_P/(A_c L_c)]^{1/2} \qquad (2a)$$

$$G = (L_T/A_T)/(L_c/A_c) \qquad (2b)$$

$$\tilde{F} = S\dot{m}_T^2 \qquad (2c)$$

$$\tilde{\tau} = (\pi RN)/(L_c B) \qquad (2d)$$

Equations $(1a)-(1d)$ constitute, respectively, the momentum balance for the compressor ducting, the momentum balance for the throttle ducting, the mass balance for the plenum, and the relaxation equation describing the compressor response to departure from steady state. The compressor ducting and plenum volume constitute a Helmoholtz resonator with frequency $\omega = a[A_c/(V_p L_c)]^{1/2}$. Time has been made dimensionless with respect to ω. In equations $(2a)-(2d)$ the system parameter B is proportional to the ratio of the Helmholtz resonator period and the transport time through the compressor ducting, G is the ratio of equivalent length to area ratios for throttle and compressor ducts, $\tilde{F}$ the throttle valve characteristic, and $\tilde{\tau}$ the time lag parameter.

Given the geometry of the system, the steady-state compressor characteristic $\tilde{C}_{ss}(\dot{m}_c)$, the valve characteristic and a relaxation time $\tilde{\tau}$, equations (1) may be solved by numerical integration starting from specified initial conditions. In case these conditions represent a steady operating point below the stall limit a stationary solution will result. However, selecting a valve parameter corresponding to a point beyond the stall limit – or introducing a large perturbation when close to the stall limit – the time evaluation of the solution describes periodic surge cycles.

Test Stand and Steady-State Characteristic

The single-stage centrifugal compressor of a small turbocharger (Holset type 4LE-556, 52168 with a vaned radial diffusor and 0.092 m diameter impeller) was driven by cold shop air supplied to the turbine. The compression system was open to the ambient at compressor inlet and downstream of the throttle valve. The test stand only permitted operation at compressor speeds below that of maximum efficiency at 60 - 65,000 rpm.

In addition to standard steady-state instrumentation for measuring characteristics and slow transients the compressor was equipped with hot-wire probes positioned to the core of the flow at inlet and exit flanges and with strain-gauge type pressure transducers for static and stagnation pressure measurements, both at flanges and at various points in the radial diffusor. Comparing simultaneous recordings of pressure and hot-wire signals the flow direction associated with hot-wire signals could always be unambigurously interpreted. Transient signals were A/D-converted (12-bit) and stored on-line in a computer for later comparison with theory.

To measure the negative branch of the steady-state characteristic shop air was fed to the compressor exit to force a steady negative flow. The negative flow branch was accurately matched with a parabola. The positive branch required a cubic polynomial. The connecting unstable and unmeasureable branch, assumed to be a smooth curve, was approximated by a cubic polynomial. For the two compressor speeds studied (30,000 and 54,000 rpm) the dimensionless characteristics closely coincided and could be represented by the equations

$$\dot{m}_c \leq 0 \quad : \tilde{C}_{ss} = 21.9\,\dot{m}_c^2 + 0.85 \qquad (3a)$$

$$0 \leq \dot{m}_c \leq 0.152:$$

$$\tilde{C}_{ss} = -254\,\dot{m}_c^3 + 58\,\dot{m}_c^2 + 0.85 \qquad (3b)$$

$$0.152 < \dot{m}_c:$$

$$\tilde{C}_{ss} = -69\,\dot{m}_c^3 + 25.6\,\dot{m}_c^2 - 3\,\dot{m}_c + 1.4. \qquad (3c)$$

Surge Measurements

At each of the two compressor speeds investigated, starting from steady state near the stall limit, the throttle valve was closed slightly to initiate stall and surge. Close to the stall limit the characteristic pressure fluctuations reported elsewhere [2, 3] were observed both in the signals of total pressure rise and at the pressure taps in the radial diffusor. However, it was impossible to operate at such conditions for extended periods. The compressor invariably went into surge cycles involving pronounced flow reversal. It was not possible to clearly identify classic surge as opposed to deep surge [1]. Surge could be established to speeds as low as 7 - 9000 rpm.

Figures $2(a)$ and $3(a)$ show the recorded time evolution of the dimensionless mass flow $\dot{m}_c = C_X/U$ and pressure rise $\Delta\tilde{P} = \Delta P/(\rho U^2/2)$. In Figures $2(b)$ and $3(b)$ the recorded data points are plotted in the dimensionless compressor map. The measured stable branches and the estimated unstable

Nomenclature

a = speed of sound at ambient
A = flow area
B = dimensionless parameter, equation $(2a)$
C_X = velocity at inlet axis
$\tilde{C}$ = pressure rise in compressor, $= \Delta p_c/(1/2\rho U^2)$
$\tilde{F}$ = throttle characteristic, equation $(2c)$
G = geometric parameter, equation $(2b)$
L = effective length of equivalent ducting
$\dot{m}$ = mass flow parameter, $= C_X/U$
N = time lag in revolutions
p = pressure
Δp = pressure difference between plenum and ambient
$\Delta\tilde{P}$ = $\Delta p/(1/2\rho U^2)$
R = impeller tip radius
S = valve parameter, $= (A_c/A_v)^2$
$\tilde{t}$ = dimensionless time, $= \omega t$
U = impeller tip speed
V_P = plenum volume
ρ = density at ambient
$\tilde{\tau}$ = compressor flow relaxation time, equation $(2d)$
ω = Helmholtz frequency, $= a[A_c/(L_c V_p)]^{1/2}$

Subscripts

c = compressor
p = plenum
ss = steady-state
T = throttle valve ducting
v = valve throat

Superscripts

~ = dimensionless variable

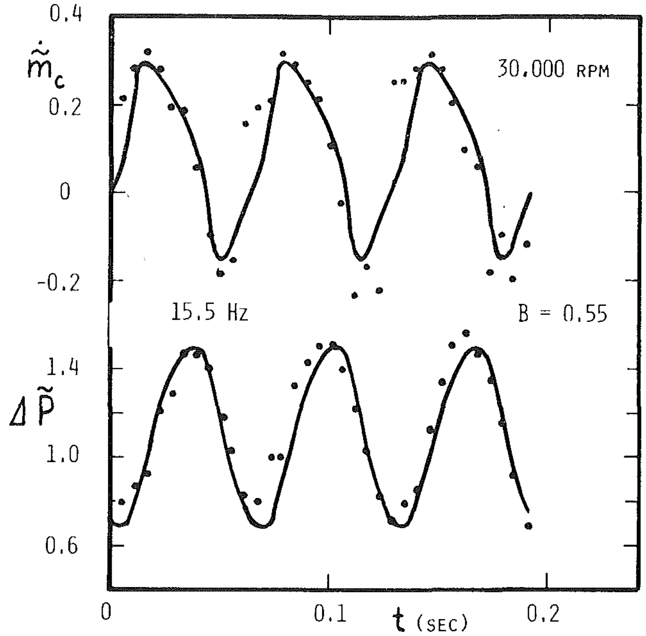

Fig. 2(*a*) Compression system surge at 30,000 ± 300 rpm. Model ——, experiment by pressure transducer and inlet hot-wire •. Uncertainty estimates (by limited sample uncertainty propagation, including fixed errors):

$\tilde{\dot{m}}_c$ = 0.18 ± 0.02 and −0.10 ± 0.04

$\Delta\tilde{P}$ = 1.48 ± 0.03 and 1.40 ± 0.03; t ± 0.005s.
Frequency: 15.5 ± 0.3 Hz.

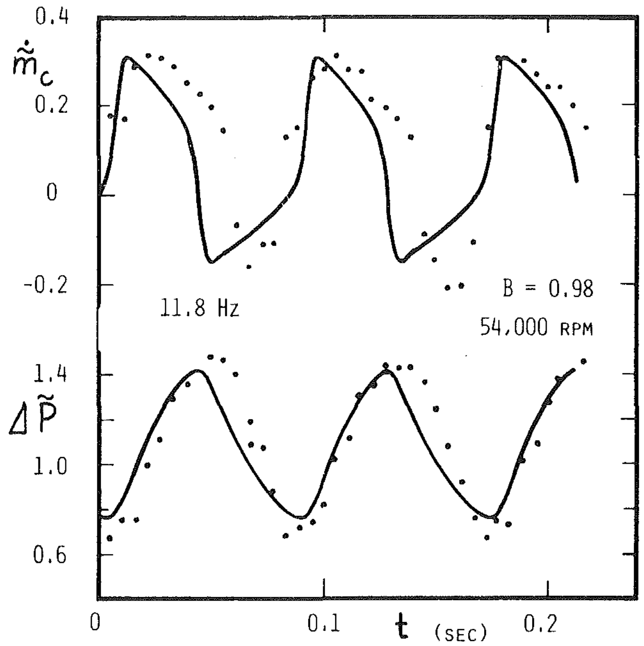

Fig. 3(*a*) Compressor system surge at 54,000 ± 300 rpm. Model ——, experiment • (see legend of Fig. 2(*a*)). Frequency: 11.8 ± 0.5 Hz.

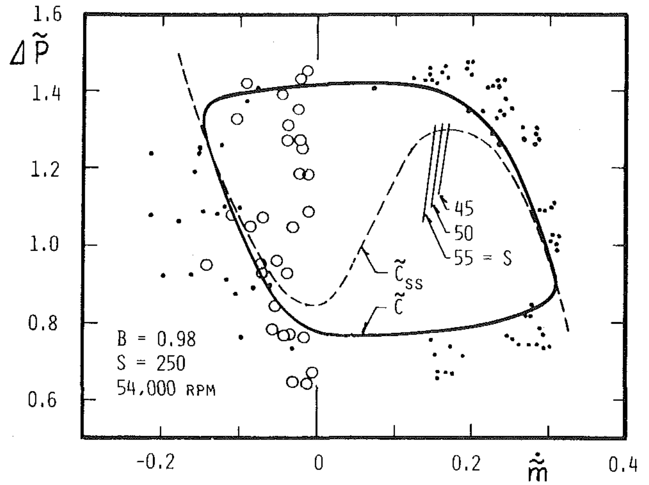

Fig. 3(*b*) Dimensionless steady-state characteristic – – – –, surge model ——, experiment • o (see legend of Fig. 2(*b*)). 54,000 ± 300 rpm.

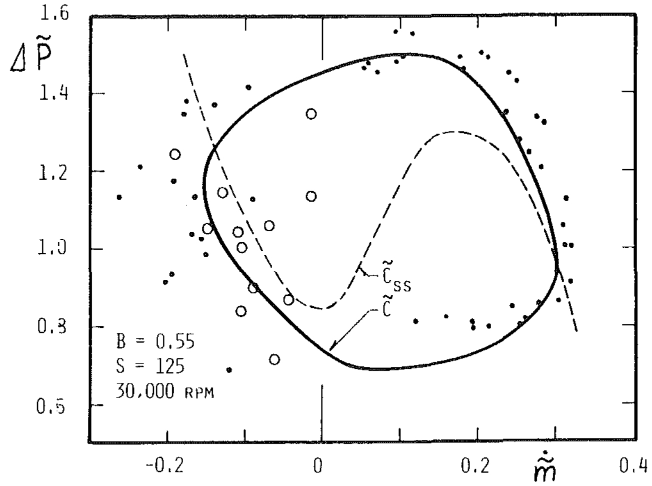

Fig. 2(*b*) Dimensionless steady-state characteristic – – – –, surge model——, experiment by pressure transducer and inlet hotwire •, negative flow by exit hot-wire o. 30,000 ± 300 rpm. For uncertainty estimates, see legend of Fig. 2(*a*).

branch given by equations (3) are also shown in these figures. The sample frequency of the data acquisition system was only 250 Hz and a considerable number of cycles were required to ensure data in the ranges of flow breakdown and reversal where the rate-of-change of mass flow was rapid. The spacing of data points is indicative of the rate of change.

Since $\tilde{\dot{m}}_c$ was calculated from velocity measured by a single hot-wire probe respectivley at inlet and exit of the compressor the data show considerable scatter, particularly at negative flow. Here, the velocity measurements at the exit were influenced by the nonuniformities of the flow returning from the plenum. Similarly, the velocity measurements at the inlet were subjected directly to the non-uniformities (swirl, large eddies) of the reversed flow through the impeller. The data may therefore reflect cyclic variations. At positive flow, however, an essentially undisturbed flow meets the hot-wire at the inlet. Data points indicated by solid circles in Figs. 2 and 3 are based on mass flow calculated from velocity measured by the inlet hot-wire for both positive and negative flows. Data points indicated by open circles in Figs. 2(*b*) and 3(*b*) are based on velocity measured by the exit hot-wire, but recorded only for negative flows. Samples of uncertainty estimates given in the legend to Fig. 2(*a*) also apply to Fig. 2(*b*) and are representative for the data in Figs. 3(*a*) and 3(*b*). Uncertainty estimates on rpm and frequency of oscillations are given in legends to figures.

The frequency of surge cycles remained constant in a given test and reproducible between tests. It was 15.5 Hz and 11.8 Hz, respectively, at 30,000 and 54,000 rpm. The decreasing values with increasing speed confirmed the trend observed by Bammert and Mobarak [3]. The Helmholtz resonator frequency of the system was $\omega/2\pi = 17.3$ Hz. It is to be

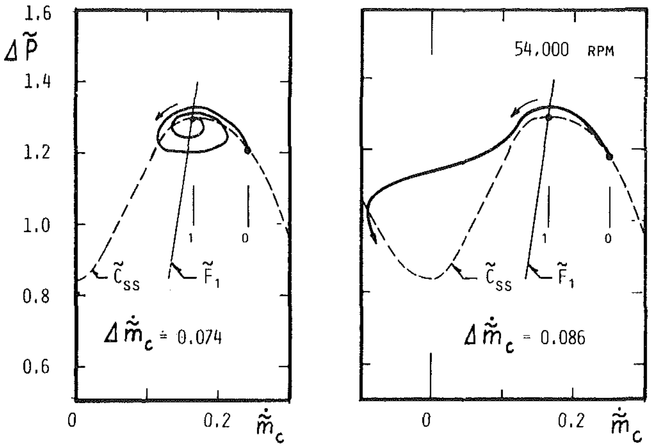

Fig. 4 Compression system model response at 54,000 rpm and S = 48.5 to perturbations $\Delta\tilde{\dot{m}}_c$ = 0.074 (stable) and = 0.086 (unstable).

expected that the frequency of finite amplitude oscillations in a nonlinear system is less than the natural frequency of the system and approaches to it as fluctuations become infinitesimal.

Theoretical Predictions

Employing the system parameters described above (Fig. 1, equations (2) and (3)) equations (1*a*)-(1*d*) were solved by a fourth-order Runge-Kutta numerical integration for different values of the yet unknown relaxation time N measured in revolutions and entering the parameter $\tilde{\tau}$. Using a value of $N = 2$, as suggested by Greitzer [1], gave poor agreement with the present data, particularly in terms of the frequency of surge cycles. On the premise that N could take a different value in the range of each of the three branches of the steady-state compressor characteristic a large number of cases were tested numerically. It was found, however, that a constant value of $N = 0.5$ gave generally good agreement with one exception. To match the cycle frequency of 15.5 Hz at 30,000 rpm a value of $N = 2$ should be used in this case for $\tilde{\dot{m}}_c \leq 0$.

Using these values of N yielded the theoretical results compared in Figs. 2(*a*) and 3(*a*) to the real time data and in Figs. 2(*b*) and 3(*b*) to the data in the dimensionless compressor map. The values of the valve parameter S given in the latter figures and used in the model could not be verified experimentally because the valve construction did not permit accurate area measurement. In view of the simplicity of the model and the uncertainty of the measurements the agreement is encouraging.

Stability Limit for Finite Amplitude Perturbations

It is known that a compressor which operates stably close to the surge line may go into surge due to a sudden external disturbance in the system, even though the throttle is not changed. Similarly, operating the system at steady-state at a throttle setting $F_0 = S_0\, \tilde{\dot{m}}^2_{c,0}$ corresponding to a point far from the stall limit, and then suddenly closing the throttle to a new setting $F_1 = S_1\, \tilde{\dot{m}}^2_{c,1}$ corresponding to another stable point closer to the stall limit, may lead to surge oscillations.

The latter phenomenon has been studied theoretically by introducing the finite amplitude perturbation $\Delta\tilde{\dot{m}} = \tilde{\dot{m}}_{c,0} - \tilde{\dot{m}}_{c,1}$ into the model equations, given initially the stable operation at $\tilde{\dot{m}}_{c,0}$. Terminal steady-state operating points $\tilde{\dot{m}}_{c,1}$ corresponding to the valve parameter S = 45 to 55 (see Fig. 3(*b*)) at a compressor speed of 54,000 rpm were studied for disturbances up to $\Delta\tilde{\dot{m}} = 0.15$.

Figure 4 for $S = 48.5$ shows both a case of an oscillatory damped transient leading to stable operation at $\tilde{\dot{m}}_{c,1}$ and a case of a diverging transient leading to continued deep surge oscillations due to the slightly larger initial perturbation. Yet, given no disturbances the operating point at $\tilde{\dot{m}}_{c,1}$ is perfectly stable. A behavior of this kind is typical of nonlinear systems, and small perturbation analysis is useless.

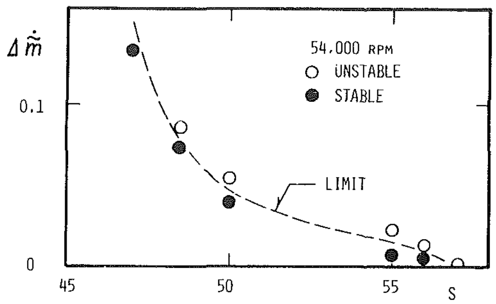

Fig. 5 Model stability limit in terms of perturbation $\Delta\tilde{\dot{m}}_c$ versus valve parameter S at 54,000 rpm. Calculations ○ ●, faired limit – – – –.

We define the stability limit for the foregoing transients as the maximum aplitude of disturbance that gives stable operation at the given valve setting S. Figure 5 summarizes the results of this theoretical study in terms of the stability limit versus terminal valve setting. $S = 57$ represents the stall limit of instability to infinitesimal disturbances. Below about $S = 46$ the system is unconditionally stable for disturbances of arbitrary magnitude.

Summary and Discussion

The lumped parameter Greitzer model developed for axial flow compression systems has been shown to give a satisfactory description of deep surge oscillations in a small single-stage centrifugal compression system at two speeds. In addition, the stability limit for one kind of finite amplitude disturbance has been studied theoretically to illustrate an application of the model. Owing to equipment limitations it was not possible to verify the latter results experimentally.

The required parameters supplied to the model equations comprise (i) system geometry, (ii) measured steady-state stable branches of positive and negative flow of the compressor characteristic, (iii) an estimated unstable branch, and (iv) the throttle valve characteristic. The model finally requires (v) the relaxation time of the compressor flow, say in terms of the number of revolutions N. Aside from the negative flow region at the lower speed, where $N = 2$ was required to match the frequency of oscillation, a constant value of $N = 0.5$ gave best agreement with the experimental surge data. This value is less than $N = 2$ used by Greitzer [1] in all cases but that for the large value of $B = 5$, where he put $N = 0$.

The compressor response to departure from steady-state operation involves complex unsteady flow phenomena that are different in axial and centrifugal compressors. It is of interest to note, however, that for the present compressor the value of N is on the order of the transport time through the impeller, - or the time to exchange its fluid volume, - at a normal operating condition.

Although the unstable branch, equation (3*b*), is only an estimate that could not be verified experimentally sample calculations have shown that its shape has little influence on the resulting solution because the periods of time spent in this range of flow are comparatively short. The differences in compressor characteristics supplied to the model equations in the present study and in [1] and [2] should be noted. Despite the considerable scatter of experimental results in the present study the direct comparisons in Figs. 2 and 3 between model and experiment show the present approach to be promising for centrifugal compression systems. The systematic discrepancies between model and data appearing particularly near and after times of flow reversal (see $\dot{\tilde{m}}_c(t)$ in Figs. 2(a) and 3(a), may be explained by the incompressibility assumption in the momentum balance for the compressor ducting, equation (1a). Here, sample calculations have shown that the ignored terms involving the time-rate-of-change of mass in the ducting may amount to as much as 25 percent of the terms retained. The fact that the time periods, during which the ignored terms are significant, are short, however, may explain why the model results are still useful.

The importance of the parameter B in determining stability of a compression system has been described in detail in [1], where the following condition for surge to occur was also derived

$$B d\dot{\tilde{C}}/d\dot{\tilde{m}} - (B\, d\dot{\tilde{F}}/d\dot{\tilde{m}})^{-1} \geq 0.$$

For the present case, employing equations (2c) and (3b), the minimum value of B that satisfies this condition is calculated to $B_{\min} = 0.105$. This value corresponds to a speed of 5800 rpm. Experiments have shown that the compression system produces weak audible surge at speeds as low as 7 - 9000 rpm. Although the stability condition does not necessarily apply to a point on the steady-state characteristic but to a range of $\dot{\tilde{m}}_c$ – values the theoretical estimate still appears to be quite accurate in the present case.

Acknowledgments

The authors are indepted to Messrs. E. Moller Christensen and J. V. Christiansen for their contributions to the experimental test stand and its instrumentation.

References

1 Greitzer, E.M., "Surge and Rotating Stall in Axial Flow Compressors. Part I: Theoretical Compression System Model," ASME *Journal of Engineering for Power,* Vol. 98, 1976, pp. 190-198.

2 Greitzer, E.M., "Surge and Rotating Stall in Axial Flow Compressors. Part II: Experimental Results and Comparison with Theory," ASME *Journal of Engineering for Power,* Vol. 98, 1976, pp. 199-211.

3 Bammert, K. and Mobarak, A., Discussion of [1] and [2]. ASME *Journal of Engineering for Power,* Vol. 98, 1976, pp. 212-215.

4 Toyama, K., Runstadler, Jr., P.W., and Dean, Jr., R.C., "An Experimental Study in Centrifugal Compressors," ASME JOURNAL OF FLUIDS ENGINEERING, Vol. 99, 1977, pp. 115-131.

5 Dean, Jr., R.C., and Young, L.R., "The Time Domain of Centrifugal Compressors and Pump Stability and Surge," ASME JOURNAL OF FLUIDS ENGINEERING, Vol. 99, 1977, pp. 53-63.

6 Kenny, D.P., "Lectures on the Radial Compressor," von Karman Institute, Brussels, May 1972.

7 Day, I.J., Greitzer, E.M., and Cumpsty, N.A., "Prediction of Compressor Performance in Rotating Stall," ASME *Journal of Engineering for Power,* Vol. 100, 1978, pp. 1-14.

discrepancies between model and data appearing particularly near and after times of flow reversal (see $\dot{\tilde{m}}_c(t)$ in Figs. 2(*a*) and 3(*a*), may be explained by the incompressibility assumption in the momentum balance for the compressor ducting, equation (1*a*). Here, sample calculations have shown that the ignored terms involving the time-rate-of-change of mass in the ducting may amount to as much as 25 percent of the terms retained. The fact that the time periods, during which the ignored terms are significant, are short, however, may explain why the model results are still useful.

The importance of the parameter B in determining stability of a compression system has been described in detail in [1], where the following condition for surge to occur was also derived

$$B d\dot{\tilde{C}}/d\dot{\tilde{m}} - (B\, d\dot{\tilde{F}}/d\dot{\tilde{m}})^{-1} \geq 0.$$

For the present case, employing equations (2*c*) and (3*b*), the minimum value of B that satisfies this condition is calculated to $B_{\min} = 0.105$. This value corresponds to a speed of 5800 rpm. Experiments have shown that the compression system produces weak audible surge at speeds as low as 7 - 9000 rpm. Although the stability condition does not necessarily apply to a point on the steady-state characteristic but to a range of $\dot{\tilde{m}}_c$ – values the theoretical estimate still appears to be quite accurate in the present case.

Acknowledgments

The authors are indepted to Messrs. E. Moller Christensen and J. V. Christiansen for their contributions to the experimental test stand and its instrumentation.

References

1 Greitzer, E.M., "Surge and Rotating Stall in Axial Flow Compressors. Part I: Theoretical Compression System Model," ASME *Journal of Engineering for Power,* Vol. 98, 1976, pp. 190-198.

2 Greitzer, E.M., "Surge and Rotating Stall in Axial Flow Compressors. Part II: Experimental Results and Comparison with Theory," ASME *Journal of Engineering for Power,* Vol. 98, 1976, pp. 199-211.

3 Bammert, K. and Mobarak, A., Discussion of [1] and [2]. ASME *Journal of Engineering for Power,* Vol. 98, 1976, pp. 212-215.

4 Toyama, K., Runstadler, Jr., P.W., and Dean, Jr., R.C., "An Experimental Study in Centrifugal Compressors," ASME JOURNAL OF FLUIDS ENGINEERING, Vol. 99, 1977, pp. 115-131.

5 Dean, Jr., R.C., and Young, L.R., "The Time Domain of Centrifugal Compressors and Pump Stability and Surge," ASME JOURNAL OF FLUIDS ENGINEERING, Vol. 99, 1977, pp. 53-63.

6 Kenny, D.P., "Lectures on the Radial Compressor," von Karman Institute, Brussels, May 1972.

7 Day, I.J., Greitzer, E.M., and Cumpsty, N.A., "Prediction of Compressor Performance in Rotating Stall," ASME *Journal of Engineering for Power,* Vol. 100, 1978, pp. 1-14.

DISCUSSION

R. S. Mazzawy[1]

The authors have presented an interesting extension of the Greitzer Model to centrifugal compression systems. In doing so they confirm the usefulness of Greitzer's technique for defining the transient stall behavior of pumping systems. There is one point, namely the relaxation time coefficient, which they appear to have used outside the original context of Dr. Greitzer's analysis. The authors used this coefficient to "trim" the analysis in order to match observed surge cycle frequency. It is clear from Greitzer's work, however, that this was not his intent. Rather the coefficient was meant to incorporate into the model the empirically observed period required for the transition from the unstalled to the stalled mode of operation. Data from axial flow compressors verify that this transition period significantly exceeds the fluid transport time through the machine alluded to by the authors. Consequently, they should look to other potential explanations (e.g. compressibility, geometry) for the observed differences between model and test surge cycle frequency. As an example, one could conceive of compression system with significant pressure rise delivering fluid to a very large plenum. In such a system the surge cycle frequency would be very low and dominated by the period of time required to empty and to refill the plenum. Obviously, in such a case, the transition period from unstalled to stalled flow would be insignificant and *not* the controlling parameter as depicted by the authors.

---

[1] Pratt & Whitney Aircraft Group, East Hartford, Conn. 06108.

Authors' Closure

The authors sincerely thank Mr. R. S. Mazzawy for his comments concerning the time lag parameter entering into the surge model. To first order of approximation, a lumped parameter model might be based on quasi-steady compressor performance. Data from axial compressors show, however, that when the stall limit is approached there is a definite time lag between onset of instability and full development of stall. We have not been able to show a similar delay in our study of the small radial compressor. Greitzer [1] models this delay by equation (2d). This equation describes, in general terms, the compressor response to departures from steady-state operation. In fact, Greitzer uses the equation throughout the surge cycle, employing a "very small" value of the time constant when not near stall. Our value of $N = 0.5$ is thought to be comparable. Neither the frequency content of our data nor the testing of different values of N suggested the existence of a longer delay as the surge line was approached. Regarding the overall cycle frequency, it was low and dominated by system behavior rather than by the delay associated with transition from unstalled to stalled flow. As pointed out by Mr. Mazzawy this gives predictions a relatively small sensitivity to the value of N. Yet, our predictions using a larger lag were less satisfactory. In general, one should probably be cautious in drawing further conclusions from such a simple model. Further refinements should include compressibility effects in ducting flows and explicit modeling of stall, which may be different in axial and radial compressors.

F. N. Lin

W. I. Moore

F. E. Lundy

NASA,
Kennedy Space Center, Fla. 32899

Torque Characteristics of a 122-Centimeter Butterfly Valve With a Hydro/Pneumatic Actuator

Actuating torque data from field testing of a 122-centimeter (48 in.) butterfly valve with a hydro/pneumatic actuator is presented. The hydraulic cylinder functions as either a forward or a reverse brake. Its resistance torque increases when the valve speeds up and decreases when the valve slows down. A reduction of flow resistance in the hydraulic flow path from one end of the hydraulic cylinder to the other will effectively reduce the hydraulic resistance torque and hence increase the actuating torque. The sum of hydrodynamic and friction torques (combined resistance torque) of a butterfly valve is a function of valve opening time. An increase in the pneumatic actuating pressure will result in a decrease in both the combined resistance torque and the actuator opening torque; however, it does shorten the valve opening time. As the pneumatic pressure increases, the valve opening time for a given configuration approaches an asymptotical value.

1 Introduction

Butterfly valves are lightweight—lighter than gate, plug or ball valves. They require the least amount of body material of any valve type. They combine on/off and throttling-control characteristics and are widely used in industry for handling liquids, gases, and slurries. Large butterfly valves are often used in critical locations in power plants and water-pumping stations. The basic operation of a butterfly valve is simple, requiring only a 90-deg rotation of the disk from its close-to-open position. For throttling service, the recommended valve opening is generally between 30 and 80 deg.

Butterfly valves are one of the oldest known types of control valves and have been studied by many investigators. The first attempt at correlating earlier published flow and torque data was made by Cohn [1] in 1951. Using the flow formula adopted by Cohn, McPherson, Strausser and Williams [2] conducted a study of butterfly valve flow characteristics. Based upon data from reduced scale model tests, Gaden [3] presented a semiempirical method for calculating torque of a butterfly valve. Utilizing the theory of free streamlines devised by Helmholtz and Kirckhoff, Sarpkaya gave an analytical method for calculating the discharge coefficient of two-dimensional butterfly valves [4] and the hydrodynamic torque of two-dimensional and axially symmetrical butterfly valves [5]. In a report prepared for Jamesbury Corporation, Tullis [6] reported test data on flow coefficient as well as dynamic and friction torques for a 61-centimeter (24 in.) butterfly valve. After a series of studies, Boger [7] concluded that a butterfly disk with a cambered or cupped shape will experience lower dynamic torque. He also presented the flow torque characteristics for this low torque disk.

In selecting a butterfly valve for throttling service with liquid flow, particularly under high heads, consideration must be given to the possibility of cavitation. If an excessive pressure drop occurs at some throttled disk position, cavitation can result. In [5], Sarpkaya also presented an analytical method for predicting the occurrence of severe cavitation. Based upon flow tests, Ball and Tullis [8] gave a semiempirical method for predicting cavitation characteristics of butterfly valves. To understand the process of cavity shedding of vortices behind the disk, Shalmev and Zhestkov [9] conducted flow visualization plane model testing on butterfly valves [9]. They also studied experimentally the cavitation induced vibration in butterfly valves.

To provide trouble-free operation, butterfly valves require proper application and careful installation. Some rules for obtaining long service life from large butterfly valves were given by Kurkjian [10]. Guides for selection, application, and installation of butterfly valves are available in the literature [11, 12, 13]. However, testing torque data for butterfly valves with diameter of 122-centimeter or larger are not available.

Torque data are necessary for proper actuator design for large butterfly valves. At any intermediate disk position, the torque that a butterfly valve is subjected to is the sum of the hydrodynamic, friction, and inertia torques. The hydrodynamic torque is more important for large butterfly valves and it is not possible to calculate this torque to any pretense of accuracy. Aerodynamics and hydrodynamics flow theory is based upon an infinite flow field; however, actual flow through valves involves bounding surface. In addition, fully separated flow exists at most disk positions and airfoil analysis assumes fully attached flow. If an excessive pressure drop occurs, the presence of cavitation will make the torque calculation even more difficult. Hence field test data become very desirable to design engineers.

Six 122-centimeter butterfly valves with hydro/pneumatic

Contributed by the Fluids Engineering Division for publication in the JOURNAL OF FLUIDS ENGINEERING. Manuscript received by the Fluids Engineering Division, March 24, 1980.

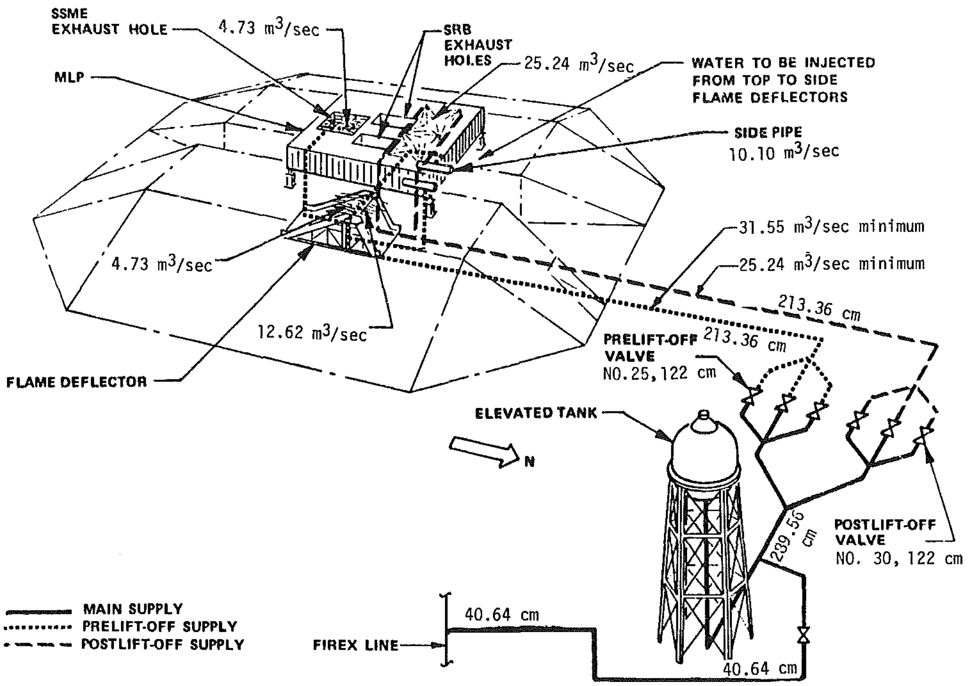

Fig. 1 The sound suppression system at KSC LC-39A

actuators are used to remotely control the water flow in the Kennedy Space Center's Sound Suppression System. To evaluate the performance of the valve/actuator units, a series of field tests was conducted recently. The purpose of this paper is to report the test results.

2 Test Procedure and Configuration

Before reporting the test results, it is fitting to briefly describe the test procedure and configuration. The tests were conducted at the Kennedy Space Center's Launch Complex 39A, which is shown in Fig. 1. The system consists of an elevated tank, a valve complex, a piping system, and the spray nozzles. The valve complex consists of six 122-centimeter (48 in.) butterfly valves to remotely control the water flow. Each valve is actuated by a piston-type, double cylinder, hydro/pneumatic actuator. The actuator utilizes a "Scotch-Yoke" linkage between the piston rod and the valve stem to generate torque from the cylinder thrust. At the valve complex, the pre-liftoff lines are the mirror images of the post-liftoff lines. To rapidly establish a minimum flow of 31.55 m^3/s (500,000 gpm) through the pre-liftoff system and 25.24 m^3/s (400,000 gpm) through the post-liftoff system, at least two pre-liftoff and two post-liftoff valves must be fully opened within 4 seconds after receiving opening commands.

The procedure used in conducting the tests was to first fill the lines and storage tank, and then open the valves. The pre-liftoff valves were first commanded to open and then 13 seconds later the post-liftoff valves. There was no flow within the system before the pre-lift valves were opened. The configuration is such that there exists, respectively, a water head of 66.35 meters and 48.52 meters across each of the pre-liftoff valves and of the post-liftoff valves. Therefore, at the time the post-liftoff valves were commanded to open, the water pressure across each of them was less than 48.52 meters. Instrumentation for recording the valve position, the cylinder pressures, etc., was installed on valve number 25 (V-25) in the pre-liftoff circuit and number 30 (V-30) in the post-liftoff circuit. Since valve number 30 was operated under less pressure, it was relatively easier to operate. Therefore, in this report, we shall limit our analysis and discussion to valve number 25.

As shown in Fig. 2, valve number 25 is installed in a section of a 122-centimeter (48 in.) diameter horizontal, straight pipe. Its shaft is horizontally located 13.97 cm behind the disk and 0.32 cm below the pipe center. The pressure drop across the valve was obtained by two pressure transducers, located in a horizontal plane passing through the pipe center; one is 167.64 cm upstream and the other is 233.68 cm downstream.

Nomenclature

A_1 = effective area of pneumatic cylinder
A_4 = effective area of hydraulic cylinder
A_r = cross-sectional area of piston rod
A_2 = $A_1 - A_r$
A_3 = $A_4 - A_r$
D = diameter of valve
GN_2 = gaseous nitrogen
GPM = gallons per minute
I = mass moment of inertia
L = distance between the piston rod center and shaft center, defined in Fig. 3
LC-39A = launch Complex 39, Pad A
MLP = mobile Launch Platform
P_1, P_2, P_3, P_4 = cylinder pressures, defined in Fig. 3
P_{GN2} = GN_2 source pressure
T = actuator opening torque, equation (3)
T_I = inertia torque, equation (6)
T_R = combined resistance torque, equation (7)
ΔP = pressure drop across the valve, defined in Fig. 2(*a*)
α = angular acceleration
β = angular position of disk, defined in Fig. 3

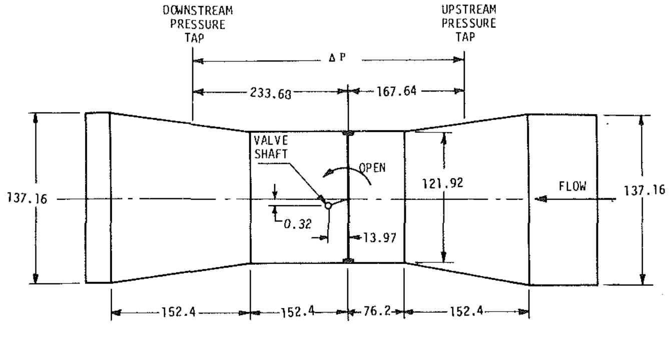

Note: All dimensions are in cm.

Fig. 2 The butterfly valve at closed position (not to scale)

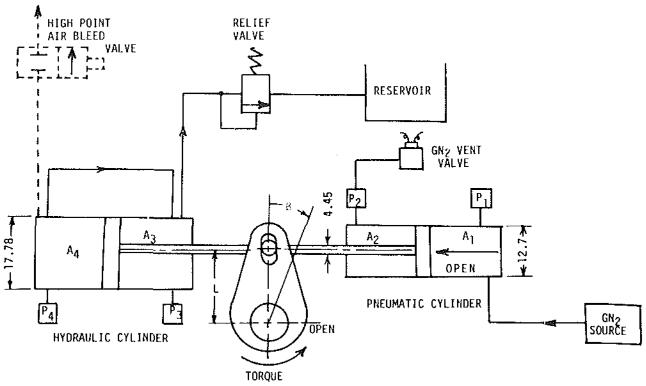

Fig. 3 The hydro/pneumatic actuator

The disk has a diameter of 118.43 cm and a basic thickness of 6.35 cm with additional structural reinforcement. The disk assembly has a mass moment of inertia of 41.72 kg-m^2.

Figure 3 shows the hydro/pneumatic actuator schematically. There are four pressure transducers for measuring the actuator cylinder pressures. The diameter of the pneumatic cylinder is 12.7 cm and that of the hydraulic cylinder is 17.78 cm. The two cylinders are connected by a piston rod which has a diameter of 4.45 cm. The distance from the center of the piston rod to the center of the disk shaft is 13.97 cm. Not shown in the sketch are two 2.54 cm diameter rods for holding the actuator assembly together. These two rods are inside the cylinders and pass through the pistons. The actuator force is provided by high pressure nitrogen gas on one side of the pneumatic cylinder piston. The hydraulic circuit is filled with MIL-H-5606 hydraulic fluid and, as we shall demonstrate later, functions as either a forward or a reverse hydraulic brake. The high point bleed valve permits venting air during the filling of the hydraulic circuit. To fully open the valve, the pistons move 27.94 cm and displace 6655 cm^3 of hydraulic fluid out of one side of the cylinder. Because of the presence of the piston rod, there are only 6221 cm^3 of volume available on the other side of the piston. The differential volume of 434 cm^3, which is the product of the rod cross-sectional area and the piston stroke, must flow through the relief valve to the reservoir. Otherwise the valve may not be opened without damaging the hydraulic circuit.

Table 1 tabulates the field tests conducted in June and July of 1979. The difference between the June and July configurations is as follows:

(1) The hydraulic relief valve setting was 689.5×10^3 N/m^2 gage for June configuration and 2069×10^3 N/m^2 gage for July.

(2) The GN$_2$ supply line for June tests had a higher flow resistance than that for July. Thus, for the same GN$_2$ source pressure, the July configuration led to a higher cylinder pressure P_1.

(3) The air bleed line in Fig. 3 was installed between the June and July tests. Thus the July tests had less air trapped in the hydraulic circuit.

3 Test Results

Neglecting the piston friction, the thrust force for opening the valve is given by

$$F=(P_1A_1-P_2A_2)-(P_4A_4-P_3A_3) \qquad (1)$$

and the corresponding actuator opening torque is

$$T=\frac{L}{\cos^2\beta}[(P_1A_1-P_2A_2)-(P_4A_4-P_3A_3)] \qquad (2)$$

Since $A_2 = A_1 - A_r$ and $A_3 = A_4 - A_r$, equation (2) can be rewritten as:

$$T=LA_2(P_1-P_2)/\cos^2\beta+LA_r(P_1-P_4)/\cos^2\beta + [-LA_3(P_4-P_3)/\cos^2\beta] \qquad (3)$$

To avoid accidentally opening the valve, P_2 was maintained at the GN$_2$ source pressure originally. Ten seconds before opening the valve,[1] the GN$_2$ vent valve was opened which dropped the P_2 pressure to almost atmospheric. The first term on the right-hand side of equation (3) is always positive and thus represents an opening torque. For a given system, this term depends on the GN$_2$ source pressure.

For a fixed hydraulic circuit and a given GN$_2$ source pressure, P_4 will depend on the hydraulic relief valve setting. Thus the second term on the right-hand side of the equation (3) represents the effect of the relief valve setting on the actuator opening torque. A lower setting will result in a higher actuator opening torque with all other conditions remaining the same. If the relief valve is set at a pressure greater than the GN$_2$ source pressure, this term will become negative and hence is a resisting torque. For all tests shown in Table 1, this term is positive.

To get some feeling about the effect of the relief valve setting on the valve opening time, three dry tests were conducted on May 24, 1979.

The test configuration was the same as the June configuration with the relief valve set at 276×10^3, 862×10^3, and 10.34×10^6 N/m^2 gage and the GN$_2$ source pressure at 8.27×10^6 N/m^2 gage. The resulting valve opening time is, respectively, 1.9, 2.0, and 2.3 s. Because of the relatively small rod cross-sectional area A_r, the effect seems to be negligibly small unless the setting is very high.

The third term on the right-hand side of equation (3) depends upon the pressure difference P_4-P_3. For a given hydraulic circuit, this pressure difference determines the rate of hydraulic flow from one side of the piston to the other side. During valve opening, P_4 is greater than P_3 and this term is negative and represents a resisting torque. If the valve, for any reason, speeds up, it will result in a higher rate of hydraulic flow and hence a higher value of P_4-P_3. This higher pressure difference will in turn result in a higher resisting torque and hence slows down the valve actuation. In this mode, the hydraulic cylinder serves as a forward brake.

For a given GN$_2$ source pressure and relief valve setting, the first two terms on the right-hand side of equation (3) will remain almost unchanged even if the valve motion slows down for any reason. But, the third term will decrease in magnitude because of the decreasing pressure difference $P_4 - P_3$. Thus, from equation (3), the actuator opening torque will increase. As the valve speed approaches zero, P_1 will approach the GN$_2$ source pressure (P_{GN2}) and P_2 will remain at atmospheric pressure. In the meantime, P_4 approaches P_3 and

---

[1] Except Test No. 1.

the actuator torque for opening the valve approaches its maximum value. Consequently, the maximum opening torque the actuator can develop is:

$$(T_{\max})_{\text{open}} = LA_2P_{\text{GN2}}/\cos^2\beta + LA_r(P_{\text{GN2}} - P_4)/\cos^2\beta \qquad (4)$$

For all tests tabulated in Table 1, $P_{\text{GN2}} > P_4$ and $A_2 >> A_r$.

It is, therefore, conservative to approximate the maximum opening torque of the actuator as

$$(T_{\max})_{\text{open}} = LA_2P_{\text{GN2}}/\cos^2\beta \qquad (5)$$

It is fitting to point out that the torque given by equations (4) or (5) is the maximum available actuator torque for opening the valve. It is not the maximum torque that the actuator can be subjected to. The maximum torque that the actuator can be subjected to depends on the hydrodynamic torque and occurs only when the hydraulic cylinder serves as a reverse brake.

As shown in [5], the hydrodynamic torque of a butterfly valve reaches its peak at about 80 percent opening. At any intermediate valve position, the hydrodynamic torque could be greater than the maximum opening torque calculated from equation (4). When this occurs, the hydrodynamic torque tends to close the valve and thus, P_4 will be less than P_3. Consequently, the third term on the right-hand side of equation (3) changes its sign and becomes positive. This means that the hydraulic and pneumatic cylinders are now working together to balance or resist the hydrodynamic torque. The hydraulic cylinder is now serving as a reverse brake and the actuator puts out its maximum torque.

Test number 4 shows that a GN_2 source pressure of 6×10^6 N/m^2 gage was unable to open the valve within 4 seconds during a two valve operation. The test data for the cylinder pressures are displayed in Fig. 4. For a time less than 1.9 seconds, P_4 is greater than P_3 and the hydraulic cylinder served as a forward brake. Because of the fluctuations of the hydrodynamic torque caused by the vortex shedding, the valve was oscillating at about 48 percent open for the time period from 5.8 to 41 s. During this period, the hydraulic cylinder served as either a forward or a reverse hydraulic brake.

During opening and at any intermediate position β, a butterfly valve sees the sum of hydrodynamic, friction and inertia torques. Let I denote the mass moment of inertia of the disk assembly about its rotation axis and α the angular acceleration at that position, the inertia torque is:

$$T_I = I\alpha \qquad (6)$$

If we call the sum of hydrodynamic and friction torques as combined resistance torque and denote it by T_R, the total torque a butterfly valve will experience is the sum of $T_R + T_I$. This total torque should be balanced by the actuator opening torque calculated from equations (2) or (3). Therefore we have

$$T = T_R + T_I, \text{ or}$$

$$T_R = T - T_I \qquad (7)$$

The pressure differential across the valve, ΔP, is one of the important factors affecting the combined resistance torque. Another means of presenting the combined resistance torque is, therefore,

$$\frac{T_R}{\Delta P} = (T - T_I)/\Delta P \qquad (8)$$

Note that the α in equation (6) was not instrumented; however, it can be evaluated numerically by taking the second derivative of angular displacement with respect to time. Since the mass moment of inertia of the disk assembly is only 41.72 kg-m^2, the term T_I in (7) is negligibly small as compared to T for all tests in Table 1.

Table 1 Sound suppression system flow tests

(Uncertainty: Pressure ± 3 percent, Time ± 0.2 percent)

Test No. and date	Valves to be opened	GN_2 source pressure, N/m^2 Gage	Valve opening time, s	Conditions
No. 1 6/20/79	1 pre-liftoff only	8.96×10^6	valve failed to open within 4 seconds	Elevated tank partially full, GN_2 venting and valve opening command given simultaneously
No. 2 6/25/79	All six valves	8.27×10^6	2.122	Elevated tank full, closing side GN_2 vented 10 seconds prior to valve opening
No. 3 6/26/79	2 pre-liftoff, 2 post-liftoff	8.27×10^6	2.142	Same as test no. 2
No. 4 6/26×79	2 pre-liftoff, 2 post-liftoff	6×10^6	pre-liftoff valves failed to open within 4 seconds	Same as test no. 2
No. 5 6/27/79	2 pre-liftoff, 3 post-liftoff	7.24×10^6	2.672	Same as test no. 2
No. 6 6/28/79	All six valves	10×10^6	1.979	Same as test no. 2
No. 7 7/17/79	All six valves	8.27×10^6	2.081	Same as test no. 2
No. 8 7/18/79	All six valves	10.34×10^6	1.877	Same as test no. 2

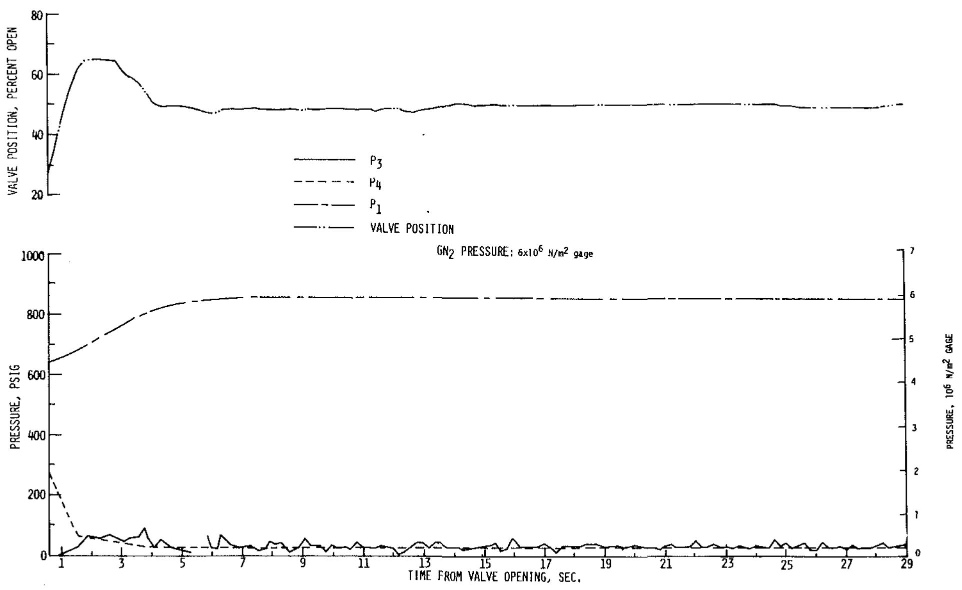

Fig. 4 Cylinder pressures and valve position for test on June 26, 1979 (uncertainty: pressure ± 3 percent, percent open ± 3 percent, time ± 0.2 percent)

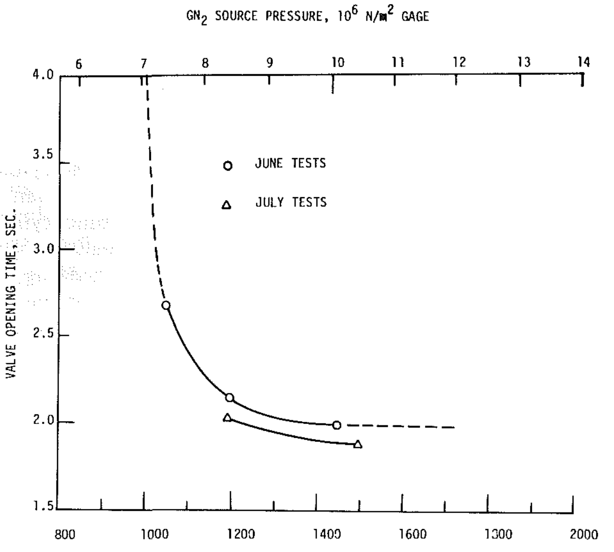

Fig. 5 Effect of GN_2 pressure on valve opening time (uncertainty: pressure ± 3 percent, time ± 0.2 percent)

During each test the valve position, cylinder pressures, etc., were recorded at 0.02 second time intervals. To see the effect of GN_2 source pressure on the valve opening time, we present Fig. 5. As we expect, a higher GN_2 pressure will shorten the valve opening time. However, there is little gain in shortening the valve opening time once the GN_2 pressure exceeds 10.34 $\times 10^6$ N/m^2 gage. This implies that a higher GN_2 pressure induces a higher hydraulic resistance and, for a given configuration, provides little additional torque to speed up the disk once the pressure exceeds a certain value.

Figure 6 shows the actuator opening torques calculated from (3) for all successful tests listed in Table 1. Since the inertia torques are small, the torque data in Fig. 6 also represent the combined resistance torques calculated from (2). It is seen that the required torque for opening the valve depends on the valve opening time or the GN_2 source pressure. A higher GN_2 pressure will result in a lower required torque. This is probably caused by the decreasing contribution of the hydrodynamic torque due to the increasing valve speed. A fast moving valve is expected to see a slower water flow since it takes a finite time to accelerate the water.

To understand the acceleration characteristics of the water flow through the valve, we have performed a computer analysis which employs the method of characteristics to solve the transient flow equations. The analysis shows that, for all tests listed in Table 1, it takes about 6 s to establish about 98 percent of their steady state velocities. Additionally, the steady state velocity for a two-valve operation is much higher than that for a three-valve operation. To conserve space we shall refrain from presenting the details.

As stated earlier, the pressure differential across the valve, ΔP, is one of the important factors which affect the combined resistance torque. With all conditions remaining the same, the ΔP during a two valve opening operation is greater than the ΔP during a three valve operation. This effect on the combined resistance torque can be realized by examining the data for tests Nos. 2 and 3 in Fig. 6. As could be expected, the valve experienced more combined resistance torque during the two-valve operation. In the meantime, the actuator also put out more opening torque to meet the system demand. This is due to the hydraulic cylinder. Note that the valve was opened more slowly in the two-valve operation.

During test number 4, a GN_2 source pressure of 6×10^6 N/m^2 gage was not able to open the valve within 4 seconds. As shown in Fig. 7, the valve disk was held at about 48 percent open for a period of about 36 s. In this time period, the inertia torque was negligible, and the actuator torque was balanced by the combined resistance torque.[2] This actuator torque together with the valve position and the pressure differential across the valve are displayed in Fig. 7. The combined resistance torque for holding the valve at 48 percent open position in a two-valve operation is fluctuating around 9628 m•N. The corresponding cylinder pressure data have been shown in Fig. 4.

At this point, it is proper to reiterate that, except for test No. 1, all tests tabulated in Table 1 were conducted with a full water tank such that there is an initial water head of 66.35 m across the valve. In addition, the GN_2 vent was initiated 10 s before opening the valve. In an attempt to open valve number

---

[2] When the valve is retreating, the combined resistance torque is the hydrodynamic torque minus the friction torque.

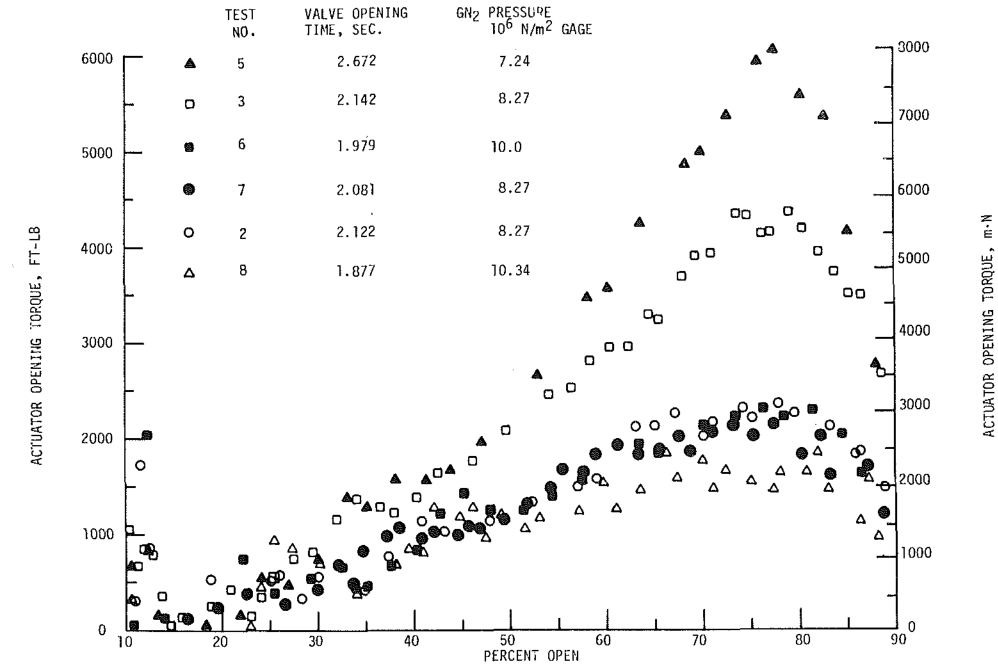

Fig. 6 Actuator opening torque versus valve opening time (uncertainty: torque ± 5 percent, percent open ± 3 percent, pressure ± 3 percent, time ± 0.2 percent)

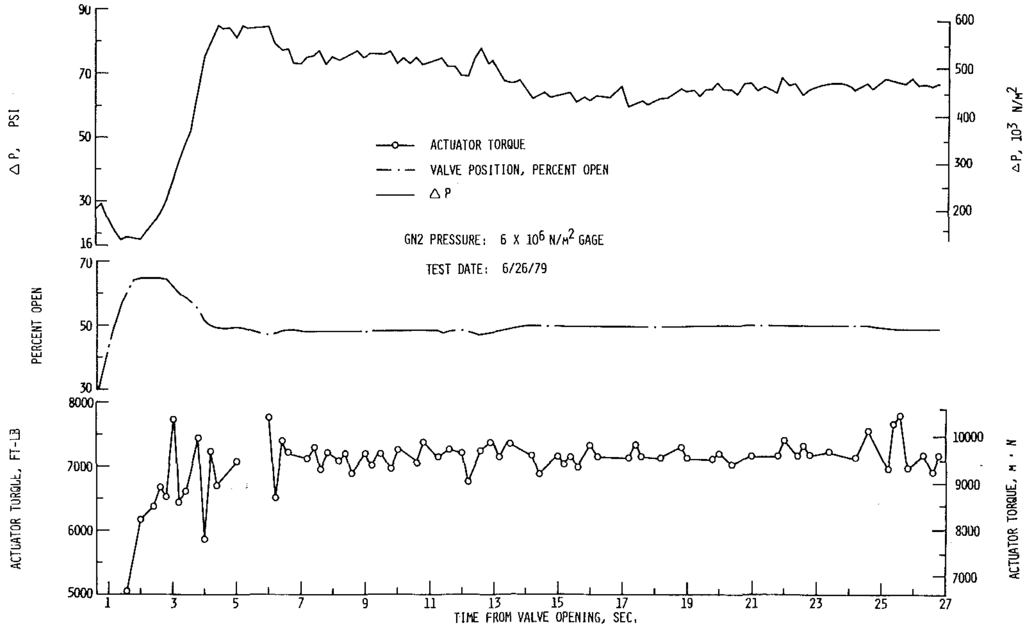

Fig. 7 The valve position, actuator torque, and Δp, for test on June 26, 1979 (uncertainty: torque ± 5 percent, percent open ± 3 percent, Δp ± 5 percent, pressure ± 3 percent, time ± 0.2 percent)

25 alone, test No. 1 was conducted, with a GN_2 pressure of 8.96×10^6 N/m^2 gage on June 20, 1979. The elevated tank was only partially filled and, thus, the initial water head across the valve was 38.56 m. Additionally, commands for opening valve number 25 and venting the GN_2 were given at the same time. All other conditions were the same as the other June tests. The data on the valve position, actuator torque and ΔP are shown in Fig. 8. The valve was opened to about 63 percent in 3.283 s, and then stalled at this point for about 14 s. During this time period, the inertia torque was negligible and, thus, the actuator torque was balanced by the combined resistance torque. From Fig. 8, the combined resistance torque for holding the valve at 63 percent position in a single valve operation is slightly fluctuating around 14,645 m•N. If the tests were to be conducted with a full tank and a higher GN_2 source pressure such that the valve also stalled at 63 percent position, the combined resistance torque should be higher and may be estimated as (14,645) (66.35)/(38.56) = 25,200 m•N. We recall that, when the valve stalls, the combined resistance torque is the hydrodynamic torque minus

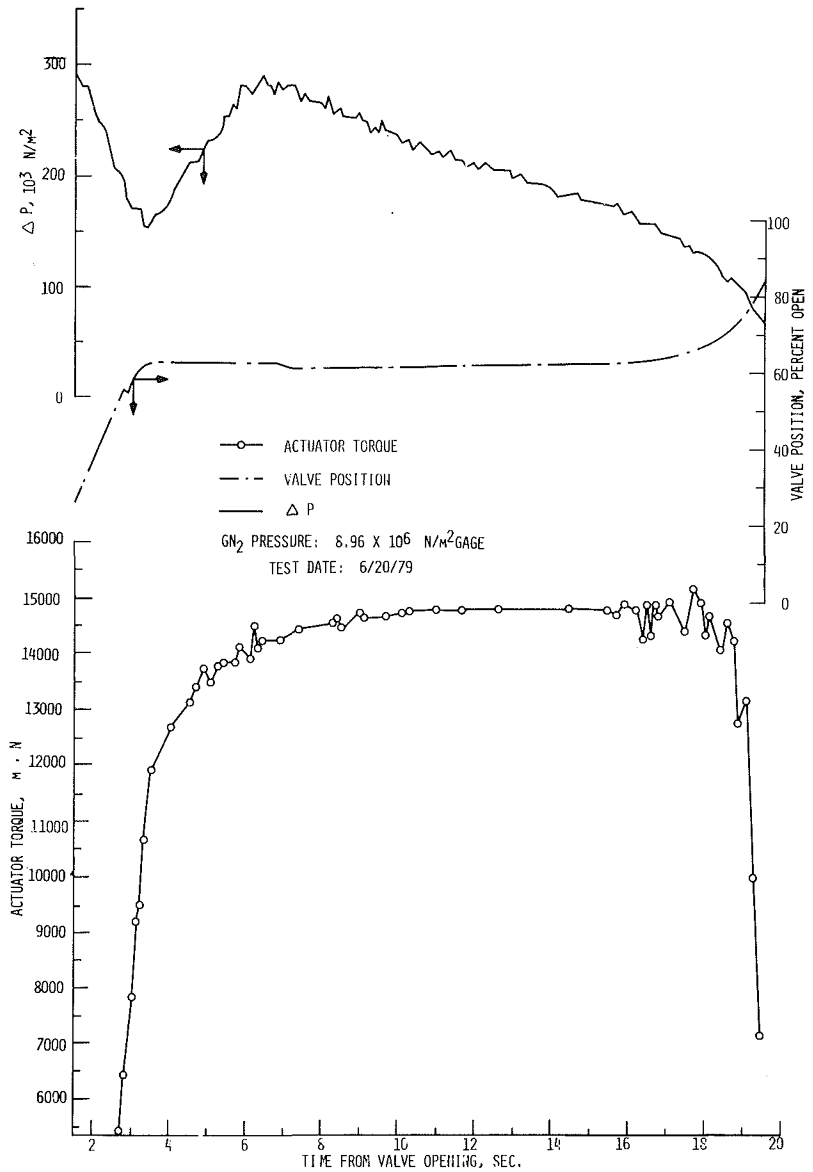

Fig. 8 The valve position, actuator torque, and Δp for test on June 20, 1979 (uncertainty: torque ± 5 percent, percent open ± 3 percent, Δp ± 5 percent, pressure ± 3 percent, time ± 0.2 percent)

the friction torque. Thus, with a full tank and in a single valve operation, the maximum hydrodynamic torque at 63 percent valve position could be much greater than 25,200 m•N.

In the butterfly valve literature, the combined resistance torque is often reduced to terms of combined resistance torque per pressure drop to be applied to any specific application condition. For the tests we have discussed, the data of $T_R/\Delta P$ have been calculated from equation (8) and shown in Fig. 9. Like the combined resistance torque, the ratio $T_R/\Delta P$ also decreases with increasing GN_2 pressure (or with increasing valve opening speed). It should be noted that the ΔP is the difference of two pressures measured at 1.4 pipe diameters upstream and 2 pipe diameters downstream from the valve.

The torque required to open the valve can be taken as either the combined resistance torque given by equation (7) or the combined resistance torque plus inertia torque given by equation (3). To be conservative we shall take the torque required to open the valve as the sum of combined resistance and inertia torques, which depends upon the GN_2 source pressure, valve position, and system configuration. To successfully open the valve, the torque required must be less than the maximum actuator opening torque given by (5) at all valve positions. Figure 10 compares these torques for test number one. The associated time/valve-position plot has been shown in Fig. 8. After receiving valve opening command, it took 3.283 s to reach point A in Fig. 10, 15.6 s to travel from A to B, and 1.293 s to go from B to 100 percent open. Between A and B, the torque required was greater than the maximum actuator opening torque and thus the valve stalled.

Figure 11 displays the maximum actuator opening torque and the torque required for opening the valve for test number 4. The corresponding time/valve-position curve is shown in Fig. 7. It took 2.631 s to reach point A in Fig. 11, 36.992 s to travel from point A to B, and 1.137 s to go from B to 100 percent open. Again, between A and B, the torque required was greater than the maximum actuator opening torque and hence the valve stalled.

The hydraulic and pneumatic pressure data have been analyzed and documented in a Kennedy Space Center Internal Report. Also discussed in the report was the safety factor of our design. Because of space limitation, we shall refrain from presenting them.

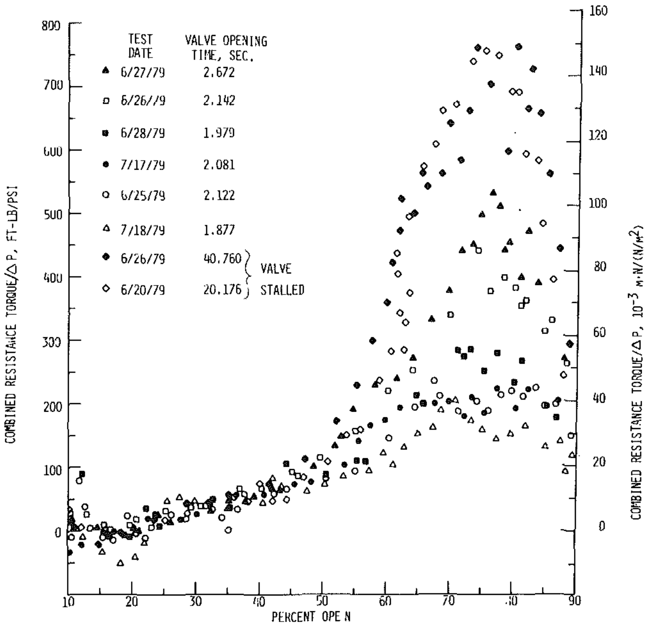

Fig. 9 Combined resistance torque per pressure drop (uncertainty: torque/Δp ± 11 percent, percent open ± 3 percent, time ± 0.2 percent)

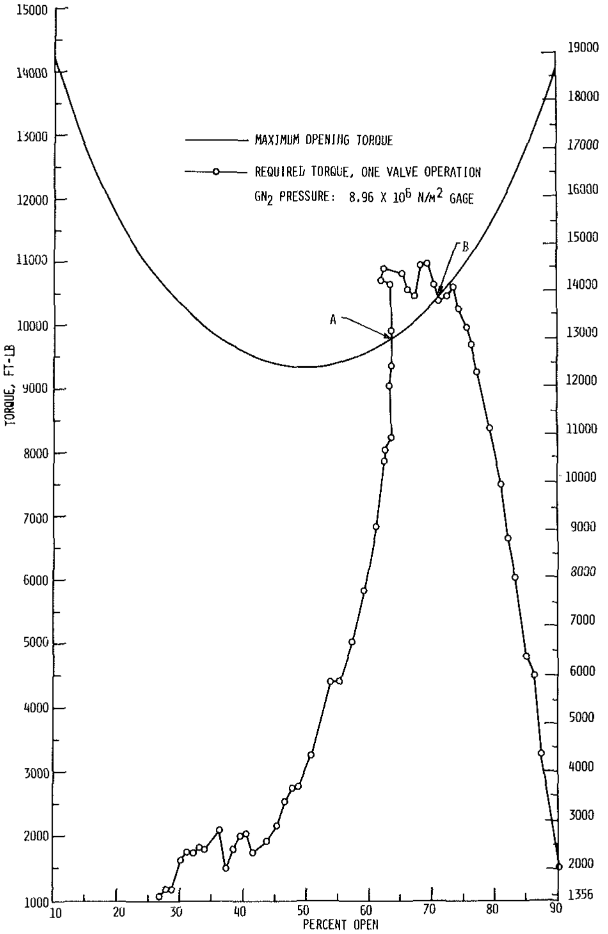

Fig. 10 Comparison of maximum opening torque and required torque for test on June 20, 1979 (uncertainty: torque ± 5 percent, percent open ± 3 percent, pressure ± 3 percent)

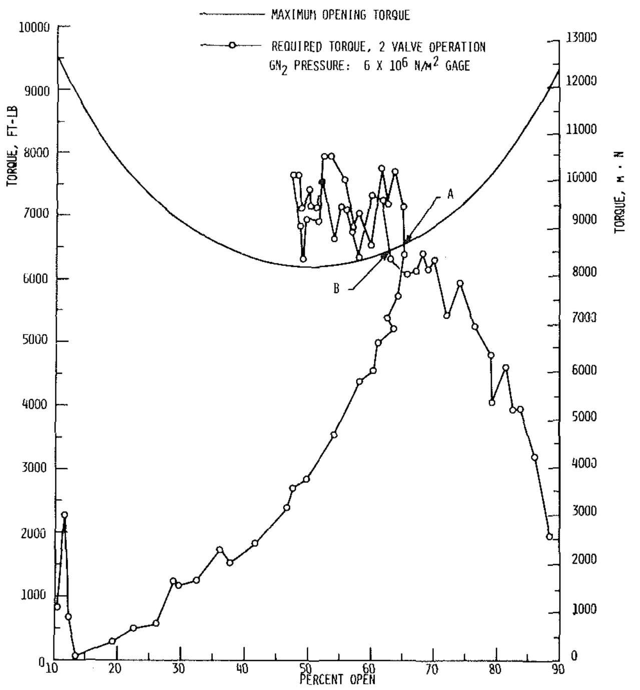

Fig. 11 Comparison of maximum opening torque and required torque for test on June 26, 1979 (uncertainty: torque ± 5 percent, percent open ± 3 percent, pressure ± 3 percent)

4 Concluding Remarks

Except for tests with stalled valve, we have observed a very linear relationship for the valve position and the time. A properly designed hydro/pneumatic actuator is expected to open a valve with a nearly constant speed and prevent a valve from slamming. With a hydro/pneumatic actuator, the valve opening speed for a given configuration approaches an asymptotical value as the pneumatic actuation pressure increases. This value may be determined by dry cycle tests.

With a hydro/pneumatic actuator, one may postulate that the combined resistance torque for geometrically similar valves is a function of ρ (Fluid density), μ (Fluid dynamic viscosity),. β, t (opening time), D, and ΔP. Thus, from dimensional analysis, the combined resistance torque coefficient $T_R/(\Delta P \cdot D^3)$ is a function of β, $\rho D^2/(t\mu)$, and $\rho D (\Delta P/\rho)^{1/2}/\mu$. The last dimensionless parameter is recognized to be the Reynolds number and has little effect on the steady hydrodynamic torque [5]. Therefore, one may regard the combined resistance torque coefficient as a function of β and $\rho D^2/(t \cdot \mu)$. Since the D, ρ, and μ are constants in all tests, the data in Fig. 9 is basically a plot of this function and may be used to design a hydro/pneumatic actuator for butterfly valves of diameters other than 122 centimeters.

In applying this data, one should bear in mind the fact that the valve pressure drop is the difference between the pressure measured at 1.4 pipe diameters upstream and 2 pipe diameters downstream from the valve. Another fact to be borne in mind is the possible variation of friction torque due to differences in the valve installation.

Acknowledgments

The authors are sincerely grateful to Mr. R. L. Clark and Mr. D. D. Buchanan for their valuable comments and suggestions. The assistance of Misses Susan Carpenter, Alison Fetner, and Maria Harwood in preparing the figures and of Mrs. Cheryl Bartoszek in typing the manuscript is greatly appreciated. Permission by Kennedy Space Center to publish the test data is gratefully acknowledged.

References

1 Cohn, S. D., "Performance Analysis of Butterfly Valves," *Instruments*, Vol. 24, Aug. 1951.

2 McPherson, M. B., Strausser, H. S., and Williams, J. C., "Butterfly Valve Flow Characteristics," *J. Hydraulics Division*, ASCE, Vol. 83, No. HY1, 1957.

3 Gaden, D., "A Contribution to the Study of Butterfly Valves," *Water Power*, Part 1, pp. 456–474, Dec. 1951 and Part 2, pp. 16–22, Jan. 1952.

4 Sarpkaya, T., "Oblique Impact of a Bounded Stream on a Plant Lamina," *Journal of the Franklin Institute*, Vol. 267, 1959.

5 Sarpkaya, T., "Torque and Cavitation Characteristics of Butterfly Valves," ASME *Journal of Applied Mechanics*, Vol. 28, 1961.

6 Tullis, J. P., "Performance of a 24-Inch Wafer Sphere Valve," Hydro Machinery Laboratory, Report No. 30, Colorado State University, 1973.

7 Boger, H. W., "Low-Torque Butterfly Valve Design," *Instrumentation Technology, Journal of Instrument Society of America*, Sept. 1970.

8 Ball, J. W., and Tullis, J. P., "Cavitation in Butterfly Valves," *J. Hydraulics Division*, ASCE, Vol. 99, No. HY9, 1973.

9 Skalnev, K. K., and Zhestkov, A. A., "Mechanism of Cavitations in Butterfly Valves," Conf. on Fluid Mech., 5th Proc., Budapest, Hungary, 1975.

10 Kurkjian, G. A., "Follow These Simple Rules to Get Long Life From Your Large Butterfly Valves," *Power*, Vol. 118, July 1974.

11 Hanssen, A. J., "Butterfly Valves," *Power*, Vol. 110, Jan. 1966.

12 Bertram, B. E., "Butterfly Valves for Flow of Process Fluids," *Chem. Eng.*, Vol. 83, Dec. 1976.

13 Freeman, M. L., and Sproul, D. H., "Butterfly Valves - Correct Installation and Alignment," *Paper Technology*, Vol. 15, Apr. 1974.

Scale Effects on Various Types of Limited Cavitation

M. L. Billet
Research Associate.

J. W. Holl
Professor of Aerospace Engineering.

Applied Research Laboratory,
The Pennsylvania State University,
State College, Pa. 16801

Scale effects on limited cavitation discussed in this paper are those departures from the classical similarity relations due to variations in size and velocity. These scale effects are an important consideration in the prediction of limited cavitation in a design process. In most cases, the limited cavitation number of a model is different from that of the prototype. Some recently published results have shown that viscous effects and free-stream nuclei can cause significant scale effects. The purpose of this paper is two-fold. First, new experimental data are presented which show scale effects for several types of cavitation. Second, these data are discussed and examined for possible rational explanations. Limited cavitation data are presented and discussed for axisymmetric headforms and three families of hydrofoils. For the hydrofoils, measurement of surface cavitation for both sheet and bubble types in addition to tip-vortex cavitation were obtained over a range of Reynolds numbers. Each family of hydrofoils is geometrically similar in planform and cross section and has chord lengths of 38.1, 76.2, 152.4 and 304.8 millimeters. The cross sections of the three hydrofoil families are:

(1) a modified Joukowski hydrofoil section with a maximum thickness of 10.6 percent.
(2) a NACA 0015 hydrofoil section and
(3) a cambered NACA 0010 section with a maximum camber of 10 percent.

These hydrofoil families were tested in the 1.22 m water tunnel at ARL/PSU. It is indicated that scale effects are due to changes in the pressure field (type #1) and to bubble dynamic and nuclei effects (type #2). The various types of cavitation are examined to determine the type of scale effects which appear to be controlling the cavitation process. Approximate analyses are presented for bubble-ring, band, tip-vortex, and fixed-patch or sheet cavitation. The latter appear to be controlled by surface roughness effects.

Definition of the Subject and Objectives of the Paper

Cavitation is the vapor and gas filled regions created by a localized pressure reduction produced by the dynamic action of a liquid in the interior and/or on the boundaries of a liquid system.

The *cavitation number* (σ) is a useful parameter for categorizing cavitating flows and is defined as

$$\sigma = \frac{P_\infty - P_v}{1/2 \rho U_\infty^2} \quad (1)$$

where P_∞ and U_∞ are the pressure and velocity at infinity, respectively. The vapor pressure (P_v) and liquid mass density (ρ) correspond to the bulk temperature of the liquid.

If σ is sufficiently large there is no evidence of cavitation whereas if σ is sufficiently small the cavitation can be well developed. *Limited cavitation* occurs at an intermediate value of the cavitation number where the amount of a given type of cavitation is minimized. The cavitation number corresponding to this state is the limited cavitation number (σ_l) where P_∞ in equation (1) is replaced by P_{∞_l}. In most cases referred to in this paper, the cavitation number for a given state of limited cavitation was determined by the desinence procedure as described by Holl [1].[1] (The desinence test procedure was apparently first employed as a standard method at the Hydrodynamics Laboratory of the California Institute of Technology as described by Kermeen [2].) Thus the limited cavitation number is equal to the desinent cavitation number and P_{∞_d} replaces P_∞ in equation (1). One can also use the incipient cavitation number (σ_i) where P_{∞_i} replaces P_∞ in equation (1) as a measure of σ_l. However, experience shows that σ_d is often a more repeatable state than σ_i and tends to be the upper bound of σ_i. However, Acosta and Hamaguchi [3] report cases at high gas contents where $\sigma_i > \sigma_d$. The inequality between σ_i and σ_d is due to so-called cavitation *hysteresis* a phenomenon which has been studied extensively [4]-[6].

Limited cavitation can be *vaporous* or *gaseous* [7]. The former type of cavitation is caused by the explosive growth of bubbles [8] due to the rapid conversion of liquid to vapor at the bubble wall whereas the latter is due to a slower mode of bubble growth caused by the transport of noncondensable gas [9].

Contributed by the Fluids Engineering Division of THE AMERICAN SOCIETY OF MECHANICAL ENGINEERS and presented at the International Symposium on Cavitation Inception, ASME Winter Annual Meeting, New York, N.Y., December 2-7, 1979. Manuscript received by the Fluids Engineering Division, February 11, 1980.

[1] Numbers in brackets refer to documents in the list of references.

Of particular importance in the study of limited cavitation is the *minimum pressure coefficient* ($C_{p_{\min}}$) given by

$$C_{p_{\min}} = \frac{P_{\min} - P_\infty}{1/2 \rho U_\infty{}^2} \tag{2}$$

where $P_{\min}$ is the minimum pressure in the liquid.

The classical theory for scaling vaporous limited cavitation states that $\sigma_l = -C_{p_{\min}}$ and $C_{p_{\min}}$ = constant provided that when scaling from one flow state to another the form of the flow field and its boundaries remain geometrically and kinematically similar. Thus, if one conducts a model experiment to find the limited cavitation number then the prototype condition is immediately known for flows satisfying the classical theory. However, it has been found that real flows often do not obey the classical theory because of so-called *scale effects* which arise from changes in velocity, size and fluid properties [7, 10, 11]. Experimental results show that in many cases the limited cavitation number can be greater or less than the minimum pressure coefficient and that the minimum pressure coefficient is not constant.

From considering the basic aspects of limited cavitation we find it natural to divide the study of scale effects into two parts [7, 10]:

Type #1 scale effects act on the flow outside the cavitation bubbles which influence the pressure in the liquid flow.

Type #2 scale effects act on the bubble growth process which cause the liquid pressure at the cavitation bubbles to depart from the equilibrium vapor pressure corresponding to the bulk temperature of the liquid.

Type #1 scale effects are primarily due to:

(1) Effects associated with changes in the flow field caused by variations in Reynolds number, Froude number and Mach number including turbulent pressure fluctuations.

(2) Effects associated with departures from exact geometric similarity such as those due to surface roughness.

Type #2 scale effects are primarily due to:

(1) Time effects
(2) Heat transfer effects
(3) Surface tension effects
(4) Transport of noncondensable gas
(5) Cavitation nuclei

Thus, type #1 scale effects cause the minimum pressure coefficient to vary whereas type #2 scale effects cause the limited cavitation number to be different than $-C_{p_{\min}}$.

It should be noted that some effects can cause both type #1 and type #2 scale effects. For example, laminar separation which is a Reynolds number related phenomenon causes a type #1 scale effect in that it has a direct influence on the pressure field. However, it can also influence the residence time of bubbles in the low pressure region and thus cause gaseous cavitation which is a type #2 scale effect.

The gross manner in which the various factors which cause scale effects can influence the cavitation number can be ascertained by employing the Rayleigh-Plesset equation to describe the growth of a "typical" cavitation bubble. As indicated by Holl and Kornhauser [12] this equation can be written in the form

$$\rho(R\ddot{R} + \frac{3}{2}\dot{R}^2) = P_G - \frac{2S}{R} - \frac{4u\dot{R}}{R} - [C_p(t) + \sigma_l + C_T(t)]\ 1/2\rho U_\infty{}^2 \tag{3}$$

where

$$C_p(t) = \frac{P(t) - P_\infty}{1/2\rho U_\infty{}^2} \tag{4}$$

and

$$C_T(t) = \frac{P_v(T_\infty) - P_v[T_R(t)]}{1/2\rho U_\infty{}^2}\ . \tag{5}$$

Thus $C_p(t)$ is the time varying pressure coefficient which describes the variation of the liquid pressure outside of the bubble. The thermodynamic coefficient (C_T) describes the effect of heat transfer on the vapor pressure in the bubble. Multiplying equation (3) by a time interval (dt), integrating over a time interval (T_C) which is typical of the cavitation process, and solving for σ_l yields

$$\sigma_l = -\bar{C}_p + \frac{\bar{P}_G - \left(\frac{\overline{2S}}{R}\right)}{1/2\rho U_\infty{}^2} - \phi - \bar{C}_T \tag{6}$$

where the bubble dynamic parameter (ϕ) is given by

$$\phi = \frac{\frac{1}{T_C}\int_0^{T_C}\left(\frac{4u\dot{R}}{R} + \rho\left\{R\ddot{R} + \frac{3}{2}\dot{R}^2\right\}\right)dt}{1/2\rho U_\infty{}^2}\ . \tag{7}$$

The bars over the symbols denote averages over the interval T_C. It is apparent that the terms $\overline{P_G}$, $\overline{2S/R}$, Φ, and $\bar{C}_T$ will all depend upon the bubble dynamics but it is convenient to group the factors which depend upon $\dot{R}$ and $\ddot{R}$ into a single term since in the absence of significant dynamic effects, such as for purely gaseous cavitation, equation (6) reduces to the equilibrium equation

$$\sigma_l = -\bar{C}_p + \frac{\bar{P}_G - \left(\frac{\overline{2S}}{R}\right)}{1/2\rho U_\infty{}^2} \tag{8}$$

which has been employed by Holl [1, 7] and other investigators.

Referring to equation (6) it is seen that the terms $\overline{P_G}$, $\overline{2S/R}$, ϕ, and C_T all cause type #2 scale effects and furthermore they all tend to reduce σ_l with the exception of the gas pressure term ($\overline{P_G}$). However, the thermodynamic coefficient will be essentially zero for the data to be discussed in this paper since it was obtained in water at or near room temperature.

The type #1 scale effects are contained within the average pressure coefficient ($\overline{C_p}$). Following Holl [7], this term can be written as

$$-\overline{C_p} = -\overline{C_{p_s}} + \frac{\overline{\Delta P_T}}{1/2\rho U_\infty{}^2} + \frac{\overline{\Delta P_R}}{1/2\rho U_\infty{}^2} \tag{9}$$

where $\overline{C_{p_s}}$ is the average pressure on the "smooth" body in the absence of surface roughness or turbulence and $\overline{\Delta P_T}$ and $\overline{\Delta P_R}$ are pressure reductions due to turbulence and surface roughness, respectively. Depending upon the nature of the surface roughness, it would be logical in many cases to combine the turbulence and roughness terms. Generally the effects of roughness and turbulence would cause σ_l to increase.

This paper has two primary objectives. First, new experimental data are presented which display scale effects for several types of cavitation. Second, these data are discussed and examined for possible rational explanations. The foregoing discussion of scale effects will be useful in this examination process.

Cavitation data for headforms and hydrofoils will be discussed in subsequent sections. The total air content (α) will be expressed in moles of air per million moles of water (ppm).

Axisymmetric Head Form Data

Changes in the cavitation number for constant form or extent constitute scale effects. Thus it is necessary that the test information disclose the form and extent of the cavitation as a function of test variables.

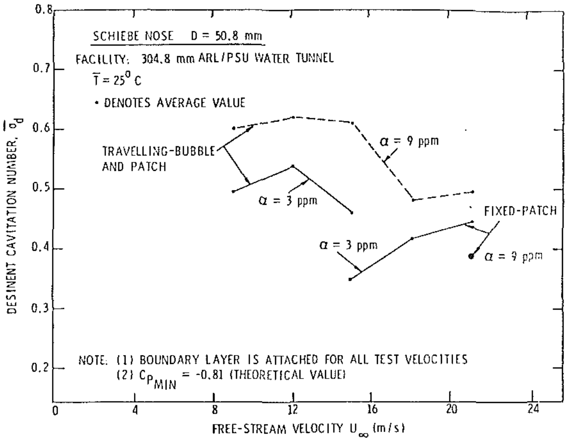

Fig. 1 Desinent cavitation data - Schiebe nose

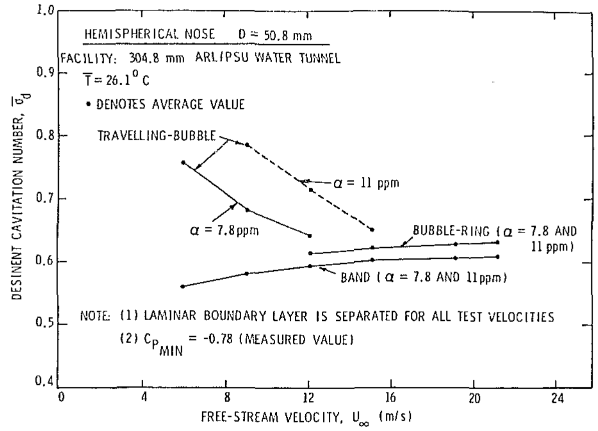

Fig. 2 Desinent cavitation data - hemispherical nose

There are several recent test programs in which limited cavitation data were obtained over a velocity range where the form of the cavitation was noted. As one example, Holl and Carroll [13] have recently reported the limited cavitation data for Schiebe, hemispherical and DTNSRDC headforms. In all cases the maximum diameter of the model was 50.8 mm. The tests were conducted over a velocity range of 6.1 to 21.3 m/s. For all three headforms the cavitation occurred at or very close to the body surface and near the minimum pressure point. The Schiebe headform [14] is generated by a combination of a normal source disk and a uniform flow and has a minimum pressure coefficient which is close to that of a hemispherical nose. Van der Meulen [15] has investigated the flow about a Schiebe headform utilizing holographic techniques and has verified that the body does not experience laminar boundary layer separation. In addition, Arakeri and Acosta [16] have shown that the hemispherical headform has laminar boundary layer separation up to an estimated Reynolds number of 5×10^6. The DTNSRDC headform is a member of the modified ellipsoid family and has a critical Reynolds number of 5×10^5 which corresponds to a velocity of 9.1 m/s for a 50.8 mm diameter nose at 23.4°C in water. Thus the DTNSRDC nose experienced both separated and unseparated flow over the velocity range employed in this program.

The cavitation data over a velocity range are shown in Fig. 1 for the Schiebe nose and in Fig. 2 for the hemispherical nose. (The forms of cavitation observed on the DTNSRDC nose were similar to those observed on the Schiebe and hemispherical headforms. Thus data for this nose will not be presented in this paper but may be found in the paper by Holl and Carroll [13].)

The limited cavitation data for the Schiebe nose in Fig. 1 were obtained at two air contents and display two types of cavitation namely, travelling cavitation and fixed-patch cavitation. The travelling cavitation, which occurs first, is in the form of quasi-spherical bubbles or patches and σ_l tends to decrease with velocity and increase with air content. At higher velocities, fixed-patch cavitation occurs and σ_l increases with velocity and decreases with air content. At the higher air content i.e., $\alpha = 9$ ppm the fixed-patch cavitation was suppressed at all velocities except at 21.3 m/s. For all types of cavitation σ_l is significantly less than $C_{p_{\min}}$.

The cavitation data in Fig. 2 for the hemispherical nose reveal three basic types of cavitation namely travelling-bubble, bubble-ring, and band. At low velocities, the desinent cavitation number decreased with velocity and increased with air content and the cavitation was in the form of travelling bubbles. Thus these trends are similar to those on the Schiebe nose. Over the remaining velocity range, the desinent cavitation number increased slightly with increasing velocity for the bubble-ring cavitation and was essentially independent of air content for $\alpha > 4$ ppm but when α was reduced below this value, bubble-ring cavitation disappeared. This form of cavitation has many small bubbles which occur inside the laminar boundary layer separation region.

The third form of cavitation observed on the hemispherical nose was band cavitation for which the cavitation number increased gradually with velocity and was nearly independent of air content. This form of cavitation occurred as a fixed sheet attached to the headform at the leading edge of the laminar boundary layer separation region.

Although the minimum pressure coefficient of the two headforms are nearly the same, the pressure distribution and hence the form of cavitation and its scale effects are different except for the travelling-bubble cavitation. The Schiebe headform has a very peaked pressure distribution located near the leading edge. In contrast, the hemispherical headform also has a very peaked pressure distribution but it is somewhat broader and the peak is located further from the leading edge.

The pressure distribution for the hemispherical headform leads to laminar boundary layer separation over the velocity range tested and hence to forms of cavitation that are related to the separated region. These forms are bubble-ring cavitation and band cavitation which has a clear and scallopy appearance. Both forms have a cavitation number which increases with velocity.

The pressure distribution for the Schiebe headform leads to natural boundary layer transition and displays three forms of limited cavitation, namely travelling-bubble, travelling-patch, and fixed-patch. The travelling type of cavitation is very sensitive to free-stream nuclei as will be discussed subsequently.

Some additional experimental information for a Schiebe headform was obtained in an investigation on cavitation scale effects conducted in the water tunnels of the California Institute of Technology (CIT) and the Applied Research Laboratory at The Pennsylvania State University (ARL/PSU). Cavitation data shown in Fig. 3 are from tests conducted in the Low Turbulence Water Tunnel (LTWT) and the High Speed Water Tunnel (HSWT) at CIT and in the 305 mm diameter water tunnel at ARL/PSU. As can be noted in the figure, there is a decrease in cavitation number with increasing velocity for the travelling-bubble form of cavitation. There is an increase in cavitation number with increasing velocity for attached cavitation. More important is the fact that the initial form of cavitation for the LTWT and the 305 mm water tunnel was travelling-bubble; but, for the HSWT the initial form of cavitation was attached. This difference in

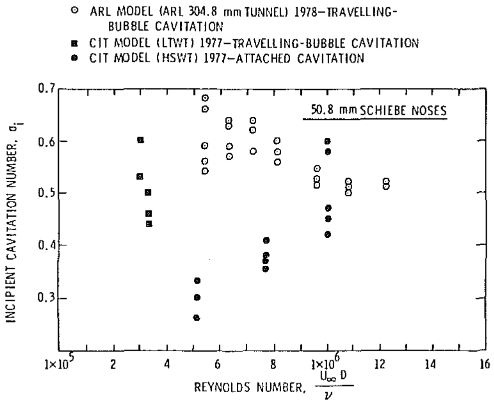

Fig. 3 Comparison of CIT and ARL/PSU inception data for 50.8 mm Schiebe noses

the form of cavitation is most probably due to the free-stream bubbles.

Gates [17] has shown that the travelling-bubble cavitation typical of headforms without laminar boundary layer separation is strongly dependent upon the distribution of free-stream nuclei. This is in contrast to flows with laminar separation bubbles where the nuclei in this region are thought to be the primary source of cavitation which is generated in the laminar separation bubble.

Some nuclei measurements have been made in the various facilities at different times. The results show that a large number of bubbles exist in both the LTWT at CIT and the 305 mm water tunnel at ARL. In contrast, tests have shown that very few free-stream bubbles exist in the HSWT at CIT. These results seem to indicate that not only does the inception of travelling-bubble cavitation depend on a large number of free-stream nuclei but also the cavitation number is largely determined by the size and distribution of the free-stream bubbles.

There have been many recent papers which discuss the influence of boundary layer behavior on cavitation inception such as Arakeri and Acosta [16, 18], Arakeri [19] and Huang and Peterson [20]. In addition there are several papers which have reported on long and short separation bubbles and pressure fluctuations in regions of reattachment [21-24]. The changes in pressures caused by the combined effects of pressure fluctuations and changes in the mean pressure due to drastic changes in the length of the laminar separation bubble can produce very interesting scale effects.

An example of the aforementioned case is the data for a 1/8 caliber ogive by Robertson, McGinley, and Holl [25] which is shown in Fig. 4. A sudden increase in the magnitude of the desinent cavitation number occurs at a Reynolds number of 5 × 10^5. A bubble form of cavitation was observed over the entire Reynolds number range; however, the location of the bubbles varied. For Reynolds numbers above the critical Reynolds number, a bubble-ring form of cavitation was observed near the nose. Below the critical Reynolds numbers, bubbles appeared in the shear layer downstream and away from the surface of the headform.

Recent tests by Arakeri, Carroll, and Holl [26] showed that the observed change in the desinent cavitation number at a critical Reynolds number on the headform is associated with the change in the physical structure of the laminar boundary layer separation region. By applying an oil-paint mixture to a 50.8 mm diameter, 1/8 caliber ogive, a long separated flow region was observed below a critical velocity and a small separated flow region was observed above this velocity. This change in boundary layer characteristics corresponds to a sudden increase in cavitation number.

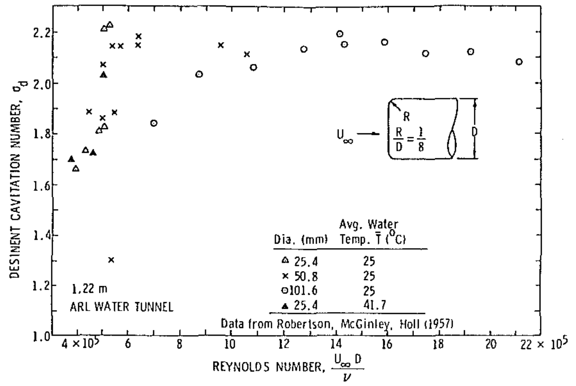

Fig. 4 Desinent cavitation number versus Reynolds number for 1/8 caliber ogives

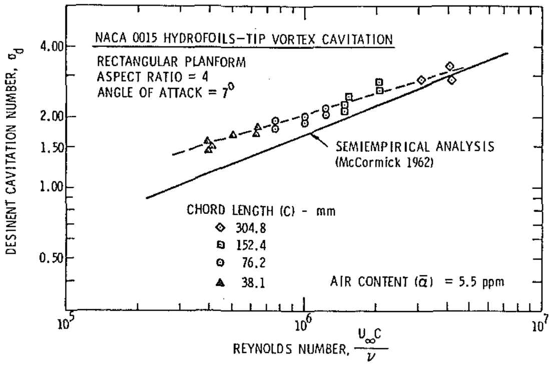

Fig. 5 Tip-vortex cavitation data for NACA 0015 hydrofoils

At low Reynolds numbers where the long separation bubble exists, the bubble form of cavitation appeared in the free shear layer away from the headform. In this Reynolds number range, the cavitation number increases rapidly with increasing velocity or Reynolds number. This trend is also observed for cavitation in the region of separation behind a sharp-edged disk as discussed by Kermeen and Parkin [27].

At high Reynolds numbers where the short separation bubble exists a bubble-ring form of cavitation appears and σ_i increases gradually with velocity. This is similar to results discussed previously for a hemispherical headform which had a short separation bubble.

Hydrofoil Data

The limited cavitation data presented on axisymmetric headforms show the dependence of cavitation number on the boundary layer behavior and on the free-stream nuclei. In addition, the form of the cavitation can also be related to the boundary layer behavior. We will now examine hydrofoil data to determine whether or not these data display characteristics which are similar to those of the headforms.

Three families of hydrofoils have recently been employed at ARL/PSU in several investigations. These data show scale effects over a large Reynolds number range of approximately 16:1. The data presented are for pressure-surface, suction-surface, and tip-vortex cavitation.

Symmetrical Hydrofoils With Rectangular Planforms. Limited cavitation data were obtained over a range of Reynolds numbers for suction-surface cavitation and tip-vortex cavitation for a family of symmetrical rectangular hydrofoils. In all, four rectangular hydrofoils were tested having chord sizes of 38.1, 76.2, and 304.8 millimeters. Each rectangular hydrofoil was mounted on a horizontal plate and projected vertically with the tip being on the centerline of the

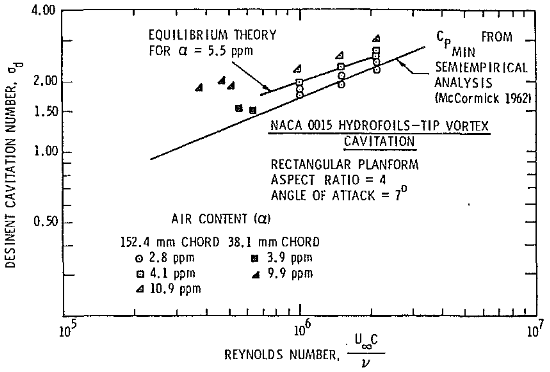

Fig. 6 Tip-vortex cavitation data at several values of air content for NACA 0015 hydrofoils

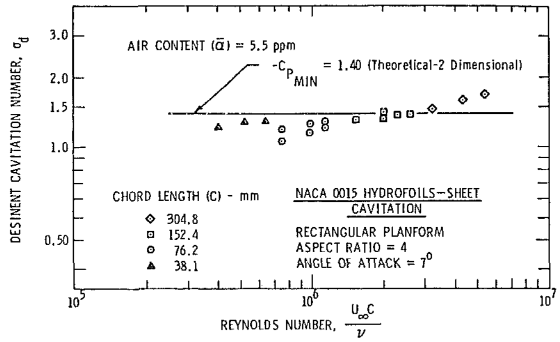

Fig. 7 Suction-surface cavitation data for NACA 0015 hydrofoils

tunnel. The tests were conducted in the 1.22 m water tunnel located in the Garfield Thomas Water Tunnel Building of the Applied Research Laboratory at The Pennsylvania State University.

The hydrofoils had a NACA 0015 airfoil section and an aspect ratio of four. These hydrofoils were similar to those used by McCormick [28, 29] for a tip-vortex cavitation study. Most of the data were obtained with the hydrofoil at an angle of attack of seven degrees and the velocity range was approximately 9.1 to 16.8 m/s. For most tests, the air content of the water was approximately 5.5 ppm.

The desinent cavitation data for tip-vortex cavitation on the rectangular hydrofoils are given in Fig. 5 over a range of Reynolds numbers. The calculated curve in the figure was based on the semiempirical analysis developed by McCormick [28, 29]. The scatter of the data is characteristic of vortex cavitation. Limited cavitation in the vortex was detached from the hydrofoil tip and was uniform for a considerable distance downstream from the hydrofoil.

McCormick [29] shows that the minimum pressure coefficient of the tip vortex depends upon the boundary-layer thickness on the pressure face of the hydrofoil and the thickness of the vortex core is apparently not determined by the induced drag of the foil. He found that the minimum pressure coefficient at a constant angle of attack could be expressed in terms of a Reynolds number to a power. The cavitation number in Fig. 5 varies as the Reynolds number to the 0.35 power. This compares favorably with a value of 0.41 obtained previously by McCormick [29]. The cavitation data are higher than the apparent minimum pressure coefficient predicted by a semiempirical analysis which suggests that the scaling relationship with Reynolds number may be dependent on the air content of the water.

The scaling of vortex cavitation is particularly interesting because the cavitation occurs away from a surface and hence the air content, which for a given tunnel facility is a crude measure of the cavitation nuclei, should be an important factor. The tip-vortex cavitation data shown in Fig. 6 indeed show that the cavitation number increases with increasing air content. An equilibrium theory [1] was used to correlate the cavitation data. (This theory is discussed in a subsequent section.) Calculated values of the limited cavitation number using the equilibrium theory are shown in Fig. 6 for the 152.4 mm hydrofoil at an air content of 5.5 ppm. It is important to note that the Reynolds number correlation changes with air content.

Sheet cavitation data for the suction surface are shown in Fig. 7 with the hydrofoils at an angle of attack of 7 degrees. The cavitation appeared near the leading edge and appeared to be attached to the surface.

The data of Fig. 7 show some degree of correlation with Reynolds number. For a given chord, the desinent cavitation number increases with Reynolds number. However, for a given Reynolds number the desinent cavitation number decreases with increasing size. Thus both size and Reynolds number are important scale factors. With the exception of the higher velocities for the largest foil, all of the cavitation data are lower than the theoretical value of $-C_{p_{\min}}$. These trends are similar to many other investigations as discussed by Holl and Wislicenus [10].

Symmetrical Joukowski Hydrofoils. As part of a program on cavitation noise [30] conducted at ARL/PSU, limited cavitation data were obtained for a family of symmetrical Joukowski hydrofoils. The hydrofoils were geometrically similar in planform and cross section and had chord lengths of 38.1, 76.2, 152.4, and 304.8 mm. In order to maintain similar flow fields for each hydrofoil, the aspect ratio was held constant at 0.66 and the hydrofoils were equipped with elliptical end plates to reduce the span-wise flow. The cross section of each hydrofoil was a modified Joukowski airfoil section with a maximum thickness of 10.6 percent of the chord length. The modification consisted of replacing the cusped trailing edge with a linear distribution for reasons of ease of manufacture. More details of the hydrofoil tests are given in reference [30]. The desinent cavitation data for suction-surface cavitation are shown in Fig. 8 for a geometric angles of attack of 4 and 7 degrees.

For an attack angle of 7 degrees, sheet cavitation occurred near the leading edge of the hydrofoil and appeared to be attached to the surface. It can be seen that over a Reynolds number range of 3.3×10^5 to 5.4×10^6, the cavitation data for an angle of attack of 7 degrees do not show a consistent scaling relationship. Also, these results do not show trends which are consistent with those of the rectangular hydrofoils in Fig. 7.

Desinent cavitation data at a geometric angle of attack of 4 degrees are also shown in Fig. 8. The cavitation occurred near mid-chord on the suction side and was in the form of travelling-bubble cavitation. These cavitation data appear to be less dependent on Reynolds number than those at an attack angle of 7 degrees.

The scaling with Reynolds number for the attached sheet cavitation is very different than the scaling for travelling-bubble cavitation. It appears that viscous effects due to boundary layer behavior influence the cavitation data for the hydrofoils at an attack angle of 7 degrees and complicate the scaling relationship. Thus a set of experiments was conducted to determine the boundary layer behavior over the Reynolds number range at the two angles of attack.

An oil-paint film was applied in a diagonal strip on the suction surface of the hydrofoil. After approximately thirty seconds of tunnel running time, the tunnel was stopped and a photograph was taken of the oil-paint film. The results showed that at an angle of attack of 4 degrees, no boundary layer separation occurred on any of the hydrofoils. At an

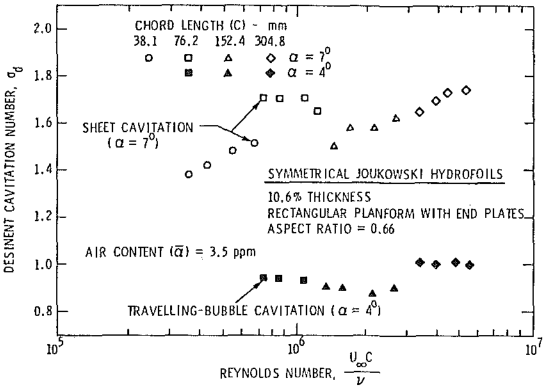

Fig. 8 Suction-surface cavitation data for Joukowski hydrofoils

angle of attack of 7 degrees, only the two smaller hydrofoils showed boundary layer separation. For the 38.1 mm hydrofoil, the separation region was very large. For the 76.2 mm hydrofoil, the separation bubble was small up to a velocity of 18.3 m/s where the separation disappeared.

The jump in cavitation number at a Reynolds number of 7 × 10^5 for the 7 degree angle of attack could be due to a transition from a long separation region to a short separation region. As discussed by Huang and Peterson [20], the presence of a long separation region can significantly reduce the magnitude of the mean minimum pressure coefficient on the body.

Cambered Hydrofoils With Quasi-Elliptical Planforms. Another set of limited cavitation data over a Reynolds number range were obtained for a family of cambered hydrofoils. Four geometrically similar hydrofoils were tested at ARL/PSU having chord sizes of 38.1, 76.2, 152.4, and 304.8 millimeters. The hydrofoils had a NACA 0010 airfoil section and an aspect ratio of four. The hydrofoils had a linear camber distribution along the span with zero percent camber at the root and a maximum of ten percent camber near the tip. In addition, the top one-third of the span had an elliptical planform.

Desinent cavitation data for suction-surface, pressure-surface and tip-vortex are given in Fig. 9. Suction-surface cavitation ocurred near the mid-chord of the hydrofoil and was in the form of travelling-bubble cavitation. Pressure-surface cavitation ocurred as fixed patches, i.e., sheet cavitation near the leading edge of the hydrofoil. Tip-vortex cavitation was detached from the hydrofoil except when leading edge pressure face cavitation occurred near the tip of the hydrofoil at which time the vortex became attached to the hydrofoil.

The data show some degree of scaling with Reynolds number. For a given chord, the desinent cavitation number for pressure-face cavitation increases with Reynolds number. The desinent cavitation number decreases with increasing size for a given Reynolds number. These results are similar to those observed for the NACA 0015 hydrofoil in Fig. 7 and the 152.4 mm and 304.8 mm Joukowski hydrofoils in Fig. 8 at 7 degree angle of attack.

For suction-surface cavitation, the desinent cavitation number decreased for increasing Reynolds number for constant hydrofoil size. At a constant Reynolds number, the desinent cavitation number increases with increasing size. These results are opposite to those observed for pressure-surface cavitation.

The desinent cavitation number for tip-vortex cavitation increased with increasing Reynolds number. The slope of the mean line through the data is approximately 0.35. This result is similar to the one found for the NACA 0015 hydrofoils in Fig. 5.

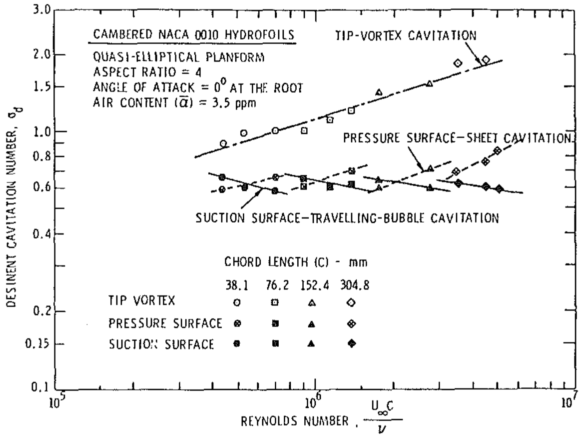

Fig. 9 Tip-vortex, pressure-surface, and suction-surface cavitation data for cambered hydrofoils

It is interesting to compare the change in cavitation number for each type of cavitation over the extremes of the test range i.e., for a Reynolds number variation from 4.4 × 10^5 to 5 × 10^6. The desinent cavitation number for tip-vortex cavitation more than doubled over this Reynolds number range. The desinent cavitation number for pressure-surface cavitation increased by a factor of 1.4 and for suction-surface cavitation decreased by a factor of 0.88. In addition, at a Reynolds number of 4.4 × 10^5, the spread in cavitation number data for the three types of cavitation was approximately 0.9 to 0.58 and at a Reynolds number of 5 × 10^6 the spread was approximately 1.9 to 0.60.

Discussion and Analysis of Cavitation Data

The intent of this section is to discuss the cavitation data presented in the preceding sections in an attempt to summarize and integrate the results and to arrive at rational explanations where possible. The pertinent form of the bubble dynamic equation from the introductory section, namely a combination of equations (6) and (9) given by

$$\sigma_l = -\overline{C_{p_s}} + \frac{\overline{\Delta P_T}}{1/2\rho U_\infty{}^2} + \frac{\overline{\Delta P_R}}{1/2\rho U_\infty{}^2} + \frac{P_G - \left(\frac{\overline{2S}}{R}\right)}{1/2\rho U_\infty{}^2} - \Phi \qquad (10)$$

will be used in the course of the discussion.

Bubble-Ring and Band Cavitation. The bubble-ring and band cavitation observed on the hemispherical nose are only encountered when the body experiences laminar separation. Band cavitation has been observed on several headforms namely the Swedish or ITTC nose [16] and the DTNSRDC nose [13]. In addition, the cavitation on the 38.1 mm and 76.2 mm Joukowski hydrofoil at 7 degree angle of attack shown in Fig. 8 had cavitation which appeared to be similar to the band cavitation and both hydrofoils suffered laminar separation as shown by oil film flow visualization techniques. Holl and Carroll [13] found that the band cavitation was essentially independent of air content and that the cavitation number increased with velocity. The increase of σ_l with velocity is also shown by the 38.1 mm Joukowski hydrofoil data in Fig. 8 but the 76.2 mm hydrofoil data show the opposite trend. The air content was not varied significantly during the tests of the Joukowski hydrofoils. Holl and Carroll analyzed the band cavitation by assuming that σ_l was only affected by type #1 scale effects so that equation (10) reduces to

$$\sigma_l = -\overline{C_{p_s}}. \qquad (11)$$

Holl and Carroll were able to correlate σ_l fairly well with a measured mean pressure coefficient near the assumed transition point.

Bubble-ring cavitation appears to be a rather unique form of cavitation for it has only been observed on hemispherical noses and 1/8 caliber ogives with short separation bubbles. The cavitation number increases gradually with velocity. Holl and Carroll show for the hemispherical nose that σ_i is insensitive to air content (α) provided α was greater than 4 ppm but for α less than this value bubble-ring cavitation was not observed. Also bubble-ring cavitation was not observed on the hemispherical nose for velocities less than about 12.2 m/s. By assuming that bubble-ring cavitation was influenced primarily by type #1 scale effects Holl and Carroll approximated σ_i by an equation of the form

$$\sigma_i = -\overline{C_{p_s}} + \frac{\overline{\Delta P_T}}{1/2\rho U_\infty{}^2}. \tag{12}$$

However, this cannot account for the air content and velocity cut-off effects. Thus this form of cavitation is evidently influenced by both type #1 and #2 scale effects. Also, Holl and Carroll show that bubble-ring cavitation is influenced by the water temperature.

Travelling Cavitation. Travelling cavitation in the form of bubbles or patches was observed by Holl and Carroll [13] on the three headforms used in the investigation namely the hemispherical, Schiebe and DTNSRDC noses. Furthermore this form of cavitation was present for both separated and attached boundary layers. It was also observed on the suction face of the cambered hydrofoil shown in Fig. 9 and on the Joukowski hydrofoil at 4 degrees attack angle in Fig. 8. Generally speaking this form of cavitation is such that the cavitation number tends to decrease with velocity. This trend had also been observed by Van der Meulen [15] for a Schiebe nose and by Schiebe [31] for an ITTC nose. Assuming that this type of cavitation is due to the response of a bubble to the mean surface pressure then σ_i would be approximated by

$$\sigma_i = -\overline{C_{p_s}} + \frac{\bar{P}_G - \left(\overline{\frac{2S}{R}}\right)}{1/2\rho U_\infty{}^2} - \Phi\ . \tag{13}$$

Holl and Carroll [13] also showed that σ_i increases with air content suggesting the importance of type #2 scale effects. The effect of body size was not investigated by Holl and Carroll for the headforms. The effect of size is displayed by the suction face cambered hydrofoil data in Fig. 9. Plotting σ_i versus Reynolds number is somewhat misleading for these data for if σ_i were plotted versus velocity the data for all four hydrofoils would be nearly on top of each other. Thus time effects as influenced by a variation in C/U_∞ where C is chord length do not appear to play a major role in the bubble dynamics for these hydrofoils. But size effects on the headforms may be different than that for the hydrofoils.

An analysis of travelling-bubble cavitation by Holl and Carroll [13] suggests that the initial bubble radius would decrease more than two orders of magnitude over the velocity range of 6.1 to 21.3 m/s in order to explain the velocity trend displayed by the headform data of Figs. 1 and 2. However, the mechanism which controls this nuclei selection process, if in fact it exists, has not been determined.

Tip-Vortex Cavitation. McCormick [29] assumed that tip-vortex cavitation is completely controlled by type #1 scale effects. He assumed that the pressure coefficient C_{p_s} was equal to the minimum pressure coefficient of a Rankine combined vortex so that

$$\sigma_i = -\overline{C_{p_s}} = -\overline{C_{p_{\min}}} \ = \ \text{constant}\left(\frac{\Gamma}{r_c U_\infty}\right)^2 \tag{14}$$

where Γ is the strength of the vortex, and r_c is the core radius. The strength of the tip vortex can be expressed as

$$\Gamma \ = \ \text{constant}\ C_L U_\infty \bar{C} \tag{15}$$

where C_L and $\bar{C}$ are the lift coefficient and mean chord, respectively. Assuming that the core radius is proportional to the boundary layer thickness on the pressure side as suggested by McCormick's experiments then for a turbulent boundary layer

$$r_c \ = \ \text{constant}\ \frac{\bar{C}}{\mathrm{Re}^{1/5}}\ . \tag{16}$$

Employing equations (15) and (16) in equation (14) yields

$$\sigma_i \ = \ \text{constant}\ C_L{}^2\mathrm{Re}^{0.4}. \tag{17}$$

The Reynolds number dependency displayed by this equation is approximated fairly well by the data of Fig. 5. (However, McCormick's measurements indicate that for a given Reynolds number σ_i varies as approximately the first power of C_L. In addition, his data show that σ_i is nearly independent of aspect ratio.) McCormick employing a more sophisticated analysis predicts a Reynolds number slope of 0.41 which compares favorably with the slope of 0.35 in Fig. 5 for the data of an air content of 5.5 ppm.

Referring to Fig. 6, it is seen that the tip-vortex cavitation is also influenced significantly by type #2 scale effects as evidenced by the strong effect of air content. This effect was analyzed by using the equilibrium theory developed by Holl [1]. Assuming the cavitation is non-vaporous, i.e., gaseous, and ignoring dynamic and surface tension effects equation (10) reduces to

$$\sigma_i \ = \ -\overline{C_{p_s}} + \frac{\overline{P_G}}{1/2\rho U_\infty{}^2}. \tag{18}$$

As indicated by Holl [1] one can approximate the gas pressure by Henry's law

$$P_G \ = \ k\alpha\beta \tag{19}$$

where α, β, and k are the dissolved gas content, Henry's law constant and an empirical adjustment factor, respectively. Assuming that $\overline{C_{p_s}}$ is approximated by McCormick's analysis and with $k = 0.45$, the plot of equation (18) at an air content of 5.5 ppm is shown by the solid line in Fig. 6 for the 152.4 mm hydrofoil. Thus it is seen that the Reynolds number dependency is a function of the air content.

The aforementioned equilibrium analysis has also been applied to other types of vortex cavitation [11], [32].

Eighth-Caliber Ogive Nose. The desinent cavitation number for an eighth-caliber ogive nose was shown as a function of Reynolds number in Fig. 4. As indicated previously, these data were originally reported by Robertson, McGinley, and Holl [25] and were recently reevaluated by Arakeri, Carroll, and Holl [26] who showed by a flow visualization technique that the jump in cavitation number at a Reynolds number of 5×10^5 is due to a change from a long to short laminar separation bubble. In reference [26] it was proposed that the change in cavitation number is given by

$$(\sigma_i)_{sb} - (\sigma_i)_{lb} = -(\bar{C}_p)_{sb} + (\bar{C}_p)_{lb} + \left(\frac{p'}{1/2\rho U_\infty{}^2}\right)_{sb} - \left(\frac{p'}{1/2\rho U_\infty{}^2}\right)_{lb} \tag{20}$$

where the subscripts sb and lb denote short bubble and long bubble, respectively. Huang and Peterson [20] have proposed an equation similar to equation (20). The pressure coefficient is given by

$$(C_P) = \frac{\bar{P}_a - \bar{P}_t}{1/2\rho U_\infty{}^2} \tag{21}$$

where $\bar{P}_a$ and $\bar{P}_t$ are the actual and theoretical mean pressures at the separation point, respectively. This coefficient is discussed by Arakeri, et al [26] for long and short bubbles. The pressure fluctuation (P') in equation (20) due to turbulence is probably different for long and short bubbles as pointed out by Arakeri, Carroll, and Holl [26] based on the work of Young and Horton [22].

It is apparent that equation (20) is based on the assumption that this flow is controlled by type #1 scale effects since the dynamic, surface tension, and gas pressure terms in equation (10) have been ignored. However, this is an approximation which will probably not apply in some cases. For the long bubble regime, the cavitation appears like that obtained in the shear layer of a sharp-edged disk. Arndt and Keller [33] have shown that disk cavitation can be sensitive to air content when the flow is supersaturated which tends to occur most frequently at low velocities.

On the other hand, the short bubble regime is characterized by bubble-ring cavitation which as shown by Holl and Carroll [13] is insensitive to air content on a hemispherical nose provided $\alpha > 4$ ppm. Below this air content bubble-ring cavitation did not occur on the hemispherical nose. (Robertson, McGinley, and Holl [25] did not report conclusive air content effects on the 1/8 caliber ogive nose data.) Thus depending upon the flow regime, i.e., long bubble versus short bubble, a body such as the 1/8 caliber ogive nose may or may not display significant air content effects, i.e., type #2 scale effects.

Fixed-Patch and Sheet Cavitation. As indicated previously, Holl and Carroll [13] observed fixed-patch cavitation on 50.8 mm diameter Schiebe and DTNSRDC headforms. They also occasionally observed fixed-patch cavitation on a 50.8 mm diameter hemispherical nose which was apparently due to dirt particles for wiping off the nose eliminated this type of cavitation in subsequent tests. However, wiping off the surface did not eliminate fixed patch cavitation on the Schiebe and DTNSRDC noses. Parkin and Holl [34] in discussing cavitation on 101.6 mm and 203.2 mm diameter hemispherical noses "observed small diamond shaped cavitation zones apparently due to very small rough spots."

As previously indicated in the discussion of Figs. 1 and 2 the fixed-patch cavitation observed by Holl and Carroll [13] is more prevalent at high velocities and the cavitation number increases with velocity. Fixed-patch cavitation was also observed on a 44.6 mm ITTC nose in the investigation by Acosta and Hamaguchi [3]. They show a photograph of fixed-patch cavitation occurring with band cavitation and indicate that patch cavitation occurred at higher velocities which is consistent with the results of Holl and Carroll. The attached cavitation data obtained for the 50.8 mm Schiebe nose in the HSWT at CIT also displays the trend of cavitation number increasing with velocity as shown in Fig. 3.

The aforementioned velocity dependency of fixed-patch cavitation together with its physical appearance strongly suggests that fixed-patch cavitation is caused by surface roughness. Based on the results of Holl [35] one would expect σ_l for an isolated roughness of height (h) in a boundary layer of thickness (δ) to increase with velocity because of the increase in relative height of roughness (h/δ) and Reynolds numbers. However, Holl and Carroll [13] report that fixed-patch cavitation is suppressed as the air content is increased. The mechanism which causes this trend has not been determined.

In addition to the headform data there are hydrofoil data which also strongly suggest that surface roughness is involved in the cavitation process. This is displayed by the sheet cavitation data of Fig. 7 (NACA 015 hydrofoils), Fig. 8 (152.4 and 304.8 mm Joukowski hydrofoils at $\alpha = 7°$) and Fig. 9 (pressure surface of the cambered hydrofoils). All of these data have the same trend namely that for a given Reynolds number the cavitation number increases with a decrease in chord length. (The hemispherical and 1.5 caliber ogive data reported by Holl and Parkin [34] for noses from 9.5 to 203.2 mm in diameter also display this type of trend.) In addition, it should be noted that sheet cavitation occurs at the leading edge where the boundary layer is very thin so that surface roughness could be of major importance. Furthermore, this type of cavitation is characterized by long streams issuing from many points a further indication of possible roughness effects.

An analysis was conducted to demonstrate the roughness effects described in the aforementioned discussions. This will now be presented.

As indicated by Holl [35] the limited cavitation number for a body with roughness (σ_{lr}) is given by the superposition equation

$$\sigma_{lr} = -\bar{C}_{p_s} + [1 - \bar{C}_{p_s}]\sigma_{lfp} \tag{22}$$

where $\overline{C_{p_s}}$ is the pressure coefficient at the location of the roughness on the "smooth" body and σ_{lfp} is the limited cavitation number of the roughness as determined from flat plate data. This equation has been revised by Arndt, Holl, Bohn, and Bechtel [36] to include bubble dynamic effects. The revised equation is

$$\sigma_{lr} = -\overline{C_{p_s}} - \Omega + [1 - \bar{C}_{p_s}]\sigma_{lfp}. \tag{23}$$

The function Ω accounts for possible bubble dynamic effects and is defined as

$$\Omega = \frac{P_v - P_{\min - r}}{1/2\rho U_\infty{}^2} \tag{24}$$

where $P_{\min - r}$ is the minimum pressure produced by the roughness. In effect, Ω includes those factors in equation (10), namely $\overline{P_G}$, $\overline{2S}/R$ and ϕ, which are influenced by the bubble dynamics. In some cases where Ω is sufficiently large equation (23) suggests that σ_{lr} can be less than $|\overline{C_p}|$. We want to apply equation (23) to the NACA 0015 hydrofoil data of Fig. 7. The estimated height of the machined roughness was 2.5×10^{-3} mm and the machining ran parallel to the span so that the roughness is two-dimensional in character. We will thus approximate the roughness by the two-dimensional triangular element which was first investigated by Holl [35]. These data and others for isolated irregularities are approximated by an equation of the form [36]

$$\sigma_{lfp} = C_1 (\frac{h}{\delta})^a (\frac{U\delta}{\nu})^b \tag{25}$$

where U the velocity at the edge of the boundary layer is given by

$$\frac{U}{U_\infty} = \sqrt{1 - \bar{C}_{p_s}}\ . \tag{26}$$

We approximate the boundary layer thickness by an equation of the form

$$\frac{\delta}{x} = \frac{C_2}{\left(\frac{U_\infty x}{\nu}\right)^{\frac{1}{m}}}. \tag{27}$$

Employing equations (26) and (27) in equation (25) yields

$$\sigma_{lfp} = \frac{C_1}{C_2{}^{(a-b)}} \left(\frac{h}{L}\right)^a \frac{\left(\frac{U_\infty L}{\nu}\right)^{\left(\frac{a-b}{m} + b\right)}}{\left(\frac{X}{L}\right)^{\frac{m-1}{m}(a-b)}} (1 - \bar{C}_{p_s})^{\frac{b}{2}} \tag{28}$$

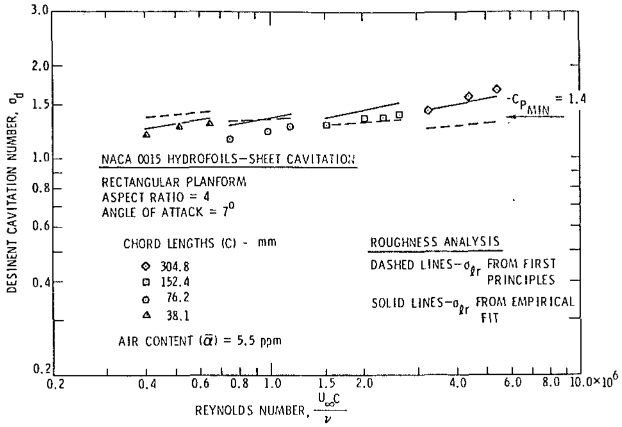

Fig. 10 Analysis of roughness effect on sheet cavitation - NACA 0015 hydrofoils

where L is a characteristic body length such as chord, diameter, etc. We assume that $\bar{C}_{p_s}$ is equal to $\bar{C}_{p_{\min}}$ in equation (23) since the pressure minimum would be near the leading edge. Then let L be the chord length C, and $-\bar{C}_{p_s} = \bar{C}_{p_{\min}} = 1.4$ at $x/C = 0.10$. From reference (36) the empirical constants for the triangular roughness are $C_1 = 0.152$, $a = 0.361$, and $b = 0.196$. The boundary layer is assumed to be turbulent so that $m = 5$ and it is assumed that $C_2 = 0.38/2$ to account for an initial laminar boundary layer. Employing these data in equation (23) and (28) and adjusting Ω so that σ_{lr} agrees with the experimental data at $C = 152.4$ mm and a Reynolds number of 1.5×10^6 yields

$$\sigma_{lr} = 1.4 - 0.445 + 0.706\left(\frac{h}{c}\right)^{0.361}\left(\frac{U_\infty c}{\nu}\right)^{0.229} \tag{29}$$

where $h = 2.54 \times 10^{-3}$ mm. The results of the calculation are shown in Fig. 10 by the dashed lines. It is seen that the Reynolds number effect is larger than predicted by equation (29). A reasonably good empirical fit to the data is given by

$$\sigma_{lr} = 1.4 - 0.92 + 0.1\left(\frac{h}{c}\right)^{0.15}\left(\frac{U_\infty c}{\nu}\right)^{0.27} \tag{30}$$

which is shown by the solid lines in Fig. 10. Further analyses of cavitation data employing the aforementioned techniques are in progress.

Experimental Uncertainty. The cavitation data in Figs. 1-9 have an experimental uncertainty of ± 5 percent. All of these data except those shown in Figs. 3 and 4 are average values.

Acknowledgments

This research was sponsored by Naval Sea Systems Command Codes 63R-31 and 05H and by the ARL E and F research program administered by Dr. M. T. Pigott.

References

1 Holl, J. W., "An Effect of Air Content on the Occurrence of Cavitation," ASME *Journal of Basic Engineering*, Vol. 82, 1960, pp. 941-946.

2 Kermeen, R. W., "Some Observations of Cavitation on Hemispherical Head Models," California Institute of Technology, Hydrodynamics Laboratory Report No. E-35.1, June 1952.

3 Acosta, A. J., and Hamaguchi, H., "Cavitation Inception on the ITTC Standard Head Form," Report No. E-149.1, Hydrodynamics Laboratory, California Institute of Technology, Mar. 1967.

4 Holl, J. W., and Treaster, A. L., "Cavitation Hysteresis," ASME *Journal of Basic Engineering*, Mar. 1966, pp. 199-212.

5 Reed, R. L., "The Influence of Surface Characteristics and Pressure History on the Inception of Cavitation," M.S. dissertation, Dept. of Aerospace Engineering, The Pennsylvania State University, Mar. 1969.

6 Gupta, S. K., "The Influence of Porosity and Contact Angle on Incipient and Desinent Cavitation," M.S. thesis, Dept. of Aerospace Engineering, The Pennsylvania State University, Dec. 1969.

7 Holl, J. W., "Limited Cavitation," *Proceedings of the Symposium on Cavitation State of Knowledge*, ASME, June 1969, pp. 26-63.

8 Plesset, M. S., "Dynamics of Cavitation Bubbles," *Journal of Applied Mechanics*, Vol. 16, Vol. 71, 1949, pp. 277-282.

9 Parkin, B. R., and Kermeen, R. W., "The Roles of Convective Air Diffusion and Liquid Tensile Stresses During Cavitation Inception," *Proceedings of IAHR-Symposium*, Sendai, Japan, Sept. 3-5, 1962.

10 Holl, J. W., and Wislicenus, G. F., "Scale Effects on Cavitation," ASME *Journal of Basic Engineering*, Vol. 83, 1961, pp. 385-398.

11 Holl, J. W., Arndt, R. E. A., and Billet, M. L., "Limited Cavitation and the Related Scale Effects Problem," *Proceedings of Second International JSME Symposium on Fluid Machinery and Fluidics*, 1972, pp. 303-314.

12 Holl, J. W., and Kornhauser, A. L., "Thermodynamic Effects on Desinent Cavitation on Hemispherical Nosed Bodies in Water at Temperatures from 80°F to 260°F," ASME *Journal of Basic Engineering*, Vol. 92, Mar. 1970, pp. 44-58.

13 Holl, J. W., and Carroll, J. A., "Observations of the Various Types of Limited Cavitation on Axisymmetric Bodies," *Proceedings of the International Symposium on Cavitation Inception*, ASME, Dec. 1979, pp. 87-99.

14 Schiebe, F. R., "Measurement of the Cavitation Susceptibility of Water Using Standard Bodies," Project Report No. 118, St. Anthony Falls Hydraulic Laboratory, University of Minnesota, Feb. 1972.

15 Van der Meulen, J. H. J., "A Holographic Study of Cavitation on Axisymmetric Bodies and the Influence of Polymer Additives," Publication No. 509, Netherlands Ship Model Basin, Wageningen, The Netherlands, 1976.

16 Arakeri, V. H., and Acosta, A. J., "Viscous Effects in Inception of Cavitation on Axisymmetric Bodies," ASME JOURNAL OF FLUIDS ENGINEERING, Dec. 1973, pp. 519-526.

17 Gates, E. M., "The Influence of Freestream Turbulence, Freestream Nuclei Populations, and a Drag-Reducing Polymer on Cavitation Inception on Two Axisymmetric Bodies," Ph.D. thesis, California Institute of Technology, 1977.

18 Arakeri, V. H., and Acosta, A. J., "Cavitation Inception Observations on Axisymmetric Bodies at Supercritical Reynolds Numbers," *Journal of Ship Research*, SNAME, Vol. 20, No. 1, Mar. 1976, pp. 40-50.

19 Arakeri, V. H., "Viscous Effects on the Position of Cavitation Separation from Smooth Bodies," *Journal of Fluid Mechanics*, Vol. 68, Part 4, 1975, pp. 779-799.

20 Huang, T. T., and Peterson, F. B., "Influence of Viscous Effects on Model/Full-Scale Cavitation Scaling," *Journal of Ship Research*, Vol. 20, No. 4, Dec. 1976, pp. 215-223.

21 Gaster, M., "The Structure and Behavior of Laminar Separation Bubbles," Advisory Group for Aerospace Research and Development, Conference Proceedings No. 4, Part 2, pp. 513-554, Technical Edition and Reproduction, Ltd., London, 1966.

22 Young, A. D., and Horton, H. P., "Some Results of Investigations of Separation Bubbles," Advisory Group for Aerospace Research and Development, Conference Proceedings No. 4, Part 2, pp. 779-811, Technical Edition and Reproduction, Ltd., London, 1966.

23 Arakeri, V. H., "A Note on the Transition Observations on an Axisymmetric Body and Some Related Fluctuating Wall Pressure Measurements," ASME JOURNAL OF FLUIDS ENGINEERING, Vol. 97, Mar. 1976, pp. 82-86.

24 Huang, T. T., and Hannan, D. E., "Pressure Fluctuations in the Regions of Flow Transition," David W. Taylor Naval Ship Research and Development Center, Report 4723, 1976.

25 Robertson, J. M., McGinley, J. H., and Holl, J. W., "On Several Laws of Cavitation Scaling," La Houille Blanche, No. 1, Sept. 1957.

26 Arakeri, V. H., Carroll, J. A., and Holl, J. W., "A Note on the Effect of Short and Long Laminar Separation Bubbles on Desinent Cavitation," ASME JOURNAL OF FLUIDS ENGINEERING, Vol. 103, Mar. 1981, pp. 28-32.

27 Kermeen, R. W., and Parkin, B. R., "Incipient Cavitation and Wake Flow Behind Sharp-Edged Disks," Report No. 85-4, Hydrodynamics Laboratory, California Institute of Technology , Aug. 1957.

28 McCormick, B. W., "A Study of the Minimum Pressure in a Trailing Vortex System," Ph.D. thesis, Dept. of Aerospace Engineering, The Pennsylvania State University, June 1954.

29 McCormick, B. W., "On Cavitation Produced by a Vortex Trailing from a Lifting Surface," ASME *Journal of Basic Engineering*, Sept. 1962, pp. 369-379.

30 Billet, M. L., and Thompson, D. E., "Blade Surface Cavitation Noise," *Proceedings of Joint Symposium on Design and Operation of Fluid Machinery*, IAHR, ASME, ASCE, June 12-14, 1978, pp. 523-542.

31 Schiebe, F. R., "The Influence of Gas Nuclei Size Distribution on Transient Cavitation Near Inception," Report No. 107, St. Anthony Falls Hydraulic Laboratory, University of Minnesota, May 1969.

32 Holl, J. W., Arndt, R. E. A., Billet, M. L., and Baker, C. B., "Cavitation Research at the Garfield Thomas Water Tunnel," *Proceedings of the Cavitation Conference*, The Institution of Mechanical Engineers, Heriot-Watt University, Edinburgh, Scotland, Sept. 3-5, 1974, pp. 81-88.

33 Arndt, R. E. A., and Keller, A. P., "Free Gas Content Effects on Cavitation Inception and Noise in a Free Shear Flow," *Proceedings of Symposium on Two Phase Flow and Cavitation in Power Generating Systems*, IAHR, Grenoble, France, Mar. 30-Apr. 2, 1976, pp. 3-16.

34 Parkin, B. R., and Holl, J. W., "Incipient Cavitation Scaling Ex-

periments for Hemispherical and 1.5 Caliber Ogive-Nosed Bodies," Report No.rd 7958-264, Applied Research Laboratory, The Pennsylvania State University, May 1954.

35 Holl, J. W., "The Effect of Surface Irregularities on Incipient Cavitation," Ph.D. dissertation, The Pennsylvania State University, June 1958.

36 Arndt, R. E. A., Holl, J. W., Bohn, J. C., and Bechtel, W. T., "The Influence of Surface Irregularities on Cavitation Performance," *Journal of Ship Research*, SNAME, Vol. 23, No. 3, Sept. 1979, pp. 157-170.

periments for Hemispherical and 1.5 Caliber Ogive-Nosed Bodies," Report No.rd 7958-264, Applied Research Laboratory, The Pennsylvania State University, May 1954.

35 Holl, J. W., "The Effect of Surface Irregularities on Incipient Cavitation," Ph.D. dissertation, The Pennsylvania State University, June 1958.

36 Arndt, R. E. A., Holl, J. W., Bohn, J. C., and Bechtel, W. T., "The Influence of Surface Irregularities on Cavitation Performance," *Journal of Ship Research*, SNAME, Vol. 23, No. 3, Sept. 1979, pp. 157-170.

DISCUSSION

S. Kamiyama[1]

The paper contains valuable contributions toward a fundamental understanding of the complex problem of various types of limited cavitation in a flow around a body.

I agree with the statement that viscous effect and free stream nuclei can cause significant scale effect and also the inception of travelling-bubble cavitation depend on a large number of free-stream nuclei.

In general, water contains a great deal of air in both the dissolved and undissolved states and then the flow is supersaturated in many actual cases (solubility of air in water at 15°C is $\alpha_s = 0.0206$ by volume fraction), though the total gas content of $\alpha = 3 \sim 11$ppm tested in this report is rather a small quantity.

Therefore, the gas bubbles expand by diffusion in the low pressure region and give the compressibility to the flow.

Namely, free stream nuclei may affect on the limited cavitation number as not only Type #1 but also type #2 scale effects.

Type #1 scale effects in this paper consider only the incompressible fluid flow outside the cavitation bubble based on equation (9) where $\bar{C}_p$ is estimated by theoretical analysis or measured in the noncavitating condition.

I would like to point out that the effects of gas bubbles on the pressure distribution is also important in some cases.

In the case of liquid including a large number of free-stream gas bubbles, it is necessary to treat the flow passing lower pressure region as a two-phase one even if the void fraction α is very small.

Bernoulli equation of a homogeneous two-phase flow is given by[2]

$$\frac{p-p_v}{\rho_l} + \frac{p_0-p_{v0}}{\rho_l}\,\frac{\alpha_0}{1-\alpha_0}\ln(p-p_v) + \frac{U^2}{2} = \text{const} \qquad (1)$$

and hence the minimum pressure coefficient of two-phase flow $(C_{p\min})_{TP}$ is

$$(C_{p\min})_{TP} \cong (C_{p\min})_{\text{incomp}} - \frac{2(p_0-p_{v0})}{\rho_l U_\infty{}^2}\left(\frac{\alpha_0}{1-\alpha_0}\right)\ln\left(\frac{p_{\min}-p_v}{p_\infty-p_v}\right) \qquad (2)$$

where suffix 0 means standard state (atmospheric condition) and the other symbols are same as the ones in the present paper.

For example, let's consider the case of water at 15°C ($p_0 = 101.325$ kPa, $p_{v0} \cong 0$ kPa, $p_v = 1.706$ kPa, $\rho_l = 999.3$ kg/m^3) and take the values of $(C_{p\min})_{\text{incomp}} = -1.40$, $p_{\min} = 17$ kPa and $U_{\max} = 10$ m/s, then, the values of $(C_{p\min})_{TP} = -1.25$ and -1.35 are obtained for $\alpha_0 = 0.03$ and 0.01, respectively.

Assumed value of $\alpha_0 = 0.03 \sim 0.01$ is reasonable one as examples of water since the dissolved air is almost diffused out in low pressure region in the case of low flow velocity.[2]

Therefore, the condition of $|C_{p\min}|_{TP} < |C_{p\min}|_{\text{incomp}}$ should also be considered why the limited cavitation numbers σ_l are lower than the theoretical value of $|C_{p\min}|_{\text{incomp}}$ especially in the case of large air content and low flow velocity.

Authors' Closure

We are grateful for Professor Kamiyama's comments and agree that the effect of compressibility on cavitation inception should be considered. Work being done by Professor Kamiyama attempts to address this interesting problem. Other researchers have also discussed the importance of compressibility and have shown that in the case of profuse cavitation on a body it can have a significant effect on the local measure. Future research will answer whether or not it is also significant at inception for low values of air content.

---

[1] Institute of High Speed Mechanics, Tohoku University, Sendai, Japan.

[2] Kamiyama, S., and Yamasaki, T., "One Predicting Method of Gaseous Cavitation Occurrence in Water and Sodium," *Bull. of the JSME*, Vol. 23, 1980-9, No. 183, pp. 1428-1434.

Observations of the Various Types of Limited Cavitation on Axisymmetric Bodies

J. W. Holl
Professor of Aerospace Engineering,
Applied Research Laboratory,
The Pennsylvania State University,
State College, Pa. 16801

J. A. Carroll[1]
Test Engineer,
McDonnell-Douglas,
Long Beach, Calif.

Observations are presented of various types of limited cavitation on 5.1 cm diameter Schiebe, hemispherical, and DTNSRDC noses. These three noses were selected to give various flow states over the range of test speeds 6.1-21.3 m/s ranging from laminar separation for all speeds (hemispherical nose) to nonseparated flow for all speeds (Schiebe nose) with the DTNSRDC nose experiencing both separated and nonseparated flow over the speed range. The types of cavitation observed fall into two broad classes, namely transient and attached. Transient cavitation was observed in three forms, namely travelling-bubble, travelling-patch and bubble-ring. Three types of attached cavitation were observed, namely band, fixed-patch and developed. Bubble-ring and band cavitation are observed only on a body with laminar separation as noted previously by Arakeri and Acosta. Bubble-ring cavitation has been observed only on hemispherical and eighth caliber ogive noses. The desinent cavitation numbers for band and bubble-ring cavitation on the hemispherical nose are related to measured mean and fluctuating pressure data. Travelling cavitation was the most prevalent type of cavitation and the cavitation number decreased with speed and increased with air content. An analysis of travelling cavitation data from several investigations is presented. The cavitation number for fixed-patch cavitation increases with speed which suggests that surface roughness effects are involved.

Introduction

The objectives of this program have been to (1) determine the various types of limited cavitation which can occur on axisymmetric bodies with and without laminar separation, (2) to determine the manner in which the cavitation number for the various types of cavitation varies with speed and air content, and (3) to ascertain, if possible, the major factors which control each type of cavitation.

In most cases referred to in this paper, the cavitation number for a given state of limited cavitation (σ_l) was determined by the desinence procedure which has been used for many years at the Garfield Thomas Water Tunnel of the Applied Research Laboratory at The Pennsylvania State University. Thus

$$\sigma_l = \sigma_d = \frac{P_{\infty_d} - P_v}{1/2 \rho V_\infty{}^2} \quad . \tag{1}$$

In some cases cavitation data for inception are employed in which case the incipient cavitation number (σ_i) is utilized.

Description of the Experiments

The tests were conducted in the 30.5 cm diameter water tunnel [1][2] which is a conventional continuous flow facility with a closed jet test section. Cavitation data were obtained for a speed range of 6.1 to 21.3 m/s for three axisymmetric noses attached to cylindrical afterbodies which were strut mounted in the test section. The maximum diameter of all noses was 5.1 cm. The total gas content as measured by a Van Slyke apparatus and expressed in moles of air per million moles of water (ppm) varied between 3 and 12 ppm. Water temperature varied from 23.3 to 34.4 deg C.

The experiments were of three general types, namely a photographic and video tape study of the various states of limited cavitation, desinence tests to determine σ_l, and pressure measurements on the hemispherical nose. Both mean and fluctuating pressures were measured.

The three bodies selected for this program were the hemispherical nose, Schiebe nose, and DTNSRDC[3] nose which are described in the sketches of Fig. 1. The DTNSRDC nose is a member of the family of so-called modified-ellipsoids whereas the Schiebe nose is a half-body formed by the addition of a disk source and a uniform stream as described by Schiebe [2]. The Schiebe nose employed in this investigation has a minimum pressure coefficient ($C_{p_{\min}}$) which is essentially the same as that of a hemispherical nose. However, in contrast to the hemispherical nose, the Schiebe nose does not experience laminar separation. It was for this

---

[1] Former Graduate Assistant at ARL/PSU

Contributed by the Fluids Engineering Division of THE AMERICAN SOCIETY OF MECHANICAL ENGINEERS and presented at the International Symposium on Cavitation Inception, ASME Winter Annual Meeting, New York, N.Y., December 2-7, 1979. Manuscript received by the Fluids Engineering Division, February 11, 1980.

[2] Numbers in brackets refer to documents in list of references.

[3] DTNSRDC stands for David Taylor Naval Ship R & D Center.

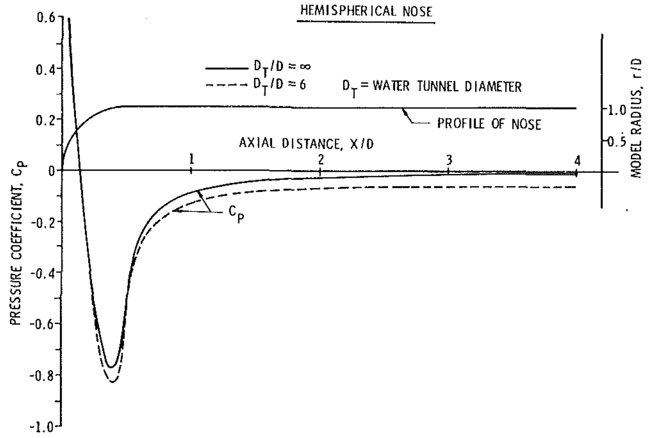

Fig. 1(a) Theoretical pressure distribution – hemispherical nose

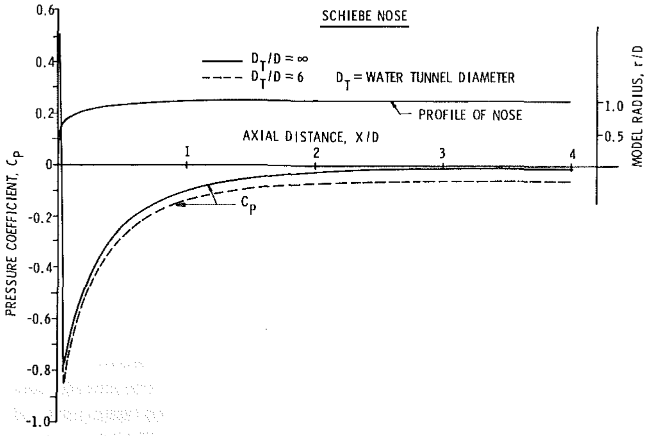

Fig. 1(b) Theoretical pressure distribution – Schiebe nose

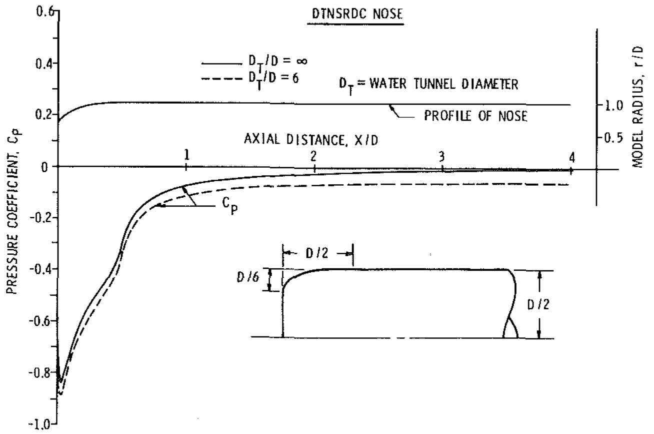

Fig. 1(c) Theoretical pressure distribution – DTNSRDC nose

reason that the Schiebe body was selected for this investigation. Similarly this shape was used in earlier investigations by van der Meulen [3]. Coordinates of the Schiebe nose are tabulated in reference [3]. As indicated by Arakeri and Acosta [4], the calculated critical Reynolds number for a hemispherical nose is 5×10^6 and thus the 5.1 cm diameter model experienced laminar separation over the entire speed range, i.e., 6.1 to 21.3 mps. It has been shown [5] that the DTNSRDC nose has a critical Reynolds number of 5×10^5 which corresponds to a velocity of 9.1 mps for a 5.1 cm diameter nose at 23.4 deg C in water. Thus the DTNSRDC nose experienced both separated and unseparated flow over the speed range employed in this program.

The theoretical pressure distributions for the three models are shown in Fig. 1. It is seen that some blockage is experienced by the 5.1 cm models in the 30.5 cm water tunnel.

Description of the Various Types of Cavitation

The various types of limited cavitation were recorded by still photography and on video tape. In addition, some high-speed motion pictures were obtained at the end of the program.

The types of limited cavitation which were observed fall into two broad classes, namely transient and attached. Transient cavitation was observed in three forms namely, travelling-bubble, travelling-patch and bubble-ring. Two types of attached cavitation were observed, namely band and fixed patch. Photographs of these various types of cavitation are shown in Figs. 2 and 3. Desinent cavitation data were obtained for the three noses at two air contents and the results are shown in Figs. 4, 5, and 6. The cavitation states of Figs. 2(*a*) and 3(*a*) correspond to the cavitation number data of Fig. 4. However, the cavitation states of Figs. 2(*b*) and 3(*b*) are at values of σ less than those shown in Fig. 5.

Transient cavitation is characterized by cavities which grow and collapse very rapidly when nuclei are subjected to pressure fluctuations due to turbulence and/or when traversing the low pressure region of a body. Because of its short life, transient cavitation is very difficult to observe under normal lighting conditions. The cavities generally appear as blurred streaks giving no indication of actual shape. On the other hand, attached cavitation usually occurs as a quasi-steady cavity which appears fixed to the body and is readily observable under normal lighting conditions.

Travelling-bubble cavitation is so named because it appears in the form of nearly spherical cavities which rapidly grow and collapse as they travel with the flow through the low pressure region of the body. Travelling-patch cavitation differs from travelling-bubble mostly by its appearance which is similar to that of a seashell inverted over the surface of the body. Like travelling-bubble cavitation, travelling-patch cavitation appears as randomly occurring cavities in the region of low pressure.

The third type of transient cavitation, namely bubble-ring cavitation, occurred on only the hemispherical nose in this investigation. However, it has also been observed on an eighth-caliber ogive nose by Robertson, McGinley, and Holl [6]. Recently, Arakeri, Carroll, and Holl [7] related the desinent cavitation characteristics of the eighth-caliber ogive nose to the effects of short and long laminar separation bubbles. Arakeri and Acosta [4] were the first to show that the bubble-ring cavitation and the so-called band cavitation occur only with laminar separation. Kermeen [8] was the first to publish photographs of these types of cavitation. (Parkin and Kermeen [9] presented a classical paper in 1962 showing detailed photographic history of the cavitation process in the laminar bubble. However, at the time it was not realized that the flow was separated.) Bubble-ring cavitation appears as macroscopic irregularly-shaped bubbles which rapidly appear and disappear within a very narrow region around the nose in the vicinity of boundary-layer reattachment. Under normal lighting this type of cavitation appears as a fuzzy ring fixed on the model.

As indicated previously, band cavitation occurs on bodies in the presence of laminar separation and thus was observed on the noses of both the hemispherical and DTNSRDC bodies in this investigation. The leading edge of the cavity is located near the point of laminar separation. The forward portion of band cavitation generally appears as a transparent cavity divided into sections by thin liquid partitions running parallel

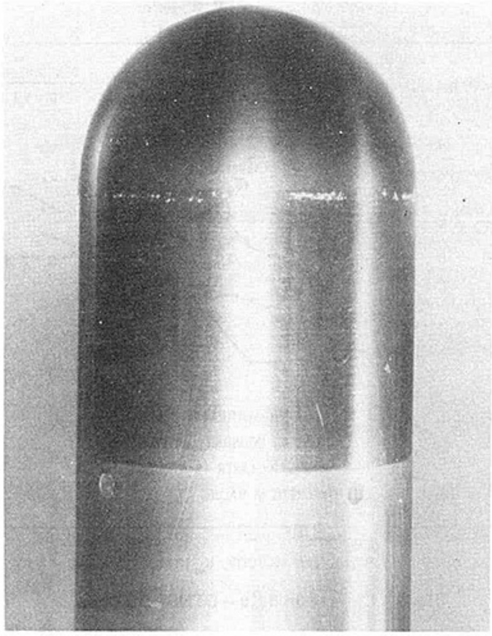

Fig. 2(*a*) Bubble-ring cavitation on the hemispherical nose ($\sigma = 0.626$, $V_\infty = 18.3$ m/s, $\alpha = 9.5$ ppm)

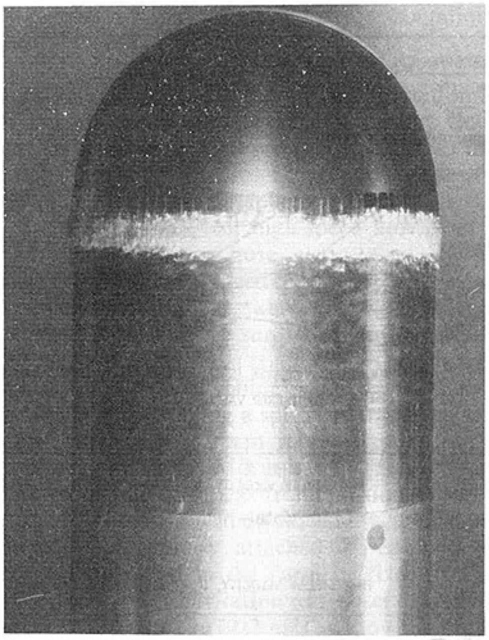

Fig. 3(*a*) Band cavitation on the hemispherical nose ($\sigma = 0.610$, $V_\infty = 18.3$ m/s, $\alpha = 9.2$ ppm)

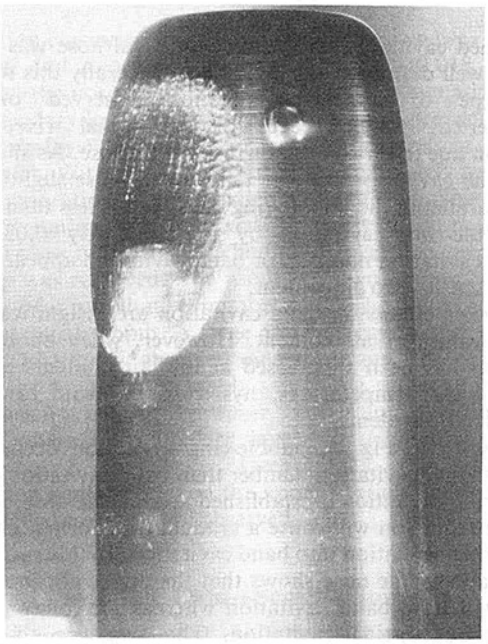

Fig. 2(*b*) Travelling-bubble and travelling-patch cavitation on the Schiebe nose ($\sigma = 0.365$, $V_\infty = 18.3$ m/s, $\alpha = 9.5$ ppm)

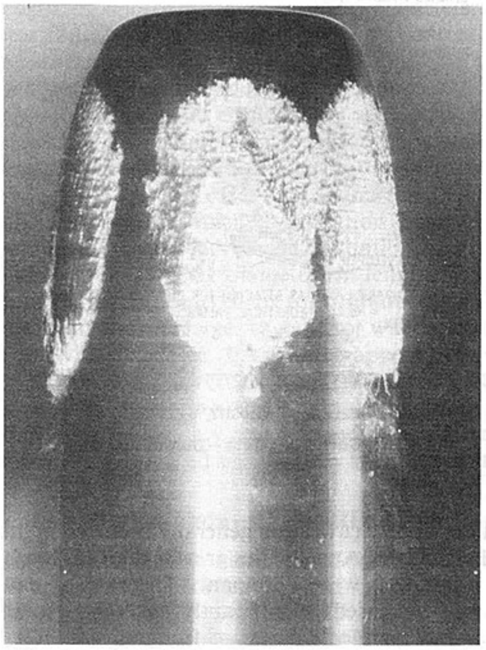

Fig. 3(*b*) Fixed-patch cavitation on the Schiebe nose ($\sigma = 0.361$, $V_\infty = 18.3$ m/s, $\alpha = 4$ ppm)

to the flow. These partitions continually shift to different locations within the cavity. Just downstream of the transparent portion of the cavity, the cavity surface becomes wavy and breaks up into myriads of frothy bubbles.

Fixed-patch cavitation is similar in appearance to travelling-patch cavitation. However, fixed-patch cavitation appears to be attached to the body surface at one or more locations on its upstream end. From the point of attachment the cavity fans out symmetrically in the downstream direction and ends in a multitude of frothy bubbles which trail off downstream. The leading edges of the cavity close to the vertex appear to be transparent as in the case of band cavitation. The downstream portion of the cavity appears translucent with wave patterns in the cavity surface.

Desinent Cavitation Data—Hemispherical Nose

Desinent cavitation data for the hemispherical nose at air contents of 7.8 and 11 ppm are given in Fig. 4. Cavitation data for the two other noses at two air contents are given in Figs. 5 and 6. (The data in Figs. 4 through 6 are not corrected for blockage. Average values of the cavitation number are shown in these figures and were determined from approximately three individual determinations in each case.) Three types of limited cavitation were observed on the hemispherical nose. Transient cavitation in the form of travelling-bubble and bubble-ring cavitation and attached cavitation in the form of band cavitation were noted for varying values of freestream velocity, air content, and cavitation number.

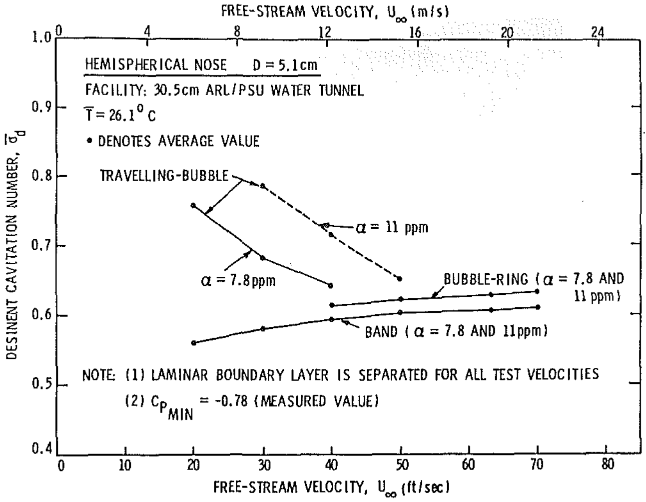

Fig. 4 Cavitation data – hemispherical nose

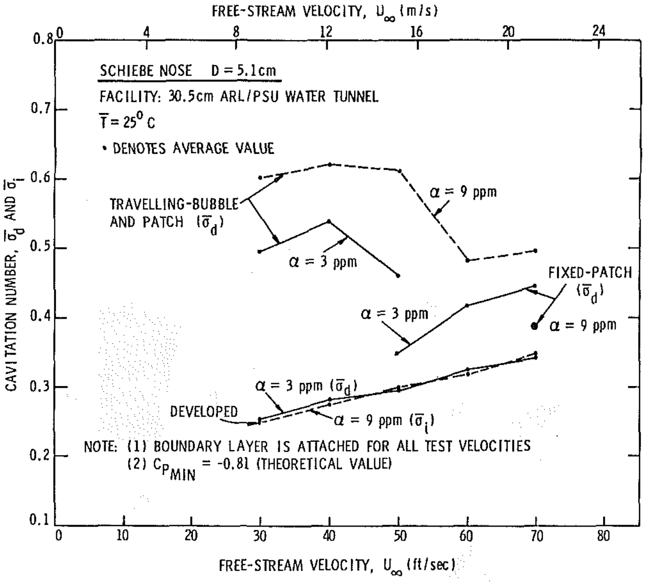

Fig. 5 Cavitation data – Schiebe nose

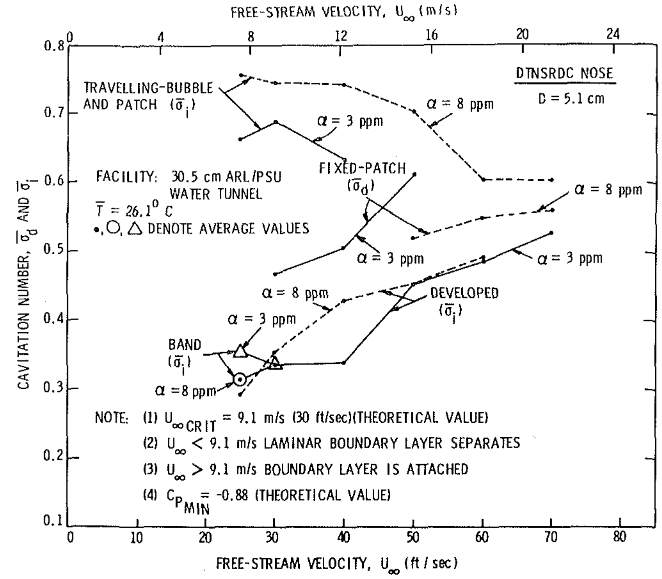

Fig. 6 Cavitation data – DTNSRDC nose

Travelling-bubble cavitation generally occurred in the speed range 6.1–15.2 m/s. At velocities greater than 15.2 m/s, other types of cavitation were dominant. The rate of cavitation occurrences increased significantly as the speed was decreased. The number and size of freestream bubbles in the test section also increased as the speed and static pressure of the tunnel were lowered. Exploratory tests indicated that hysteresis effects on travelling-bubble cavitation were not significant. From Fig. 4, it is seen that the desinent cavitation number for this type of cavitation is very dependent upon speed and air content: it decreases with speed and increases with air content. This form of cavitation is accompanied by audible snapping sounds which apparently arise when the individual cavities collapse upon entering regions of higher pressure.

The second type of transient cavitation observed on the hemispherical nose was bubble-ring cavitation. This type of cavitation generally occurs at the high end of the speed range, i.e., 12.2 to 21.3 m/s. In Fig. 4 it is seen that the cavitation number increases slightly with speed. Variation of the air content in the range 7.8 to 11 ppm seemed to have no effect on the cavitation number. (However, the desinent cavitation number for bubble-ring cavitation at constant gas content decreased with temperature. These data will be discussed subsequently.) However, for very low values of the air content, i.e., less than 4 ppm, bubble-ring cavitation was not observed.

Attached cavitation on the hemispherical nose was in the form of well defined band cavitation. Generally this was the only type of attached cavitation observed on the hemispherical nose except for occasional fixed-patch cavitation due to dirt on the surface of the nose. As shown in Fig. 4, the cavitation number tends to increase slightly with speed, parallel to the bubble-ring data, and is less than σ_d for the bubble-ring cavitation by approximately 0.03. The desinent cavitation number for band cavitation appears to be nearly insensitive to air content.

Hysteresis effects on band cavitation are insignificant for average values of air content. However, when bubble-ring cavitation has been suppressed at low air contents and increased water temperatures, hysteresis on band cavitation becomes quite evident.

As shown in Fig. 4, bubble-ring cavitation occurs at a slightly higher cavitation number than band cavitation. When bubble-ring cavitation is established around the nose, a small pressure reduction will cause a gradual transformation from bubble-ring cavitation into band cavitation. In this situation a photograph of the nose shows that the upper portion of the model will have band cavitation whereas the lower portion displays bubble-ring cavitation. The sequence of events observed for transforming bubble-ring cavitation to band cavitation in an inception test is the reverse of that observed in a desinence test. The initial presence of bubble-ring cavitation during an inception test assures the gradual development of band cavitation. On the other hand, if bubble-ring cavitation does not occur first, for example when the air content is quite low, then band cavitation may either develop gradually or suddenly as a well developed cavity.

Band cavitation is also influenced by the presence of travelling-bubble cavitation. If a large number of these bubbles pass over the nose when band cavitation is present, the band cavitation has been observed to vanish leaving only travelling-bubble cavitation. This effect was previously observed by Gates [10]. Apparently the bubbles are causing premature transition which eliminates the laminar separation bubble.

The placement of a boundary-layer trip on the hemispherical nose resulted in a drastic change in the

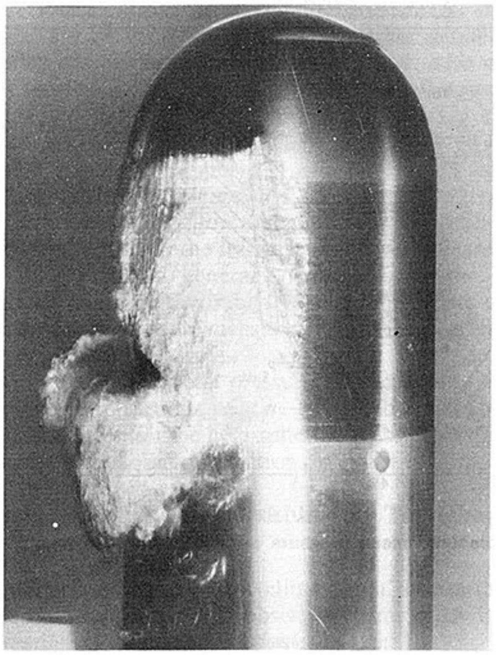

Fig. 7 Effect of trip on laminar separation (trip on upper 180 deg of the hemispherical nose, $\sigma = 0.382$, $V_\infty = 18.3$ m/s, $\alpha = 4$ ppm)

cavitation characteristics of this body as shown previously by Arakeri and Acosta [5]. By placing a thin (0.018 cm) wax band on the nose at about 30-deg from the stagnation point, the boundary-layer was energized enough to prevent laminar boundary-layer separation for freestream speeds of 10.7 m/s or greater. With the wax trip installed completely around the body, separation was eliminated and neither bubble-ring nor band cavitation were observed. To assist in emphasizing the effectiveness of tripping the boundary layer, the lower half of the trip was removed. The result is shown in the photograph of Fig. 7 for a cavitation number of 0.382 at 18.3 m/s and an air content of 4 ppm. A large attached cavity in the form of band cavitation is observed on the bottom half of the nose where the flow is presumably separating since the boundary layer was not tripped. However, on the upper portion of the model where the boundary layer was tripped there is no evidence of cavitation. Occasionally travelling-bubble cavitation would occur on the upper portion of the nose but no attached cavities were observed.

Desinent Cavitation Data—Schiebe Nose

Three types of limited cavitation were observed on the Schiebe nose, namely transient cavitation in the form of travelling-bubble cavitation and travelling-patch cavitation and attached cavitation in the form of patches. In addition to the aforementioned forms of limited cavitation, developed states of cavitation also played an important role for the Schiebe nose. The desinent cavitation number data for these types of cavitation are presented in Fig. 5.

Both transient forms of cavitation generally appeared together for the same conditions of freestream speed, cavitation number and air content. It was noted, however, that travelling-patch cavitation appeared to be more predominant at high speeds. At low speeds, travelling-bubbles were much more numerous. Both types were significantly influenced by air content: they increased in abundance with an increase in air content. The cavitation data are presented collectively for both types of transient cavitation in Fig. 5 for air contents of 3 and 9 ppm. The cavitation number tends to decrease with speed and increases with air content in a manner similar to that of the travelling-bubble cavitation for the hemispherical nose in Fig. 4.

Observations of an intermediate form of transient cavitation suggests that travelling patch-cavitation is a more developed form of travelling-bubble cavitation. Occasionally spherical bubbles were observed which had two tails which trailed behind the bubble. Closer inspection of the video tapes revealed an entire range of spherical bubbles having larger and larger tails. Subsequent high-speed movies of transient cavitation on a Schiebe nose were taken by David R. Stinebring at a freestream speed of 9.0 mps. Large numbers of spherical travelling bubbles were observed, emerging very close to the minimum pressure location, growing as they moved downstream and then collapsing. The development of what appeared to be a travelling patch was also observed. It emerged initially resembling a spherical travelling bubble. As it grew and moved downstream, it appeared to drag along the model surface and thereby form a tail. The cavity continued to elongate and the spherical front portion broke off. The remaining cavity then moved downstream and collapsed.

As mentioned previously, attached limited cavitation on the Schiebe nose appeared in the form of fixed-patch cavities. Generally, this type of cavitation was observed only at higher speeds, i.e., $U_\infty = 15.2$ to 21.3 m/s as shown in Fig. 5. At the least value of air content (3 ppm), the cavities would appear evenly arranged around the model. During a desinence test, the cavities were observed to shrink with increasing pressure to a length of approximately 0.5 body diameters and then disappear. At an increased value of the air content (9 ppm), the cavities appeared to be rather unstable for they continually shifted to different locations around the body. In addition, at this higher air content they were only observed at a speed of 21.3 m/s. Referring to Fig. 5, it is seen that the cavitation number for fixed-patch cavitation increases with an increase in speed and decreases with an increase in air content.

A second form of attached cavitation observed on the Schiebe nose is that of developed cavitation which was approximately 1 to 1.5 body diameters in length. This type of cavitation has been observed to form gradually when either fixed-patch cavitation merges together or when a multitude of transient cavities coalesce. It may also appear very suddenly in the absence of any precursor cavities, usually at low air content values. Referring to Fig. 5, it is seen that the cavitation number for this type of cavitation increases with speed but is not influenced significantly by air content.

Desinent Cavitation Data—DTNSRDC Nose

All forms of cavitation observed on the hemispherical and Schiebe noses, except for bubble-ring cavitation, were also observed on the DTNSRDC nose. (As previously indicated the bubble-ring cavitation appears to be a rather special type of cavitation for it has been observed on only two bodies; 0.5 caliber (or hemisphere) and 0.125 caliber ogives.) This is perhaps not surprising since the DTNSRDC nose experienced both separated and unseparated flow over the entire operating range (7.6–21.3 m/s) and thereby encompassed the boundary-layer flow states of both the hemispherical and Schiebe noses. The cavitation number data for the various types of cavitation are given in Fig. 6.

As with the Schiebe nose, travelling-patch cavitation was more abundant at high speeds and travelling-bubble cavitation prevailed at lower speeds. No differences were observed in the transient cavitation characteristics between subcritical separating flow and supercritical nonseparating flow for the DTNSRDC nose. As shown in Fig. 6, the desinent cavitation number for the transient cavitation shows a decreasing trend with increase in speed and increases with air content. These trends agree with those of the hemispherical and Schiebe noses.

The forms of attached cavitation observed on the DTNSRDC nose were band cavitation, fixed-patch cavitation and developed cavitation. Desinent cavitation number data for these types of cavitation are given in Fig. 6 for air contents of 3 and 8 ppm.

At speeds of 7.6 and 9.1 m/s, band cavitation was observed on the DTNSRDC nose well downstream, near the theoretically determined location of laminar boundary-layer separation. The appearance of band cavitation on the DTNSRDC nose was much more unstable and not as well defined as band cavitation on the hemispherical nose. (Bubble-ring cavitation, which often preceded band cavitation on the hemispherical nose, was never observed on the DTNSRDC nose.) In Fig. 6 no trend of σ_d with speed can be determined because of the limited speed range. The cavitation number appears to decrease with increased air content. For high air contents when many freestream bubbles were present, transient cavitation was abundant and no band cavitation was observed. This observation is similar to the elimination of band cavitation by the presence of transient cavitation on the hemispherical nose as described earlier.

The appearance and characteristics of fixed-patch cavitation and developed cavitation on the DTNSRDC nose were similar to that observed on the Schiebe nose. Fixed patch cavitation was somewhat more predominant on the DTNSRDC nose than on the Schiebe nose under similar test conditions. Desinent cavitation data are presented in Fig. 6 for air contents of 3 and 8 ppm. As on the Schiebe nose, the desinent cavitation number increased rapidly with speed and decreased with air content. Fixed-patch cavitation appeared more stable at higher speeds and for low values of the air content this type of cavitation was able to persist at lower speeds than on the Schiebe nose. Freestream bubbles and transient cavitation appeared to cause fixed-patch cavitation to shift erratically about the model. As shown in Fig. 6, the desinent cavitation number for developed cavitation increases strongly with speed but shows little change with variation in air content, except for the possibly spurious data at 12.2 m/s. The cavity length was approximately 1 to 1.5 body diameters for this developed state of cavitation.

Mean Pressure Measurements on the Hemispherical Nose

The correlation of band and bubble-ring cavitation with laminar boundary-layer separation has resulted in a renewed interest in the viscous effects on the pressure distribution on a hemispherical nose. Earlier meaurements by Rouse and McNown [11] did not reveal the presence of laminar separation bubbles due to relatively large spacing between pressure taps. By means of Schlieren photography, Arakeri and Acosta [4] showed that laminar separation exists on a 5.1 cm diameter hemispherical nose for Reynolds numbers in excess of 1×10^6. (The calculated critical Reynolds number is 5×10^6.) However, they did not measure the pressure distribution and consequently it was advisable to measure the mean pressure over the range of test speeds used in this investigation.

Mean pressure measurements on a 5.1 cm diameter hemispherical nose were performed in the 30.5 cm water tunnel. A total of 18 pressure taps each 0.034 cm in diameter were employed. The stainless steel body was made in two parts with pressure taps located in a removable hatch. Pressure lines ran through a hollow afterbody, down through the mounting strut and out of the tunnel into a 48-position scanna-valve. All pressures were measured with a Bell and Howell differential type pressure transducer. For each test speed, the pressure was read five times and an average of the readings was obtained.

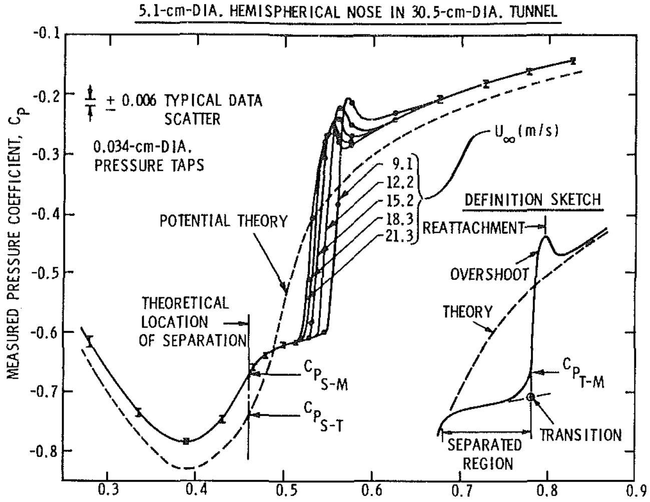

Fig. 8 Measured mean pressure distribution on the hemispherical nose

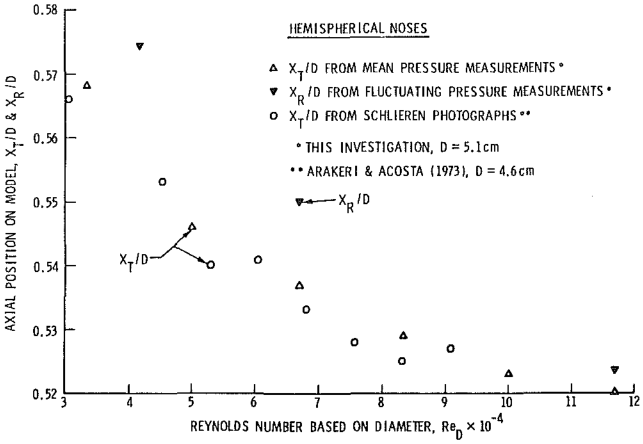

Fig. 9 Location of transition and reattachment versus Reynolds number – hemispherical noses

The measured mean pressure distribution is presented in Fig. 8 for speeds from 9.1 to 21.3 m/s. The data are presented in the form of pressure coefficients (C_p) versus axial distance (X/D) along the model. The theoretical curve for a hemispherical nose with the appropriate blockage is also shown. The influence of laminar boundary-layer separation on the measured pressure distributions is quite evident. The actual location of laminar separation cannot be determined accurately from the measured pressure distributions. However, the theoretical location ($X/D = 0.462$) is not inconsistent with the measured data. Also the data in the region of laminar separation do not change appreciably with velocity. Both Arakeri and Acosta [4] and van der Meulen [3] reported that the experimental location of laminar separation remains constant with changing speed on the hemispherical nose. They also reported good agreement between the theoretical and experimenal locations of laminar boundary-layer separation. In Fig. 8, it is seen that the indicated region of separation is immediately followed by a pressure recovery region marked by a very steep adverse pressure gradient. The pressure then appears to "overshoot" somewhat and then decreases fairly sharply before rising in a manner parallel to the theoretical curve.

A sketch is provided in Fig. 8 to define important features of the pressure distribution curves. The locations of transition and reattachment as arbitrarily defined in the sketch of Fig. 8

are observed to move systematically upstream as the speed increases. The location of transition (X_T/D) as defined in Fig. 8 is plotted against Reynolds number in Fig. 9. Also shown in Fig. 9 are transition data calculated from the separation bubble length data of Arakeri and Acosta [4] for a 4.6 cm diameter hemispherical nose. They define the end of the separation bubble as the position where the free shear layer, visible by Schlieren, disappears as a result of turbulent mixing. In this investigation the end of the separation region is arbitrarily located at the transition point as indicated by the sketch in Fig. 8. In general the data from the two investigations compare favorably. Reattachment data obtained from fluctuating pressure measurements are also given in Fig. 9.

The results of the mean pressure measurements in Fig. 8 have several implications relative to the observed formation of band cavitation on the hemispherical nose. This discussion is presented in a subsequent section.

Discussion of Travelling-Bubble and Travelling-Patch Cavitation

Travelling-bubble and travelling-patch cavitation were perhaps the most commonly observed forms of cavitation in this investigation. Major characteristics are:

1. Travelling cavitation showed no apparent preference for a particular boundary-layer state, i.e., separated, attached, laminar or turbulent for it was observed on all three models.
2. The value of the limited cavitation number (σ_l) for travelling cavitation was significantly influenced by air content. Particularly at low speeds, increasing the air content may increase σ_l to a value approaching $|C_{p_{\min}}|$ of the body.
3. In most cases, the value of σ_l for travelling cavitation was observed to decrease with an increase in freestream speed. However, in some cases the opposite trend was observed. Travelling cavitation is probably very sensitive to changes in freestream nuclei which may be the primary cause of the various trends of σ_l versus speeds.
4. Travelling-bubble cavitation was more dominant than travelling-patch cavitation at low speeds. As the speed was increased, travelling-patch cavitation became more dominant.

The observed characteristics of travelling cavitation in the present investigation are consistent with the work of Schiebe [2] who reports that the formation of transient cavitation is largely controlled by the number and size of nuclei in the free stream. A similar conclusion is reported by Gates [10]. Thus if the nuclei populations of two water tunnel facilities are very different, one can expect to see differences in the travelling cavitation characteristics of the same model tested in both facilities. In particular, differences should be evident in cavitation tests performed in facilities with and without resorbers. A very important example of a facility with a resorber is the High Speed Water Tunnel of the California Institute of Technology (CIT). The resorber minimizes the amount of free gas, i.e., undissolved gas, in the water and consequently travelling cavitation is seldom observed in this facility [9].

The tendency for σ_l of travelling cavitation to approach $|C_{p_{\min}}|$ with an increase in the nuclei population has also been reported by Gates [10] in his experiments in the 30.5 × 30.5 cm Low Turbulence Water Tunnel at the California Institute of Technology. In his investigation, an increase in the free gas content for a constant total gas content resulted in an increase in the incipient cavitation number. The results of Arakeri and Acosta [4] from their electrolysis tests with the so-called ITTC nose or Swedish nose in the High Speed Water Tunnel at CIT are consistent with Gates' results. By providing cavitation nuclei by means of electrolysis they were able to produce cavitation at an incipient cavitation number which is less than $|C_{p_{\min}}|$ but significantly greater than σ_i determined in the absence of seeding the flow with nuclei.

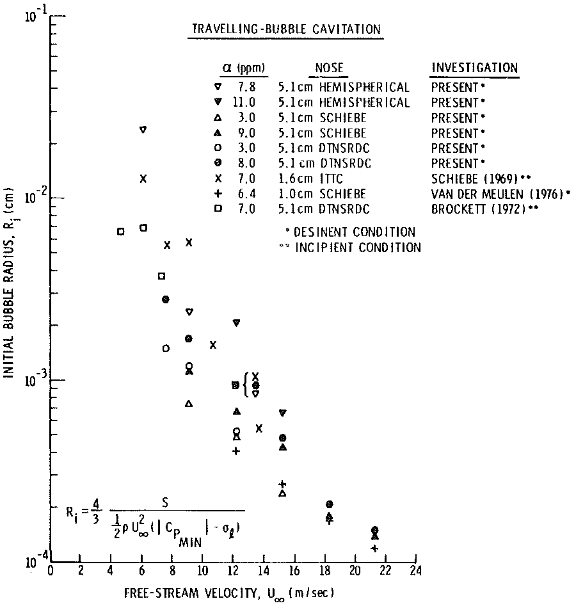

Fig. 10 Analysis of travelling-bubble cavitation from four investigations

The decreasing trend of σ_l with speed for travelling cavitation is consistent with the results reported by both van der Meulen [3] for 1 cm Schiebe nose and Schiebe [12] for a 1.6 cm ITTC nose. Brockett [13] reports a slight increasing trend in σ_l with speed for travelling cavitation on a 5.1 cm DTNSRDC nose at speeds from 4.6 to 7.3 m/s.

An analysis of travelling-bubble cavitation was conducted using the equilibrium equation for a spherical bubble. The initial or critical bubble radius (R_i) is given by

$$R_i = \frac{4}{3} \frac{S}{P_v - P_i} \tag{2}$$

where S, P_v, and P_i are the surface tension, vapor pressure and initial or critical pressure, respectively. This result has been noted by many authors. See for example references [14-16]. Equation (2) was employed to analyze travelling cavitation data from several investigations including this investigation. It was assumed that P_i corresponded to the minimum mean pressure on the body for the measured limited cavitation number. Thus equation (2) can be expressed as

$$R_i = \frac{4}{3} \frac{S}{1/2\rho U_\infty{}^2(|C_{p_{\min}}| - \sigma_l)} \cdot \tag{3}$$

Results from the application of equation (3) to various data are given in Fig. 10. The six sets of data from Figs. 4, 5, and 6 are presented from this investigation for the three nose shapes at two different air contents. Van der Meulen [3], Schiebe [12] and Brockett [13] also reported travelling-bubble cavitation data for a 1 cm Schiebe nose, a 1.6 cm ITTC nose, and a 5.1 cm DTNSRDC nose, respectively. Equation (3) was also applied to these data and the results are shown in Fig. 10. It is seen that over the speed range of 6.1 to 21.3 m/s, the critical nuclei size decreases by over two orders of magnitude. It is interesting to note that none of the water tunnels employed to obtain the data of Fig. 10 have resorbers. The High-Speed Water Tunnel at CIT is equipped with a resorber and, as mentioned previously, travelling-bubble cavitation is rarely seen in this facility. Evidently values of R_i calculated by equation (3) for the CIT facility would fall below the band of data in Fig. 10.

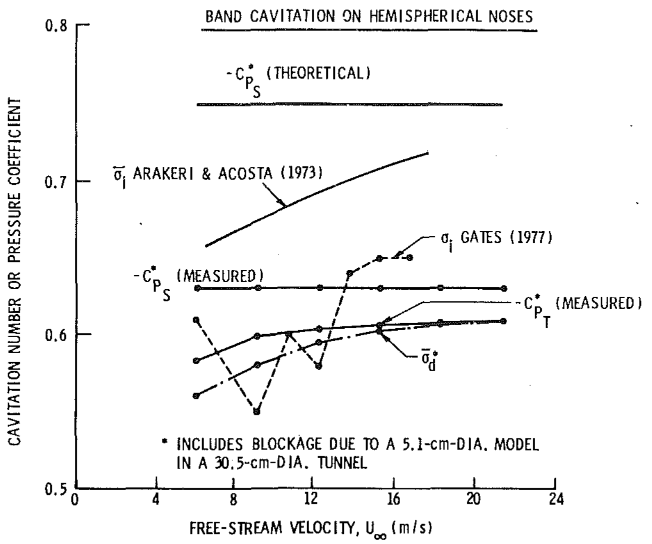

Fig. 11 Comparison of cavitation number and pressure coefficient data for band cavitation on hemispherical noses

Discussion of Band Cavitation

By means of Schlieren photography, Arakeri and Acosta [4] provided convincing evidence of the dramatic role that laminar separation can play in the inception process. However, there were several investigators in the United Kingdom (namely, Alexander [17] and Bailey and Casey [18]) who were also investigating these matters. In particular, Bailey and Casey proposed that σ_i be equated to the pressure coefficient at the laminar separation point. Thus

$$\sigma_i = |C_{p_s}| \tag{4}$$

Independently of this work, Arakeri and Acosta [4] also proposed that σ_i should be related to C_{p_s} for band cavitation.

Pressure coefficients and cavitation numbers for band cavitation are compared in Fig. 11. Three sets of cavitation data are given, namely those of Arakeri and Acosta [4], Gates [10] and the averaged values of σ_d for the tests at two air contents from this investigation. In addition, three sets of pressure coefficient data are presented, that is, the theoretical value of C_{p_s} and the measured values of C_{p_s} and C_{p_T} from Fig. 8. It is seen that the cavitation data obtained in this investigation is approximated fairly well by the relation

$$\sigma_i \simeq |C_{p_T}|_M \tag{5}$$

whereas

$$\sigma_i < |C_{p_s}|_M \tag{6}$$

where the subscript M denotes a measured value.

In order to compare the CIT data of Arakeri, Acosta, and Gates with the ARL data from this investigation, it is necessary to increase the incipient cavitation numbers by approximatley 8.5 percent in order to add blockage. The CIT σ_i data are thus generally greater than the ARL data, and the reasons for these discrepancies have not been explained. Generally the measured coefficients C_{p_s} and C_{p_T} would not be available, whereas, in principle, one can obtain C_{p_s} by theoretical means. Thus, comparing all data for the blocked state indicates that in most cases the cavitation number satisfies the relation

$$\sigma_i < |C_{p_s}|_T \tag{7}$$

where the subscript T denotes a theoretical value.

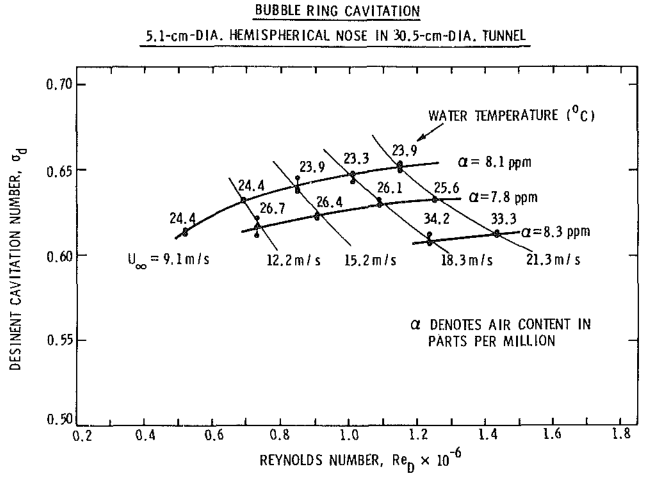

Fig. 12 Effect of water temperature on bubble-ring cavitation on the hemispherical nose

Discussion of Bubble-Ring Cavitation

As indicated previously, bubble-ring cavitation, which was only observed on the hemispherical nose in this investigation, is associated with band cavitation and both are caused by laminar separation. Bubble-ring cavitation occurs in the reattachment region where large turbulent pressure fluctuations have been reported [19-21]. As shown in Fig. 4, the cavitation number for bubble-ring cavitation (σ_{BRC}) was greater than the cavitation number for band cavitation (σ_{BC}) by nearly a constant amount ($\Delta\sigma$). Thus

$$\sigma_{\mathrm{BRC}} = \sigma_{\mathrm{BC}} + \Delta\sigma \simeq |C_{p_T}|_M + \Delta\sigma \tag{8}$$

where

$$\Delta\sigma \simeq 0.03 \quad . \tag{9}$$

It may be that $\Delta\sigma$ is approximated by a normalized pressure fluctuation ($P_R{}'$) associated with the reattachment region. That is

$$\Delta\sigma \simeq \frac{P_R{}'}{1/2\rho U_\infty{}^2} \quad . \tag{10}$$

Fluctuating pressure measurements were made in this investigation in the reattachment region and it was found that the peak RMS pressure readings lie between 0.06 and 0.08 over the speed range of 7.6 to 21.3 m/s. This is the same order of magnitude as $\Delta\sigma$ given by equation (9).

Several tests were conducted to determine the effect of air content on bubble-ring cavitation. The results showed some rather interesting effects of both air content and water temperature on the formation of bubble-ring cavitation. Generally, bubble-ring cavitation was observed for all air contents from 4 ppm to the maximum employed in the test which was 12 ppm. No bubble-ring cavitation was observed for air contents less than 4 ppm. Its appearance with regard to number density of individual cavities and overall steadiness of the ring formation frequently differed from one test to the next, often with no apparent correlation to the change in air content. In separate cavitation tests at similar air contents, scatter of as much as 6 percent was noted in the desinent cavitation number data. It was subsequently discovered that this data scatter was apparently due to temperature, for the cavitation number correlated quite well with the operating water temperature. This is shown by the results presented in Fig. 12 for three separate tests. The air contents for the three tests were all about 8 ppm. It is apparent that σ_i decreases slightly with increasing water temperature. Also, as the temperature increased, bubble-ring cavitation was eliminated at reduced values of the speed. Recently B. R. Parkin [22–23] has conducted an extensive analysis of bubble-ring cavitation based on bubble-dynamic considerations using the Rayleigh-Plesset equation. This theory predicts the air content and speed cut-off effects referred to in the previous discussion.

In this and other investigations laminar separation has been observed on hemispherical, eighth caliber, ITTC, and DTNSRDC noses. However, it is curious that bubble-ring cavitation has been observed on only two noses, namely the hemispherical and eighth caliber. This is probably due to peculiarities associated with the mean pressure distribution and pressure fluctuations in the reattachment region. Arakeri [24] shows that the thickness of the laminar separation bubble on the hemispherical nose is much thicker than that on the ITTC nose. Thus the thicker bubble on the hemispherical nose may be a factor in creating the proper environment for bubble-ring cavitation.

Discussion of Fixed-Patch Cavitation

Fixed-patch cavitation was observed on the Schiebe nose and the DTNSRDC nose in this investigation. It was also occasionally observed on the hemispherical nose which was attributed to dirt particles (wiping off the nose eliminated fixed-patch cavitation in subsequent tests). However, wiping off the surface did not eliminate fixed-patch cavitation on the Schiebe and DTNSRDC noses.

Fixed-patch cavitation was also observed on a 4.5 cm ITTC nose in the investigation by Acosta and Hamaguchi [25]. They show an excellent photograph of fixed-patch cavitation occurring with band cavitation. Their indication that this type of cavitation occurred at higher speeds is consistent with the results of the present investigation. Parkin and Holl [26], in discussing cavitation on 10.2 cm and 20.4 cm diameter hemispherical noses, also reported the observation of "small diamond shaped cavitation zones apparently due to very small rough spots."

As previously indicated in the discussion of the cavitation data in Figs. 4-6, fixed-patch cavitation is more prevalent at high speeds and the cavitation number increases with speed. These characterisitcs, together with the physical appearance, strongly suggests that fixed-patch cavitation is caused by surface roughness. Based on the results of Holl [27] one would expect σ for an isolated roughness of height h to increase with speed. However, as indicated previously, high air content values appear to suppress the formation of fixed-patch cavitation causing a decrease in the desinent cavitation number. The mechanism which causes this trend has not been determined.

As indicated by Holl [27], the critical cavitation number for a body with roughness (σ_{cr}) is given by the superposition equation

$$\sigma_{cr} = -C_p + [1 - C_p]\sigma_{cfp} \tag{11}$$

where C_p is the pressure coefficient at the location of the roughness and σ_{cfp} is the cavitation number of the roughness as determined from flat plate data. This equation has been revised by Arndt, Holl, Bohn, and Bechtel [28] to include bubble dynamic effects. The revised equation is

$$\sigma_{cr} = -C_p - \Omega + [1 - C_p]\sigma_{cfp} \tag{12}$$

The function Ω accounts for possible bubble dynamic effects and is defined as

$$\Omega = \frac{P_v - P_{\text{min-}r}}{1/2\rho U_\infty{}^2} \tag{13}$$

where $P_{\text{min-}r}$ is the minimum pressure produced by the roughness. In some cases where Ω is sufficiently large, equation (12) suggests that σ_{cr} can be less than $|C_p|$. Application of equation (12) to some of the fixed-patch cavitation encountered in this investigation indicated this type of behavior.

The analysis of fixed-patch cavitation using equation (12) and cavitation data for isolated roughnesses has been successfully applied to sheet cavitation on hydrofoils [29] and fixed-patch cavitation on hemispherical noses [30].

Conclusions and Recommendations

The cavitation data presented in the previous sections show that many types of cavitation can be produced by various flow conditions. The fact that so many different types of cavitation can occur emphasizes the need for more detailed reporting of experimental observations. The mechanisms which control the various types of cavitation need to be clarified further. In particular, a dynamical analysis of travelling-bubble cavitation should be conducted and related to measurements of cavitation nuclei. Also, from this investigation and others at ARL, it appears that surface roughness can play a major role in controlling fixed-patch cavitation on headforms and sheet cavitation on hydrofoils.

Experimental Uncertainty

The cavitation data in Figs. 4, 5, 6, 11, and 12 have a maximum uncertainty of about ±5 percent. This maximum uncertainty is primarily associated with travelling-bubble cavitation. The other types of cavitation have reduced uncertainties. The pressure coefficient data in Fig. 8 have an absolute uncertainty, i.e., spread in C_p, of approximately ± 0.006.

Acknowledgments

This investigation was sponsored by NAVSEA Code 63R31 and the ARL E and F Program administered by Dr. M. T. Pigott.

References

1 Holl, J. W., "Cavitation Research Facilities at the Ordnance Research Laboratory of The Pennsylvania State University," *Proceedings of the ASME Symposium on Cavitation Research Facilities and Techniques*, 1964, pp. 11-18.

2 Schiebe, F. R., "Measurement of the Cavitation Susceptibility of Water Using Standard Bodies," Report No. 118, St. Anthony Falls Hydraulic Laboratory, University of Minnesota, Feb. 1972.

3 van der Meulen, J. H. J., "A Holographic Study of Cavitation on Axisymmetric Bodies and the Influence of Polymer Additives," Publication No. 509, Netherlands Ship Model Basin, Wageningen, The Netherlands, 1976.

4 Arakeri, V. H., and Acosta, A. J., "Viscous Effects in the Inception of Cavitation on Axisymmetric Bodies," ASME JOURNAL OF FLUIDS ENGINEERING, Vol. 95, No. 4, Dec. 1973, pp. 519-528.

5 Arakeri, V. H., and Acosta, A. J., "Cavitation Inception Observations on Axisymmetric Bodies at Supercritical Reynolds Numbers," *Journal of Ship Research*, SNAME, Vol. 20, No. 1, Mar. 1976, pp. 40-50.

6 Robertson, J. M., McGinley, J. H., and Holl, J. W., "On Several Laws of Cavitation Scaling," La Houille Blanche, No. 4, Sept. 1957.

7 Arakeri, V. H., Carroll, J. A., and Holl, J. W., "A Note on the Effect of Short and Long Laminar Separation Bubbles on Desinent Cavitation," ASME JOURNAL OF FLUIDS ENGINEERING, Vol. 103, Mar. 1981, pp. 28-32.

8 Kermeen, R. W., "Some Observations of Cavitation on Hemispherical Head Models," Report No. E 35.1, Hydrodynamics Laboratory, California Institute of Technology, June 1952.

9 Parkin, B. R., and Kermeen, R. W., "The Roles of Convective Air Diffusion and Liquid Tensile Stresses During Cavitation Inception," *Proceedings of the IAHR Symposium on Cavitation and Hydraulic Machinery*, Sendai, Japan, 1962, pp. 17-35.

10 Gates, E. M., "The Influence of Freestream Turbulence, Freestream Nuclei Populations and a Drag-Reducing Polymer on Cavitation Inception on Two Axisymmetric Bodies," Ph.D. thesis, California Institute of Technology, Apr. 1977.

11 Rouse, H., and McNown, J. S., "Cavitation and Pressure Distribution—Head Forms at Zero Angle of Yaw," Studies in Engineering Bulletin 32, University of Iowa, 1948.

12 Schiebe, F. R., "The Influence of Gas Nuclei Size Distribution on

Transient Cavitation Near Inception," Report No. 107, St. Anthony Falls Hydraulic Laboratory, University of Minnesota, May 1969.

13 Brockett, T., "Some Environmental Effects on Headform Cavitation Inception," Report No. 3974, DTNSRDC, Oct. 1972.

14 Dergarabedian, P., "The Rate of Growth of Vapor Bubbles in Superheated Water," ASME *Journal of Applied Mechanics*, Vol. 75, Dec. 1953, pp. 537-545.

15 Daily, J. W., and Johnson, V. E., "Turbulence and Boundary-Layer Effects on Cavitation Inception from Gas Nuclei," *Trans. ASME*, Vol. 78, 1956, pp. 1695-1706.

16 Holl, J. W., "Nuclei and Cavitaton," ASME *Journal of Basic Engineering*, Vol. 92, Dec. 1970, pp. 681-688.

17 Alexander, A. J., "An Investigation of the Relationship Between Flow Separation and Cavitation," Ship TM 230, National Physical Lab., 1968.

18 Bailey, A. B., and Casey, M. V., "Cavitation Parameter for Inception on a Hydrofoil at Moderate Incidence," Report No. 1025/71, Oxford University Engineering Laboratory, 1971.

19 Gaster, M., "The Structure and Behavior of Laminar Separation Bubbles," from Separated Flows, Part 2, AGARD - NATO Conference Proceedings, No. 4, May 1966, pp. 813-854.

20 Huang, T. T., and Hannan, D. E., "Pressure Fluctuations in the Regions of Flow Transition," Report 4723, DTNSRDC, Dec. 1975.

21 Arakeri, V. H., "A Note on the Transition Observations on an Axisymmetric Body and Some Related Fluctuating Wall Pressure Measurements," ASME JOURNAL OF FLUIDS ENGINEERING, Vol. 97, No. 1, Mar. 1975, pp. 82-86.

22 Parkin, B. R., "A Theory for Cavitation Inception in a Flow Having Laminar Separation," ARL TM 79-198, The Pennsylvania State University, Nov. 19, 1979.

23 Parkin, B. R., "Conditions Favorable for Gaseous Microbubble Growth in Laminar Separation Bubbles," ASME Cavitation and Polyphase Forum 1980, pp. 1-6.

24 Arakeri, V. H., "Viscous Effects in Inception and Development of Cavitation on Axi-Symmetric Bodies," Ph.D. thesis, California Institute of Technology, 1973.

25 Acosta, A. J., and Hamaguchi, H., "Cavitation Inception on the ITTC Standard Head Form," Report No. E 149.1, Hydrodynamics Laboratory, California Institute of Technology, Mar. 1967.

26 Parkin, B. R., and Holl, J. W., "Incipient Cavitation Scaling Experiments for Hemispherical and 1.5 Caliber Ogive-Nosed Bodies," Report Nord 7958-264, Ordnance Research Laboratory, The Pennsylvania State University, May 1954.

27 Holl, J. W., "The Inception of Cavitation on Isolated Surface Irregularities," ASME *Journal of Basic Engineering*, Vol. 82, No. 1, Mar. 1960, pp. 169-183.

28 Arndt, R. E. A., Holl, J. W., Bohn, J. E., and Bechtel, W. T., "The Influence of Surface Irregularities on Cavitation Performance," *Journal of Ship Research*, SNAME, Vol. 23, No. 3, Sept. 1979, pp. 157-170.

29 Billet, M. L., and Holl, J. W., "Scale Effects on Various Types of Limited Cavitation," *Proceedings of ASME International Symposium on Cavitation Inception*, Dec. 1979, pp. 11-23.

30 Billet, M. L., Holl, J. W., and Parkin, B. R., "Scale Effects on Cavitating Flows Due to Surface Roughness and Laminar Separation," *Proceedings of the 10th Symposium of IAHR*, Tokyo, Sept. 1980, pp. 39-52.

On the Equilibrium of Cavitation Nuclei in Liquid-Gas Solutions

Y. S. Cha
Components Technology Division,
Argonne National Laboratory,
Argonne, Ill. Mem. ASME

The stability of a spherical bubble in a two-component two-phase system is examined by employing the thermodynamic theory of dilute solutions. It is shown that a bubble can remain in a state of stable equilibrium provided that the ratio of the total number of moles of the solute to the total number of moles of the solvent in the system is not extremely small and that the system pressure falls between an upper bound (dissolution limit) and a lower bound (cavitation limit). The results of the analysis provide a theoretical basis for the persistence of microbubbles in a saturated liquid-gas solution. Thus to a certain extent, the results also help to resolve the dilemma that exists in the field of cavitation due to (1) the necessity of postulating the existence of microbubbles; and (2) the lack of theoretical justification for the persistence of such bubbles in a liquid.

Introduction

It is well known that the theoretical tensile strength of a liquid is much larger than that usually observed. This discrepancy between theory and experimental observations of tensile strength can be resolved by postulating the existence of nuclei, or microbubbles, in the liquid [1]. However, vapor bubbles cannot persist in a liquid since these bubbles cannot exist in equilibrium when the system pressure is greater than the vapor pressure and are in unstable equilibrium states when the system pressure is less than the vapor pressure. Gas bubbles are also considered unstable since these bubbles grow indefinitely in a supersaturated solution and dissolve completely in an undersaturated solution. Even in a saturated solution, gas bubbles will dissolve because of surface tension according to the theoretical work reported by Epstein and Plesset [2]. Numerous models were proposed in the past to explain the persistence of long-lived nuclei in a liquid [3], So far, the most plausible explanation is the one proposed by Harvey, et al. [4]; they suggested that nuclei could be stabilized in cracks on the surfaces of solid particles in the liquid. Solid particles tend to settle down and fall to the bottom of the liquid. However, if the solid particles were small enough, say less than 5×10^{-7} meters in radius, they can be maintained in suspension by the mechanism of Brownian motion [3]. One of the important characteristics of cavitation is that the tensile strength or cavitation threshold tend to increase as the waiting time increases. This effect is usually attributed to the presence of relatively large solid particles which tend to settle out in the liquid. However, this behavior could be explained by the presence of undissolved bubbles rising out of the liquid or completely dissolving into solution [1]. In addition, the "free nucleus" model is extremely useful in clarifying many of the complex phenomena associated with cavitation although there still remains considerable mystery about the nature of these microbubbles [3].

In this paper, the stability of a spherical gas-vapor bubble in a state of equilibrium is examined by employing the thermodynamic theory of dilute solutions. Conditions of equilibrium and stability criteria are derived. Numerical examples are presented. The results show that, for a given two-component two-phase system, a "free" bubble can remain in a state of stable equilibrium in a saturated liquid-gas solution under certain circumstances which depend primarily on the system pressure, the radius of the bubble, and the total number of moles of the solute and the solvent in the system.

Conditions of Equilibrium

Consider a spherical bubble in a dilute liquid-gas solution. A solution is dilute when the amount of solute is small compared to the amount of solvent. Let the solution be composed of n_1' moles of solvent and n_2' moles of solute, then for dilute solutions,

$$n_2' << n_1'. \tag{1}$$

When the solution is sufficiently dilute and can be assumed to be ideal, the chemical potential of each component in the solution can be written as

$$\mu_1' = \mu_{01}'(T,P') + RT \ ln \ x_1', \tag{2}$$

and

$$\mu_2' = \mu_{02}'(T,P') + RT \ ln x_2'. \tag{3}$$

Assuming that the spherical bubble contains a mixture of ideal gases, then the chemical potential of each component in the ideal mixture can be written as

$$\mu_1'' = \mu_{01}''(T) + RT \ln p_1'', \tag{4}$$

and

$$\mu_2'' = \mu_{02}''(T) + RT \ln p_2''. \tag{5}$$

Contributed by the Fluids Engineering Division and presented at the International Symposium on Cavitation Inception, ASME Winter Annual Meeting, New York, N.Y., December 2-9, 1979 of THE AMERICAN SOCIETY OF MECHANICAL ENGINEERS. Manuscript received by the Fluids Engineering Division, February 11, 1980.

During an infinitesimal reversible isothermal transformation, the variation in free energy of the system is,

$$dF = dF' + dF'' + \sigma dA$$

$$+ = -P'dV' + \mu_1' dn_1' + \mu_2' dn_2' - P''dV''$$

$$+ \mu_1'' dn_1'' + \mu_2'' dn_2'' + \sigma dA, \tag{6}$$

Assuming that the total volume of the system and the total number of moles of each component in the system remain constant during the transformation,

$$V' + V'' = V = \text{constant} \tag{7}$$

$$n_1' + n_1'' = N_1 = \text{constant}, \tag{8}$$

and

$$n_2' + n_2'' = N_2 = \text{constant}. \tag{9}$$

In addition, we have

$$V'' = 4\pi r^3/3, \tag{10}$$

$$A = 4\pi\gamma^2, \tag{11}$$

and

$$x_1' + x_2' = 1. \tag{12}$$

Substituting equations (7) through (11) into equation (6),

$$dF = (P' - P'' + 2\sigma/r) dV'' + (\mu_1'' - \mu_1') dn_1''$$

$$+ (\mu_2'' - \mu_2') dn_2''. \tag{13}$$

The following equilibrium equations are obtained by letting $dF = 0$,

$$P' - P'' + 2\sigma/r = 0, \tag{14}$$

$$\mu_1' = \mu_1'', \tag{15}$$

and

$$\mu_2' = \mu_2''. \tag{16}$$

By assuming that the liquid is incompressible, it can be shown that equation (15) leads to the following equation:

$$p_1'' = x_1' p_{01}'' \exp\left[v_1' (P' - P_0')/RT\right], \tag{17}$$

where p_{01}'' is the vapor pressure of the pure solvent over a curved interface; and P_0' is the corresponding pressure of the solvent in its pure state. p_{01}'' can be expressed in terms of the vapor pressure of the pure solvent acting over a flat interface (p_{01}),

$$p_{01}'' = p_{01} \exp\left[v_{01}'(P_0' - p_{01})/RT\right]. \tag{18}$$

Substituting equations (3) and (5) into equation (16):

$$p_2''/x_2' = \exp\left[(\mu_{02}' - \mu_{02}'')/RT\right]. \tag{19}$$

In general, μ_{02}' is a function of temperature and pressure. However, if the solution is assumed to be incompressible, μ_{02}' becomes a function of temperature only [5], and equation (19) becomes,

$$p_2''/x_2' = K_2(\mathrm{T}), \tag{20}$$

where K_2 is the Henry's law constant between the solute and the solvent with a curved interface. It will be assumed that the effect of curvature on the solubility of the gas in the liquid is small and can be neglected. Thus, K_2 is taken to be the same as the Henry's law constant between the solute and the solvent with a flat interface. For dilute solutions, the following approximation can be employed for equation (20),

$$p_2'' = K_2 x_2' = K_2 n_2' / (n_1' + n_2') \simeq K_2 n_2' / n_1' \tag{21}$$

For the ideal mixture in the bubble,

$$P'' = p_1'' + p_2'', \tag{22}$$

where

$$p_1'' = n_1'' RT/V'', \tag{23}$$

$$p_2'' = n_2'' RT/V''. \tag{24}$$

Substituting equations (21) and (24) into equation (9) and employing equations (8) and (23), it can be shown that

$$p_2'' = N_2 \Big/ \left[N_1/K_2 + V''(1 - p_1''/K_2)/RT\right]. \tag{25}$$

Substituting equations (22) and (25) into equation (14),

$$P' = p_1'' + N_2 \Big/ \left[N_1/K_2 + V''(1 - p_1''/K_2)/RT\right] - 2\sigma/r. \tag{26}$$

The volume of the solution is defined as,

$$V' = n_1' v_1' + n_2' v_2'. \tag{27}$$

Substituting equations (8), (9), (23), (24), and (27) into equation (7),

$$V - V'' = v_1'\left(N_1 - \frac{p_1'' V''}{RT}\right) + v_2'\left(N_2 - \frac{p_2'' V''}{RT}\right). \tag{28}$$

For a given system, N_1, N_2, V, and T remain constant. p_{01}, v_{01}', K_2, and σ can be obtained directly since these quantities are functions of temperature only. There are still nine unknowns ($x_1', x_2', p_1'', p_2'', v_1', v_2', P_0'$, P', and V'' or r) with only seven equations, i.e., equations (12), (17), (18), (20), (25), (26), and (28). Theoretically, it is possible to obtain two additional equations which express v_1' and v_2' in terms of other unknowns. This would allow one to calculate all the equilibrium quantities by simultaneously solving these equations. However, for most practical applications, it is not necessary to carry out such a lengthy procedure. For dilute solutions, the following approximation can be adopted

$$v_1' \simeq v_{01}'.$$

Nomenclature

A = interfacial area
F = Helmholtz free energy
K_2 = Henry's law constant between solute 2 and solvent 1
n = number of moles
N = total number of moles (equations (8) and (9))
p = partial pressure of gases
p_{01} = vapor pressure of the solvent under its own pressure with a flat interface
p_{01}'' = vapor pressure of the pure solvent over a curved interface
P = pressure
P_0' = pressure of the solvent in its pure state over a curved interface
r = radius of the bubble
R = universal gas constant
T = absolute temperature
v = molar specific volume
v_{01}' = molar specific volume of the pure solvent
V = volume or total volume (equation (7))
x = mole fraction
μ = chemical potential
μ_0 = chemical potential of the pure component
σ = surface tension

Subscripts

1 = solvent component
2 = solute component

Superscripts

$'$ = liquid phase
$''$ = gas or vapor phase

Equations (17) and (18) can be combined to give,

$$p_1''=x_1'p_{01}\exp\left[v_{01}'(P'-p_{01})/RT\right]. \qquad (29)$$

Equations (12), (20), (25), (26), and (29) can then be employed to calculate the equilibrium radius for a prescribed system pressure. Furthermore, the molar specific volume of the vapor is usually much larger than that of the solvent, therefore, the difference between p_1'' and p_{01} is small and can be neglected,

$$p_1''\simeq p_{01},$$

and equation (26) becomes,

$$P'=p_{01}+N_2\Big/\left[N_1/K_2+V''(1-p_{01}/K_2)/RT\right]-2\sigma/r. \qquad (30)$$

For given values of N_1, N_2, and T, equations (30) provides the relationship between the system pressure P' and the equilibrium radius r in terms of known quantities.

It should be noted that equation (26) or (30) is different from that reported by Mori, et al. [6]. They employed n_1' and n_2, which are variables, in their equation whereas equation (26) or (30) employs N_1 and N_2 which are constants for a given system. If the gas is insoluble in the liquid ($K_2 \to \infty$), equation (26) reduces to

$$P'=p_1''+RTN_2/V''-2\sigma/r. \qquad (31)$$

Stability Criteria

In order that the bubble be in a state of stable equilibrium, d^2F must be greater than zero. For the present system, it can be shown that

$$\begin{aligned} d^2F \;=\; & a_{11}(dV'')^2+a_{12}dV''dn_1''+a_{13}dV''dn_2'' \\ & +a_{21}dn_1''dV''+a_{22}(dn_1'')^2+a_{23}dn_1''dn_2'' \\ & +a_{31}dn_2''dV''+a_{32}dn_2''dn_1''+a_{33}(dn_2'')^2, \end{aligned} \qquad (32)$$

where

$$a_{11}=\left[\partial(2\sigma/r-P'')/\partial V''\right]_{n_1'',n_2''}-(\partial P'/\partial V')_{n_1',n_2'} \qquad (33a)$$

$$a_{22}=(\partial\mu_1'/\partial n_1')_{n_2',V'}+(\partial\mu_1''/\partial n_1'')_{n_2'',V''}, \qquad (33b)$$

$$a_{33}=(\partial\mu_2'/\partial n_2')_{V',n_1'}+(\partial\mu_2''/\partial n_2'')_{V'',n_1''}, \qquad (33c)$$

$$a_{12}=a_{21}=(\partial\mu_1'/\partial V')_{n_1',n_2'}+(\partial\mu_1''/\partial V'')_{n_1'',n_2''}, \qquad (33d)$$

$$a_{23}=a_{32}=(\partial\mu_1'/\partial n_2')_{V',n_1'}+(\partial\mu_1''/\partial n_2'')_{V'',n_1''}, \qquad (33e)$$

$$a_{13}=a_{31}=(\partial\mu_2'/\partial V')_{n_1',n_2'}+(\partial\mu_2''/\partial V'')_{n_1'',n_2''}. \qquad (33f)$$

Equation (32) is of the quadratic form in variables dV'', dn_1'', and dn_2''. This quadratic form must be positive-definite in order to make $d^2F>0$. A necessary and sufficient condition that the quadratic form be positive-definite is given by the following expressions:

$$a_{11}>0, \qquad (34)$$

$$\begin{vmatrix} a_{11} & a_{12} \\ a_{21} & a_{22} \end{vmatrix}>0, \qquad (35)$$

and

$$\begin{vmatrix} a_{11} & a_{12} & a_{13} \\ a_{21} & a_{22} & a_{23} \\ a_{31} & a_{32} & a_{33} \end{vmatrix}>0. \qquad (36)$$

Employing equations (2) to (5) and the assumption that the liquid is incompressible, it can be shown that

$$(\partial P'/\partial V')_{n_1',\ n_2'}=0, \qquad (37a)$$

$$\left[\partial(2\sigma/r-P'')/\partial V''\right]_{n_1'',\ n_2''}=P''/V''-2\sigma/(3rV''), \qquad (37b)$$

$$(\partial\mu_1'/\partial n_1')_{n_2',\ V'}=RT\,x_2'/n_1', \qquad (37c)$$

$$(\partial\mu_1''/\partial n_1'')_{n_2'',\ V''}=RT/n_1'', \qquad (37d)$$

$$(\partial\mu_2'/\partial n_2')_{V',\ n_1'}=RTx_1'/n_2', \qquad (37e)$$

$$(\partial\mu_2''/\partial n_2'')_{V'',\ n_1''}=RT/n_2'', \qquad (37f)$$

$$\begin{aligned}(\partial\mu_1'/\partial V')_{n_1',\ n_2'} &= (\partial\mu_2'/\partial V')_{n_1',\ n_2'} \\ &=(\partial\mu_1''/\partial n_2'')_{V'',\ n_1''}=0, \end{aligned} \qquad (37g)$$

$$(\partial\mu_1''/\partial V'')_{n_1'',\ n_2''}=(\partial\mu_2''/\partial V'')_{n_1'',\ n_2''}=-RT/V'', \qquad (37h)$$

$$(\partial\mu_1'/\partial n_2')_{V',n_1'}=-RT/(n_1'+n_2'). \qquad (37i)$$

Substituting equations (14), (33), and (37) into the inequalities (34), (35), and (36), the stability criteria become,

$$P'>-4\sigma/3r, \qquad (38)$$

$$P'>p_1''\Big/\left[x_1'+x_2'N_2/(N_1-p_1''V''/RT)\right]-4\sigma/3r, \qquad (39)$$

and

$$P'>(x_2'p_2'N_1+x_1'p_1''N_2)/(x_1'^2N_2+x_2'^2N_1)-4\sigma/3r. \qquad (40)$$

Since the first terms on the right-hand sides of (39) and (40) are positive quantities, it is obvious that (39) and (40) are more stringent than (38). To compare (39) with (40), let

$$P_a'=p_1''\Big/\left[x_1'+x_2'N_2/(N_1-p_1'V''/RT)\right]-4\sigma/3r, \qquad (41)$$

$$P_b'=(x_2'p_2''N_1+x_1'p_1''N_2)/(x_1'^2N_2+x_2'^2N_1)-4\sigma/3r. \qquad (42)$$

It can be shown that,

$$P_b'-P_a'=$$

$$\frac{x_2'n_1'N_1p_2''(1-x_2'-p_1''/K_2)+x_2'^2N_1^2p_2''+x_1'x_2'N_1N_2p_1''}{(x_1'^2N_2+x_2'^2N_1)(n_1'x_1'+N_1x_2')}.$$

Thus, $P_b' > P_a'$ provided that the following condition is satisfied,

$$1-x_2'-p_1''/K_2>0. \qquad (43)$$

K_2 is usually very large compared to p_1'' and x_2' is small compared to unity for dilute solutions. Therefore, (43) is satisfied for most practical applications. Under such circumstances, (40) alone is sufficient to determine the stability of the system.

If the gas is insoluble ($x_1' = 1$ and $x_2' = 0$), P_a' becomes equal to P_b',

$$P_a'=P_b'=p_1''-4\sigma/3r. \qquad (44)$$

Equation (44), together with equation (31), gives the critical pressure below which there is no equilibrium radius for a bubble. This result, which is a special case of the present analysis, has been frequently employed to explain the onset of cavitation in a liquid [7].

Results and Discussions

As an example, the results of a nitrogen (solute) and water (solvent) system will be presented. Numerical constants

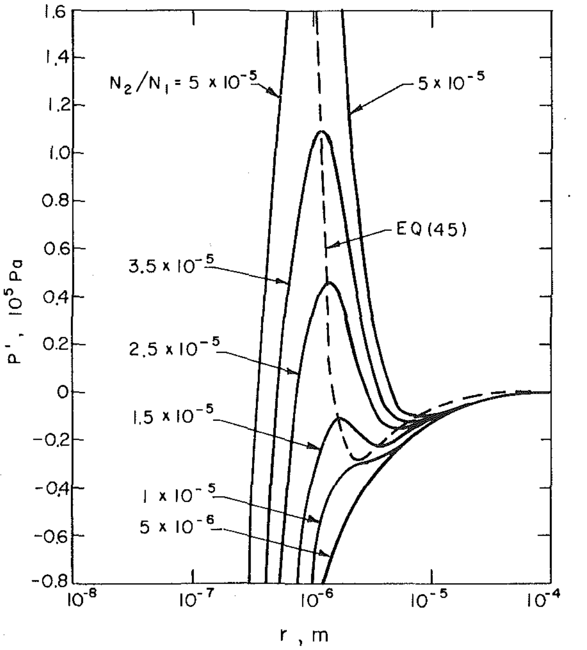

Fig. 1 Variation of system pressure with equilibrium bubble radius for a N_2 – H_2O system with T = 293 K and N_1 = 10^{-10} g-mol for various values of N_2/N_1

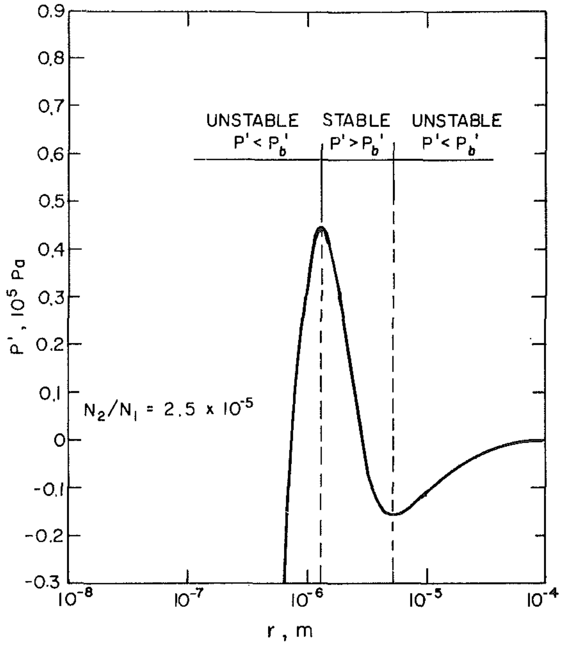

Fig. 2 Variation of system pressure with equilibrium bubble radius for a N_2 – H_2O system with T = 293 K, N_1 = 10^{-10} g-mol, and N_2/N_1 = 2.5 x 10^{-5}

employed in the calculations are: T = 293K, p_{01} = 2.337 × 10^3 Pa, R = 8.313 J/g-mol/K, σ = 7.32 × 10^{-2} N/m, and K_2 = 8.13 × 10^9 Pa. At this temperature, p_1'' is nearly equal to p_{01}. Therefore, only equation (30) is needed to calculate the equilibrium radii for given values of P', N_1, and N_2. It is also obvious that K_2 is much larger than p_1'' and (43) is satisfied. The stability of the system is then determined by (40).

Figure 1 shows the typical variation of system pressure (P') with equilibrium radius for given values of N_1 and N_2 calculated by employing equation (30). The dashed line in Fig. 1 is the limiting conditions obtained by letting

$$P' = P_b', \tag{45}$$

where P' and P_b' are given by equations (30) and (42), respectively. Stability criterion (40) indicates that the equilibria are stable if the slopes of the equilibrium curves in Fig. 1 are negative ($\partial P'/\partial r < 0$) and the equilibria are unstable if the slopes of the equilibrium curves are positive ($\partial P'/\partial r > 0$). For example, Fig. 2 shows the stable and unstable regions of a particular case (N_2/N_1 = 2.5 × 10^{-5}) in Fig. 1. If the ratio of N_2/N_1 is relatively small, say less than 10^{-5} in Fig. 1, the equilibria are always unstable. As the ratio of N_2/N_1 is increased beyond 10^{-5} the equilibria can either be stable or unstable, and the stability of the equilibrium depends on the values of r and P'. The dashed line in Fig. 1 provides the stability boundary for a given value of N_1. The upper right corner bounded by the dashed line in Fig. 1 is in the stable equilibrium region and the rest of the area is in the unstable equilibrium region. By varying the value of N_1, a number of stability boundaries can be generated and they are shown in Fig. 3. For relatively large values of N_1 ($>10^{-5}$ g-mol), only relatively large bubbles can remain in stable equilibria when the system pressure is above the vapor pressure of the solvent and no bubble can remain in stable equilibrium when the system pressure is below the vapor pressure of the solvent. As N_1 is decreased, smaller bubbles can remain in stable equilibria even when the system pressure is negative. It is obvious from Fig. 3 that, depending on the value of N_1, bubbles with radii as small as 10^{-7} m and as large as 10^{-2} m can remain in stable equilibria in the absence of gravity. In practice, however, large bubbles tend to rise to the surface and only very small bubbles with radii in the order of 10^{-6} m or smaller can persist in a liquid for an extended period of time. For example, it takes approximately thirty seconds for a bubble with a radius of 10^{-4} m to rise a distance of one meter, whereas it may take one hundred hours for a bubble with a radius of 10^{-6} m to rise the same distance. Thus, in a system that contains microbubbles of various sizes in stable thermodynamic equilibria, the "aging effect" can be explained by the presence of free nuclei instead of solid particles in a liquid. In order to obtain consistent results in

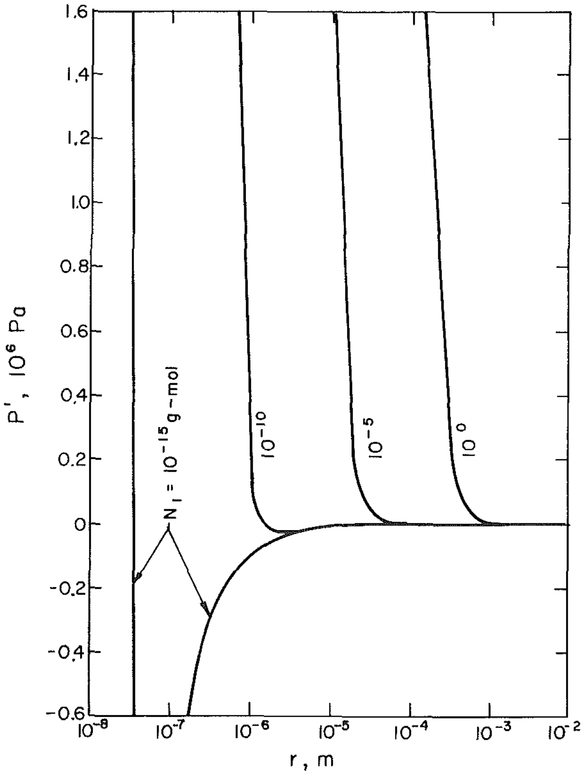

Fig. 3 Stability boundary calculated by employing equation (45) for a N_2 – H_2O system at T = 293 K for various values of N_1

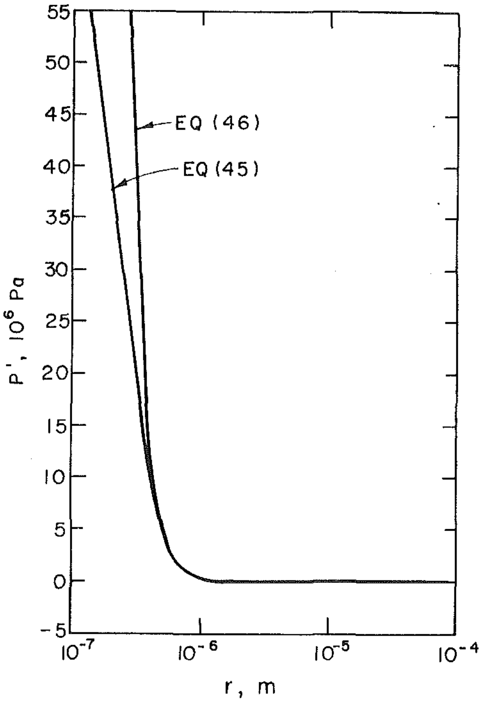

Fig. 4 Comparison between the stability boundary calculated by using equation (45) and the loci of maxima and minima calculated by using equation (46) for a N_2 − H_2O system with T = 293K and N_1 = 10^{-10} g-mol

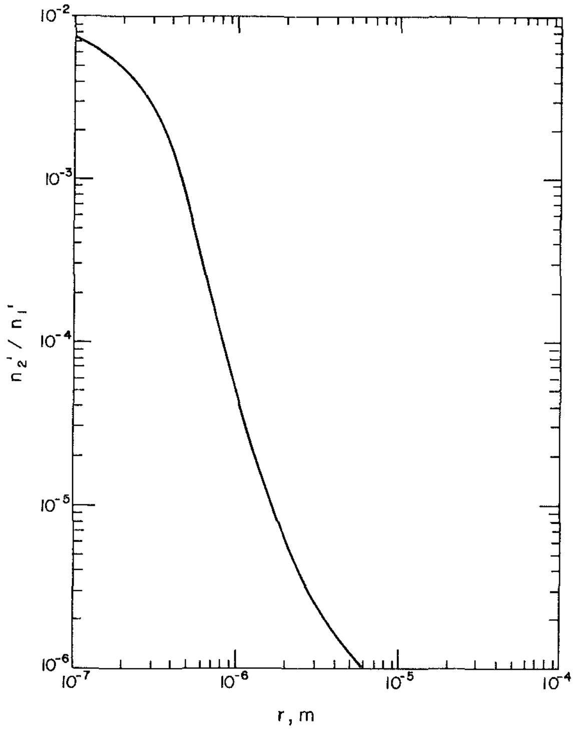

Fig. 5 Variation of n'_2/n'_1 with r for a N_2 − H_2O system with T = 293K and N_1 = 10^{-10} g-mol

laboratory tests, sufficient waiting time must be allowed so that only extremely small bubbles still exist in the liquid.

It can be observed from Fig. 2 that there are two limiting pressures for a bubble in a state of stable equilibrium. These two limiting conditions correspond to the relative maximum and minimum in Fig. 2. The relative minimum corresponds to the lowest pressure and the relative maximum corresponds to the highest pressure that such a bubble can remain in stable equilibrium. The pressure at the relative minimum point can be considered as the highest pressure required to initiate the indefinite growth of the bubble (cavitation limit) and is well known in the field of cavitation. The pressure at the relative maximum point can be considered as the lowest pressure required to dissolve completely the bubble (dissolution limit). The dissolution limit was first reported by Mori, et al, and supported by their experimental results [6]. The present analysis bridged the gap and demonstrated that both the cavitation and the dissolution limits exist for a bubble in a state of stable equilibrium.

It can be observed from Fig. 1 that the stability boundary calculated by employing equation (45) appears to coincide with the loci of maxima and minima of the equilibrium curves. The loci of maxima and minima of the equilibrium curves in Fig. 1 can be obtained by setting $\partial P'/\partial r$ equal to zero in equation (26),

$$(\partial P'/\partial r)_{N_1,\ N_2} = 2\sigma/r^2 - 4\pi r^2 p_2''^2(1 - p_1''/K_2)/(N_2RT) = 0, \qquad (46)$$

where $p_1'' = p_{01}$ and p_2'' is given by equation (25). It is obvious that equations (45) and (46) are not identical. Figure 4 shows the comparison between the stability boundary obtained by employing equation (45) and the loci of maxima and minima of the equilibrium curves obtained by employing equation (46) for $N_1 = 10^{-10}$ g-mol over a wide range of system pressure. When the bubble is relatively large and the system pressure is relatively low, the difference between equation (45) and equation (46) is negligible. This difference increases as the bubble becomes smaller and the system pressure becomes higher. The basic assumption made in the present analysis is that the solution be dilute so that the inequality (1) can be satisfied. This assumption requires that the system pressure be relatively low so that the solution can remain dilute. Figure 5 shows the variation of the ratio n_2/n_1 with r for the same case as that shown in Fig. 4 with $N_1 = 10^{-10}$ g-mol. It is obvious that n_2/n_1 increases as r decreases for a given value of N_1. Figure 4 indicates that deviation between equation (45) and (46) begins to appear when r approaches 4×10^{-7}m. At this radius, it can be observed from Fig. 5 that the ratio n_2'/n_1' becomes very large and the assumption expressed by the inequality (1) can no longer be satisfied. However, as long as the solution is dilute and the inequality (1) is strictly satisfied, the difference between equation (45) and equation (46) is small and can be neglected. Under such circumstance, (40) becomes equivalent to

$$(\partial P'/\partial r)_{N_1,\ N_2} < 0, \qquad (47)$$

and the stability of the system can be determined directly by examining the equilibrium curves. This result was found to be valid for other values of N_1 in a nitrogen-water system and for other combinations of solute and solvent. If the gas is insoluble in the liquid, it can be shown that equation (45) and equation (46) become identical. Under such circumstance, there is only one limit (cavitation limit) for a bubble and such a bubble can always remain in stable equilibrium when the system pressure is greater than the vapor pressure.

Summary and Conclusions

By employing the thermodynamic theory of dilute solutions, it is shown that a gas-vapor bubble in a state of stable equilibrium can have both a cavitation limit and a dissolution limit. The cavitation limit is the minimum pressure and the dissolution limit is the maximum pressure that such a bubble can remain in a state of stable equilibrium in a given system. It is demonstrated that microbubbles can remain in stable equilibrium and persist in a liquid in the absence of gravity over a wide range of pressure. The stability criterion is shown to be approximately equivalent to that expressed by the inequality (47) and thus the stability of a bubble can be determined directly by examining the equilibrium curves.

References

1 Plesset, M. S., "Physical Effects in Cavitating Flow," NASA SP-304, Part I, 1974, pp. 341-349.

2 Epstein, P. S., and Plesset, M. S., "On the Stability of Gas Bubbles in Liquid-Gas Solutions," *Journal of Chemical Physics*, Vol. 18, No. 11, 1950, pp. 1505-1509.

3 Flinn, H. G., "Physics of Acoustic Cavitation in Liquids," in *Physical Acoustics*, Vol. 1, Part B, Edited by W. P. Mason, Academic Press, New York, 1964, pp. 57-172.

4 Harvey, E. N., Barnes, D. K. McElroy, W. D., Whiteley, A. H., Pease, D. C., and Cooper, K. W., "Bubble Formation in Animals. I, Physical Factors," *Journal of Cellular and Comparative Physiology*, Vol. 24, No. 1, 1944, pp. 1-22.

5 Fermi, E., *Thermodynamics*, Dover, New York, 1956, pp. 113-138.

6 Mori, Y., Hijikata, K., and Nagatani, T., "Fundamental Study of Bubble Dissolution in Liquid," *International Journal of Heat and Mass Transfer*, Vol. 20, 1977, pp. 41-50.

7 Knapp, R. T., Daily, J. W., and Hammitt, F. G., *Cavitation*, McGraw-Hill, New York, 1970, pp. 76-82.

bubble can be determined directly by examining the equilibrium curves.

References

1 Plesset, M. S., "Physical Effects in Cavitating Flow," NASA SP-304, Part I, 1974, pp. 341-349.

2 Epstein, P. S., and Plesset, M. S., "On the Stability of Gas Bubbles in Liquid-Gas Solutions," *Journal of Chemical Physics*, Vol. 18, No. 11, 1950, pp. 1505-1509.

3 Flinn, H. G., "Physics of Acoustic Cavitation in Liquids," in *Physical Acoustics*, Vol. 1, Part B, Edited by W. P. Mason, Academic Press, New York, 1964, pp. 57-172.

4 Harvey, E. N., Barnes, D. K. McElroy, W. D., Whiteley, A. H., Pease, D. C., and Cooper, K. W., "Bubble Formation in Animals. I, Physical Factors," *Journal of Cellular and Comparative Physiology*, Vol. 24, No. 1, 1944, pp. 1-22.

5 Fermi, E., *Thermodynamics*, Dover, New York, 1956, pp. 113-138.

6 Mori, Y., Hijikata, K., and Nagatani, T., "Fundamental Study of Bubble Dissolution in Liquid," *International Journal of Heat and Mass Transfer*, Vol. 20, 1977, pp. 41-50.

7 Knapp, R. T., Daily, J. W., and Hammitt, F. G., *Cavitation*, McGraw-Hill, New York, 1970, pp. 76-82.

DISCUSSION

M. S. Plesset[1]

In the paper on this subject Dr. Cha has undertaken a re-examination of the possibility of stable existence of gas bubbles in a liquid-gas solution. He concludes that a gas-vapor bubble can persist in a liquid-gas solution. If this result were correct such bubbles could serve as sites for the initiation of cavitation without any necessity for the assumption of an effective reduction of surface tension for gas pockets on solid particles or at a solid boundary.

I believe that Dr. Cha's conclusion is incorrect and that his analysis contains some errors. As a general remark, it may be said that the discussion of the equilibrium condition, $\delta R = 0$, where F is the free energy of the system is somewhat lax. Cha assumes that the total volume is fixed, but only the liquid which is essentially incompressible has a fixed volume so that any change in the system volume is the change in the gas volume $\delta V''$. The free energy of the system is therefore not fixed but its change is given by $\delta F = -p'\delta V''$. Fortunately, this error does not lead to any error in his equilibrium relations (14)–(16) which could have been written down directly.

A more substantive error is, however, introduced subsequently into the discussion when it is stated that the vapor pressure of a liquid in a curved cavity is different from the vapor pressure of the liquid over a flat surface. They are the same, but Dr. Cha may be forgiven for this error since it is contained in some textbooks. This result for liquid vapor pressure is easily understood if one observes that the thermodynamic properties of a liquid are determined by its thermodynamic potential which is a function only of its temperature T and its pressure p. Thus, if a liquid is at T and p at a flat interface and at T and p at a curved interface, the vapor pressure is the same at both interfaces. The increased vapor pressure of a liquid drop is understood as the consequence of the increased pressure in the liquid because of surface tension rather than merely ascribed to a geometric effect of curvature.

The problem of the growth or dissolution of a gas bubble in a liquid can be given a straightforward solution in dynamic terms as was done by Epstein and Plesset in 1950. Thermal effects are essentially negligible for the isothermal processes which are of concern. One, of course, may seek to rederive Henry's law for dilute solutions of a gas in a liquid and may compute second derivatives of the free energy, but one is exposed to an algebraically more complex computation with an increased probability of a calculational error.

I would like to conclude my comments by discussing the work of reference [6] in Cha's paper. This paper by Mori, Hijikata and Nagatani on a "Fundamental Study of a Bubble Dissolution in Liquid" presents both an analytical and an experimental study of the stability of a gas bubble within a liquid drop with this system suspended in a second liquid in which the gas has quite low solubility. The drop was composed of liquid Freon-21 and the gas bubble within the drop was He, N_2, O_2, or CO_2, and the system was suspended in glycerine. The authors show with a thermodynamic analysis that the gas bubble would be stable provided it was not too small. Their analytical results were very elegantly verified by experimental observations.

This behavior is readily understood on simple physical grounds. The liquid drop of Freon-21 had a small volume with a finite and relatively small inventory of dissolved gas. At the outside boundary of the drop there was a solubility barrier of a liquid (glycerine) with essentially zero solubility for the gas. We now understand the observed stability of the bubble: Expansion of the bubble would have to draw on the limited inventory of dissolved gas in the drop and would thereby be inhibited; contraction of the bubble would increase the dissolved gas inventory, and the contraction would thereby be inhibited. Of importance here, of course, is the relationship between the two gas inventories, the one in the bubble and the second in the liquid. If either one were to be large relative to the other, this stability could not result and this is why no stability was found in their work for bubbles which were initially very small and which were found to dissolve.

As a final point, Mori, Hijikata and Nagatani also point out explicitly that there is no possibility of any stable gas bubble if the drop size becomes large. This is, of course, the physically correct result. I must add a word of praise for their elegant work although I would not have performed the stability analysis as they have done. But they have explored an interesting physical system, exposed a new behavior of gas bubbles, and succeeded in carrying forward the complicated thermodynamic calculations to a correct conclusion.

Authors' Closure

Professor Plesset raises two criticisms regarding the analysis presented in the paper. The author would like to address these criticisms separately.

The first criticism is that the derivation of the equilibrium equations contains an error even though the results are correct. First of all, we must point out that Professor Plesset is incorrect in stating that the liquid volume is fixed ($dV' = 0$) because the liquid is incompressible. The liquid volume can change as a result of mass diffusion and evaporation across the bubble interface, even though the liquid is incompressible. This is evident from equation (27) in the paper,

$$V' = n_1' v_1' + n_2' v_2'$$

The incompressible assumption requires that the specific volumes v_1' and v_2' be constants, but the liquid volume (V') can change as a result of the changes in n_1' and n_2'. Thus, we now understand that Professor Plesset is trying to place an additional constraint ($dV' = 0$) on the present analysis, and attempting to demonstrate incorrectly that there is an error in the derivation of the equilibrium equations. All we can say is that the present analysis is certainly correct within its constraints. It is proper here to point out an important difference between the present analysis and the analysis reported by Mori, et al. (reference [6] in the paper), since the constraint

---

[1] California Institute of Technology, Pasadena, Calif.

that the liquid volume is fixed ($dV' = 0$) is contained in their analysis. The present analysis employs a different constraint, i.e., the total volume of the system is constant. It would be desirable to perform a more general analysis of the system employed by Mori et al., by removing the constraint that the liquid volume is fixed. The results of this general analysis will reveal whether there are both a cavitation and a dissolution limit for a bubble in a state of stable equilibrium (as demonstrated in the present paper) for the bubble-droplet system studied experimentally by Mori, et al. Such an analysis is currently underway and will be reported elsewhere. It can be stated here that the equilibrium equation of the present paper (equation (30)) still applies. This is equivalent to saying that equation (30) also applies to the present analysis without the constraint that the total volume is fixed.

The second criticism raised by Professor Plesset is that the vapor pressure of a liquid in a curved cavity is equal to the vapor pressure of the liquid over a flat surface, and that the increased vapor pressure of a liquid drop is the result of surface tension instead of the effect of curvature. It should be pointed out that the surface tension and the radius of curvature always appear simultaneously in the expression $2\sigma/r$ regardless of the system being a drop or a bubble. Whether the effect is due to surface tension or curvature is irrelevant here; the important matter is to find out how serious is the question raised by Professor Plesset regarding the vapor pressure in affecting the results and conclusions presented in the paper. In this regard, it should be pointed out that between equations (29) and (30), we have assumed that the effects of surface tension (or curvature) and the presence of a second gas on the vapor pressure is negligible. Therefore, the criticism raised by Professor Plesset in no way affects the results and conclusions of the paper.

In summary, both criticisms raised by Professor Plesset do not affect the results and conclusions of the paper. Therefore, Professor Plesset's statement that Dr. Cha's conclusion is incorrect cannot be substantiated.

Professor Plesset also made some comments on the paper by Mori, et al., and stated that their observation of the impossibility of any stable gas bubble if the drop size (surrounding liquid) becomes large. This result is a direct consequence of the present stability analysis. Consider the case that the volume of liquid surrounding the bubble becomes very large ($n_1' \to \infty$). In order to have a finite concentration, the number of moles of solute in the liquid phase must also be infinitely large ($n_2' \to \infty$). Thus, the ratio of the total number of moles of solute to the total number of moles of solvent becomes,

$$\frac{N_2}{N_1} = \frac{n_2' + n_2''}{n_1' + n_1''} \doteq \frac{n_2'}{n_1'} \doteq x_2' = \text{finite} \qquad \text{(A)}$$

Under such conditions, it is also obvious that $N_1 \to \infty$ and $N_2 \to \infty$. The equilibrium equation (equation (26) in the paper) can be rewritten as

$$P' = p_1'' + \frac{1}{\dfrac{N_1}{N_2 K_2} + \dfrac{V''(1 - p_1''/K_2)}{N_2 RT}} - \frac{2\sigma}{r} \qquad \text{(B)}$$

Employing equation (A) and the result that $N_2 \to \infty$, equation (B) becomes

$$P' = p_1'' + K_2 x_2' - 2\sigma/r \qquad \text{(C)}$$

Equation (C) is the equilibrium equation of a bubble in an infinite sea. It is obvious that equation (C) does not depend upon the size (N_1) of the system and depends only on the intensive parameter x_2'. By employing equation (A), the stability criterion (inequality 40 in the paper) can be reduced to

$$P' > \frac{x_1' p_1'' + K_2 x_2'}{(x_1')^2 + x_2'} - \frac{4\sigma}{3r} \qquad \text{(D)}$$

For dilute solutions,

$$x_1' \doteq 1 \text{ and } x_2' << 1$$

and the inequality (D) becomes

$$P' > p_1'' + K_2 x_2' - \frac{4\sigma}{3r} \qquad \text{(E)}$$

Substituting equation (C) into the inequality (E) resulted in the right-hand side of (E) being greater than the left-hand side of (E). Thus, the equilibrium of a finite bubble in an infinite sea is always unstable.

The foregoing analysis revealed one limiting condition ($N_1 \to \infty$) of the general analysis described in the paper. As indicated in the paper, another limiting condition (the case that the gas is insoluble in the liquid, $K_2 \to \infty$) also exists. Under such circumstance, the equilibrium condition does not depend on the size of the system (N_1), but it does depend on the total amount of gas in the bubble (N_2) as indicated by equation (31) in the paper. Under this limiting condition, it can easily be shown that a bubble is always in stable equilibrium when the system pressure is greater than the vapor pressure.

Fluid Flow Through a Class of Highly-Deformable Porous Media

Part I: Experiments With Air

G. S. Beavers
Mem. ASME

A. Hajji

Department of Aerospace Engineering
and Mechanics.

E. M. Sparrow
Department of Mechanical Engineering.
Mem. ASME

University of Minnesota,
Minneapolis, Minn. 55455

This paper, together with a companion paper which follows, describes a many-faceted experimental investigation aimed at determining basic characteristics of fluid flow through deformable porous media. A major focus of the work is to establish the validity and the range of applicability of a simple analytical model for the fluid flow. The present paper describes experiments with a gas (air) as the working fluid, while the companion paper (Part II) deals with liquid-flow (i.e., water-flow) experiments. The experiments encompassed three distinct phases. In the first phase, the stress-deformation characteristics were measured (without fluid flow). In the second, flow-related material properties that are relevant to the analytical model (e.g., permeability, Forchheimer coefficient) were determined. The third phase consisted of measurements of mass flow rate as a function of applied pressure differential. The results of the first two phases were used as input to the analytical model, which yielded predictions of mass flow versus applied pressure. These predictions were shown to be in very good agreement with the experimental results, for those conditions where the model is applicable. Two unusual features of the participating deformable materials (polyurethane foams) were encountered, namely, a decrease of cross-sectional area with increasing compression and a slow relaxation of the internal stresses at a fixed compression.

1 Introduction

The study of fluid flow in rigid permeable media is an old, but still very active, research area embracing many branches of engineering and science. There are, however, a number of natural and industrial processes in which the medium through which the fluid is flowing is not rigid. For these materials the forces which are exerted by the flow can cause substantial deformations of the medium. These deformations can, in turn, have a very large effect upon the fluid flow itself if the properties of the material which govern the flow change with the deformation. The flow and deformation are then coupled, and an analysis of the problem requires the simultaneous solution of the flow and deformation equations.

The first work on the fluid flow within a deformable permeable material was probably that of Biot [1], who considered the deformation of liquid-saturated materials within the scope of infinitesimal elastic strain theory. It is only in the last decade or so, however, that a rather broad spectrum of applications of fluid flows through deformable permeable media has emerged, mainly with specific objectives in view.

In addition, analytical studies have been reported (e.g., [2-7]) which attempt to deal with more general flow-deformation situations. These analyses are usually limited to incompressible fluids, and the flow is usually assumed to be slow enough to be governed by Darcy's Law. These analyses often require a knowledge of many parameters which characterize the material and its detailed pore structure, and as such they are often difficult to test experimentally.

In an earlier paper [8] we attempted to develop a simple model to describe the one-dimensional flow through a deformable permeable material. The model was not restricted to small deformations or to flow velocities within the Darcy regime. The Darcy flow restriction was removed by the use of a Forchheimer-type relationship [9-11] to describe the pressure gradient in terms of both linear and quadratic velocity terms supplemented by a constant term which reflects the fact that a threshold pressure gradient may be required to open the pores of the material. In [8] the model was tested by means of experiments on a single sample of polyurethane foam using air as the working fluid. The agreement between the predicted and measured mass flow rates was quite good, thereby lending support to the idea that the model could be used to provide an adequate description of the flow through a deformable material.

It is clear, however, from the limited scope of the experiments of [8] that a more comprehensive and more thorough experimental investigation was necessary in order to enable a definitive appraisal of the validity and range of applicability of the model. Such an investigation should include materials of different deformation and fluid flow properties. It should also include a liquid and a gas as the working fluids since it is not unreasonable to expect that the

---

Contributed by the Fluids Engineering Division for publication in the JOURNAL OF FLUIDS ENGINEERING. Manuscript received by the Fluids Engineering Division, March 26, 1980.

nature and extent of the deformation of the material may be affected by the inter-fiber lubrication provided by the fluid. The experiments should also encompass measurements of the stress-deformation characteristics of the materials in addition to fluid flow experiments. We have attempted to provide some of the needed information by means of two complementary experimental programs involving several polyurethane foams, one utilizing air as the working fluid and the other using water. In this paper, we review the model and then present the results from the air experiments, and in a companion paper (Part II) we describe and evaluate the experiments using water.

2 Analytical Model

Rather than recount the model as set forth in [8], it will be developed here along different lines in order to better demonstrate its foundation. We are concerned here with steady, one-dimensional fluid flow through a deformable porous medium. The geometry of the flow is shown in Fig. 1. To attain one-dimensional conditions, transverse flows must not occur; the accommodation of this condition will be dealt with later when the experimental arrangement is discussed.

As indicated in the figure, the undeformed length of the porous specimen is denoted by L_0. When fluid is caused to flow by means of an applied pressure difference, and the downstream end is held fixed, the specimen is compressed to a length less than L_0. The coordinate x' is implanted in the material and moves with the specimen as it deforms, while the coordinate x is measured from a fixed origin and is undeformed. Note that x' is a Lagrangian-type coordinate in that a given material particle is endowed with an invariant value of x' regardless of the extent of the deformation.

Consider a plane which passes through the porous medium and is oriented perpendicular to the direction of fluid flow. Let A denote a typical area which lies in the plane and which is large compared with the pore size. The forces exerted on A will now be considered. If p denotes the pressure of the fluid in the pores and A_f is the pore area contained within A, then the fluid exerts a force pA_f. Next, let σ_s denote the compressive stress in the solid material such that $\sigma_s A_s$ is the force exerted on A by the solid. Here, A_s represents the area of the solids contained within A. Therefore, from the foregoing, the total force F exerted on A is

$$F=pA_f+\sigma_s A_s \tag{1}$$

Whereas the meaning of σ_s is conceptually clear, it is difficult to measure. It will, therefore, be eliminated in favor of an effective material stress σ which was measured during one of the stages of the investigation.

The measurement of σ was made in a nonflow experiment in which the porous specimen was compressed mechanically by pressing a plane surface against its free face (i.e., the left-hand face of the specimen in Fig. 1). In such an experiment, F is a constant throughout the material, and the pressure p is also a constant. The magnitude of F can thus be evaluated in terms of the force exerted by the compression plate on the porous specimen.

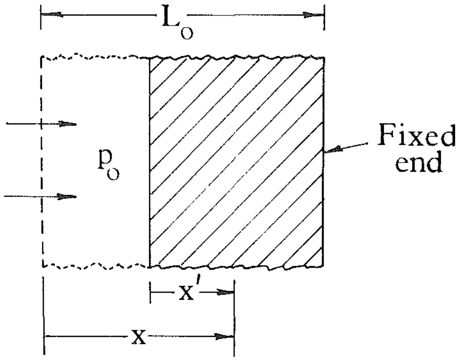

Fig. 1 Coordinates and dimensional nomenclature for the analytical model

Suppose that the compression plate is of area A which is equal to the total cross-section of the specimen. The force that it transmits to the porous specimen includes two components. One of these is the force pA due to the pressure p acting on the back face of the plate (i.e., the face away from the porous material). The other force is the externally applied force F_e which is delivered to the plate through a shaft. We define

$$\sigma=F_e/A \tag{2}$$

and note that σ is a directly measured quantity. In view of the foregoing, the force exerted by the compression plate on the porous material is $pA + \sigma A$. Thus, since F = constant throughout the material, it follows from equation (1) that

$$pA_f+\sigma_s A_s=pA+\sigma A \tag{3}$$

or

$$\sigma=(\sigma_s-p)A_s/A \tag{4}$$

Equation (4) enables σ to be interpreted physically. It is the incremental stress in the solid (over and above the pressure) referred to the total area A.

In view of the fact that σ is measured and σ_s is not, it is convenient to eliminate the latter in favor of the former. It follows at once from equations (1) and (3) that

$$F/A=\sigma+p \tag{5}$$

In the fluid flow situation, when inertia and compressibility are negligible, the equilibrium condition is that $d/dx(F/A) = 0$ or that

$$d\sigma/dx=-dp/dx \tag{6}$$

Also, at the exposed face of the specimen ($x' = 0$), $F/A = p_0$ and $p = p_0$, so that

$$\sigma=0 \text{ at } x'=0 \tag{7}$$

We now assume that the pressure gradient dp/dx can be expressed as a generalization of the Forchheimer equation [9-11]. In the cited literature, it was demonstrated that the Forchheimer equation provides a very good representation for non-Darcy flow in a wide range of porous media. There are, of course, competing approaches but, in the view of the

Nomenclature

A = total cross-sectional area
c = Forchheimer coefficient
k = permeability
$\dot{m}$ = mass flow rate
P = threshold pressure gradient
p = static pressure
p_0 = upstream pressure
Δp = pressure drop
L_f = final length
L_0 = uncompressed length
U = mean filter velocity
x = fixed-origin coordinate
x' = implanted coordinate
λ = ratio of compressed to uncompressed length
μ = viscosity
ρ = density
σ = effective normal stress in the solid

authors, they do not provide a better representation than the Forchheimer equation. The generalized Forchheimer relation to be used here is

$$-dp/dx = -P + (\mu/k)U + (c/\sqrt{k})\rho U^2 \tag{8}$$

where U is the so-called mean filter velocity. The quantities μ and ρ are, respectively, the viscosity and density of the fluid, k is the permeability of the porous material, and, for undeformable porous materials, c is a constant whose value depends on the class of porous materials under consideration.

Equation (8) differs from the usual form of the Forchheimer relationship by the addition of the term P, as well as by the dependence of k and c on the local stress. The quantity P represents a threshold pressure gradient which must be exceeded before a flow can pass through the material. It is included to account for the experimental observation that the polyurethane foams we have used require an initial small pressure gradient to open the pores sufficiently to establish a continuous flow path through the material.

With the substitution of (8) into (6), there is obtained

$$d\sigma/dx = -P + (\mu/k)U + (c/\sqrt{k})\rho U^2 \tag{9}$$

Before considering the integration of equation (9), it should be noted that the boundary condition (7) is stated in terms of the material coordinates x'. It is, therefore, appropriate to recast equation (9) into the x' coordinate system by the relation

$$\lambda = dx/dx' \tag{10}$$

where λ may be termed the compression ratio. Also, if $\dot{m}$ denotes the mass flow passing through the area A, then

$$U = \dot{m}/\rho A \tag{11}$$

If equations (10) and (11) are substituted into (9) and integration is performed between $x' = 0$ and $x' = L_0$, there is obtained

$$L_0 = \int_0^{\sigma(L_0)} \frac{d\sigma}{\lambda\left[-P + \dfrac{\mu}{k\rho A}\dot{m} + \dfrac{c}{\sqrt{k}\rho A^2}\dot{m}^2\right]}, \tag{12}$$

where the lower limit of the integral follows from equation (7). An alternate form of equation (12), which is convenient for computation, may be obtained by using the compression ratio λ as the independent variable rather than the effective stress σ. This gives

$$L_0 = \int_0^{\lambda(L_0)} \frac{\dfrac{d\sigma}{d\lambda}\, d\lambda}{\lambda\left[-P + \dfrac{\mu}{k\rho A}\dot{m} + \dfrac{c}{\sqrt{k}\rho A^2}\dot{m}^2\right]}. \tag{13}$$

The stress σ and the material parameters k, c, and P are all functions of λ, and this information can be determined from auxiliary tests on specimens of the porous material. Equation (13) is used to generate a family of curves of L_0 versus λ, parameterized by $\dot{m}$ (for a fixed cross section A and for a given fluid). The relationship between $\dot{m}$ and λ for a fixed L_0 is then obtained from these curves.

Next, it may be noted that from (6) and (10)

$$d\sigma/dx' = -dp/dx' \tag{14}$$

so that, upon integration,

$$\sigma(L_0) = \Delta p \tag{15}$$

where Δp is the pressure drop across the porous medium. Finally, the $\dot{m}$ versus λ graph is used in conjunction with the measured σ versus λ result and equation (15) to generate the relationship between $\dot{m}$ and the pressure drop Δp across the material.

The model can be tested by comparing measured and predicted values of $\dot{m}$ versus Δp. If account is taken of all the information needed to obtain the $\dot{m}$, Δp prediction, then it is seen that the experimental verification of the model involves a four-step procedure:

(i) Measure the stress σ versus compression ratio λ characteristics of the material.
(ii) Measure the dependence of k, c, and P upon λ.
(iii) Predict $\dot{m}$ versus Δp.
(iv) Measure $\dot{m}$ versus Δp.

It should be emphasized that the material properties measured here (the aforementioned steps (i) and (ii)) were purposefully limited to those needed for the implementation of the analytical model.

3 Experimental Equipment for Air Experiments

The experimental apparatus employed to test the validity of the analytical model consisted of three separate pieces of equipment. In this section, we describe each apparatus in turn and include a brief description of the polyurethane foams employed for these experiments.

(*a*) The Stress Versus Deformation Apparatus. This apparatus consisted of a square plexiglas channel, 7.62 cm on a side (internal dimension) and 47 cm long, mounted vertically on the wall of the laboratory. The piece of foam to be tested was carefully cut to size so that it could just slide freely in the channel without contacting the walls. When inserted into the channel, the specimen rested on a square platform which moved vertically within the channel without touching the channel walls. A second square plate, inserted through the upper end of the channel, was positioned so that it just contacted the top of the specimen, and it was clamped in this position so that it could not move relative to the walls.

Upward vertical motion of the platform was achieved by means of a very low speed electric motor through a rack and pinion drive. With this system, very small changes in length of the specimen could be achieved, and, in addition, the specimen could be held at a fixed compressed length indefinitely.

The stress within the material was obtained from a U-shaped strain gage dynamometer which was incorporated in the drive system just beneath the platform. The deformed length of the material was recorded using a cathetometer capable of being read to 0.05 mm.

The operating procedure was to compress the specimen extremely slowly to the desired value of the compression ratio λ, after which the force was recorded from the dynamometer. The specimen was held at this compression ratio and the force monitored over a long enough time interval for it to reach an equilibrium value. Then, the platform was advanced to the next of the desired λ values and the procedure repeated. The force measured at each compression ratio was converted to the stress σ by employing equation (2). It may also be noted that the results were not affected by the vertical orientation of the apparatus since the specimens did not deform under their own weight.

During the experiments, considerable attention was given to the stress relaxation properties of the porous materials, as will be reported shortly.

(*b*) The Flow Apparatus. The flow apparatus consisted of an open-circuit airflow system with two test sections in series. The upstream test section was used to determine the dependence of the material flow parameters k, c, and P on the compression ratio λ, while the downstream test section was used to measure the mass flow rate through a deformed specimen as a function of the applied pressure drop across the specimen. Air was delivered to the apparatus from a large compressor and storage tank system which delivers a continuous flow. Flow rates were measured by means of one of several rotameters, chosen to cover the complete range of flows encountered in the experiments. All pressures were measured using a Baratron capacitance-type pressure meter and appropriate pressure heads.

The test section for the determination of the material flow parameters was an aluminum duct of square cross section. The internal dimensions were 7.62 cm on a side, with a wall thickness of 1.10 cm. It was 1.22 m long with an available test section of 35.5 cm. The working section had a series of slots, 3.2 mm deep, machined into the bottom and side walls at various intervals. The slots were used for locating retaining screens which held the porous specimen at a fixed compressed length while flow measurements were made. When not in use, the slots were filled with precisely machined brass inserts. The upper wall of the working section of the duct was made of plexiglas and was designed so as to be readily removable in order to facilitate the installation and extraction of test specimens. Pressure taps were installed along both sides of the duct.

The technique for obtaining the λ-dependence of k, c, and P consisted of compressing the specimen manually to a chosen value of λ and then inserting it in the test section between two restraining screens set in the appropriate slots. Pressure distributions along the specimens were recorded for each of several mass flow rates. The flow rates were always chosen small enough so that no compression of the specimen occurred as a result of the applied pressure gradient.

The test section for the measurement of $\dot{m}$ versus Δp was of similar construction to the other test section, except that there were no slots in the duct wall for multiple screens. Rather, this test section was fitted with a single retaining screen at the downstream end to prevent motion of the specimen there. The removable portion of the upper wall was made of teflon-coated aluminum, with a narrow plexiglas viewing slot along the centerline. Furthermore, in the experiments utilizing this test section, the flow rates were chosen so that the material deformed under the influence of the applied pressure difference.

With regard to the just-mentioned experiments on flow-induced deformation, certain factors relating to the design of the apparatus are worthy of discussion. To avoid unwanted transverse velocities which would result if air were to pass through the lateral faces of the specimen, it is necessary that the specimen be situated in a duct during the experiments. Correspondingly, consideration was given to means of minimizing possible friction between the lateral faces of the specimen and and the duct walls. As a primary preventative measure, all walls of the duct were permanently coated with teflon. Second, each specimen was cut so that, in the undeformed state, it would glide freely along the teflon-coated walls. Since, as will be demonstrated shortly, the cross section of the specimen actually contracts during deformation, the deformed specimen should experience even less frictional resistance than the undeformed specimen. Finally, the cross-sectional dimensions were made as large as possible to increase the ratio of cross-sectional area to perimeter. It is believed that these measures were sufficient to eliminate wall friction as an important effect.

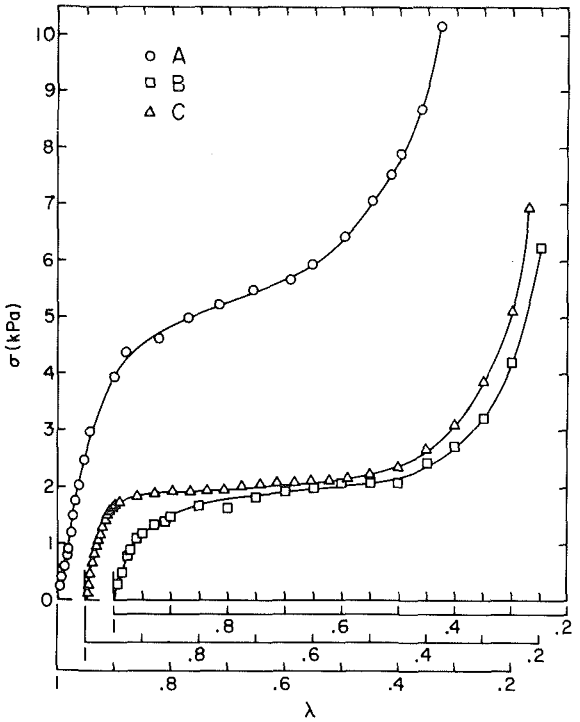

Fig. 2 Stress-deformation characteristics of the deformable porous media (uncertainty of ordinate variable ± 2 percent; uncertainty of abscissa variable ± 0.5 percent)

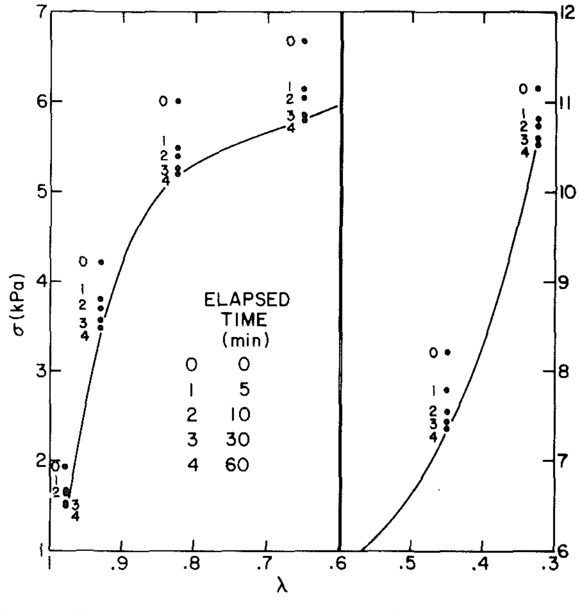

Fig. 3 Illustration of stress relaxation with time, type A material (uncertainty of ordinate variable ± 2 percent; uncertainty of abscissa variable ± 0.5 percent)

(*c*) **The Permeable Materials.** Samples of three different types of polyurethane foam, manufactured by the Scott Paper Company, were chosen for these experiments. All three types were highly compressible, with bulk densities as follows: type A, 70.5 kg/m^3; type B, 25.9 kg/m^3; type C, 27.8 kg/m^3. These particular materials were chosen because they appeared to be significantly different in structural form, and it was expected that they would possess appreciable differences in material and flow characteristics, thus providing a much broader test of the analytical model than the experiments on a single material reported in [8]. Two specimens of each type were employed, one 25.7 cm long and the other 12.0 cm long. All specimens had a cross-sectional area of 7.62 cm × 7.62 cm.

4 Material Properties and Flow Parameters

(*a*) **Stress Versus Deformation.** The first step in the experimental program was the determination of the stress versus compression ratio characteristics of the permeable materials. This was accomplished using the larger of each pair of samples, and the final results are shown in Fig. 2. Along the abscissa, decreasing values of λ correspond to increasing amounts of compression, with $\lambda = 1$ representing the initial, uncompressed state of the specimen. All samples of polyurethane foam that were investigated exhibited the same general characteristics, namely, a very rapid increase in stress during the first ten percent of compression, followed by a much less rapid increase as the material is compressed further (for some foams, the increase in this region is barely measurable), and finally another rather rapid increase.

The procedure for obtaining the data of Fig. 2 was very time-consuming because of the stress relaxation properties of the materials. After each change in compressed length of the specimen, the internal stress as indicated on the strain gage dynamometer would undergo a slow relaxation which could continue over a long time period. This is illustrated for a sample of type A material in Fig. 3, where we have shown the measured stresses at several fixed compression ratios for the first hour of relaxation, with the left and right-hand panels of the figure respectively conveying results for small and large compressions. The figure shows that at any fixed λ, the stress relaxation is most rapid at early times and becomes slower as time proceeds. We have found that we were able to detect stress relaxations for some materials at the high compressions up to 48 hours after the application of the compression.

This stress relaxation effect raises the question as to what is the appropriate steady-state value to be used in the predictive calculations for the mass flow rate. In our measurements of σ versus λ, we attempted to take account of the relaxation effect by allowing the material specimens to relax for two hours, because by this time the material had undergone at least 80 percent (and usually much more) of its total relaxation at that compressed length. It is worth noting that we have not been able to fit a simple empirical expression relating the stress to the relaxation time; among others, an exponential did not fit the data.

(*b*) **Flow Parameters.** The procedure used here for the determination of k, c, and P as functions of λ was basically the same as that used in our earlier experiments [8]. The specimens were compressed to a chosen λ value and held at this compression between two screens in the test section. Very small pressure differences were applied across the material to avoid further compression. For each applied pressure gradient, the flow rate was measured, from which the mean filter velocity U could be determined.

The data were then used with equation (8) to yield a value of $P(\lambda)$ by means of a second-order least-squares technique. The value of $P(\lambda)$ thus obtained was then used with equation(8) rewritten in the form

$$-\frac{1}{\mu U}\left(\frac{dp}{dx} - P\right) = \frac{1}{k} + \frac{c}{\sqrt{k}}\,\frac{\rho U}{\mu} \qquad (16)$$

to yield values of $1/k$ and $c/\sqrt{k}$, both functions of λ, from a first-order least-squares fit. Typical results obtained from these two computational procedures are illustrated in Fig. 4 for different λ values for the type A material. The second-order least-squares fit is compared with the experimental data points in a plot of

$$-\frac{1}{\mu U}\left(\frac{dp}{dx}\right)$$

against $\rho U/\mu$ (right-hand ordinate), and the final linear least-squares fit is shown in a plot

$$-\frac{1}{\mu U}\left(\frac{dp}{dx} - P\right)$$

against $\rho U/\mu$ (left-hand ordinate).

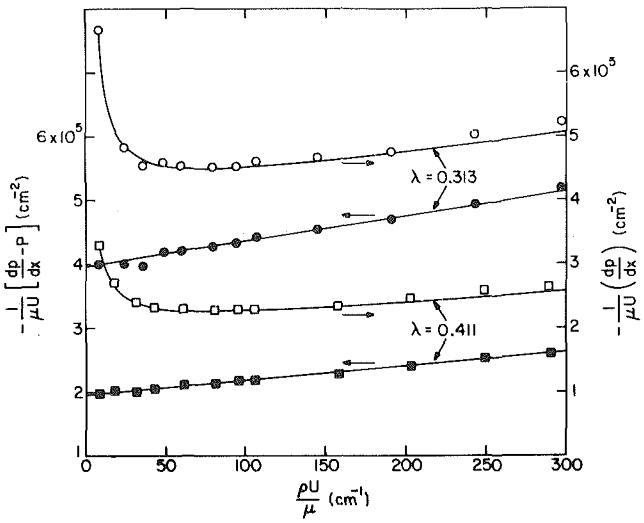

Fig. 4 Illustrative data and curve fits for the flow-parameter experiments, type A material (uncertainty of ordinate variable ± 5 percent; uncertainty of abscissa variable ± 2 percent)

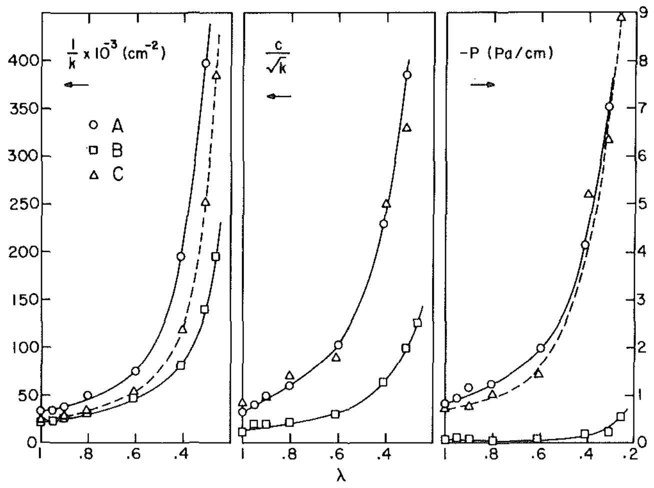

Fig. 5 Experimentally determined flow parameters of the deformable porous media (uncertainty of ordinate variable ± 5 percent; uncertainty of abscissa variable ± 0.5)

The values of P, $1/k$ and $c/\sqrt{k}$ are shown in Fig. 5 as functions of λ for each of the three types of foam.

Finally, we remark on a property of the polyurethane foams which caused an accommodatable difficulty in this phase of the experiments. This is the tendency of the cross-sectional area to decrease as the material is compressed. This property is illustrated in Fig. 6 which shows a specimen of type C material viewed from above with the top of the test section removed. In the upper photograph of Fig. 6, the material is in the undeformed state and just fits into the duct. The reduction in cross section as the material is held at two different compressed lengths is very evident in the middle and lower photographs.

We were able to compensate for the area change in this phase of the experiments by the insertion of suitable shims between the material and the test section walls, because the compression is applied externally. However, in the next phase of the experiments, where the material deforms under the influence of the pressure gradient, the reduction in cross-sectional area ultimately limits the range of applied pressure gradients over which valid mass flow measurements can be made.

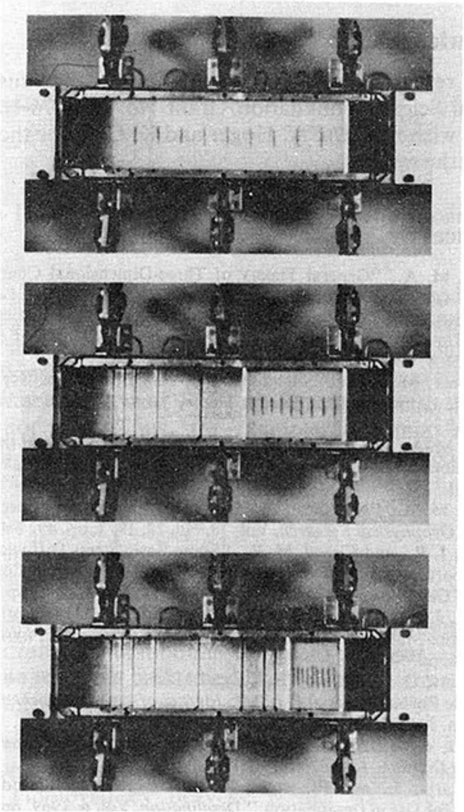

Fig. 6 Photographs documenting the decrease of cross-sectional area with increasing compression

5 Flow Results

The integration of equation (13) was carried out using the data shown in Figs. 2 and 5 for various preselected values of the mass flow rate $\dot{m}$. The resulting solutions for L_0 as a function of λ for the type A and type B materials are shown in Figs. 7 and 8, respectively. The graphs for the type C material are very similar to those shown in Fig. 8. Cross-plotting at values of L_0 of 25.7 cm and 12.0 cm, and using the data of Fig. 2, yields the mass flow rate as a function of applied pressure difference.

The predicted values are compared with experimentally measured values in Fig. 9. There is excellent agreement between measured and predicted values at the lower values of the applied pressure difference, but as the value of Δp increases the experimentally measured mass flow rates tend to exceed the predicted values. The deviations between measured and predicted values first appear at the point where the porous material begins to exhibit a reduction in cross-sectional area, with a resultant separation from at least one wall of the test section duct. This creates an alternative flow path for the fluid (i.e., a leakage path) where the resistance is much less than through the material, so that a larger total flow is measured than would occur through the material alone.

A second test of the model can be carried out by comparing the measured final compressed length of the porous specimen for various applied pressure differences with corresponding predicted lengths. The predicted final length is given by

$$L_f=\int_0^{\lambda(L_f)} \frac{\dfrac{d\sigma}{d\lambda}\,d\lambda}{\left[-P+\dfrac{\mu}{k\rho A}\dot{m}+\dfrac{c}{\sqrt{k}\rho A^2}\dot{m}^2\right]} \qquad (17)$$

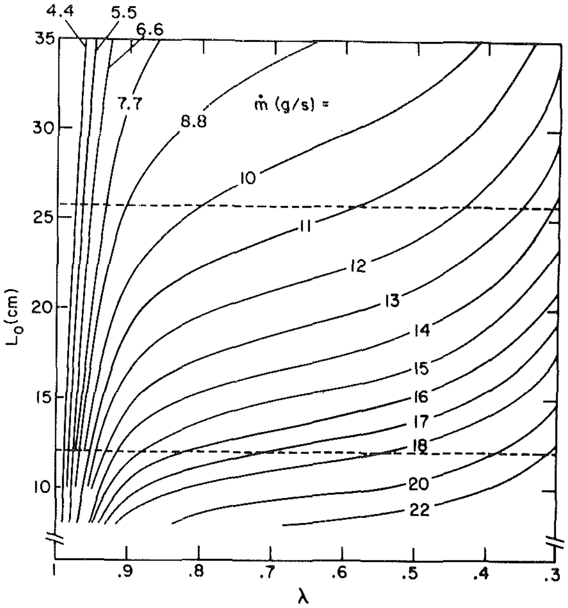

Fig. 7 Relationship between L_0 and λ, type A material

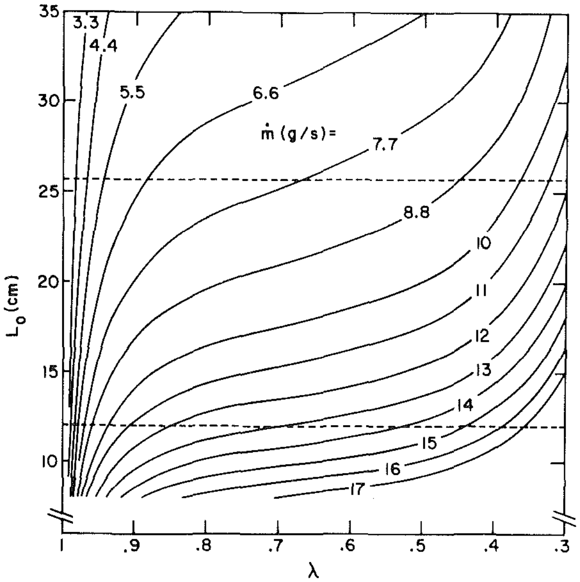

Fig. 8 Relationship between L_0 and λ, type B material

which can then be plotted in the form L_f versus Δp for any given $\dot{m}$, as illustrated in Fig. 10 for the type A material.

The predicted variations of L_f with Δp for the two specimens of type A material used in these experiments are traced out on Fig. 10 and are compared with experimental measurements. The measurement of L_f was subject to some inaccuracy because it had to be performed through a very narrow viewing slit, which often made it difficult to locate the front edge of the material. We only attempted these measurements on the type A material. The discrepancy between the measured and predicted lengths in Fig. 10 is consistent with the material separating from one of the walls, thus allowing flow to pass along the side of the material, with a consequent smaller compression of the material (i.e., a larger L_f).

6 Concluding Remarks

In this paper, we have attempted to present definitive ex-

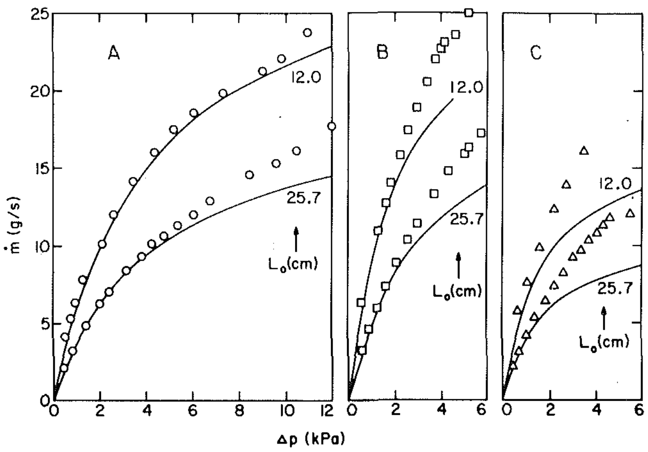

Fig. 9 Comparison between experimental and predicted results for mass flow rate versus applied pressure difference (uncertainty of ordinate variable ± 1 percent; uncertainty of abscissa variable ± 1 percent)

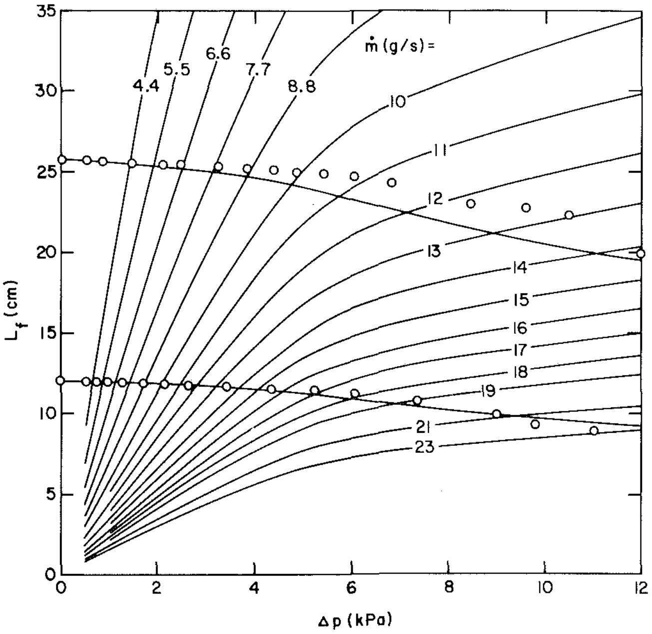

Fig. 10 Relationship between L_f and Δp, type A material (uncertainty of ordinate variable ± 5 percent at the higher Δp values; uncertainty of abscissa variable ± 1 percent)

perimental evidence to support an earlier analytical model [8] for the prediction of one-dimensional flow through a highly-deformable porous material. The experiments presented here represent a painstaking attempt to eliminate all major sources of experimental uncertainty. We believe that the present experiments with air give strong support to the validity of the analytical model.

We are convinced that wall friction played a very minor role in the present experiments, and that the principal cause of discrepancy between the predictions of the model and the measured values is the property of the polyurethane foams to undergo a reduction in cross-secitonal area as the compressed length is decreased. In addition to the aforementioned cross-sectional contraction, another pathological characteristic of the foam materials, encountered during the experiments, is the tendency for the internal stresses to relax slowly when the material is held at a fixed compression. Besides adding very substantially to the difficulty and duration of experiments, this characteristic augers ill for the quest for a universally applicable model for flow through deformable porous media.

Acknowledgments

This research was performed under the auspices of National Science Foundation Grant No. ENG76-16422. The authors wish to thank A. Hoger and K. Cole for their help in parts of the work.

References

1 Biot, M. A., "General Theory of Three-Dimensional Consolidation," *Journal of Applied Physics*, Vol. 12, 1941, pp. 155–164.

2 Crochet, M. J., and Naghdi, P. M., "On Constitutive Equations for Flow of Fluid Through an Elastic Solid," *International Journal of Engineering Science*, Vol. 4, 1966, pp. 383–401.

3 Crochet, M. J., and Naghdi, P. M., "Small Motions Superposed on Large Static Deformations in Porous Media," *Acta Mechanica*, Vol. 4, 1967, pp. 315–335.

4 Biot, M. A., and Willis, D. G., "The Elastic Coefficients of the Theory of Consolidation," ASME *Journal of Applied Mechanics*, Vol. 79, No. 4, 1957, pp. 594–601.

5 Biot, M. A., "Nonlinear and Semilinear Rheology of Porous Solids," *Journal of Geophysical Research*, Vol. 78, No. 23, 1973, pp. 4924–4937.

6 Rice, J. R., and Cleary, M. P., "Some Basic Stress Diffusion Solutions for Fluid-Saturated Elastic Porous Media With Compressible Constituents," *Reviews of Geophysics and Space Physics*, Vol. 14, No. 2, 1976, pp. 227–241.

7 Watt, J. P., Davies, G. F., and O'Connell, R. J., "The Elastic Properties of Composite Materials," *Review of Geophysics and Space Physics*, Vol. 14, No. 4, 1976, pp. 541–563.

8 Beavers, G. S., Wilson, T. A., and Masha, B. A., "FLow Through A Deformable Porous Material," ASME *Journal of Applied Mechanics*, Vol. 97, Vol. 42, No. 3, 1975, pp. 598–602.

9 Ward, J. C., "Turbulent Flow in Porous Media," *Journal of the Hydraulics Division*, ASCE, Vol. 90, 1964, pp. 1–12.

10 Schwartz, J., and Probstein, R. F., "Experimental Study of Slurry Separators for Use in Desalination," *Desalination*, Vol. 6, 1969, pp. 239–266.

11 Beavers, G. S., and Sparrow, E. M., "Non-Darcy Flow Through Fibrous Porous Media," *Journal of Applied Mechanics*, Vol. 91, No. 4, Vol. 36, 1969, pp. 711–714.

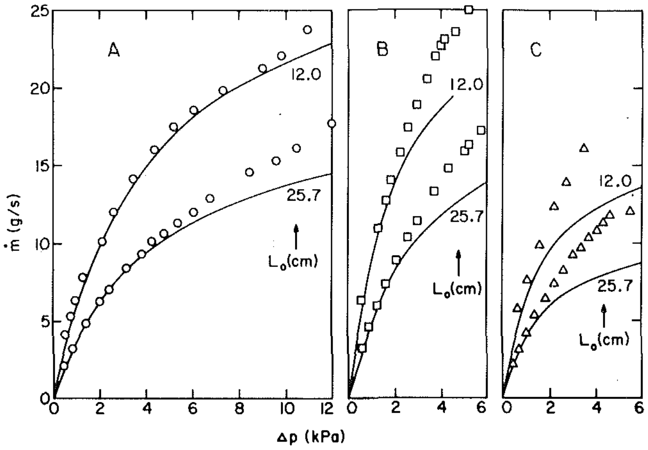

Fig. 9 **Comparison between experimental and predicted results for mass flow rate versus applied pressure difference (uncertainty of ordinate variable ± 1 percent; uncertainty of abscissa variable ± 1 percent)**

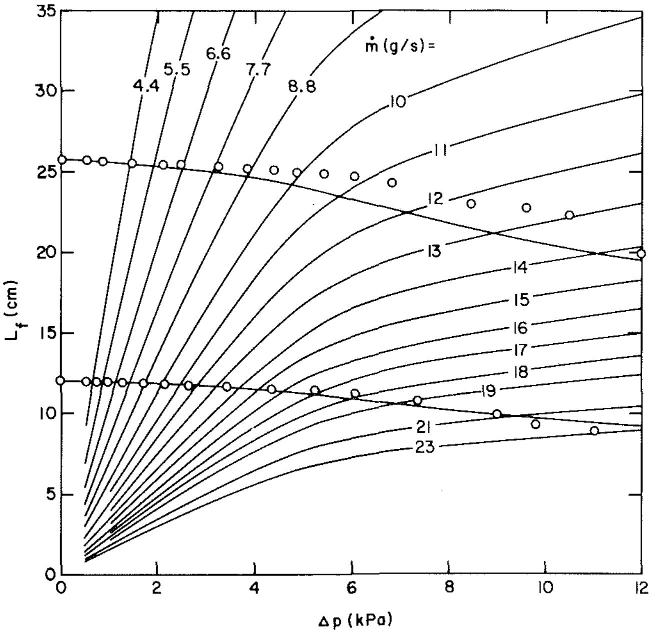

Fig. 10 **Relationship between L_f and Δp, type A material (uncertainty of ordinate variable ± 5 percent at the higher Δp values; uncertainty of abscissa variable ± 1 percent)**

perimental evidence to support an earlier analytical model [8] for the prediction of one-dimensional flow through a highly-deformable porous material. The experiments presented here represent a painstaking attempt to eliminate all major sources of experimental uncertainty. We believe that the present experiments with air give strong support to the validity of the analytical model.

We are convinced that wall friction played a very minor role in the present experiments, and that the principal cause of discrepancy between the predictions of the model and the measured values is the property of the polyurethane foams to undergo a reduction in cross-secitonal area as the compressed length is decreased. In addition to the aforementioned cross-sectional contraction, another pathological characteristic of the foam materials, encountered during the experiments, is the tendency for the internal stresses to relax slowly when the material is held at a fixed compression. Besides adding very substantially to the difficulty and duration of experiments, this characteristic augers ill for the quest for a universally applicable model for flow through deformable porous media.

Acknowledgments

This research was performed under the auspices of National Science Foundation Grant No. ENG76-16422. The authors wish to thank A. Hoger and K. Cole for their help in parts of the work.

References

1 Biot, M. A., "General Theory of Three-Dimensional Consolidation," *Journal of Applied Physics*, Vol. 12, 1941, pp. 155-164.

2 Crochet, M. J., and Naghdi, P. M., "On Constitutive Equations for Flow of Fluid Through an Elastic Solid," *International Journal of Engineering Science*, Vol. 4, 1966, pp. 383-401.

3 Crochet, M. J., and Naghdi, P. M., "Small Motions Superposed on Large Static Deformations in Porous Media," *Acta Mechanica*, Vol. 4, 1967, pp. 315-335.

4 Biot, M. A., and Willis, D. G., "The Elastic Coefficients of the Theory of Consolidation," ASME *Journal of Applied Mechanics*, Vol. 79, No. 4, 1957, pp. 594-601.

5 Biot, M. A., "Nonlinear and Semilinear Rheology of Porous Solids," *Journal of Geophysical Research*, Vol. 78, No. 23, 1973, pp. 4924-4937.

6 Rice, J. R., and Cleary, M. P., "Some Basic Stress Diffusion Solutions for Fluid-Saturated Elastic Porous Media With Compressible Constituents," *Reviews of Geophysics and Space Physics*, Vol. 14, No. 2, 1976, pp. 227-241.

7 Watt, J. P., Davies, G. F., and O'Connell, R. J., "The Elastic Properties of Composite Materials," *Review of Geophysics and Space Physics*, Vol. 14, No. 4, 1976, pp. 541-563.

8 Beavers, G. S., Wilson, T. A., and Masha, B. A., "FLow Through A Deformable Porous Material," ASME *Journal of Applied Mechanics*, Vol. 97, Vol. 42, No. 3, 1975, pp. 598-602.

9 Ward, J. C., "Turbulent Flow in Porous Media," *Journal of the Hydraulics Division*, ASCE, Vol. 90, 1964, pp. 1-12.

10 Schwartz, J., and Probstein, R. F., "Experimental Study of Slurry Separators for Use in Desalination," *Desalination*, Vol. 6, 1969, pp. 239-266.

11 Beavers, G. S., and Sparrow, E. M., "Non-Darcy Flow Through Fibrous Porous Media," *Journal of Applied Mechanics*, Vol. 91, No. 4, Vol. 36, 1969, pp. 711-714.

DISCUSSION

S. K. Garg[1]

The authors of this two part paper deserve to be congratulated for providing new data on fluid flow through highly deformable porous materials. The following comments should not be construed to detract from the significance of this interesting and important paper.

The analytical model developed in this paper can be simplified and improved by utilizing the existing concepts in soil/rock mechanics literature. Figure 11 shows the schematic of a non-flow experimental set up. The force F—applied to the compression plate—must be exactly balanced by the pressure p_0 in the fluid layer and also by the total stress τ in the fluid-saturated porous material. Thus

$$F = p_0 A = \tau A \tag{1}$$

Note that F (and not F_e as implied by Beavers, et al.) is the externally applied force which is delivered to the plate through a shaft. The stress-equilibrium condition for the fluid-saturated porous material is (see e.g., [1]):

$$\partial\tau/\partial x = 0; \quad \tau = p_0 \text{ at } x' = 0 \tag{2}$$

Introducing the Terzaghi-Hubbert-Rubey [2, 3] "effective stress σ"

$$\sigma = \tau - p \tag{3}$$

Equation (2) can be rewritten as:

$$\frac{\partial\sigma}{\partial x} = -\frac{\partial p}{\partial x}; \quad \sigma = 0,\ p = p_0 \text{ at } x' = 0 \tag{4}$$

---

[1] Systems, Science and Software, La Jolla, Calif. 92038.

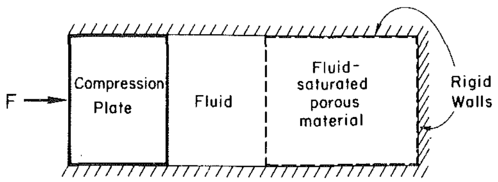

Fig. 11 Schematic of a nonflow compression experiment

Although the above definition for effective stress σ is identical with that given by Beavers, et al. I would like to emphasize that σ is a derived (i.e., not directly measurable) quantity.

In deriving their equation (13), Part I, Beavers, et al. assume that σ, k, c, and P are all functions of λ; this is, in general, not true. Thus, for example, for uniaxial strain conditions and assuming that the fluid-saturated porous material exhibits a linear elastic response, we have [1, 4, 5]:

$$1-\lambda=C_m\left(\sigma+\frac{K}{K_s}p\right), \tag{5}$$

where

C_m = drained uniaxial compressibility of porous material
K = drained bulk modulus of porous material, and
K_s = unjacketed bulk modulus of porous material (= intrinsic bulk modulus)

Equation (5) implies that $\lambda \equiv \lambda(\sigma)$ if and only if $K << K_s$. Although the inequality $K << K_s$ should hold for the materials employed by Beavers, et al., we note that this inequality may not be satisfied for other porous materials (e.g., rocks). Finite-deformation response of fluid-saturated porous materials is considered in [6] and [7].

Finally, I would like to raise a query in regard to the experimental procedure employed to compute the flow parameters k, c, and P. In their description of the experimental set up, Beavers, et al. state that very small pressure differences were applied across the material to avoid further compression. Utilizing $\rho = 0.001205$ gm/cm^3 and $\mu = 183 \times 10^{-6}$ poise (typical values for air at room conditions), and the data of Fig. 4 (Part I), we have at maximum flow rates:

$$\frac{\partial p}{\partial x} \approx (0.2-0.4)\text{kPa/cm, or } \Delta p \approx (5-10)\text{kPa}$$

The above pressure difference is comparable to values of σ for which significant compression of porous materials was observed. The authors' comments on this part of the experiments would, therefore, be most illuminating to the readers.

Additional References

1 Biot, M. A., and Willis, D. G., "The Elastic Coefficients of the Theory of Consolidation," ASME *Journal of Applied Mechanics*, Vol. 24, 1957, p. 594.

2 Terzaghi, K., "Die Berechnung der Durchlassigkeitsziffer des Tones aus dem Verlauf der Hydrodynamischen Spannungerscheinungen," Sitzungsber. Akad. Wiss. Wien, Vol. 132, 1923, p. 125.

3 Hubbert, M. K., and Rubey, W. W., "Role of Fluid Pressure in Mechanics of Overthurst Faulting," *Bulletin Geological Society of America*, Vol. 70, 1959, p. 115.

4 Nur, A., and Byerlee, J. D., "An Exact Effective Stress Law for Elastic Deformation of Rock with Fluids," *Journal of Geophysical Research*, Vol. 76, 1971, p. 6414.

5 Garg, S. K., and Nur, A., "Effective Stress Laws for Fluid-Saturated Porous Rocks," *Journal of Geophysical Research*, Vol. 78, 1973, p. 5911.

6 Garg, S. K., Brownell, D. H., Jr., Pritchett, J. W., and Herrmann, R. G., "Shock-Wave Propagation in Fluid-Saturated Porous Media," *Journal of Applied Physics*, Vol. 46, 1975, p. 702.

7 Carroll, M. M., "Mechanical Response of Fluid-Saturated Porous Materials," in *Theoretical and Applied Mechanics: Postprints ICTAM Toronto 15th International Congress of Theoretical and Applied Mechanics*, (Edited by F. P. J. Rimrott and B. Tabarrok), p. 251, North-Holland, Amsterdam, 1980.

Authors' Closure

We appreciate Dr. Garg's interest in our work. It is gratifying to note that his derivation corroborates that given in the paper. We continue to prefer that of the paper because it relates to the physical system being studied.

Dr. Garg is correct in noting that the maximum pressure differences applied across the material during the determination of k, c, and P approach the values for which significant compression of the porous material would occur if the material were originally in the uncompressed state and free to deform. However, in the measurement of those parameters, the material specimens are first compressed mechanically to a given compression ratio and then held at that compression ratio by screens fixed in place in the channel. Further deformation of the material does not take place until the applied pressure difference exceeds that required to compress the material naturally to the same compression ratio.

G. S. Beavers
Mem. ASME

K. Wittenberg

Department of Aerospace
Engineering and Mechanics.

E. M. Sparrow
Department of Mechanical Engineering.
Mem. ASME

University of Minnesota,
Minneapolis, Minn. 55455

Fluid Flow Through a Class of Highly-Deformable Porous Media Part II: Experiments With Water

Experiments were performed to explore the relationships between liquid-saturated and gas-saturated deformable porous media. Water and air served as the participating fluids. From quasi-static compression experiments (no fluid flow), it was found that the force required to compress a given deformable porous material is substantially less when the material is water-saturated than when it is in air. Water flow measurements yielded flow rate—pressure drop results which are compared with analytical predictions. The predictions were based on input values of certain material flow parameters which had been determined in previous air flow experiments. The observed level of agreement between the predictions and the water flow measurements lends support to the notion that the flow parameters are independent of the participating fluid. In the course of establishing the effects of the participating fluid, the stress relaxation and aging phenomena were quantified. The former is a relaxation of the internal stress in a deformable material which occurs after a compression is imposed and maintained. The latter is a process whereby the deformation characteristics change when the material is subjected to a succession of compressions.

1 Introduction

This paper is the second of a pair of papers aimed at providing experimental evidence to establish the validity and the range of applicability of a simple analytical model [1] to describe the flow of a fluid through a highly-deformable porous material. In Part I [2], we formulated the problem, redeveloped the model on a firmer foundation, and presented experimental data from a series of experiments involving the flow of gas (air) through several polyurethane foams. The present paper deals with another aspect of the experimental program. We report here the results of experiments intended to investigate the influence of fluid properties on the flow-deformation characteristics of deformable porous media. In particular, we will explore the issue of whether the analytical model of [1] can be used with input values of the material flow parameters obtained from experiments using one fluid (e.g., air) to predict the mass flow rate as a function of overall pressure difference for a different fluid (water).

In presenting the results of our experiments with water, we will not repeat any of the discussion of the analytical model which was set forth in detail in Part I [2]. We will simply refer to the appropriate equations given in Part I as they are required here in the presentation of the experimental data. Furthermore, since the same symbols will be used, the Nomenclature listing of Part I also pertains here. We also present in this paper some interesting results that have evolved from studies of the deformation characteristics of the samples of polyurethane foams that were employed in the water and air experiments.

2 Experimental Equipment for Water Experiments

Three pieces of apparatus were employed during the course of the experiments. These were: (*a*) an apparatus to measure the stress versus compression ratio characteristics in water; (*b*) a setup to remove the air from a porous specimen and to saturate it completely with water; and (*c*) a flow system capable of yielding accurate measurements of the dependence of mass flow rate upon applied pressure gradient. The principal features of each apparatus will be described here. Complete details of the equipment can be found in [3].

(*a*) The Compression Equipment. The compression testing equipment is illustrated in Fig. 1. It was designed to apply small changes in compressed length to a rectangular sample of material held horizontally between two vertical flat plates. One plate was held fixed (i.e., the left-hand plate in Fig. 1) while the other one was advanced by means of a precisely machined, calibrated screw drive. Changes in length of the specimen as small as 0.0254 mm could be applied and maintained with this system.

The force within the porous specimen was measured by means of two force gages, one installed at the movable plate and the other at the fixed plate. The use of two force gages provides a redundant check on all force measurements. The gage at the movable end consisted of an inverted U-shaped device (see figure) which rested in two needle points between the plate and the screw drive. Between the vertical legs of the

---

Contributed by the Fluids Engineering Division for publication in the JOURNAL OF FLUIDS ENGINEERING. Manuscript received by the Fluids Engineering Division, March 26, 1980.

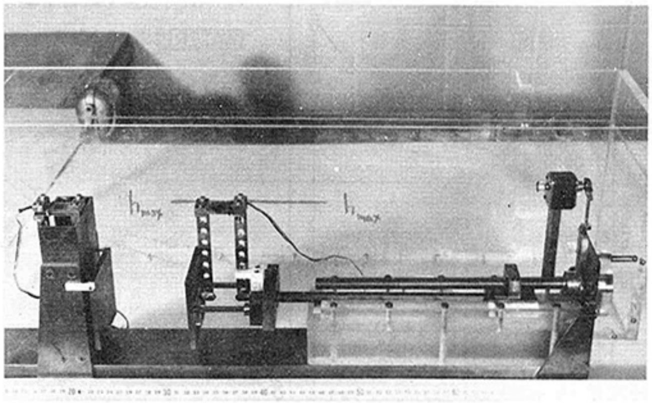

Fig. 1 Apparatus for measurement of stress as a function of compression

gage was a brass flex-plate to which a strain gage was attached, and the legs were made long enough to ensure that the flex-plate and strain gage were above water level for all tests carried out with specimens held under water. The force gage at the stationary end consisted of a very stiff vertical cantilever beam supported at its upper end, with the stationary plate bearing on the lower end through a stainless steel shaft passing through a fixed ball bushing. This measurement arrangement was designed so that its strain gage would always be above water level. The entire system provided a very effective means for measuring small changes in both length and average stress within the material.

(*b*) The Evacuation-Saturation Equipment. One of the major problems encountered in experiments involving the flow of liquids through porous media is the uncertainty about whether the material is fully saturated. The small-pore polyurethane foams used for this study were particularly difficult to saturate by simple submersion especially since squeezing of the material was deemed inadvisable. A saturation procedure using a vacuum technique was ultimately employed.

The porous specimen was placed in a large vacuum bell jar, which was oriented with the open end upwards and which was about two thirds full of water. The specimen was held under water by means of a wire-screen restraining cage, and the bell jar was sealed at the open end by means of a heavy metal plate. The air from the bell jar was then evacuated using a conventional mechanical vacuum pump, which was allowed to run for about thirty minutes. After this, air was allowed to bubble out of the material for about thirty minutes, and then the pumping was restarted for another thirty minute period. This cycle was repeated several times, after which the material was allowed to sit for several hours with no further air bubbles being expelled from the material. At this stage, it was assumed that the material was fully saturated, and it showed no tendency to float if released from its restraining cage. Air was then reintroduced into the bell jar, with the porous material maintained under water. The material was then removed from the bell jar and installed in the test apparatus using a simple transfer device which kept the material completely submerged in water at all times.

With a view to evaluating the effectiveness of the vacuum saturation procedure, a calculation was undertaken to estimate the amount of air, if any, that remained in the porous medium at the moment of sinking. This calculation was hampered by the lack of precise data for the intrinsic density of the foam material. On the basis of an estimate of 1.034 for the intrinsic specific gravity and for a porosity of 0.97, the upper limit for the volume occupied by residual air is 0.1 percent of the total volume. It is expected that the actual volume percentages were lower than this estimate.

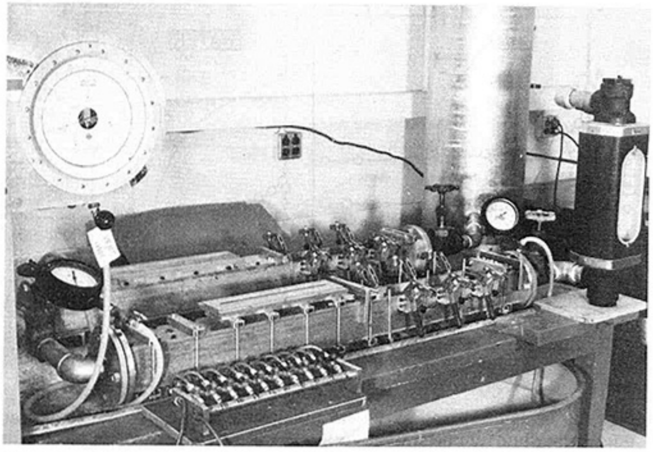

Fig. 2 Apparatus for the fluid flow experiments

(*c*) The Flow Apparatus. The principal features of the flow system are shown in Fig. 2. As seen there, the system is a once-through loop, with the discharge being discarded in a drain. In view of the high rates of throughflow, the use of treated water was not feasible. Water from the city mains was fed into a pressurized settling tank from where it was admitted through a valving system into a filter section. This section consisted of a square duct which housed a scavenger porous specimen whose function was to remove any air bubbles and particulate materials that might have been present in the water. The porous specimens used as scavengers were selected to have the smallest pores among all the materials available. As an indication of their effectiveness, it may be noted that no air bubbles were ever observed downstream of the filter section. After this, the water entered the test section containing the test specimen of porous material. This test section was the same as that used in the corresponding air experiments described in Part I [2]. A specially calibrated Fischer and Porter Series 700 Flowrator was situated just downstream of the test section for mass flow rate measurements, and the water exhausted from the flowmeter to the room drain.

For the pressure measurements, the odd-numbered taps along one side of the test section were connected to a manifold, and the even-numbered taps were connected to another manifold. Each connection was made through a toggle valve so that the pressure in the manifold could be selected to be that at any one of the tap locations feeding the manifold. The output of each manifold was connected to the bottom of one of the legs of a standard compresed-air-over-water manometer system. With this arrangement, the pressure difference between neighboring pressure tap locations (or between any pair of even and odd numbered locations) could be determined.

(*d*) The Porous Media. The materials used for these experiments consisted of new samples of three different members of a family of ester-type polyurethane foams manufactured by the Scott Paper Company. The structure of the material is a latticework of polyurethane fibers with no free fiber ends interior to the material. The three types had nominal pore distributions of 30, 55, and 100 ppi (pores per linear in.), with corresponding bulk densities of 33.1, 26.9, and 26.8 kg/m^3. The void fraction is given as 0.97 for each type of material, which we verified by a water displacement experiment. With regard to the aforementioned variation of bulk density, it is consistent with void fraction differences such as 0.967–0.973 for a fixed intrinsic density of the solid. Alternatively, there may have been variations in intrinsic

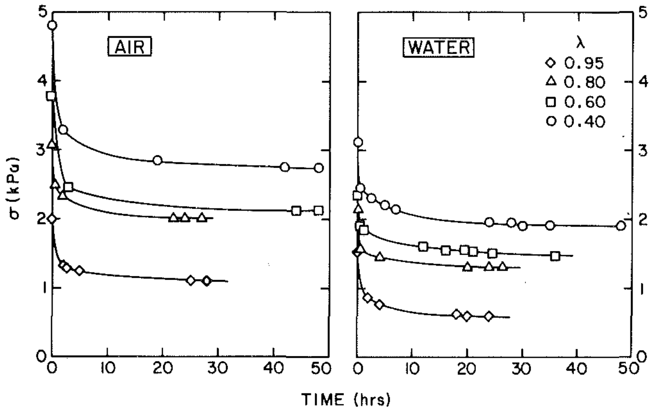

Fig. 3 Stress relaxation in an air-saturated and water-saturated porous medium (uncertainty of ordinate variable ± 2 percent)

density. All the specimens used in the present experiments had cross sections of 7.62 by 7.62 cm, with lengths of either 10.2 or 25.4 cm. The technical literature on these materials states that the tensile strength of the material was found to be unaffected by submersion in tap water for one year at room temperature.

3 Some Properties of the Porous Materials

The experiments with polyurethane foams in air (Part I, [2]) revealed that the stress within the material relaxes after the material is compressed to any value of the compression ratio and held at that compression. Thus, the first objective of the present compression experiments was to examine the relaxation properties of the materials with a view to determining a suitable relaxation time at which stress-compression data could be recorded in subsequent parts of the experimental program.

To accomplish this, two identical new samples of 100 ppi material were compressed using the equipment of Fig. 1, one in air and the other in water. The specimens were compressed slowly to a preselected value of the compression ratio λ and held at that compression until the force recorded on the strain gage dynamometers ceased to change. Four values of λ were chosen, namely, 0.95, 0.80, 0.60, and 0.40. The results from these relaxation tests are presented in Fig. 3, where the stress σ is the recorded axial compressive force divided by the total cross-sectional area of the specimen. The compression ratio λ is the compressed length of the specimen divided by its original length.

The stress relaxation in both air and water can continue for tens of hours, with the relaxation time increasing for smaller values of λ (i.e., for higher compressions). For example, at a λ value of 0.4 the material exhibited a stress relaxation for over 40 hr.

There are several other interesting observations to be made from Fig. 3. First, the magnitude of the force required to compress the material to a given λ is smaller in water than in air. In particular, the final (i.e., fully relaxed) value in water is approximately two thirds of the final value in air. We have observed this characteristic of a reduction in the compressive force when a specimen is completely saturated and submerged in water for all the polyurethane foams that we have used in our experiments. Although the mechanism underlying this behavior cannot be identified with certainty, it is believed that the liquid (i.e., water) tends to lubricate the deforming solid and thereby diminishes the resistance to deformation. It may also be noted that in air, the stress relaxes to a final value which is approximately 55 percent of the value immediately after the cessation of the compression process, while the corresponding final value in water is about 60 percent of the initial value.

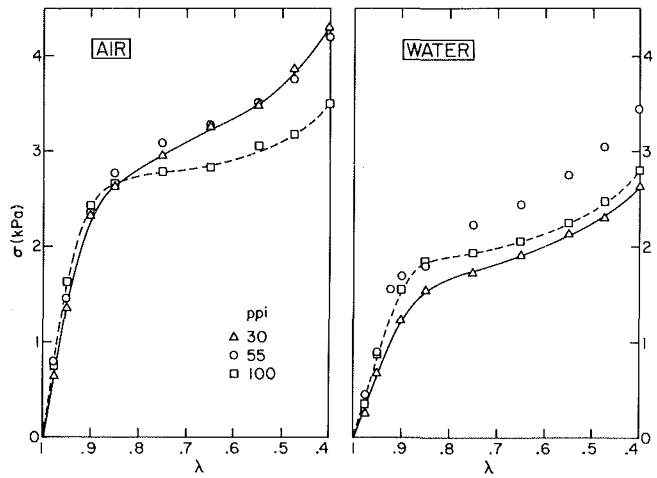

Fig. 4 Comparison of stress versus compression results for air-saturated and water-saturated porous media (uncertainty of ordinate variable ± 2 percent; uncertainty of abscissa variable ± 0.5 percent)

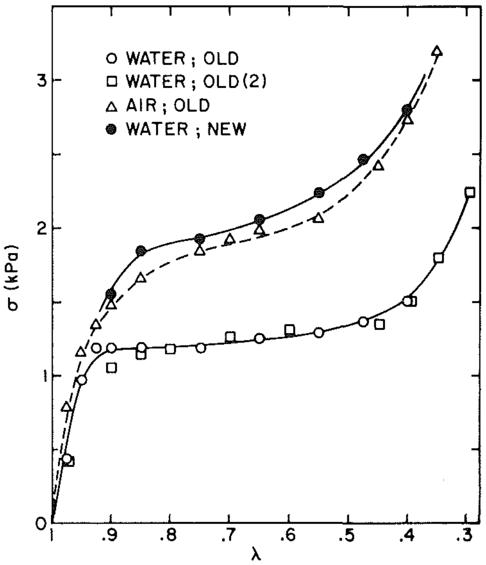

Fig. 5 Effects of repeated compressions on the deformation properties (uncertainty of ordinate variable ± 2 percent; uncertainty of abscissa variable ± 0.5 percent)

The relaxation process is initially much faster than an exponential decay. More than 50 percent of the stress relaxation occurs within the first 30 min, and more than 80 percent of the relaxation occurs within the first two hours, irrespective of the fluid medium. In all subsequent compression tests, we chose to terminate the relaxation process after two hours, and we also used this time interval for recording data in the flow experiments.

Preliminary compression tests with samples of polyurethane foams indicated that the deformation properties may change with the number of times a specimen is compressed, especially when a new specimen is employed. For this reason, to obtain a valid comparison between the stress-deformation characteristics in water and in air, two identical previously uncompressed samples were used. Two such specimens, each 10.2 cm long, were cut from the parent sample of each of the three types of material under investigation. One of each pair was used to generate the stress-deformation curve in air and the other was used in water. The results of these experiments are shown in Fig. 4. The influence of the participating fluid is again readily apparent, with the forces in water being considerably smaller than the

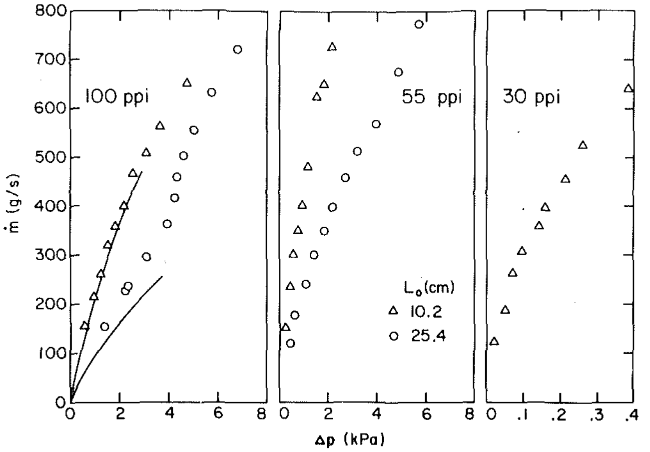

Fig. 6 Water mass flow rate as a function of pressure drop (uncertainty of ordinate variable ± 1 percent; uncertainty of abscissa variable ± 1 percent). ***The solid lines in the left-hand panel represent the predictions of the analytical model.***

corresponding forces in air. It is interesting to note that the ordering of the curves in air and in water is not the same, and we are unable to explain this at this time.

In order to illustrate the change in the deformation properties of polyurethane foam with repeated compressions, we have plotted some stress versus compression ratio variations for the 100 ppi material in Fig. 5. A 25.4 cm-long test specimen which had been used for many preliminary compression experiments was used to generate a σ versus λ curve in air and in water. These curves are labeled "air; old" and "water; old" in Fig. 5, and are compared with that obtained from a completely new and unused specimen of the same material in water, labeled "water; new." The figure shows that compressive force for a well-used material saturated with water is 30-40 percent less than the force required when the material is brand new. The same statement can be made for a material in air, as can be seen by comparing the appropriate curves from Figs. 4 and 5.

Also appearing in Fig. 5 are points labeled "water; old (2)." These are results obtained from an experiment with a cylindrical specimen of the 100 ppi material, in which the specimen was cycled several hundred times (intermittently over a period of several months) in a hydraulic compression machine. These stress-deformation results agree remarkably well with those obtained for the "old" specimen of the present experiments, suggesting that the material probably reaches a mature, unchanging state after numerous compressions. This effect is well known for unbonded fibrous mats (e.g., [4] and [5]), and the material is said to be conditioned. We have also observed the same effect in experiments with thick beds of bonded fibrous material (i.e., fiberglass). In order to eliminate uncertainties arising from a lack of knowledge of the history-dependence of the material behavior, we chose to use new specimens of material for each stage of our experiments. We believe, however, that the analytical model should perform equally well for conditioned materials as well as for new materials, provided that all needed material-property inputs are available for the conditioned material.

4 Flow Results and Comparison With Predictions

The measurements of water mass flow rate as a function of applied pressure drop across the material are shown in Fig. 6, with the results for the 100, 55, and 30 ppi specimens, respectively, displayed in the left, middle, and right-hand panels. All tests were performed on previously uncompressed specimens of material. The general character of the mass flow—pressure difference relationship is qualitatively similar to the results obtained in the experiments with air [2]. The effects of pore size are very pronounced in Fig. 6, with the mass flow rate for a given length and pressure difference increasing markedly with increasing pore size (note the expanded Δp scale in the right-hand panel).

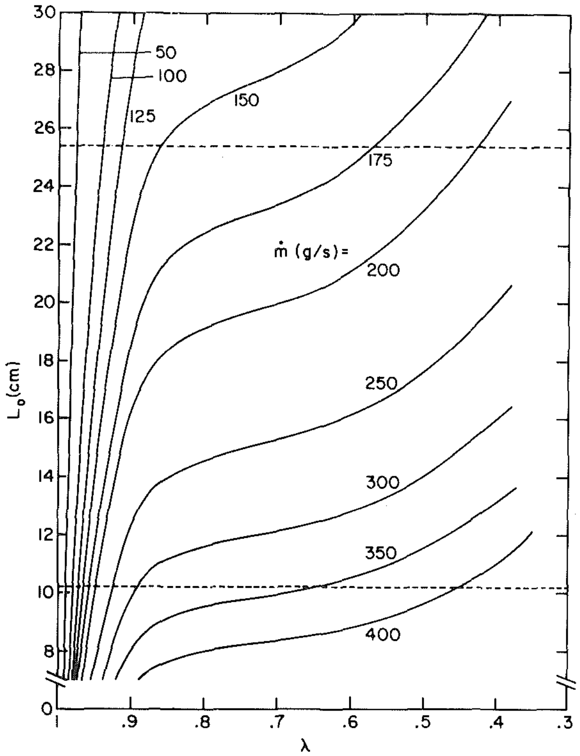

Fig. 7 Relationship between L_0 and λ, 100 ppi material

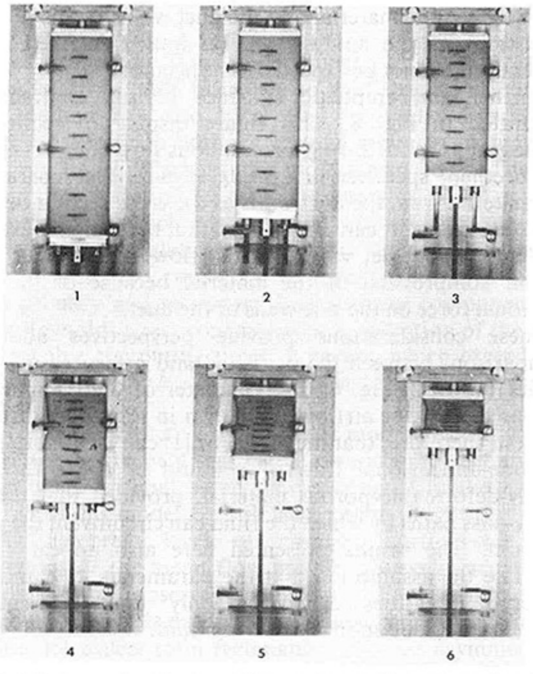

Fig. 8 Photographs showing deformation and cross sectional contraction during a continuous slow compression

In order to compare the measured mass flow rates with the predictions of the model of [1], it is necessary to have available values of the material parameters k, c, and P as functions of λ, as discussed in the analysis presented in Part I [2]. These quantities are material parameters which govern the flow of fluid through the porous medium. For nondeformable materials, it is generally assumed in the literature that the flow parameters depend only on the material and not upon the fluid which flows through the material. It seems reasonable to assume that when a deformable porous material is compressed to a predetermined value of the compression ratio the internal structure of the material is essentially the same no matter what fluid is filling the pore space. On this basis, it follows that the values of k, c, and P as functions of λ should not depend upon the fluid within the material.

Among the three types of foam used in the water experiments, one, the 100 ppi material, was also employed in the air experiments of Part I (designated there as type B). Thus, we have available from Fig. 5 of that paper the variations of $1/k$, $c/\sqrt{k}$, and P as functions of λ. We used these results, together with the stress versus λ relationship for the 100 ppi material in water (Fig. 4), in the integration of equation (13) of Part I to generate the curves of L_0 versus λ shown in Fig. 7. From this figure, we then determined the predicted mass flow rate variations shown as the solid lines for the 100 ppi material in Fig. 6.

The range of Δp over which the calculations for the mass flow rate can be carried out is limited by the range of λ-values over which the value of $\sigma(\lambda)$ is available. However, this is not a major limitation in view of the pathological material behavior which accompanies compression. On the basis of the findings of [2], it is expected that with increasing compression associated with an increase in Δp, the cross section of the material decreases, with the result that the material no longer fills the cross section of the test section. Once this occurs, the fluid takes advantage of the by-pass afforded by the clearance gap between the material and the duct wall. At this point, the conditions of the analysis are no longer fulfilled and its predictions cannot be expected to be accurate.

Further and emphatic evidence of the contraction is illustrated in Fig. 8. This figure displays a sequence of photographs taken during a continuous slow compression of a polyurethane specimen in a plexiglas duct. The separation of the material from the duct walls as the cross section decreases in quite evident. It can also be seen that the material exhibits a tendency to buckle, which, in the flow experiments, would inhibit compression of the material because of the added frictional force on the side walls of the duct.

These considerations provide perspectives about the comparisons between the predicted and measured mass flow values shown in Fig. 6. The character of the comparison is similar to that for airflow, as shown in Fig. 9 of Part I. We suggest, therefore, that the model of [1] can be used to predict the one-dimensional flow of a liquid or a gas through a highly-deformable porous material, provided that there are no by-pass paths by which the fluid can circumvent the porous medium. The results presented here also appear to substantiate the assumption that the parameters k, c and P are material quantities depending only upon the material geometry and not upon the flowing fluid.

5 Concluding Remarks

As a necessary prelude to the comparison of gas and liquid flows through deformable porous media, it was necessary to obtain quantitative information about stress relaxation and aging. When a deformable material is compressed and the degree of compression is maintained, the internal stresses relax and finally approach an equilibrium value. For the materials examined here, the stress relaxation may occur over tens of hours, but the most rapid relaxation occurs shortly after the compression. The findings of these experiments led to the selection of a relaxation time (2 hr) at which the stress data corresponding to a given compression were recorded.

It was found that the force needed to compress a water-saturated material is substantially less than that needed to compress the same material in air. For the specific material investigated, the force for compression in water was about one-third less than for air.

When a new specimen of deformable material is compressed a number of times, its deformation properties were found to change. The aging process appears ultimately to lead to "conditioned" material whereby further aging no longer alters the deformation properties. In order to avoid ambiguities associated with aging, all comparisons involving air and water were made with new (i.e., previously uncompressed) specimens.

The pressure-driven water flow through a deformable material was determined both experimentally and analytically. The experiments showed that for a given specimen length and given overall pressure drop the mass flow rate increased with increasing pore size (i.e., fewer pores per inch). Predictions were made by applying the model of [1] with the following inputs: (*a*) stress-deformation information measured with the material in the water-saturated state, (*b*) material flow properties k, c, P as functions of the compression ratio which had been determined in the air-saturated state in [2].

The predictions and experimental results agreed as long as there was no fluid bypassing of the porous medium. Such bypassing occurs with increasing compression and is the result of the contraction of the cross section of the material. The outcome of the comparisons lends support to the notion that the flow parameters k, c, and P are independent of the participating fluid.

Acknowledgment

This research was performed under the auspices of Grant No. ENG 76-16422. The authors wish to thank A. Hoger for her assistance in parts of the work.

References

1 Beavers, G. S., Wilson, T. A., and Masha, B. A., "Flow Through a Deformable Porous Material," ASME *Journal of Applied Mechanics*, Vol. 97, No. 3, 1975, pp. 598–602.

2 Beavers, G. S., Hajji, A., and Sparrow, E. M., "Flow Through Highly-Deformable Porous Media. Part I: Experiments With Air," published in this issue pp. 432–439.

3 Wittenberg, K., "Flow Through Deformable Porous Material," M.S. thesis, University of Minnesota, 1979.

4 Elias, T. C., "Investigation of the Compression Response of Ideal Unbonded Fibrous Structures," *Technical Association of the Pulp and Paper Industry*, Vol. 50, No. 3, 1967, pp. 125–132.

5 Jones, R. L., "The Effect of Fiber Structural Properties on Compression Response of Fiber Beds," *Technical Association of the Pulp and Paper Industry*, Vol. 46, No. 1, 1963, pp. 20–27.

F. B. Gessner
Professor.
Mem. ASME

A. F. Emery
Professor.
Mem. ASME

Department of Mechanical Engineering,
University of Washington,
Seattle, Wash. 98195

The Numerical Prediction of Developing Turbulent Flow in Rectangular Ducts

Comparisons are made between experimental data and numerical predictions based on a three-dimensional length-scale model applicable to developing turbulent flow in rectangular ducts of arbitrary aspect ratio. The numerical method utilizes an explicit (Dufort-Frankel) differencing scheme for the axial momentum equation and involves no iterative procedures. Although the basic technique has been applied previously to another class of three-dimensional flows, it has not been applied until now to slender shear flows dominated by secondary flow of the second kind. The merits of the length-scale model and the computational procedure are assessed by means of comparisons with results referred to both $k-\epsilon$ and full Reynolds stress closure models which have been applied in recent years.

Introduction

The ability to model and predict complex turbulent flows has progressed rapidly during the past decade. In particular, techniques have been developed for predicting flow in ducts with streamwise corners, such as rectangular ducts, in which the local flow structure is dominated by a traverse mean flow commonly known as secondary flow. The state-of-the-art in modeling the flow has now progressed from methods which are heavily weighted with empiricism [1-4], to either one-or two-transport equation models [5-9] or models based on the full set of Reynolds stress (RS) transport equations [10, 11]. In the early stages of model development, only fully developed flow in a square duct was considered, and empirical data were used to model gradients of the transverse normal stresses in the axial vorticity equation in order to predict the secondary flow field [1, 2, 4]. From a predictive point of view, none of these empirical methods is wholly satisfactory, because each method relies on either experimentally measured stress or velocity distributions in order to predict other features of the flow. The situation was improved considerably by Launder and his co-workers, who modelled the anisotropy of the normal stresses, first in terms of the turbulence kinetic energy and position coordinates [5], and then in terms of a prescribed length scale [6]. A one-equation (k) turbulence model was used in both studies, and predictions agreed well with experimental results for the special case of fully developed flow in a square duct. The second study [6] also clearly demonstrated that all mean flow properties could be predicted satisfactorily through the use of a geometrically prescribed length scale.

More recent studies have employed a two-equation ($k-\epsilon$) model of turbulence in order to provide greater flexibility in modeling the flow. The initial efforts of Tatchell [7] led to the successful prediction of developing flow in a square duct, albeit with some discrepancies, most notably in the form of delayed secondary flow development, which Neti [8] has shown is attributable primarily to grid spacing effects. The $k-\epsilon$ method has also been used to predict overall heat transfer behavior in both square and rectangular ducts with good results [9]. Perhaps the most advanced model at the present time is the full RS transport equation model proposed by Reece [11], which accounts for near-wall pressure-strain effects in its formulation. This model performs very well in terms of accurately predicting all salient features of the flow (both primary and secondary flow velocity components and all six Reynolds stress components). Application of the model does involve computing times, however, which exceed those associated with the $k-\epsilon$ model by a factor of at least one and one-half [11].

In terms of predictive capability at moderate cost, the $k-\epsilon$ model appears to be a reasonable compromise, but even this model is not without some shortcomings. Computing times referred to this model are still longer than those referred to a wholly algebraic level of closure. Furthermore, $k-\epsilon$ predictions of the mean flow are not always in accord with experimentally observed behavior. For example, the secondary flow cells predicted by Ramachandra and Spalding [9] in a 3:1 aspect ratio rectangular duct are asymmetrically located with respect to a corner bisector, whereas the experimental results of Hoagland [12] and Tracy [13] indicate that the cells should be approximately centered about the bisector.

In the present paper, it will be shown that a three-dimensional length-scale model offers a viable alternative to both partial ($k-\epsilon$) and full RS transport equation models, at least with respect to the prediction of the developing mean flow structure in a square duct and certain aspects of the local turbulence structure. This model can also be applied to predict local heat transfer behavior within a square duct with good accuracy for both symmetric and asymmetric heating conditions at the wall [14]. The use of a three-dimensional length-scale model tailored to corner flow data admittedly introduces

---

Contributed by the Fluids Engineering Division for publication in the JOURNAL OF FLUIDS ENGINEERING. Manuscript received by the Fluids Engineering Division, January 7, 1980.

a relatively high level of empiricism into the overall model (cf. equation (8) developed by Gessner and Emery [15]). This limitation can perhaps be circumvented by developing an algebraic stress model based on planar, two-dimensional length-scale considerations alone. So [16] has suggested an alternate model following this approach, but the algebraic stress equations he proposes are deficient in certain respects when applied to turbulent corner flows (cf. comments by Gessner [17]). Further work will be required to determine whether or not subsequent revisions suggested by So [18] will lead to a model which constitutes a viable alternative to the present model. This work is beyond the scope of the present paper, however, which is intended to demonstrate the full predictive capabilities of the final form of our model when applied to developing rectangular duct flows.

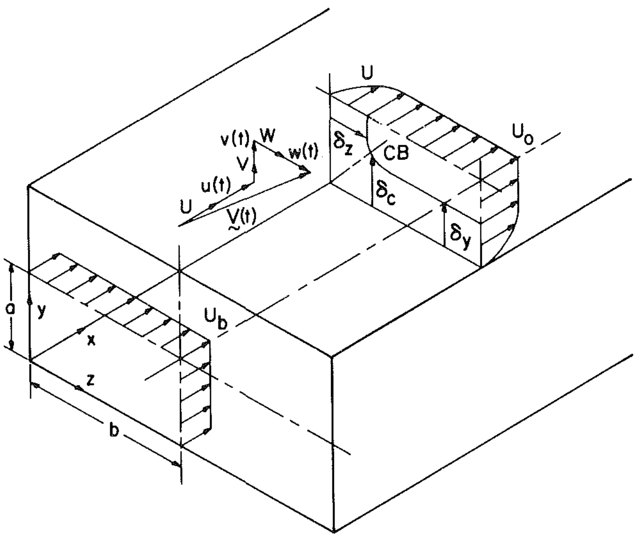

Fig. 1 Coordinate system and pertinent variables

Model

The coordinate system and pertinent variables, as they apply for developing flow in a rectangular duct of arbitrary aspect ratio, are shown in Fig. 1. The overall model employed in the present study consists of the continuity equation and reduced forms of the x, y, and z momentum equations, coupled with an algebraic model for all six components of the Reynolds stress tensor (cf. equations (1)-(4) and equations (44)-(49) of reference [19]). The length-scale variation was prescribed by equation (8) of reference [15] and the specified values for the coefficients with one exception: C_{11} was changed from 0.4 to 0.5 so that the asymptotic value of l_p/a would approach Buleev's [20] analytical value (0.159), rather than the empirical value (0.132) specified in the paper. This modification was necessary in order to predict axial centerline velocities which more closely approximated experimentally measured values for fully developed flow. The values for α_1 and α_2 were prescribed as 0.94 and 0.26, respectively, as suggested in reference [15], and correspond to the values of $c_{\phi 1}$ and $c_{\phi 2}$ chosen by Hanjalic and Launder in their model [21]. The value for F_{12} was, however, modified from the value suggested in reference [15] (0.600) to a lesser value (0.535), which corresponds to a value for the anisotropy coefficient (c) approximately the same as that specified by Launder and Ying [6] in their model. This manuever was necessary in order to avoid pedicted multiple secondary flow cells in an octant of the flow and overly distorted isotach patterns, a result similar to that noted by Launder and Ying [6] in their predictions. Although the values for c specified in the present study and by Launder and Ying lead to reasonable predictions of the mean flow field, neither model can simultaneously predict the observed anisotropy between $\overline{v^2}$ and $\overline{w^2}$, which acts as the primary vorticity generating mechanism in the flow. This anomaly appears to be directly related to the neglect of near-wall pressure-strain effects in both models. The consequences of this omission will be discussed in more detail when comparisons between predictions and experiment are made.

Numerical Method of Solution

The numerical method which was used to solve the system of equations employs an explicit differencing scheme for the axial momentum equation. As such, the method differs from the implicit methods used by other investigators (e.g., [6-11]), which are all variations of the Patankar-Spalding method [22]. Although the present method has been applied previously to two-dimensional boundary layer flows [23, 24], and to another class of three-dimensional flows [25], it has not been applied until now to slender shear flows dominated by secondary flow of the second kind. In the finite-difference form of the momentum equations, each Reynolds stress

Nomenclature

a = duct half width (Fig. 1)
a' = diagonal half width (Fig. 6(b))
b = duct half span (Fig. 1)
c = anisotropy coefficient
$c_{\phi 1}, c_{\phi 2}$ = empirical coefficients
C_{11} = empirical coefficient in length-scale model
D_h = hydraulic diameter
f = friction factor
F_{12} = empirical coefficient in Reynolds stress model
k = turbulence kinetic energy
l_p = Prandtl's mixing length
Re = Reynolds number (Re $\equiv U_b D_h / \nu$)
u,v,w = fluctuating velocity components (Fig. 1)
$\overline{u^2}, \overline{v^2}, \overline{w^2}$ = Reynolds normal stress components
$\overline{uv}, \overline{uw}$ = Reynolds shear stress components
$u_\tau, \bar{u}_\tau$ = local and average friction velocities, respectively
U,V,W = mean velocity components (Fig. 1)
U_b = bulk flow velocity
U_0 = axial centerline velocity
V' = mean velocity component along diagonal (Fig. 7(b))
$\mathbf{V}$ = velocity vector (Fig. 1)
x,y,z = cartesian coordinates (Fig. 1)
y' = cartesian coordinate along diagonal (Fig. 6(b))
y^+ = dimensionless coordinate ($y^+ \equiv y u_\tau / \nu$)
ν = kinematic viscosity
α_1, α_2 = empirical coefficients in Reynolds stress model
$\delta_y, \delta_z, \delta_c$ = boundary layer thicknesses at U/U_0 = 0.995 (Fig. 1)
ϵ = dissipation rate
κ = empirical coefficient in length-scale model
$\tau_w, \bar{\tau}_w$ = local and average wall shear stress, respectively

component is expressed in terms of components of a nonscalar eddy viscosity. In performing the computations, eddy viscosity component values are spatially averaged about each nodal point in a consistent manner for all Reynolds stress components to ensure numerical stability and accuracy. The axial step size is successively doubled to within the limits imposed by numerical stability to ensure computational efficiency in the axial direction. The axial mean velocity and mean static pressure are determined by using Dufort-Frankel differencing and conservation of mass. The in-plane (yz) velocity and pressure field are determined, respectively, by the ADI method and a direct solution of the difference equations using a matrix solver. The resulting accuracy is such that no iterations are necessary to specify V, W, and the transverse pressure field. These and other features of the method are described in more detail in a related paper [26].

In applying the technique, it is necessary to specify only *one* nonwall boundary condition, namely the variation of the local axial mean velocity on the first mesh line. This was done by applying the law-of-the-wall with coefficients based on recently obtained near-wall data in a square duct [27]. The modified form of the van Driest damping function postulated in an earlier paper [15] has also now been confirmed experimentally [27], so that the first mesh line could be located relatively close to a wall ($y^+ \simeq 30$), without incurring deficiencies in modelled length-scale behavior. In order to compute local flow development in a square duct from an initially uniform flow at the duct inlet ($U = U_b$, $V = W = 0$ at $x = 0$) to a location 100 hydraulic diameters downstream, the typical CPU time on a CDC 6600 computer is 2.2 min for a 10×10 uniform mesh grid.[1] This computational time compares favorably with that required for a 10×10 grid when the $k-\epsilon$ model and an implicit computational scheme are employed [7]. Additional computations were also performed with 20×20 and 30×30 uniform mesh grids. The CPU time for predictions over the interval $0 \leq x/D_h \leq 100$ is approximately 9 min when a 20×20 mesh grid is used, and increases to 45 min when a 30×30 mesh grid is specified, primarily because smaller axial step sizes are required for stable solutions.

Experimental Data Selected for Comparison

The comparisons between predictions and experiment reported in this paper include comparisons with data obtained in our laboratory and with data obtained by other investigators. Data from our laboratroy include local wall shear stress and friction factor data taken by Lund [27], Reynolds stress distributions measured by Po [28], and axial and transverse mean velocity profiles measured by the senior author. These data were taken in the entrance region of a square duct with a low intensity, essentially uniform mean flow at the duct inlet over a bulk Reynolds number range from 25,000 to 250,000.[2] The duct is made of Formica-lined (hydraulically smooth) walls and is approximately 22 m (72 ft) in length. In constructing the duct, the distance between opposite walls was maintained at 0.254 m ± 0.25 mm (10.00 in. ± 0.01 in.), and adjacent walls were set perpendicular to within ± 0.05 degrees. With the aid of a transit, the bottom (horizontal) wall of the duct was maintained flat to within ± 0.40 mm (± 1/64 in.) over its entire length ($0 \leq x/D_h \leq 84$). For these specified conditions, flow developed symmetrically within the duct to within the accuracy described by Gessner, et al. [29]. Other details of the duct configuration and overall flow system are given in that reference.

Instrumentation. Static pressure measurements for determining the friction factor were made by means of wall taps located on opposite walls of the duct at $2D_h$ intervals between $x/D_h = 26$ and $x/D_h = 84$. Axial mean velocity components were measured by means of a miniature Kiel probe (United Sensor KAC-8) used in conjunction with a wall static pressure tap. The differential pressure was read on an E. Vernon Hill Type A micromanometer having a resolution accuracy of ± 0.025 mm (± 0.001 in.) of water. Preston tubes aligned with the axial flow direction and referenced to a wall static pressure tap were used to measure the local wall shear stress.[3] The differential pressure associated with these measurements was monitored on a Datametrics Barocel electronic manometer, Model 1174, used in conjunction with a Barocel pressure sensor, Type 571C-10T-1C1-V1. This particular combination facilitated measurements in the range between 0.001 mm Hg and 19.99 mm Hg with three-place accuracy. The differential pressure data were converted to local wall shear stress values by means of tabulated calibration data presented by Head and Ram [30], as modified by Lund [27]. Secondary flow (transverse) velocity components were determined by means of single wire rotation using a Wheatstone bridge and RC filtering. Details of the circuit and technique are described by Page [31] and Lund [27], respectively.

Turbulence measurements were made with normal and inclined wire probes, similar in design to configurations recommended by Comte-Bellot and her co-workers [32, 33] for minimal prong interference effects. The exact configurations are described by Lund [27]. The longitudinal stress component ($\overline{u^2}$) was measured by means of a single wire probe normal to the flow which was calibrated before and after each run in the potential core of a free jet. The remaining Reynolds stress components were measured by means of a rotatable, inclined wire probe which was calibrated before and after each run in the jet and in fully developed turbulent pipe flow. The latter calibration was performed in order to prescribe an appropriate value for the tangential cooling factor (as defined by Champagne, et al. [34]) of each wire. The hot-wire probes were operated by means of a Thermo-Systems Inc., Model 1010 Constant Temperature Anemometer. The bridge output voltage was fed into a DISA Turbulence Processor, Model 52B25, and the mean square voltage was read to a DISA Integrating Digital Voltmeter, Model 55D31. Reynolds stress components were evaluated by means of equations referenced by Po [28] which are based on the response model suggested by Hill and Sleicher [35]. Both normal and inclined wire probes were mounted on a traversing machanism with the probe stem parallel to the axial (x) flow direction. Each probe was positioned at points in the transverse (yz) plane to within an estimated accuracy of ± 0.1 mm (±0.004 in.) relative to the set position. The inclined wire probe was rotated in 45-degree increments by means of a bevel gear arrangment in order to orient the wire in the xy and xz planes, and in intermediate planes which bisected these planes (8 angular positions). This technique permitted $\overline{v^2}$, $\overline{w^2}$, $\overline{uv}$, $\overline{uw}$, and $\overline{vw}$ to be measured simultaneously at each point in the flow after $\overline{u^2}$ was determined from normal wire measurements. Because all mean

---

[1] This grid applies for a quadrant of the flow, and does not include image points about solid boundaries and lines of symmetry. Only uniform mesh grids were prescribed in the present study.

[2] At $x/D_h = 0$, with Re = 250,000, the relative boundary layer thickness on the duct midplane, δ/a, was approximately 0.02, and the core flow turbulence level at this location was less than 0.0035.

[3] Application of this technique presumes that the two-dimensional form of the law-of-the-wall (with fixed coefficients) applies in the entire near-wall layer, i.e., over the interval $30 \leq y^+ \leq 300$ with $y \leq z$, regardless of corner proximity, and that secondary (transverse) velocity components in the near-wall region are typically less than 5 percent of the local axial flow component. Both of these conditions were satisfied for the Reynolds number range over which data were taken (cf. Lund [27]).

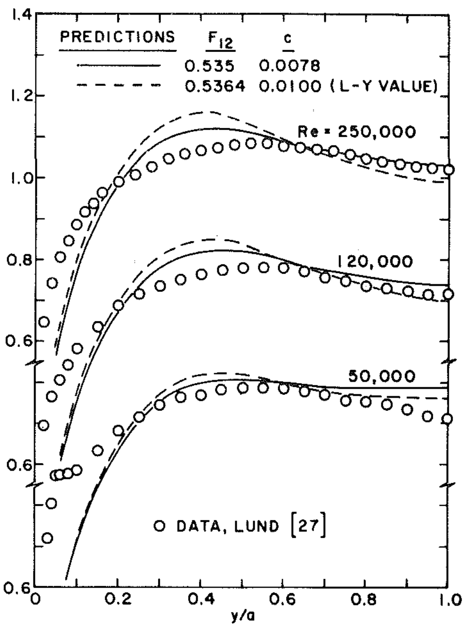

Fig. 2 Local wall shear stress distributions for fully developed flow in a square duct, Re variable

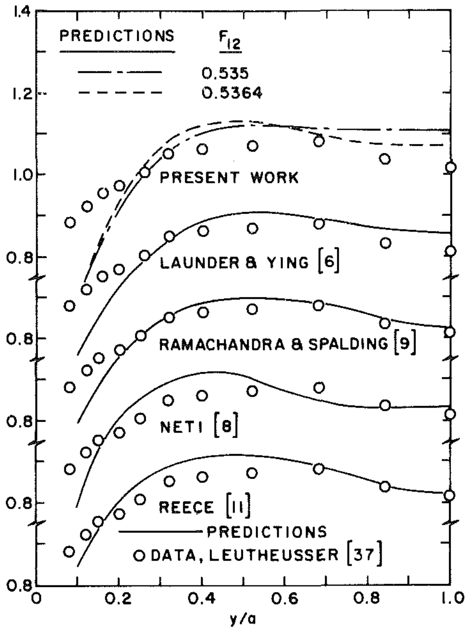

Fig. 3 Local wall shear stress distributions for fully developed flow in a square duct, Re = 34,000

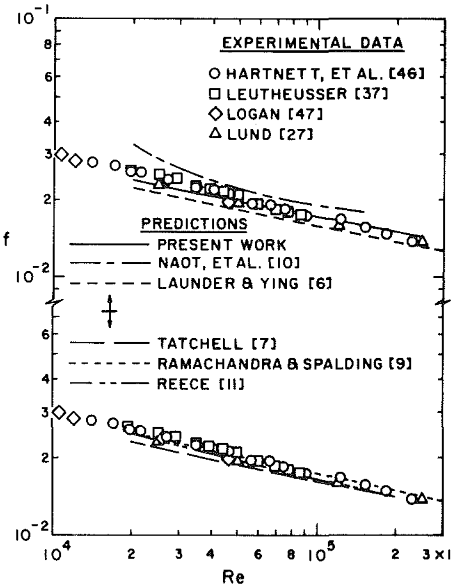

Fig. 4 Friction factor distributions for fully developed flow in a square duct

flow and turbulence data were taken at points in the flow where wall interference effects can be neglected, no wall-effect corrections have been applied to the data.

Uncertainty Estimates. The uncertainties associated with experimentally determined values of the local wall shear stress, friction factor, and axial mean velocity are due primarily to variations in time-averaged differential pressure readings. On the basis of these observed variations, it is estimated that measured values of f, $\tau_w/\bar{\tau}_w$, and U/U_b are accurate to within ± 0.001, ± 0.02, and ± 0.01, respectively (20:1 odds). The estimated uncertainty in measured values of V/U_b (± 0.002) is associated with a possible error of ± 0.1 degrees in the angular position of the wire corresponding to exact bridge balance. Estimated uncertainties in measured Reynolds stress values are based on observed variations in mean and mean-square bridge voltage readings, uncertainty in the tangential cooling factor, as evaluated before and after a given run, and drift effects on wire calibration, as reflected in a change of the mean bridge voltage intercept value over a given run. For these conditions, the estimated peak uncertainties in measured values of $\overline{u^2}/U_b^2$, $\overline{v^2}/U_b^2$, $\overline{w^2}/U_b^2$, $\overline{uv}/U_b^2$, and $\overline{uw}/U_b^2$ are ±3, ±6, ±6, ±2, and ±2 ($\times 10^{-4}$), respectively, at 20:1 odds. On the basis of these estimates, the corresponding peak uncertainty in k/U_b^2 is $\pm 4.5 \times 10^{-4}$ if the limited-sample uncertainty model proposed by Kline and McClintock [36] is employed.

Comparisons Between Predictions and Experiment

Local Wall Shear Stress Profiles. Predicted and experimentally measured local wall shear stress distributions for fully developed flow in a square duct are shown in Fig. 2. In performing the computations, a 10 × 10 mesh grid was found to be adequate for purposes of comparison. Additional predictions based on a value for F_{12} (0.5364) corresponding to Launder and Ying's [6] anisotropy coefficient ($c = 0.010$) are also shown in Fig. 2. Predictions based on the present value of F_{12} (0.535) correspond to an anisotropy coefficient (0.0078) which is approximately 20 percent less than Launder and Ying's value. This reduction corresponds to a reduction in the modeled anisotropy between $\overline{v^2}$ and $\overline{w^2}$ and leads to improved agreement between predictions and experiment, especially at the higher Reynolds numbers (120,000 and 250,000). At the lowest Reynolds number (50,000), an inflection point exists in the data near $y/a = 0.1$, which is also evident in Leutheusser's [37] data at Re = 34,000. The predicted profiles based on $F_{12} = 0.535$ tend to overestimate local wall shear stress values in the vicinity of the wall bisector ($y/a = 1$). This effect is amplified at lower Reynolds numbers, as shown in Fig. 3, where comparisons are made with Leutheusser's [37] results. If F_{12} is increased slightly to 0.5364, Fig. 3 shows that the level of agreement between predictions and experiment is comparable to that observed when either a $k-\epsilon$ [8, 9] or full RS closure [11] model is employed. It should be noted that all models tend to overpredict local overshoot behavior and underpredict values in the near corner region. The magnitude of the discrepancy in the near corner region diminishes, however, with increasing model complexity, as can be seen by comparing predicted and measured values at $y/a = 0.1$ in Fig. 3.

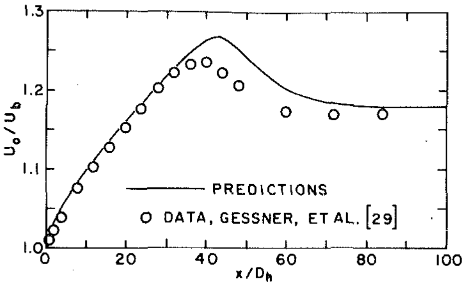

Fig. 5(*a*) Re = 250,000

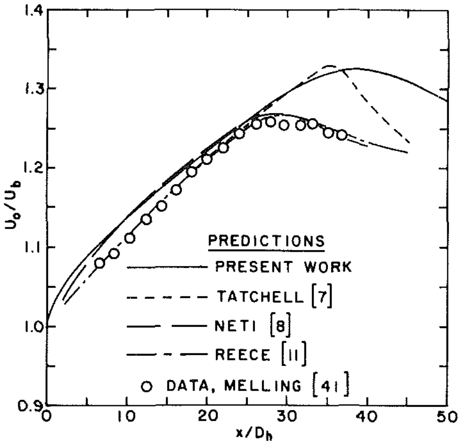

Fig. 5(*b*) Re = 42,000

Fig. 5 Axial centerline velocity distributions

Friction Factor Behavior. The friction factor distributions predicted by various investigators for fully developed flow in a square duct are compared with the present predictions and experimentally determined values in Fig. 4. The data shown were selected on the basis of a recent survey of corner flow data by the senior author [38]. From the figure it can be seen that the present predictions agree well with the data, except at the lower Reynolds numbers (Re < 50,000). The lack of agreement between Launder and Ying's distribution and the data is attributable primarily to an underprediction of the turbulent shear stress field for the coefficient values specified in their study (cf. Fig. 7 of reference [39]). The tail-off behavior of the present predictions at the lower Reynolds numbers is perhaps the result of neglecting convective and diffusive transport effects in the present turbulence model, both of which are included in the higher-order models employed by other investigators [7, 9, 11], whose predictions are also shown in Fig. 4. The present predictions fully justify the use of Buleev's length-scale function for friction factor predictions, provided that $\kappa = 0.45$, as suggested in references [15] and [39] and as specified in the present model. These results also indicate that the anomalous behavior observed by Quarmby [40] must be due to some aspect of Buleev's model other than his method of length-scale specification.[4]

Primary Flow Development. The predicted variation of the axial centerline velocity in a square duct for uniform inlet flow conditions is shown in Fig. 5. At the higher Reynolds number (Fig. 5(*a*)) the results agree well with experimentally measured values, both in the developing flow region and in the shear layer interaction region where local peaking is observed ($x/D_h \simeq 40$). The approach to a fully developed state is also predicted with reasonable accuracy. At the lower Reynolds number, however (Fig. 5(*b*)), the present model and

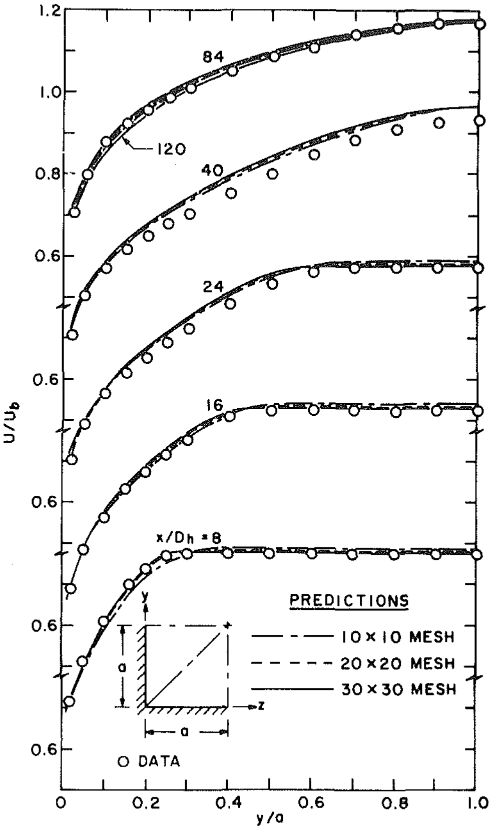

Fig. 6(*a*) wall bisector ($z/a = 1$)

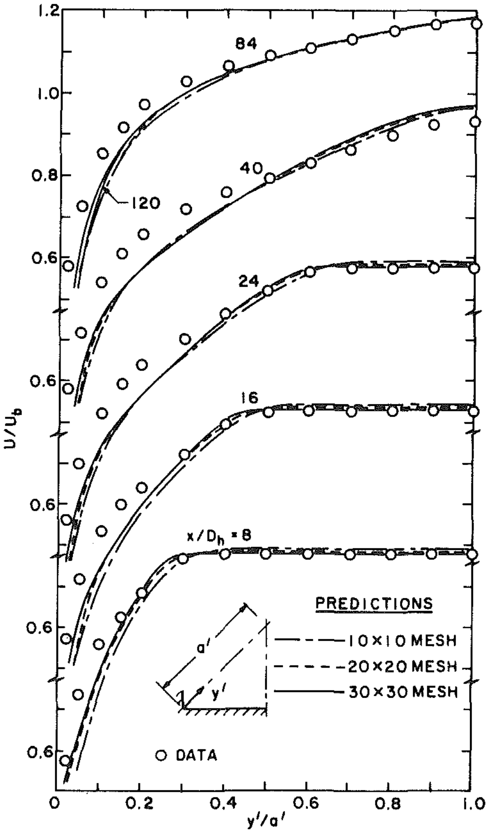

Fig. 6(*b*) corner bisector

Fig. 6 Axial mean velocity distributions, Re = 250,000

---

[4] In that study Buleev's overall Reynolds stress model was employed and predicted friction factor values *increased* with an increase in Reynolds number.

Tatchell's [7] $k-\epsilon$ computations referred to a 10×10 uniform mesh grid overpredict the experimental distribution measured by Melling [41] when $x/D_h \geq 30$. The inability of the present algebraic stress model to predict local peaking near $x/D_h = 30$ and observed behavior further downstream is probably attributable to the length-scale model employed, which was "fine-tuned" with data obtained at a high Reynolds number condition (Re = 250,000), for which local peaking occurs near $x/D_h = 40$ (refer to Fig. 5(*a*)). The improved agreement between the data and Neti's [8] predictions, in comparison to Tatchell's [7] predictions, indicates that use of the $k-\epsilon$ model, in conjunction with a nonuniform grid (nodal points relatively close to the wall), can overcome the deficiencies associated with the use of 10×10 uniform mesh grid.

Figure 6 shows a comparison between the present predictions and axial mean velocity profiles measured along wall and corner bisectors of a square duct at various streamwise locations. The results demonstrate that predicted primary flow velocity distributions are relatively insensitive to grid spacing effects, and that a 10×10 uniform mesh grid is adequate for prediction purposes. The predicted wall bisector distributions (Fig. 6(*a*)) are in good agreement with their experimental counterparts, but predicted distributions along a corner bisector lie somewhat below experimental values within the boundary layer (Fig. 6(*b*)). Similar behavior was noted by Tatchell [7] when he compared predicted profiles based on the $k-\epsilon$ model and a 10×10 uniform mesh grid with Ahmed's [42] data.

Secondary Flow Development. Comparisons between predicted and measured secondary flow profiles are shown in Fig. 7. This figure clearly indicates that secondary flow predictions are sensitive to mesh size when a uniform grid is used. The corner bisector profiles (Fig. 7(*b*)) show that secondary flow is not predicted in the near entrance region ($x/D_h = 8$) when a relatively coarse (10×10) uniform mesh grid is used, i.e., $-V'$ is negative everywhere. This behavior is the same as that which has been observed when the $k-\epsilon$ model is employed and a similar grid configuration is specified. Tatchell's results, for example, show that wholly outward motion ($-V'$ negative) is predicted along a corner bisector at $x/D_h = 10$ when a 10×10 uniform mesh grid and an axial step size approximately $0.1D_h$ are specified (cf. Fig. 6.32-2a of reference [7]). Neti [8], using essentially the same model and numerical technique as Tatchell, has observed that this outward motion will persist until $x/D_h = 40$ if the axial step size is increased to one hydraulic diameter. His results also indicate, however, that the problem can be alleviated if a nonuniform grid and smaller axial step size are employed. The present predictions show that the problem can also be overcome if a relatively fine, uniform mesh grid is used.

Although predicted and measured secondary flow profiles on a corner bisector indicate a level of agreement similar to that observed by Neti [8] and Reece [11] in their comparisons with Melling's [41] data, it is apparent that predicted transverse flow velocities on a wall bisector lie well below experimental values, especially at $x/D_h = 40$ (Fig. 7(*a*)). This behavior corresponds to delayed secondary flow development in the central region of the duct, and also occurs when the $k-\epsilon$ model is used with a relatively coarse, uniform mesh grid [7]. For the $k-\epsilon$ model, Neti [8] has shown that this deficiency can be largely overcome if the grid is altered so that the first mesh line is relatively close to the wall. Inasmuch as the present predictions in the entrance region ($x/D_h \leq 40$) are not markedly improved by a reduction in grid size (Fig. 7(*a*)), it would appear that the observed discrepancies at $x/D_h = 40$ are attributable primarily to the exclusion of transport effects in the present turbulence model. It should also be noted that even though the present length-scale model is independent of x when $x/D_h \geq 72$, the secondary flow continues to evolve well

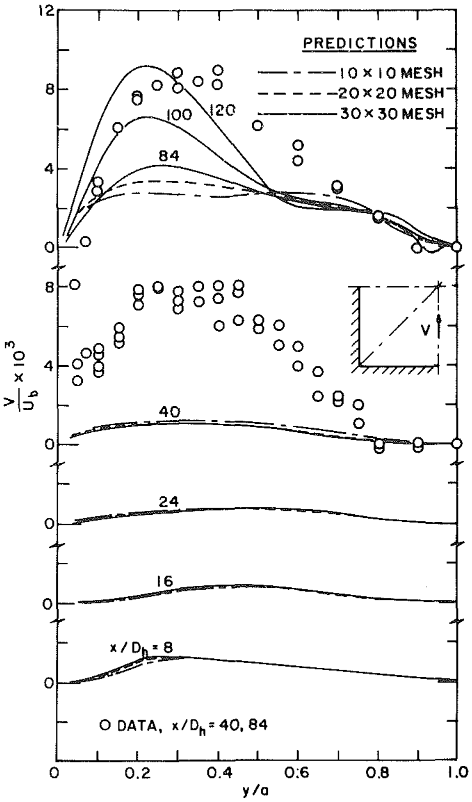

Fig. 7(*a*) wall bisector ($z/a = 1$)

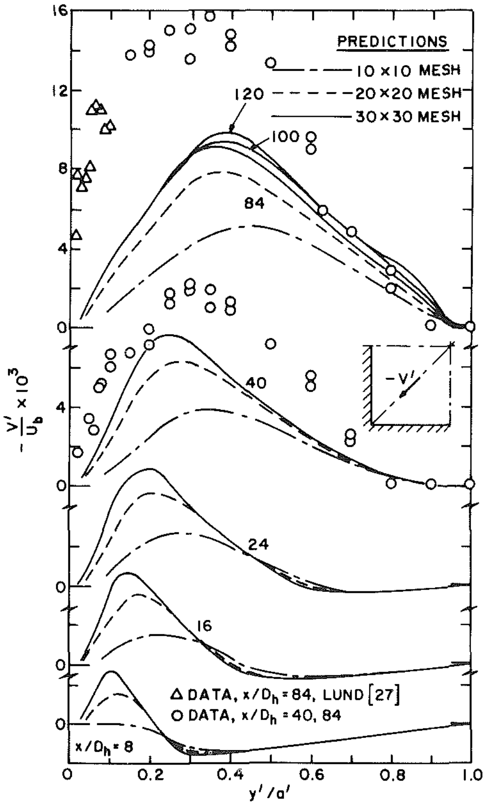

Fig. 7(*b*) corner bisector

Fig. 7 Secondary flow velocity distributions, Re = 250,000

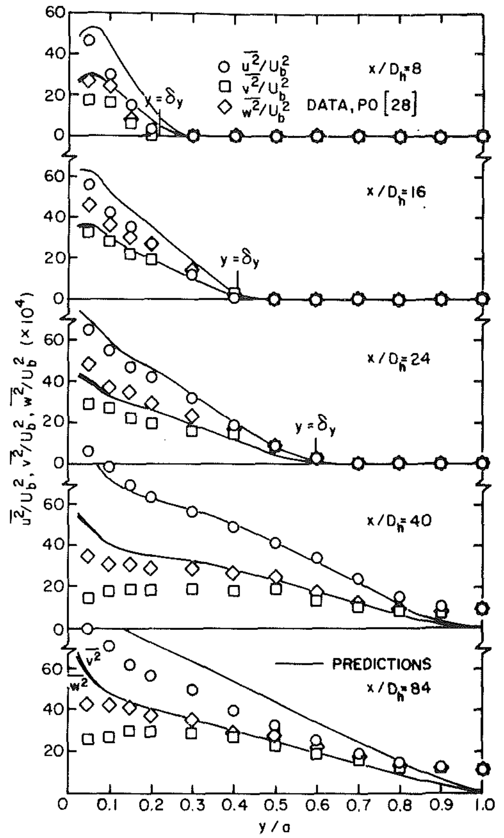

Fig. 8(*a*) normal stress

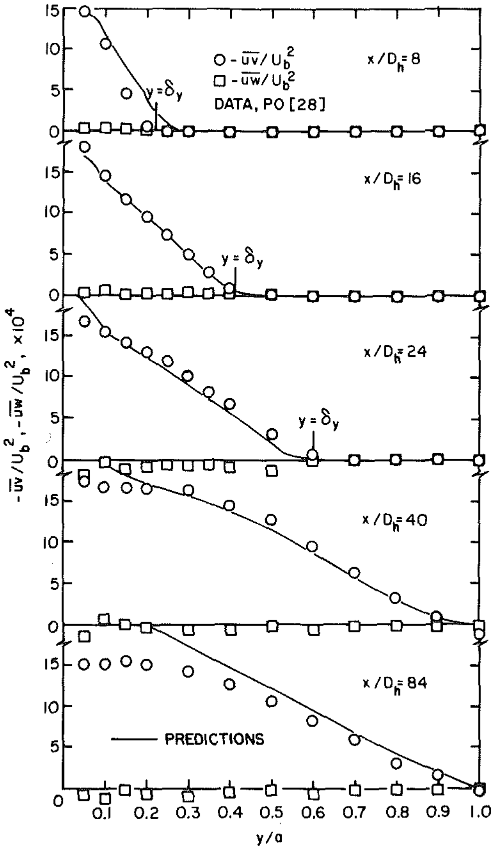

Fig. 8(*b*) shear stress

Fig. 8 Reynolds stress distributions along the wall bisector $z/a = 1$, Re = 250,000

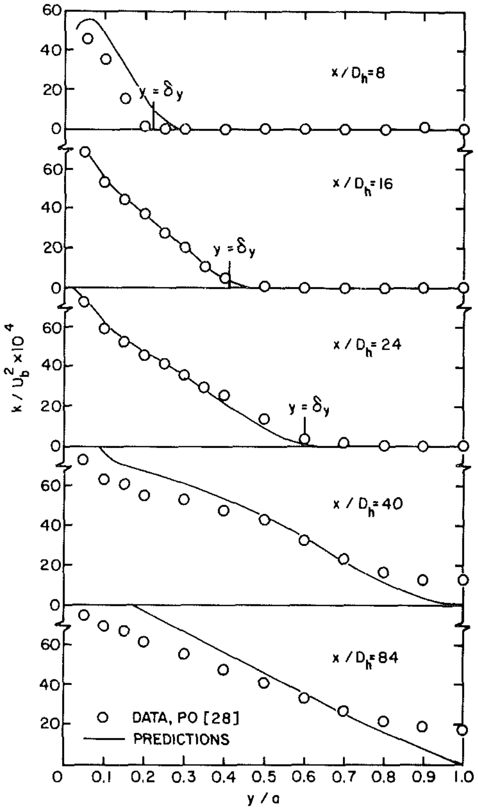

Fig. 9(*a*) wall bisector ($z/a = 1$)

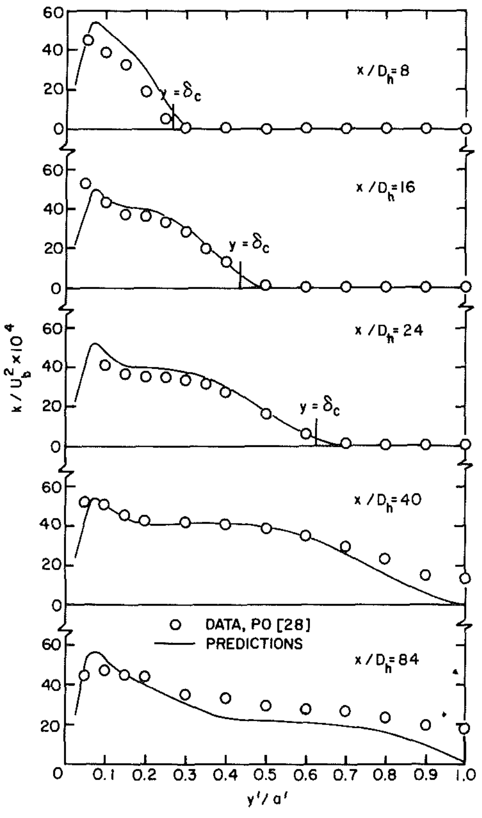

Fig. 9(*b*) corner bisector

Fig. 9 Turbulence kinetic energy distributions, Re = 250,000 downstream of this location (cf. the predicted profiles at x/D_h = 84, 100, and 120 in Fig. 7(*a*)). This development occurs without a marked influence on profiles along a corner bisector (Fig. 7(*b*)) or the primary flow velocity field (Figs. 6(*a*) and 6(*b*)).

Reynolds Stress Distributions. Predicted and measured Reynolds stress distributions along a wall bisector in the developing flow region of a square duct are shown in Fig. 8. In this and subsequent figures the predicted results are based on computations performed with a 20 × 20 mesh grid, and the reference boundary layer thicknesses (δ_y and δ_c) are as defined in Fig. 1. In general, the predicted normal stress (Fig. 8(*a*)) and shear stress (Fig. 8(*b*)) distributions agree well with the measured results. The observed anisotropy between $\overline{v^2}$ and $\overline{w^2}$ is not modelled well, however, because the predicted distributions for $\overline{v^2}$ and $\overline{w^2}$ differ by an imperceptible amount, except near the wall. This behavior is the same as that noted by Kacker [43] and Launder [44] in their discussions of previous related work. According to Launder, a pressure-strain model which omits near-wall effects in its formulation apparently cannot predict both the secondary flow field and the transverse normal stress field simultaneously. Reece's predictions [11] tend to support this claim, because they demonstrate that both the secondary flow field and the observed anisotropy between $\overline{v^2}$ and $\overline{w^2}$ can be predicted accurately when near-wall pressure-strain effects are included in the turbulence model.

Although the present model does not predict the observed anisotropy between $\overline{v^2}$ and $\overline{w^2}$ properly, it does yield reasonable predictions of the turbulence kinetic energy field. Figure 9 compares predicted and measured turbulence kinetic energy profiles along both wall (Fig. 9(*a*)) and corner (Fig. 9(*b*)) bisectors in the developing flow region of a square duct. All predicted profiles agree well with the experimental distributions, and the observed plateau-like behavior along a corner bisector (Fig. 9(*b*)) is predicted with reasonable accuracy. The results in Fig. 9(*b*) also show that predicted turbulence kinetic energy values decrease between the shear layer interaction region (x/D_h = 40) and a location where the primary flow in nominally fully developed (x/D_h = 84), which is in accord with experimentally observed behavior.

Fully Developed Flow Behavior. In order to examine more closely the relative capabilities of the present length-scale (zero-equation) model in comparison to the full RS (seven-equation) model used by Reece [11], additional comparisons were made with data obtained under nominally fully developed flow conditions. The predicted and measured isotach distributions in Fig. 10(*a*) indicate that the present predictions compare favorably with the predictions of Reece, and that isotach contours in the vicinity of a wall bisector are especially well predicted. The level of agreement is comparable to that observed when comparisons are made with data obtained by Leutheusser [37] and Alexopoulos [45] at a lower Reynolds number (Re ≃ 80,000); cf. Fig. 4 of reference [14]. Figure 10(*b*) shows a comparison between predicted secondary flow profiles (based on a 30 × 30 mesh grid) and those measured by Launder and Ying [6]. At z/a = 0.2 the measured profile is not a suitable basis for comparison because continuity is not well satisfied. (The total flow rate away from the wall z = 0 exceeds the flow rate toward the wall by a factor of five.) Comparisons at the other locations (z/a = 0.5 and 0.8) indicate that the present predictions are in good agreement with both Launder and Ying's data and with Reece's predictions. The slight distortion which is evident in the present predictions at z/a = 0.8 near the corner bisector, where the secondary flow is relatively weak, was also observed for the 10 × 10 and 20 × 20 mesh grids, and is probably due to the cumulative effects of numerical errors. At x/D_h = 84, for example, the predicted secondary flow profile at z/a = 0.8 near the corner bisector was not distorted, whereas further downstream, at x/D_h = 120 (nominally fully developed flow), the secondary flow profile was slightly distorted, as shown in Fig. 10(*b*), for all mesh sizes considered.

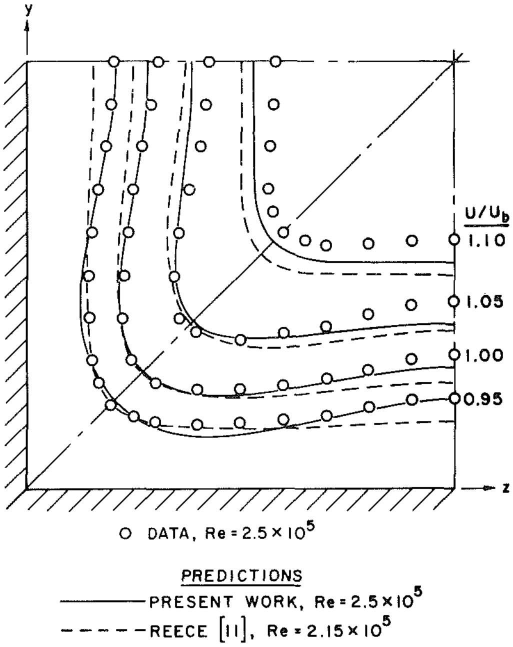

Fig. 10(*a*) isotach distributions

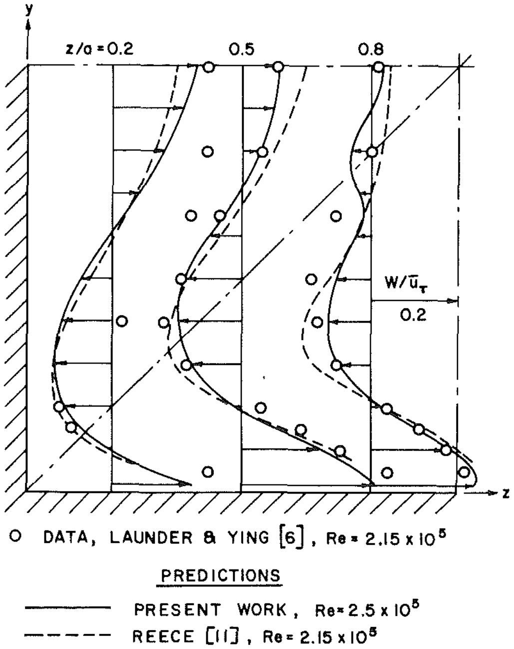

Fig. 10(*b*) secondary flow profiles

Fig. 10 Velocity distributions for fully developed flow in a square duct

Concluding Remarks

The present length-scale model offers a viable alternative to higher-order closure models for predicting local flow development in a rectangular duct. The computational method compares favorably with other methods, both in terms of ease of computation and central processing time. Although comparisons in the present paper are limited to developing and fully developed turbulent flow in a square duct, the model can also be applied to rectangular ducts of arbitrary aspect ratio, including two-dimensional duct flows, as demonstrated in a previous paper [24]. The present predictions indicate that the primary flow structure in a square duct can be predicted with reasonable accuracy with a relatively coarse (10 × 10) uniform mesh grid. Axial mean velocity profiles, friction factor behavior and local wall shear stress distributions are all in good agreement with the data. Secondary flow velocity profiles are predicted well in the corner region for a sufficiently fine (30 × 30) uniform mesh grid, but are underestimated in the vicinity of the wall bisector. Certain aspects of the local turbulence structure, namely $\overline{u^2}$, $\overline{uv}$, and k distributions, are also predicted with reasonable accuracy, but the observed anisotropy between $\overline{v^2}$ and $\overline{w^2}$ cannot be predicted with the present model. This shortcoming does not, however, limit the usefulness of the model for mean flow predictions.

Acknowledgment

This study was sponsored by the National Science Foundation under NSF Grant ENG 76-11818. The authors would like to express their appreciation to the National Science Foundation for their support of this work.

References

1 Ibragimov, M. K., Petrishchev, V. S., and Sabelev, G. I., "Calculation of Secondary Flow in a Turbulent Fluid Stream," *Fluid Dynamics*, Vol. 4, No. 4, 1969, pp. 114-116.

2 Wilson, N. W., Azad, R. S., and Trupp, A. C., "An Analysis of the Effect of Secondary Flows on the Longitudinal Velocity Distribution in Square Ducts," *Symposium on Internal Flows*, University of Salford, England, April 1971, pp. B10-B17.

3 Gerard, R., "Finite Element Solution for Flow in Non-Circular Ducts," *Journal of the Hydraulics Division, Proc. ASCE*, Vol. 100, No. HY3, Mar. 1974, pp. 425-441.

4 Gerard, R., "Secondary Flow in Noncircular Conduits," *Journal of the Hydraulics Division, Proc. ASCE*, Vol. 104, No. HY5, May 1978, pp. 755-773.

5 Launder, B. E., and Singham, J. R., "The Prediction of Fully-Developed Flow in Non-Circular Ducts," *Symposium on Internal Flows*, University of Salford, England, Apr. 1971, pp. B18-B26.

6 Launder, B. E., and Ying, W. M., "Fully Developed Turbulent Flow in Ducts of Square Cross Section," Report TM/TN/A/11, Department of Mechanical Engineering, Imperial College of Science and Technology, London, 1971. (See also *Proceedings of the Institution of Mechanical Engineers*, Vol. 187, 1973, pp. 455-461.)

7 Tatchell, D. G., "Convection Processes in Confined, Three-Dimensional Boundary Layers," Report HTS/75/20, Department of Mechanical Engineering, Imperial College of Science and Technology, London, 1975.

8 Neti, S., "Measurement and Analysis of Flow in Ducts and Rod Bundles," Ph.D. thesis, Mechanical Engineering Department, University of Kentucky, 1977. (See also *Turbulent Boundary Layers*, ASME Publication, New York, 1979, pp. 179-186.)

9 Ramachandra, V., and Spalding, D. B., "Fluid Flow and Heat Transfer in Rectangular-Sectioned Ducts," Report HTS/76/21, Department of Mechanical Engineering, Imperial College of Science and Technology, London, 1976.

10 Naot, D., Shavit, A., and Wolfshtein, M., "Numerical Calculation of Reynolds Stresses in a Square Duct with Secondary Flow," *Wärme und Stoffübertragung*, Vol. 7, No. 3, 1974, pp. 151-161.

11 Reece, G. J., "A Generalized Reynolds-Stress Model of Turbulence," Ph.D. thesis, University of London, 1977.

12 Hoagland, L. C., "Fully Developed Turbulent Flow in Straight Rectangular Ducts," Ph.D. thesis, Massachusetts Institute of Technology, 1960.

13 Tracy, H. J., "Turbulent Flow in a Three-Dimensional Channel," *Journal of the Hydraulics Division, Proc. ASCE*, Vol. 91, No. HY6, Nov. 1965, pp. 9-35.

14 Emery, A. F., Neighbors, P. K., and Gessner, F. B., "The Numerical Prediction of Developing Turbulent Flow and Heat Transfer in a Square Duct," ASME *Journal of Heat Transfer*, Vol. 102, No. 1, 1980, pp. 51-57.

15 Gessner, F. B., and Emery, A. F., "A Length-Scale Model for Developing Turbulent Flow in a Rectangular Duct," ASME Journal of Fluids Engineering, Vol. 99, No. 2, 1977, pp. 347-358.

16 So, R. M. C., "A Note in Comment on 'A Reynolds Stress Model for Turbulent Corner Flows'," ASME Journal of Fluids Engineering, Vol. 99, No. 3, 1977, pp. 593-595.

17 Gessner, F. B., Discussion, ASME Journal of Fluids Engineering, Vol. 99, No. 3, 1977, pp. 596-597.

18 So, R. M. C., Author's Closure, ASME Journal of Fluids Engineering, Vol. 99, No. 3, 1977, pp. 597-598.

19 Gessner, F. B., and Emery, A. F., "A Reynolds Stress Model for Turbulent Corner Flows, Part I, Development of the Model," ASME Journal of Fluids Engineering, Vol. 98, No. 2, 1976, pp. 261-268.

20 Buleev, N. I., "Theoretical Model of the Mechanism of Turbulent Exchange in Fluid Flows," AERE Translation 957, Atomic Energy Research Establishment, Harwell, England, 1963.

21 Hanjalic, K., and Launder, B. E., "A Reynolds Stress Model of Turbulence and Its Application to Thin Shear Flows," *Journal of Fluid Mechanics*, Vol. 52, Part 4, 1972, pp. 608-638.

22 Patankar, S. V., and Spalding, D. B., "A Calculation Procedure for Heat, Mass, and Momentum Transfer in Three-Dimensional Parabolic Flows," *IJHMT*, Vol. 15, No. 10, 1972, pp. 1787-1806.

23 Nelson, R. M., and Pletcher, R. H., "An Explicit Scheme for the Calculation of Confined Turbulent Flows with Heat Transfer," *Proceedings of the 1974 Heat Transfer and Fluid Mechanics Institute*, Stanford University Press, 1974, pp. 154-170.

24 Emery, A. F., and Gessner, F. B., "The Numerical Prediction of Turbulent Flow and Heat Transfer in the Entrance Region of a Parallel Plate Duct," ASME *Journal of Heat Transfer*, Vol. 98, No. 4, 1976, pp. 594-600.

25 East, J. L., Jr., and Pierce, F. J., "Explicit Numerical Solution of the Three-Dimensional Incompressible Turbulent Boundary Layer Equations," *AIAA J*, Vol. 10, No. 9, 1972, pp. 1216-1223.

26 Emery, A. F., Neighbors, P. K., and Gessner, F. B., "A Computational Procedure for Developing Turbulent Flow and Heat Transfer in a Square Duct," *Numerical Heat Transfer*, Vol. 2, 1979, pp. 399-416.

27 Lund, E. G., "Mean Flow and Turbulence Characteristics in the Near Corner Region of a Square Duct," M.S. thesis, Department of Mechanical Engineering, University of Washington, 1977.

28 Po, J. K., "Developing Turbulent Flow in the Entrance Region of a Square Duct," M.S. thesis, Department of Mechanical Engineering, University of Washington, 1975.

29 Gessner, F. B., Po, J. K., and Emery, A. F., "Measurements of Developing Turbulent Flow in a Square Duct," *Turbulent Shear Flows I*, (edited by Durst, et al.), Springer-Verlag, New York, 1979.

30 Head, M. R., and Ram, V. V., "Simplified Presentation of Preston Tube Calibration," *The Aeronautical Quarterly*, Vol. 22, Part 3, 1971, pp. 295-300.

31 Page, R. J., "An Experimental Study of Developing Turbulent Flow in a Square Duct," M.S. thesis, Department of Mechanical Engineering, University of Washington, 1971.

32 Comte-Bellot, G., Strohl, A., and Alcaraz, E., "On Aerodynamic Disturbances Caused by Single Hot-Wire Probes," ASME *Journal of Applied Mechanics*, Vol. 38, No. 4, 1971, pp. 767-774.

33 Strohl, A., and Comte-Bellot, G., "Aerodynamic Effects Due to Configuration of X-Wire Anemometers," ASME *Journal of Applied Mechanics*, Vol. 40, No. 3, 1973, pp. 661-666.

34 Champagne, F. H., Sleicher, C. A., and Wehrmann, O. H., "Turbulence Measurements with Inclined Hot-Wires—Part 1. Heat Transfer Experiments With Inclined Hot-Wire," *Journal of Fluid Mechanics*, Vol. 28, Part 1, 1967, pp. 153-175.

35 Hill, J. C., and Sleicher, C. A., "Equations for Errors in Turbulence Measurements with Inclined Hot-Wires," *Physics of Fluids*, Vol. 12, No. 5, 1969, pp. 1126-1127.

36 Kline, S. J., and McClintock, F. A., "Describing Uncertainties in Single-Sample Experiments," *Mechanical Engineering*, Vol. 75, 1953, pp. 3-8.

37 Leutheusser, H. J., "Turbulent Flow in Rectangular Ducts," *Journal of the Hydraulics Division, Proc. ASCE*, Vol. 89, No. HY3, 1963, pp. 1-19.

38 Gessner, F. B., "Preliminary Report: Corner Flow Data Evaluation," Department of Mechanical Engineering, University of Washington, Jan. 1979.

39 Gessner, F. B., and Po, J. K., "A Reynolds Stress Model for Turbulent Corner Flows, Part II, Comparisons Between Theory and Experiment," ASME Journal of Fluids Engineering, Vol. 98, No. 2, 1976, pp. 269-277.

40 Quarmby, A., "An Evaluation of Buleev's Model of Turbulent Exchange," *IJHMT*, Vol. 19, 1976, pp. 1319-1327.

41 Melling, A., "Investigation of Flow in Non-Circular Ducts and Other Configurations by Laser Doppler Anemometry," Ph.D. thesis, University of London, 1975, (See also *Journal of Fluid Mechanics*, Vol. 78, Part 2, 1976, pp. 289-315.)

42 Ahmed, S., "Turbulent Flow in Non-Circular Ducts," Ph.D. thesis, Department of Mechanical Engineering, Univeristy of Waterloo, 1971. (See also *IJHMT*, Vol. 14, 1971, pp. 365-375.)

43 Kacker, S. C., Discussion, *Proceedings of the Institution of Mechanical Engineers*, Vol. 187, 1973, pp. D147-D148.

44 Launder, B. E., Discussion, ASME Journal of Fluids Engineering, Vol. 98, No. 2, 1976, pp. 276-277.

45 Alexopoulos, C. C., "Temperature and Velocity Distributions and Heat Transfer for Turbulent Air Flow in a Square Duct," M.A.Sc. thesis, Department of Mechanical Engineering, University of Toronto, 1964.

46 Hartnett, J. P., Koh, J. C. Y., and McComas, S. T., "A Comparison of Predicted and Measured Friction Factors for Turbulent Flow Through Rectangular Ducts," ASME *Journal of Heat Transfer*, Vol. 84, 1962, pp. 82-88.

47 Logan, S. E., "Measurement of Reynolds Stress and Turbulence in Dilute Polymer Solution by Laser Velocimeter," *Proceedings of the Third Symposium on Turbulence in Liquids*, (edited by G. K. Patterson and J. L. Zakin), University of Missouri-Rolla, 1973, (published 1975), pp. 91-105.

DISCUSSION

S. Neti[5]

The paper is a good comparative work, particularly in bringing out the features of transport ($k-\epsilon$ and RS) models of turbulence and the nontransport model as they pertain to rectangular ducts. As a first reaction, one does have to be wary of the greater amount of empiricism in the length scale model used without a significant gain in the computational costs. The author's comment regarding the use of planar, two-dimensional length scale models is probably the best alternative if one is committed to the use of nontransport models.

Computational schemes for the prediction of duct flows that use stream function and vorticity (ψ, ω) as dependent variables require the calculation of second derivatives of ($\bar{v}^2 - \bar{w}^2$) as source terms in the vorticity equation. In the Launder and Ying [6] model this is achieved by calculation of ($\bar{v}^2 - \bar{w}^2$) using equation (14). It has to be noted that the anisotropy coefficient is built into this equation as an explicit constant (c) and $L-Y$ used a much smaller value of this coefficient (0.01) than implied by experimental results (0.22). Schemes that use primitive variables have the more difficult task of calculating the first derivatives of the normal stresses $\bar{v}^2$, $\bar{w}^2$ themselves as source terms in the secondary velocity equations. A $k-\epsilon$ model that uses primitive equations includes algebraic equations for $\bar{v}^2$ and $\bar{w}^2$ and it is not possible to predict these normal stresses and secondary flows accurately without taking the near wall pressure-strain effects into consideration. Thus it appears it is more difficult to predict these parameters accurately in schemes that use primitive dependent variables and might explain some of the discrepancies in the paper. In this context it is interesting to note that though the absolute values of the normal stresses (Fig. 8(a)) are overpredicted, their gradients are in much better agreement, particularly away from the wall, and probably are a contributing factor for the successes reported here.

Secondary flow computations are seen to be sensitive to the mesh size with the uniform grid used here and this reiterates the importance of near wall spatial resolution. Also, as mentioned by the authors, the underprediction of the secondary flows by the length scale model seems to confirm the advantage in using the transport equation models.

The continued development of the secondary velocity profiles (Fig. 7(a)) after the axial velocity development is completed is cause for concern and warrants checking for continuity or continued minute changes in the axial velocity profiles.

Joseph A. C. Humphrey[6]

In a series of papers [14, 15, 19, 26, 39] the authors have successively refined a mixing length model for predicting, developing, incompressible, turbulent flow and heat transfer in rectangular ducts of arbitrary aspect ratio. In the model, closure to the conservation equations is accomplished by means of algebraic relations for the turbulence correlations (Reynolds stresses) which appear in the equations. The three-dimensional isotropic length scale appearing in the turbulence correlations is specified by equation (8) of [15]. This equation contains 15 constants which are optimized principally by reference to the data of Po [28]. The full predictive capabilities of the final form of the authors' model is evaluated by them in the communication subject to discussion. Prior to offering a few comments and posing a question this discussor notes with appreciation the degree of care and detail with which the authors have developed their model and conducted the experiments for its evaluation.

Two of the model's defficiencies noted by the authors in their paper are:

(i) the absence of near-wall pressure-strain effects in the formulation;
(ii) the high level of empiricism introduced by the use of a three-dimensional length-scale tailored to corner flow.

The first deficiency was discussed by Launder [44] and appears to be responsible for the inability of the model to predict correct levels of cross-stream normal stress anisotropy and secondary motion simultaneously. This notion is confirmed by the better quality predictions of Reece [11] using full Reynolds stress closure in developing square duct flow. The second defficiency relates to the degree of general applicability of the model to other ducted flows of similar geometry. For example, the authors note that the inability of the model to predict local peaking in the axial center-line velocity data of Melling [41] (Re = 42,000) is "probably attributable to the length-scale model employed, which was "fine-tuned" with data obtained at a high Reynolds number condition (Re = 250,000)." While such sensitivity to "tuning" probably does not seriously limit the usefulness of the model for practical mean flow predictions, it does point to a serious problem; that of an inherent lack of universality which is built into any model which relies extensively on experimental information specific to the geometry of interest for its formulation

A third defficiency in the authors' turbulence model is the neglect of convective and diffusive transport of Reynolds stresses which appears to be responsible for the lack of agreement between measurements and predictions of the friction factor and cross-stream flow respectively. Such a limitation does not appear in the two equation ($k-\epsilon$) algebraic stress model of Ramachandra and Spalding [9] nor in the Reynolds stress model of Reece [11], both of which predict developing rectangular duct flow as well as (or better than) the present model.

It is concluded by this discussor that in view of the more general nature, and hence (in principle) more general applicability, of models in [9, 11], the major advantage of the formulation offered by the authors lies in the provision of a finely tuned, numerical scheme; a predictive tool which can be used with confidence, and relatively inexpensively, over the range of flow conditions and duct geometries to which it has been fitted. In the hands of the design engineer this tool is certainly useful, provided the flow conditions of interest fall within the validated range of the model.

At this point, the question I would ask the authors is, what recommendations would they offer to turbulence modelers seeking to predict more complicated three-dimensional ducted flow geometries such as, for example, the roughened duct flows of Humphrey and Whitelaw [45] and Fujita [46]? To carry out a measurement program which would allow the accurate specification of mixing lengths for all possible geometries is inconceivable, and yet, these flows have still to be shown to be predictable accurately and at reasonable costs by means of advanced closure schemes such as that of [11].

---

[5] Department of Mechanical Engineering, Lehigh University, Bethlehem, Pa.

[6] Department of Mechanical Engineering, University of California, Berkeley, Calif. 94720.

Do the authors agree with the view that an intermediate level of closure, such as that of [9] for example, is the way to proceed?

Additional References

45 Humphrey, J. A. C., and Whitelaw, J. H., "Turbulent Flow in a Duct with Roughness," pp. 174-188, *Turbulent Shear Flows 2*, Editors: J. S. Bradbury, F. Durst, B. E. Launder, F. W. Schmidt, and J. H. Whitelaw, Springer-Verlag, Berlin Heidelberg, 1980.

46 Fujita, H., "Turbulent Flows in Square Ducts Consisting of Smooth and Rough Planes," Research Report of the Faculty of Engineering, MIE Unviersity, Vol. 3, 1978, p. 11.

Authors' Closure

Professors Neti and Humphrey raise some pertinent questions about the computational aspects of our work and the limitations of our proposed length-scale model. Professor Neti suggests that the primitive variable formulation which we employ might explain some of the discrepancies between theory and experiment noted in the paper. We do not feel that this is the case, however, because the evaluation of $\overline{v^2}$ and $\overline{w^2}$, as well as their first derivatives, were all treated in a consistent manner [26]. The crux of the matter, in our opinion, lies in the exclusion of near-wall effects in the pressure-strain model which forms the basis of our length-scale model, a contributing factor mentioned in both the paper and by the two discussors.

Professor Neti's comment that predicted secondary flow velocity profiles continue to develop after predicted axial flow development is complete is not strictly correct. Our computations show that the secondary flow continues to evolve well downstream of a location where the axial mean flow is nominally fully developed ($x/D_h = 84$), but small changes still occur in predicted axial velocity components downstream of this location. For example, Fig. 7(*a*)) shows that predicted secondary flow components along the wall bisector of a square duct more than double between $x/D_h = 84$ and $x/D_h = 120$ in the near-wall region. Over this same interval, predicted axial velocity components at corresponding points in the flow change systematically, but by less than 3 percent in the immediate vicinity of the wall and by less than 1 percent in the outer two-thirds of the boundary layer. This point is noted indirectly in the paper where the statement is made that "this (secondary flow) development occurs without a marked influence on . . . . the primary flow velocity field." The continued evolution of secondary flow in the vicinity of a wall bisector is not the result of violating continuity, therefore, but is due to the prescribed turbulence model, for which the resultant anisotropy between $\overline{v^2}$ and $\overline{w^2}$ (source effect) is not sufficient to ensure rapid propagation of the secondary flow into the mid-plane region of the duct.

The authors appreciate Professor Humphrey's kind remarks about the care which went into the development of the model described in this paper and in previous papers. Professor Humphrey states that by not accounting for direct convective and diffusive transport effects on the Reynolds stresses in our model, there is lack of agreement between our predicted friction factor distribution and experimentally measured distributions. This is not true, however, because close scrutiny of Fig. 4 shows that the level of agreement between our predicted distribution (the solid line distribution in the upper part of the figure) and the data is comparable to that which exists when higher-order closure models (e.g., [7], [9], [11]) are used. The present model is deficient, however, in the sense that extension of the model to other rectangular duct configurations (e.g., those with streamwise curvature or with a mixed smooth-roughened wall condition) is impractical, because the length-scale cannot be prescribed conveniently for these flow situations.

The intermediate level of closure suggested by Professor Humphrey, namely the $k-\epsilon$ model, will, in our opinion, bear the most fruit in terms of predictive capability at moderate cost for a variety of flow situations. This, indeed, is the course of action we are now pursuing. Our present efforts have led to the development of an improved version of the $k-\epsilon$ model which includes functionally dependent coefficients (as opposed to constant coefficients) in the transport equations for k and ϵ and in the algebraic expressions for the individual stress components [50]. More specifically, the coefficient c_μ which appears in all of these equations is no longer constant (e.g., 0.09), but depends, instead, on the local value of P/ϵ (the ratio of the production to dissipation rate, which is unity near a wall and approaches zero in the outer portion of the boundary layer). This coefficient is also functionally dependent on the decay function (as defined by Launder, Reece, and Rodi [51]) which, in turn, depends on position coordinates in the flow. These modifications should lead to improved agreement between predicted and measured results in comparison to that observed in previous studies which employ the conventional form of the $k-\epsilon$ model [7 – 9]. It is our intent to examine the full predictive capabilities of this model in the near future.

Additional References

50 Eppich, H. M., "Development of a Pressure-Strain Model for Turbulent Flow Along a Streamwise Corner," M.S. thesis, Department of Mechanical Engineering, University of Washington (in preparation).

51 Launder, B. E., Reece, G. J., and Rodi, W., "Progress in the Development of a Reynolds Stress Closure Model," *Journal of Fluid Mechanics*, Vol. 68, Part 3, 1975, pp. 537-566.

C. K. G. Lam
Graduate Student.

K. Bremhorst
Reader.

Department of Mechanical Engineering,
University of Queensland, St. Lucia,
Brisbane, Australia 4067

A Modified Form of the k-ϵ Model for Predicting Wall Turbulence

The high Reynolds number form of the k-ϵ model is extended and tested by application to fully developed pipe flow. It is established that the model is valid throughout the fully turbulent, semilaminar and laminar regions of the flow. Unlike many previously proposed forms of the k-ϵ model, the present form does not have to be used in conjunction with empirical wall function formulas and does not include additional terms in the k and ϵ equations. Comparison between predicted and measured dissipation rate in the important wall region is also possible.

1 Introduction

The k-ϵ model of turbulence has recently emerged as a powerful tool for prediction of many complex flow problems including jets, wakes, wall flows, reacting flows and flows with buoyancy, centrifugal, and Coriolis forces. The basis of the model is that it solves the transport equations for the turbulence energy and the isotropic turbulence dissipation rate. The set of model equations recommended by Launder and Spalding [1] for high Reynolds number flows has been most widely employed. For wall flows, these equations are normally used in conjunction with empirical wall function formulas. The success of this method depends on the "universality" of the turbulent structure near the wall and when disagreements are found between measurements and predictions, it is difficult to judge whether the weakness of the method lies in the basic model equations or in the wall function formulas.

Jones and Launder [2, 3] extend the original k-ϵ model to the low Reynolds number form which allows calculations right to the wall. Later, other forms of the k-ϵ model were developed for the same purpose, but still include extra terms in the transport equations in order to improve predictions in the wall region, or for computational expediency.

This paper describes the development of a new form of the high Reynolds number k-ϵ model, predictions with which are then compared with measurements for fully developed pipe flows.

2 The Proposed Model

It is assumed that turbulence can be characterized by the turbulence kinetic energy and the isotropic component of the turbulence energy dissipation rate which are determined from the transport equations

$$\frac{Dk}{Dt}=\frac{\partial}{\partial x_j}\left[\left(\frac{\nu_t}{\sigma_k}+\nu_l\right)\frac{\partial k}{\partial x_j}\right]+\nu_t\left(\frac{\partial U_i}{\partial x_j}+\frac{\partial U_j}{\partial x_i}\;\frac{\partial U_i}{\partial x_j}\right)-\epsilon \qquad (1)$$

$$\frac{D\epsilon}{Dt}=\frac{\partial}{\partial x_j}\left[\left(\frac{\nu_t}{\sigma_\epsilon}+\nu_l\right)\frac{\partial \epsilon}{\partial x_j}\right]+C_1 f_1 \nu_t\frac{\epsilon}{k}\left(\frac{\partial U_i}{\partial x_j}+\frac{\partial U_j}{\partial x_i}\right)\frac{\partial U_i}{\partial x_j}-C_2 f_2\frac{\epsilon^2}{k} \qquad (2)$$

The time-averaged flow field can be determined through the eddy viscosity given by

$$\nu_t=C_\mu f_\mu k^2/\epsilon \qquad (3)$$

where σ_k = 1.0, σ_ϵ = 1.3, C_1 = 1.44, C_2 = 1.92, C_μ = 0.09 as recommended in [1].

These equations are a general form of those given by Launder and Spalding [1] in which the functions f_1, f_2, and f_μ are all assumed to be identically unity. It has been found that this assumption cannot be valid within a laminar sublayer and appropriate functions must be chosen to ensure satisfactory predictions consistent with physical arguments. The following sections describe the development of these functions.

2.1 Development of the Function f_μ. For fully developed pipe flows, Rodi [4] has shown for C_μ=0.09 that f_μ is approximately 2.0 at the symmetry line and varies almost linearly with radius. However, the measurements used for evaluation of ν_t and k^2/ϵ are both subject to large errors and hence the calculated values of f_μ at any radius may not be reliable. Numerous successful applications of the high Reynolds number form of the k-ϵ model with wall function formulas suggest that f_μ should approximately equal unity in fully turbulent regions remote from solid walls. This is also consistent with the usual understanding of turbulence that properties should be fairly uniform in regions where viscous effects are small compared to turbulent ones. In regions very near a wall where viscous effects become important, properties will change rapidly and f_μ will also differ considerably from unity. Formulas for f_μ which have been proposed to account for wall effects include,

(i) $$f_\mu = \exp\left[-A_m/(1+R_tA_r)\right] \qquad (4)$$

This is proposed by Jones and Launder [2, 3] with A_m and

Contributed by the Fluids Engineering Division for publication in THE JOURNAL OF FLUIDS ENGINEERING. Manuscript received by the Fluids Engineering Division, August 10, 1979.

A_r given the values 2.5 and 0.02, respectively. Hoffman [5] later suggested that A_m should be 1.75 instead of 2.5. In either case, f_μ and ν_t will become a unique function of R_t. In this formulation f_μ is affected only indirectly by the presence of a wall through R_t.

(ii) $$f_\mu = R_k/(A_m+R_k) \qquad (5)$$

This is proposed by Chien [6] with $A_m = 210.0$. f_μ is now directly dependent on the normal distance from a wall.

(iii) $$f_\mu = 1-\exp(-A_m R_t) \qquad (6)$$

This is proposed by Hassid and Poreh [7] with $A_m = 0.0015$. As in (i), f_μ and ν_t depend only on R_t.

The above formulas have been shown to yield good results when used with the forms of the k-ϵ model employed by the respective proponents. Not all of the above formulas for f_μ can, however, be used with a physically correct boundary condition for ϵ and the unmodified transport equations (1) and (2) as seen from the following argument.

At a wall ϵ is finite and $k=\partial k/\partial y=0$. The variation of k and ϵ near the wall may be expanded in a Taylor series to give

$$k = p_2y^2 + p_3y^3 + \ldots$$
$$\epsilon = q_0 + q_1y + q_2y^2 + q_3y^3 + \ldots$$

where the p's and q's are functions of the streamwise distances. At very small distances from the wall ν_t will be proportional to y^4, y^6 and y^8 if equations (4), (5), and (6), respectively, are used. Therefore, only equation (4) can provide near wall variation of ν_t consistent with the findings of Elrod [8] and the famous Van Driest formula

$$v_t \propto v_l y^{+2}(1-\mathrm{e}^{-\nu+/26})^2 \frac{\partial U^+}{\partial y^+}$$

The assumption that ν_t is dependent only on R_t remains doubtful as it seems plausible that the presence of a wall should have a direct influence on ν_t such as that given in equation (5). Hence, an alternative formula is required and can be obtained by using the succcessful Hassid-Poreh one-equation model employed by Gibson, et al. [9] in which ν_t and ϵ are given by

$$\nu_t = 0.2274yk^{1/2}(1-e^{-0.01189R_k}) \qquad (7)$$

$$\epsilon = 0.4\frac{k^{3/2}}{y}(1-e^{-0.01189R_k}) + 2.0\nu_l\frac{k}{y^2} \qquad (8)$$

Treating R_k as a separate independent variable, equations (7) and (8) can be combined to eliminate y thus expressing ν_t in terms of k, ϵ, R_k and ν_l:

$$\nu_t = \frac{0.09}{2}\frac{k^2}{\epsilon}(1-e^{0.01189R_k})^2\Bigg[1 + \sqrt{1+50.0\frac{\nu_l\epsilon}{k^2}(1-e^{-0.01189R_k})^{-2}}\Bigg] \qquad (9)$$

Comparison with equation (3) for $C_\mu = 0.09$ shows that

$$f_\mu = 0.5(1-e^{\;0.01189R_k})^2\Bigg[1 + \sqrt{1+50.0/[R_t(1-e^{-0.01189R_k})^2]}\Bigg] \qquad (10)$$

Instead of equation (10), the simpler relationship of equation (11) is postulated

$$f_\mu = (1-e^{-A_\mu R_k})^2\left(1+\frac{A_t}{R_t}\right) \qquad (11)$$

which still renders f_μ a function of both R_k and R_t and ν_t is proportional to y^4 near the wall. The presence of a wall now has a direct and an indirect influence on f_μ. For high turbulence levels, f_μ will tend to unity at large distances from the wall but retain the R_k dependence near the wall. The values of the constant A_μ and A_t are determined by trial and error.

2.2 Development of the Function f_1. Computations with the high Reynolds number form of the model with wall function formulas suggest that f_1 is approximately unity remote from a wall. In the near wall region it is found that f_1 assumes larger values in order to increase the predicted dissipation rate thereby reducing the predicted turbulence level to match available experimental data. If f_1 is held constant and equal to unity, additional destruction terms [2, 3, 5-7] would be required in the k-transport-equation to yield reasonable predictions. It is proposed that

$$f_1 = 1 + (A_{C1}/f_\mu)^3 \qquad (12)$$

Nomenclature

A_m, A_r, A_μ, A_{C1}, A_t = turbulence model constants
C_1, C_2, C_μ = turbulence model constants
D = pipe diameter
f_1, f_2, f_μ = turbulence model functions
k = turbulence energy = $\frac{1}{2}\,\overline{u_i'u_i'}$
n = power law index
Re = Reynolds number $\frac{U_bD}{\nu_l}$
R_k = turbulence Reynolds number $\frac{k^{1/2}y}{\nu_l}$
R_t = turbulence Reynolds number $\frac{k^2}{\nu_l\epsilon}$
r = radial coordinate
U = time-averaged axial velocity
U_b = bulk velocity
U^* = shear velocity $\sqrt{\tau_w/\rho}$
U^+ = ratio of U/U^*
u' = instantaneous fluctuating component of axial velocity
U_i, U_j = tensor notation for velocities in the i and j directions, respectively
v' = instantaneous fluctuating components of radial velocity
x_i, x_j = tensor notation for space coordinates
y = normal distance from wall
y^+ = distance from wall defined as U^*y/ν_l
ϵ = isotropic turbulence dissipation rate = $\nu_l\overline{\frac{\partial u_i'}{\partial x_j}\frac{\partial u_i'}{\partial x_j}}$
ϕ = generalized variable
ν = viscosity
σ_k = diffusion Prandtl number for turbulence energy
σ_ϵ = diffusion Prandtl number for dissipation rate
τ_w = shear stress at the wall

Subscripts

eff = effective
j = jth node
l = laminar
max = maximum
t = turbulent
w = at wall

Superscripts

$'$ = instantaneous fluctuating component
$-$ = time mean value

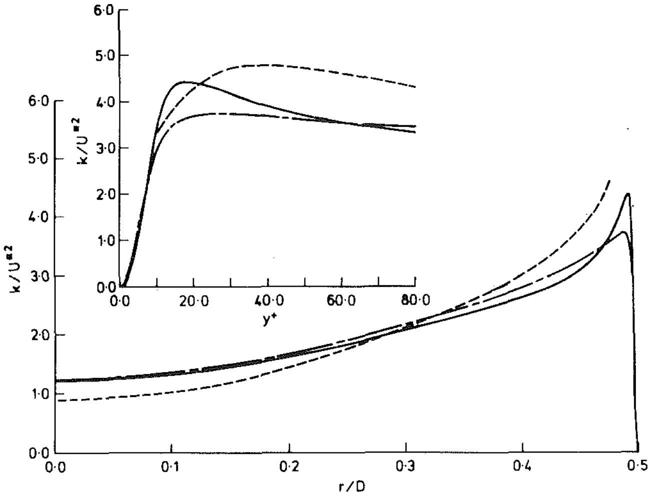

Fig. 1(a) turbulence kinetic energy

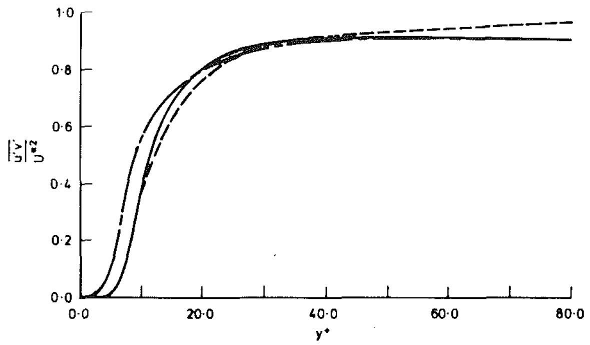

Fig. 1(b) turbulence shear stress

——————— present model, Re = 41667

—— – —— Jones and Launder's model, Re = 41667

------------ measurement, Hinze [12], Re ≃ 41000

Fig. 1 Comparison for various turbulence quantities

which makes f_1 a function of f_μ only. The constant A_{C1} should have a small value so that remote from a wall and when the turbulence level is high, f_μ and hence f_1 will be approximately unity. Close to a wall, f_μ will be small but finite and f_1 will become large. The value of the constant A_{C1} is again obtained by trial and error.

2.3 Development of the function f_2. Low Reynolds number forms of the k-ϵ model [2, 3, 6–8] employ the assumption

$$f_2 = 1 - 0.3e^{-R_t^{\,2}} \tag{13}$$

Since ϵ and its derivatives $\partial\epsilon/\partial x_j$ and $\partial^2\epsilon/\partial x_j^2$ are not infinite at a wall, f_2 must tend to zero as R_t tends to zero. Hence, equation (13) is not directly applicable but can be rectified by omitting the factor 0.3 in front of the exponential term, that is

$$f_2 = 1 - e^{-R_t^{\,2}} \tag{14}$$

2.4 Boundary Condition for ϵ. Since $\nu_t = \partial k/\partial r = 0$ at the wall and ν_l is constant, equation (1) reduces to $\epsilon_w = \nu_l(\partial^2 k/\partial r^2)_w$ the finite difference analog of which is obtained from a Taylor series expansion of k about the wall.

3 Application of the Model

3.1 Optimum Values of the New Constants A_μ, A_t and A_{C1}. Calculations were performed [10] for different Reynolds numbers by using a finite difference scheme with successive over-relaxation. For most cases, 91 grid points and a relaxation factor of 1.51 were used together with the convergence criterion

$$|(\phi_j^{(N)} - \phi_j^{(N-1)})/\phi_j^{(N)}| \le 0.0001$$

where $\phi_j^{(N)}$ is the value of ϕ at the j^{th} grid node after the N^{th} iteration cycle and $\phi_j^{(N-1)}$ that for the $(N\text{-}1)^{\text{th}}$ iteration cycle. Best agreement with the measurements of Nikuradse (as reported in [11]) and those of Laufer reported in [12] was obtained for $A_\mu = 0.0165$, $A_t = 20.5$, and $A_{C1} = 0.05$.

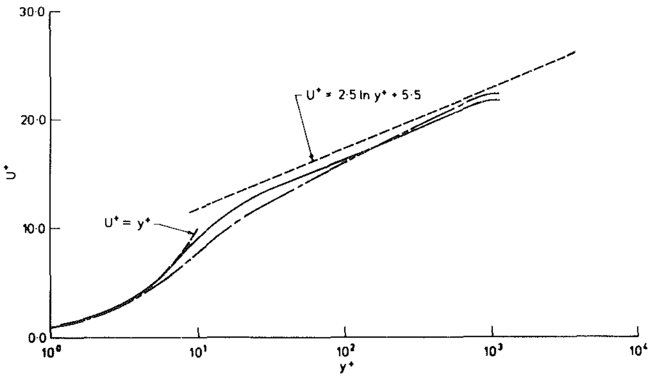

Fig. 2 Variation of mean velocity, Re = 41667

——————— present model

—— – —— prediction with Jones and Launder model

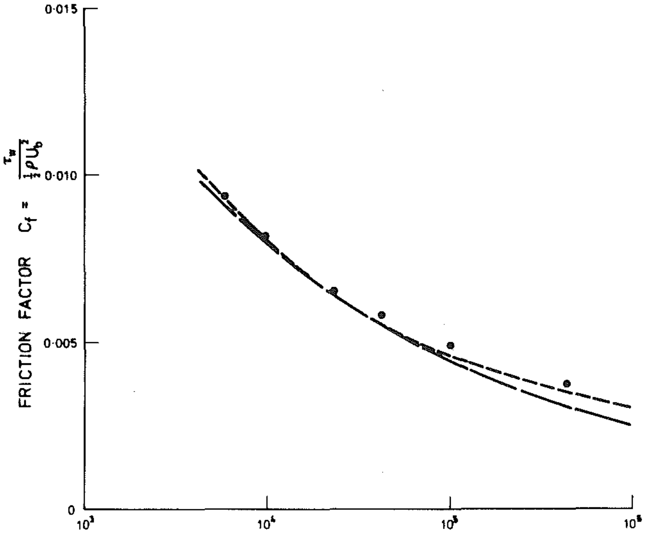

Fig. 3 Variation of friction factor with Reynolds number

⊙ present model, computed points

—— —— —— Blasius [11]

------------ Nikuradse [11]

3.2 Comparison of Predictions With the Present Model and Previous Data. Typical predictions for various turbulence quantities are compared in Figs. 1(*a*) and (*b*) with the model of Jones and Launder using the present finite difference scheme, and with Laufer's measurements made at Re ≃ 41000 as reported by Hinze [12], although, the extrapolated experimental results for $\overline{u'v'}$ at small y^+ have not been shown in Fig. 1(*b*). This is because of the lack of reliable measurements to permit correct extrapolation to meet the known limiting derivatives of $\overline{u'v'}$ at the wall, namely, $\partial[\overline{u'v'}]/\partial y = 0$ and $\partial^2\overline{u'v'}/\partial y^2 = 0$. The present model meets both these values as well as Elrod's [8] limiting

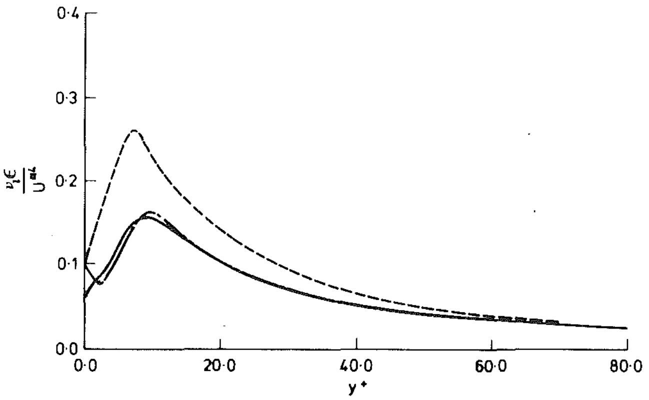

Fig. 4(*a*) Variation of dissipation rate near the wall
__________ present model, Re = 41667
___ - ___ prediction with equation (16) for f_1
- - - - - - - - measurement, Hinze [12] Re = 41000

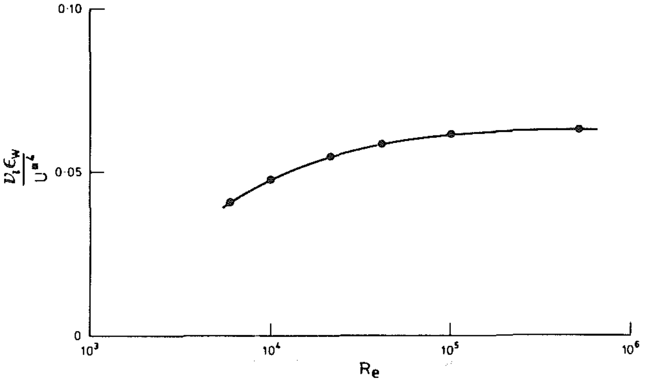

Fig. 4(*b*) Dissipation rate at the wall as a function of Reynolds number
-⊖- present model, computed points

relationship of $\overline{u'v'} \propto y^4$. Predicted velocity distributions using the two models are also compared with the universal velocity profile, Fig. 2. It can be seen that the present model is at least equal to, if not better than that of Jones and Launder.

Comparisons of the friction factor C_f from Nikuradse's data [11] and the Blasius formula

$$C_f = 0.079(\text{Re})^{-0.25} \tag{15}$$

are shown in Fig. 3 for 6000 $\leq$ Re $\leq$ 417000. At low Reynolds numbers (Re < 30000), the agreement is excellent but for higher Reynolds numbers, predicted values appear to be slightly too high. To obtain C_f, full solutions of the equations were obtained [10] at all Re of Fig. 3. For the Re range covered, distributions are similar to those of Figs. 1 and 2.

3.3 Wall Dissipation Rate. The computed near wall variation of dissipation is compared in Fig. 4(*a*) with measurements as reported by Hinze [12]. A discrepancy of about 45 percent is noted at the wall but such a measurement is subject to larger errors. It is shown in [10] that the wall dissipation rate estimated by Hinze from Laufer's data [13] is approximately 1.9 times the correct value, thus favoring the present prediction.

It is also noted that the computed profile for ϵ shows a small "kink" at a $y+$ value of about 5. During an early stage in the development of the present model, it was found that a pronounced "kink" can be produced by choosing a different function for f_1. For example the broken line shown in Fig. 4 was obtained using

$$f_1 = 1 + \left(\frac{0.05}{f_\mu}\right)^2 \tag{16}$$

with $A_\mu = 0.04$, $A_t = 20.54$ and Re = 23300. This is in line with the recent measurements of Schildknecht, et al. [14] who have demonstrated that the measurable portion of ϵ does exhibit such a phenomenon. Until more information for dissipation rate is available, it will be difficult to assert positively the relationship between f_1 and f_μ but it appears that f_1 should be large when f_μ is small, and that f_1 may take the form of

$$f_1 = 1 + \left(\frac{A_{C1}}{f_\mu}\right)^n \tag{17}$$

thus expressing the hypothesis that enhanced dissipation rate near a solid boundary is associated with an increased damping of turbulence length scales.

The dissipation rate at the wall as a function of Reynolds number computed with the present model is shown in Fig. 4(*b*). No experimental data for comparison appear to be available.

3.4 Sensitivity Test. The aim of this test is to study the sensitivity of the solutions with respect to changes in the new constants A_μ, A_t, and A_{C1}. The test was carried out at Re = 23300 for A_μ ± 5 percent and A_{C1} and A_t ± 10 percent about the optimum values of Section 3.1. Detailed results are available in [10] and give changes in C_f of 2.6 percent and −4.0 percent, −3.7 percent and 5.6 percent, and 0.4 percent and −2.0 percent, respectively. Although the predicted friction factor can change by a few percent by varying the constants, the predicted distributions of variables were found not to exhibit noticeable differences except for the dissipation rate, in which the "kink" becomes more pronounced with decreased A_{C1}.

4 Conclusions

A new form of the k-ϵ model has been developed and tested by application to fully developed turbulent pipe flow. The present model is defined by the set of equations (1)-(3). The values of the constants C_μ, C_1, C_2, σ_k, and σ_ϵ have been established by previous workers. The functions f_μ, f_1, and f_2 have the forms given by equations (11), (12), and (14), respectively. The values of the additional constants A_μ, A_t, and A_{C1} are reported in Section 3. Satisfactory predictions have been obtained with the present model and agreement with available experimental data is found to be good. It is also found that the predicted distributions of variables are not very sensitive to small changes in the values of the constants A_μ, A_t, and A_{C1}.

It is established that the present model is valid throughout the fully turbulent, semilaminar and laminar regions in fully developed pipe flows. In contrast to previous forms of the high Reynolds number k-ϵ model, the present one does not require the use of wall function formulas and does not require the introduction of additional terms into the transport equations. The present model also allows a study of predicted versus measured ϵ in the important wall region to be made. Computed profiles for dissipation rate show a small "kink" near the wall which agrees with recent measurements. It is demonstrated that the size of the kink can be altered by adjusting the values of n and A_{C1} in equation (17) but firmer recommendations must await the availability of reliable data for dissipation rate near the wall.

Acknowledgment

The authors gratefully acknowledge the financial support of the Australian Institute of Nuclear Science and Engineering for the work. The authors are also indebted to Mr. J. D.

Hooper for his generous help in the use of the IBM 360/65 computer in the Australian Atomic Energy Establishment.

References

1 Launder, B. E., and Spalding, D. B., "The Numerical Computation of Turbulent Flows," *Computer Methods in Applied Mechanics and Engineering*, Vol. 3, 1974, pp. 269–289.

2 Jones, W. P., and Launder, B. E., "The Prediction of Laminarization With a 2-Equation Model of Turbulence," *International Journal of Heat and Mass Transfer*, Vol. 15, 1972, pp. 301–314.

3 Jones, W. P., and Launder, B. E., "The Calculation of Low-Reynolds Number Phenomena With a Two-equation Model of Turbulence," *International Journal of Heat and Mass Transfer*, Vol. 16, 1973, pp. 1119–1130.

4 Rodi, W., "A Note on the Empirical Constant in the Kolmogorov-Prandtl Eddy-Viscosity Expression," ASME JOURNAL OF FLUIDS ENGINEERING, Vol. 97, 1975, pp. 386–389.

5 Hoffman, G. H., "Improved Form of the Low Reynolds Number k-ϵ Model," *Physics of Fluids*, Vol. 18, No. 3, Mar. 1975, pp. 309–312.

6 Chien, J. C., "Numerical Analysis of Turbulent Separated Subsonic Diffuser Flow," Symposium on Turbulent Shear Flows, University Park, Pennsylvania, Vol. 1, 1977, pp. 18.19–18.25.

7 Hassid, S., and Poreh, M. "A Turbulent Energy Dissipation Model for Flows With Drag Reduction," ASME JOURNAL OF FLUIDS ENGINEERING, Vol. 100, Mar. 1978, pp. 107–112.

8 Elrod, H. G., Jr., "Note on the Turbulent Shear Stress Near a Wall," *Journal of Aeronautical Sciences*, June 1957, pp. 468–469.

9 Gibson, M. M., Spalding, D. B., and Zinser, W., "Boundary-Layer Calculations Using Hassid-Poreh One-Equation Energy Model," Letters in *Heat and Mass Transfer*, Vol. 5, 1978, pp. 73–80.

10 Lam, C. K. G., and Bremhorst, K., "A Modified Form of the k-ϵ Model for Predicting Wall Turbulence," University of Queensland Department of Mechanical Engineering Research Report 3/78, Apr. 1978.

11 Knudsen, J. G., and Katz, D. L., *Fluid Dynamics and Heat Transfer*, International Student Edition, McGraw-Hill, 1958, pp. 152–172.

12 Hinze, J. O. *Turbulence*, McGraw-Hill, 1975, pp. 725–737.

13 Laufer, J., "The Structure of Turbulence in Fully Developed Pipe Flow," NACA Technical Report 1174, 1954.

14 Schildknecht, M., Miller, J. A., and Meier, G. E. A., "The Influence of Suction on the Structure of Turbulence in Fully Developed Pipe Flow," *J. Fluid Mech.*, Vol. 90, 1979, pp. 67–107.

H. B. Awbi
Lecturer,
Mechanical Engineering Department,
University of Technology,
Baghdad, Iraq

S. H. Tan
Formerly Graduate Student,
Mechanical and Production Engineering Department,
Trent Polytechnic,
Nottingham, U.K.

Effect of Wind-Tunnel Walls on the Drag of a Sphere

The wind-tunnel wall interference effect on the drag and base pressure coefficients is investigated experimentally in the range of Reynolds-number independence. The drag results of Achenbach for large blockage ratios are also included, thus covering a range of blockage ratio between 6.3 to 83.9 percent. The measured drag is corrected using blockage correction formulas for three-dimensional flow obtained by the method of images and the analytical equation of Maskell. The results given by Maskell's method are found to be under-corrected by up to 20 percent and the method of images is totally inadequate. Replacing the blockage factor, ϵ, in Maskell's equation by an empirically determined value improved the corrections considerably.

1 Introduction

Due to its complexity, the flow over bluff bodies has recently been receiving intensive investigation by mathematicians and fluid dynamicists. Apart from the academic interest, there is also a need for better understanding of the problem in the industrial and environmental fields. Consequently, numerous wind tunnel investigations are being carried out using bluff-body models of different shapes. The measurements taken on these models suffer, to different extents, from wall constraints. To decrease the wall effects, it is necessary to reduce the size of the model relative to that of the wind tunnel, that is the blockage ratio. On the other hand, to minimize the scale effect by maintaining large models, it is often required to employ large wind tunnels that are costly to construct and expensive to run.

There is, therefore, a necessity for accurate methods of blockage correction. The most reliable theory presently available for bluff body wall constraint is that of Maskell [1]. However, it has been found by different investigators [2–7] that Maskell's original equation is not a universal relation and it requires certain modifications, particularly for correcting the drags and pressures of rectangular prisms and round bodies, the flow over which is dependent upon the Reynolds number.

To the authors' knowledge, there is no published information to attest the suitability of Maskell's method, or any other method, for correcting for the effect of wall constraint on the aerodynamic coefficients for a sphere. The purpose of this investigation was to study the effect of blockage on the drag and base pressure coefficients for a sphere in the Reynolds number range where these aerodynamic coefficients acquire constant values. The experimental results obtained are corrected using blockage formulas that are derived from the method of images for three-dimensional flow [8] and also using Maskell's formula. A semiempirical method of correction, which was based on Maskell's theory, was found to improve the corrections considerably, particularly for large blockage.

2 Experimentation

The wind-tunnel used for this investigation was an open-circuit, suction-type, powered by two contrarotating fans producing a maximum wind speed of 36 m/s in the test section. The air enters the tunnel through a 9:1 contraction leading to a square test section 0.305 m + 0.305 m and 0.61 m long.

The spherical models used were round bottom, commercially available, "quick fit" glass of nominal diameters ranging from 86.31 mm to 188.65 mm covering a blockage ratio, S/C, range between 0.063 to 0.301. The roundness of these flasks was within 0.1 mm of nominal diameter, and the average neck diameter was between 0.14 d and 0.21 d depending on the size of sphere. A 2 mm diameter hole was drilled through the glass wall of each flask close to its neck-end using a high speed engraving machine. The flask was supported by a hollow sting 9.5 mm outside diameter that was connected to an optical manometer for measuring the base pressure.

The drag on the spherical models was measured using a strain gage balance specially constructed for this purpose, Fig. 1. The strain produced at the root of a cantilever 15.9 mm wide, 3.2 mm thick, and 152 mm long was measured on a Wheatstone Bridge. The cantilever was integrated with a streamlined section made of balsa wood to reduce the drag force acting on the cantilever and also to minimize the effect of support interference on the flow. A dummy support system that was fixed to the tunnel floor was used to support the sphere rigidly in its normal position upstream of the "live" support system to evaluate the drag force acting on the live support itself. As a result, a calibration of the supports drag with wind speed was obtained for each sphere.

The buoyancy correction, resulting from the pressure gradient along the tunnel axis caused by the wall boundary layers, was not taken into consideration because it is believed to be insignificant for bluff bodies with high drag. Fur-

---

Contributed by the Fluids Engineering Division for publication in the JOURNAL OF FLUIDS ENGINEERING. Manuscript received by the Fluids Engineering Division, October 1, 1979.

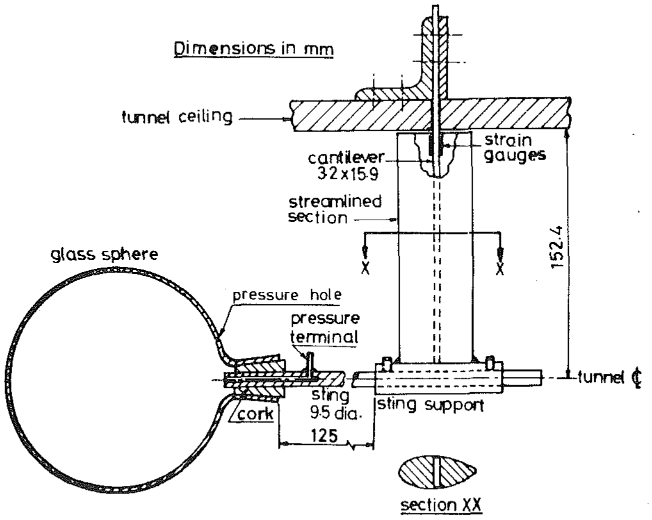

Fig. 1 Sphere support system

thermore, the maximum displacement thickness of the wall boundary layer was estimated to be less than 2 mm.

3 Experimental Results

3.1 Drag Coefficient. In Fig. 2 the drag coefficient, C_D, for the sphere is plotted as a function of Reynolds number, Re, for various blockage ratios. The results of Achenbach [9, 10] for a sphere in a free jet (assumed zero blockage) and in a circular duct representing blockage ratios up to 0.839 are also plotted in the same figure. It should be mentioned here that Achenbach's results given in Fig. 2 are based on the free-stream velocity (i.e., $C_D = \text{drag}/\frac{1}{2}\rho U^2 S$), whereas those given in reference [10] are in terms of minimum gap velocity. The results of the present investigation show that C_D is invariant over the Reynolds number range 6.5×10^4 to 2.2×10^5. As expected, the effect of increasing S/C is to increase the value of C_D; however Achenbach's values are affected by blockage more than the present results. This is presumably due to the development of the boundary layer along the circular duct that Achenbach used for testing his spheres. It is also noted that the increase in C_D as a result of blockage is considerably lower for critical Re than it is for subcritical Re. This is due to the much narrower wakes (hence lower wake blockage effect) for the critical Re flows.

The transition Reynolds number could not be achieved in the present tests. However, Achenbach's data indicate a decrease in the value of transition Re with increasing blockage. At $S/C = 0.839$ the transition Re is approximately 7×10^4 as compared to the unconfined stream value of about 3×10^5.

3.2 Base Pressure Coefficient. The effect of blockage ratio on the base pressure coefficients measured near the necks of the spherical flasks is shown in Fig. 3 for Re = 6.5×10^4 to 2.2×10^5. Over this range of Re, C_{pb} has a constant value which is only affected by blockage. The higher the value of S/C the lower is the pressure coefficient.

The results of Achenbach [9], Calvert [11], and Fage [12] for subcritical Re are plotted in Fig. 3. There is quite a large difference between the C_{pb} values at the lowest blockage ratio ($S/C = 0.063$) and those obtained from references [9, 11, and 12]. It is not immediately obvious why there is such a difference. However, it is worth noting that Calvert's values are not the actual pressures at the surface; they are in fact the

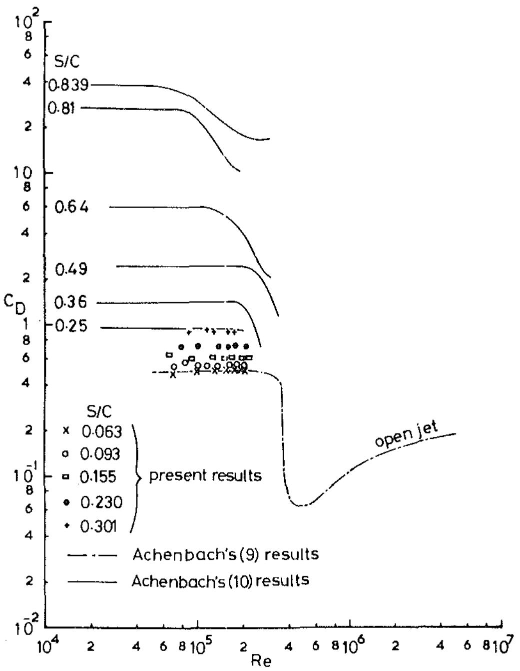

Fig. 2 Effect of Reynolds number and blockage on drag coefficient

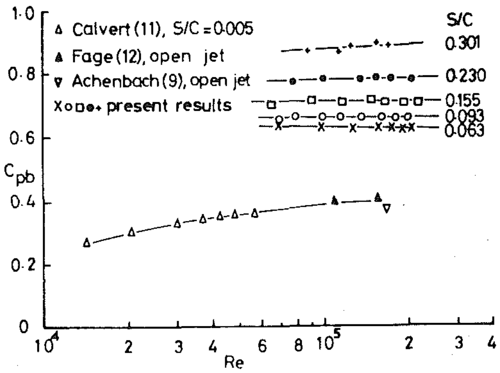

Fig. 3 Base pressure coefficient as affected by Reynolds number and blockage

Nomenclature

C = cross-sectional area of wind tunnel test section
C_D = drag coefficient, drag force/$\frac{1}{2}\rho U^2 S$
C_p = pressure coefficient
C_{pb} = base pressure coefficient
d = diameter of sphere
n = effective dynamic pressure increase factor
Re = Reynolds number, Ud/ν
S = maximum cross-sectional area of sphere, $\pi d^2/4$
U = free-stream velocity
δ = total blockage factor in the method of images, $\delta = \delta_s + \delta_w$
δ_s = solid blockage factor
δ_w = wake blockage factor
ϵ = blockage factor in Maskell's equation
θ = angle measured from front stagnation point
ν = kinematic viscosity
c = subscript denoting a value corrected for blockage

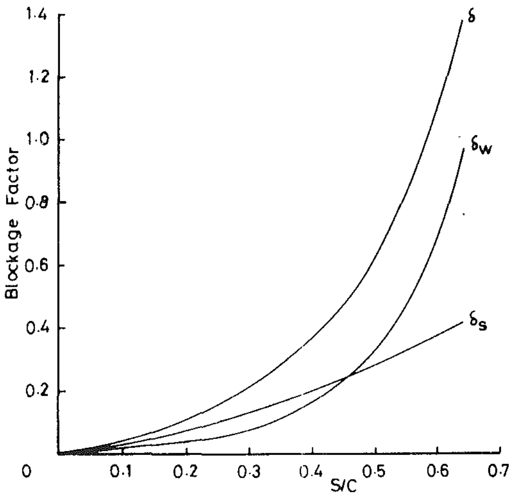

Fig. 4 Solid and wake blockage factors for a sphere

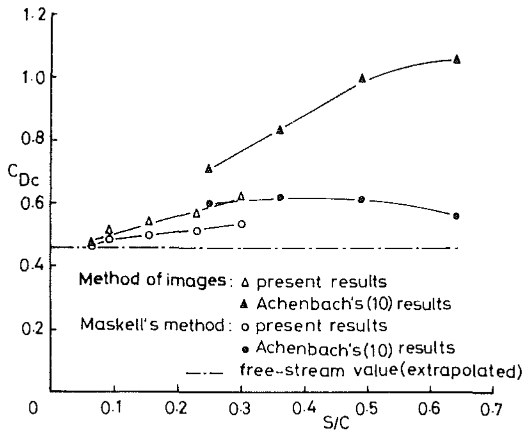

Fig. 5 Corrected drag coefficient using the images and Maskell's methods

readings of a pitot tube set at the aftermost point of the sphere. Furthermore, the measurements of Achenbach [9] and Fage [12] were conducted in an open jet wind-tunnel which gives a negative blockage effect [8], i.e., a higher value of base pressure coefficient than the free-stream value.

A comparison of measured values of C_{pb} and C_D for different blockage ratios shows that $|C_{pb}|$ is greater than C_D (except for the largest S/C). The results of references [9, 12, 13] however, show that for subcritical Re, $C_D > |C_{pb}|$. The latter is to be expected since Achenbach [9] and Fage [12] have found that boundary layer separation takes place at $\theta = 82$ deg from the front stagnation point and between this point and $\theta = 180$ deg, C_{pb} is almost constant. This suggests that the present pressure coefficients in Fig. 3 which were measured on the surfaces of the spherical flasks between $\theta =$ 160 and 170 deg, do not represent true values of *mean* base pressure coefficients for a sphere. As pressure distribution over the base is not available, it is not possible to explain, with certainty, these low pressures. However, it is clear that the position of the pressure tapping was too close to the sphere's neck and interference to the flow in that vicinity, due to the presence of the neck and the supporting sting, could have caused a reduction of pressure in that region of the flask.

4 Methods of Blockage Correction

4.1 Method of Images. The classical approach of blockage correction for streamlined objects that represent aerofoils and parts of aircrafts, is to separate the effect into a component due to the physical dimensions of the model, usually termed "solid blockage," and another component due to the wake, appropriately called "wake blockage." The solid and wake blockage effects are represented by factors, δ_s and δ_w, respectively, such that the net wall effect is taken as an "induced velocity" added to the value of tunnel velocity. That is,

$$U_c = U(1+\delta) \tag{1}$$

where U = tunnel velocity and U_c = corresponding free-stream velocity and $\delta = \delta_s + \delta_w$. The values of δ_s and δ_w are usually determined separately using the method of images, e.g., see references [8, 14].

For a sphere in a square test section, reference [8] gives the following formula due to C. N. H. Lock:

$$\delta_s = 0.809(S/C)^{3/2} \tag{2}$$

The wake blockage factor has been represented by *A*. Thom (see reference [8]) in terms of the measured drag coefficient for the body, thus:

$$\delta_w = \frac{1}{4} C_D S/C \tag{3}$$

The above concept implies that constraint increases the effective dynamic pressure by a factor n (assuming incompressible flow), so that forces and surface pressures increase as given by the following equation:

$$n = \left(\frac{U_c}{U}\right)^2 = \frac{C_D}{C_{Dc}} = \frac{1-C_p}{1-C_{pc}} \tag{4}$$

Suffix c denotes corrected value. Applying equation (1), n becomes:

$$n = (1+\delta)^2 \tag{5}$$

Using equations (2) and (3) the solid and wake blockage factors δ_s and δ_w were calculated and are shown plotted in Fig. 4 together with the total blockage factor, δ. It is noted that for $S/C < 0.45$, δ_w is less than δ_s and this is irrational knowing that the flow over a sphere at subcritical Re consists of a large separated region. However, as S/C increases further and the measured drag becomes very large, δ_w increases much more rapidly than δ_s. The shortcoming of equation (3) is not surprising bearing in mind that the equation was originally derived for streamline flow with a small or no separated region. The corrected drag coefficients obtained using equations (4) and (5) are plotted in Fig. 5. This figure depicts that the effect of blockage has been underestimated particularly at large blockages.

4.2 Maskell's Method. Maskell's [1] wake blockage theory requires little introduction, for it has received considerable attention in recent years, for the blockage correction of bluff bodies. It was originally developed for correcting the drag and pressure coefficients of thin flat plates of various shapes set normal to the wind or at high incidence such that full flow separation takes place. Consequently, the theory was tested for bluff bodies of different shapes and in various flow situations [2 to 7]. The results of these investigations indicate that Maskell's scheme is not universal as it has previously been anticipated.

Maskell's correction equation is given by:

$$n = 1 + \epsilon\, C_D S/C \tag{6}$$

where

$$\epsilon = -\frac{1}{C_{pbc}} \tag{7}$$

There are certain boundary conditions imposed during the development of the theory to arrive at equation (6). Assuming that the blockage ratio is not too large so that the wake does not fill the tunnel cross section, these conditions are:

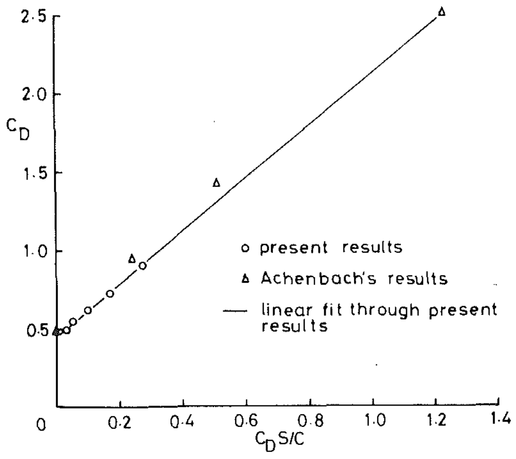

Fig. 6 Dependence of drag coefficient on blockage parameter

(i) fixed separation positions on the model;
(ii) constant base pressure which is equal to the static pressure along the outer wake boundary;
(iii) the pressure distribution on the model is invariant under constraint.

Although these conditions were found to be true for flat plates normal to the flow, the second condition did not apply to rectangular-section prisms [2]. In the latter case, the blockage factor, ϵ, as given by equation (7) was found to be inadequate for correcting the drags and pressures of those prisms.

The drag coefficients which are corrected using equations (6) and (4) and a value of $C_{pbc} = -0.40$ (i.e., $\epsilon = 2.5$) taken from references [9, 12], are shown in Fig. 5. As depicted in the figure, Maskell's correction, although underestimates the effect of constraint at large values of S/C, predicts values of C_{Dc} that are nearer to the extrapolated value ($C_{Dc} = 0.46$) than those estimated using the method of images.

4.3 Semi-Empirical Method. It has been shown [2] that, for moderate blockage ratios, the measured drag and base pressure coefficients for bluff bodies of various shapes bear a linear relationship to the blockage parameter $C_D\ S/C$, as predicted by equation (6). Figure 6 depicts that this is also true for a sphere under wall constraint, at subcritical Re, up to $C_D\ S/C = 1.23$ which corresponds to a blockage ratio of 0.5. Above this value of S/C, linearity breaks down and indeed correction for wall constraint becomes meaningless, because at large blockage the sphere wake almost fills the tunnel test section. The blockage factor obtained from Fig. 6 is $\epsilon = 3.58$, c.f. 2.5 from equation (7). The drag coefficients corrected using the empirical value of ϵ are plotted in Fig. 7. As would be expected the corrected drag coefficients of this investigation are very close to the extrapolated value, and those of Achenbach are within 10 percent of the extrapolated value for up to $S/C = 0.64$.

Although the pressures measured on the surfaces of the spheres do not represent mean base pressures as outlined previously, it is thought advantageous to obtain the value of ϵ required to correct these pressures. A value of $\epsilon = 0.63$ was found from the slope of the straight line of Fig. 8 and the corrected pressures are also shown in the same figure. This value of ϵ is vastly different from that of 3.58 for correcting the drag coefficients. This difference signifies that, for the present investigation at least, the drag is affected by wall constraint significantly more than the base pressure.

5 Conclusions

(i) The method of separating the effect of solid blockage from that of wake blockage is not feasible for correcting the drag of a sphere at subcritical Re. For $S/C < 0.5$ this method gives a lower estimate of the blockage effect of the wake than that due to the physical size of the sphere representing the solid blockage.

(ii) Maskell's equation predicts the total blockage effect quite well for low blockage, i.e., $S/C < 0.1$. At larger blockage, the equation gives less accurate estimation of the effect.

(iii) The linear relation between C_D and $C_d\ S/C$ is valid for $S/C < 0.5$. The value of the blockage factor obtained from this plot, when used in Maskell's equation, give corrected drag coefficients that are independent of blockage.

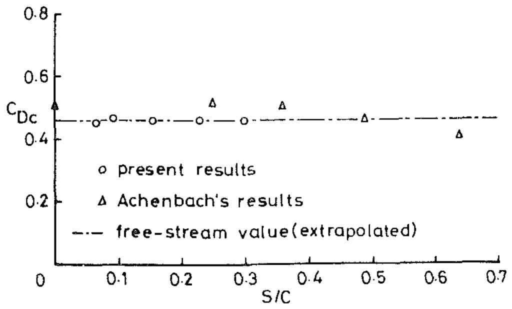

Fig. 7 Corrected drag coefficient using semiempirical equation

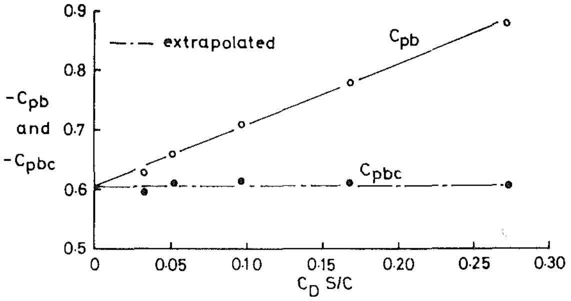

Fig. 8 Corrected and uncorrected base pressure coefficient

Acknowledgment

The encouragement given by Dr. H. M. Al-Samirrai, Head of Mechanical Engineering Department, University of Technology, Baghdad, is acknowledged with gratitude.

Experimental Uncertainty

The tables below represent the uncertainty limits for the figures that display the experimental data obtained during this investigation. The uncertainty intervals were estimated using the single-sample uncertainty method of Kline and McClintock (1953). The fixed errors were estimated to be much smaller than the random uncertainty intervals given and therefore have no influence on the trends of the output graphs.

Fig. 2

Uncertainty of (C_D Re $\times 10^{-5}$)

Coordinate	Uncertainty
(0.50, 0.99)	(±0.05, ±0.02)
(0.90. 1.55)	(±0.05, ±0.04)

Absolute values; 20:1 odds

Fig. 3

Uncertainty of ($-C_{pb}$ Re $\times 10^{-5}$)

Coordinate	Uncertainty
(0.63, 1.29)	(±0.02, ±0.03)
(0.89. 1.55)	(±0.07, ±0.04)

Absolute values; 20:1 odds

Fig. 5

Uncertainty of (C_{Dc}, S/C)

Coordinate	Uncertainty
(0.49, 0.093)	(±0.03, ±0.007)
(0.54. 0.301)	(±0.01, ±0.002)

Absolute values; 20:1 odds

Fig. 6

Uncertainty of (C_D,C_DS/C)

Coordinate	Uncertainty
(0.55, 0.051)	(±0.04, ±0.004)
(0.90, 0.272)	(±0.05, ±0.016)

Absolute values; 20:1 odds

Fig. 7

Uncertainty of (C_{Dc},S/C)

Coordinate	Uncertainty
(0.47, 0.093)	(±0.03, ±0.007)
(0.47, 0.301)	(±0.05, ±0.002)

Absolute values; 20:1 odds

Fig. 8

Uncertainty of ($-C_{pb}$,C_DS/C)

Coordinate	Uncertainty
(0.66, 0.051)	(±0.02, ±0.004)
(0.88, 0.272)	(±0.07, ±0.016)

Absolute values; 20:1 odds

References

1 Maskell, E. C., "A Theory of Blockage Effects on Bluff Bodies and Stalled Wings in a Closed Wind Tunnel," *ARC* R & M 3400, 1963.

2 Awbi, H. B., "Wind Tunnel Wall Constraint on Two-Dimensional Rectangular-Section Prisms," *J. Ind. Aerodynamics*, Vol. 3, No. 4, 1978, pp. 285-306.

3 Cowdrey, C. F., "The Application of Maskell's Theory of Wind-Tunnel Blockage to Very Large Models," *NPL* Aero Report 1247, 1967.

4 Sykes, D. M., "Blockage Corrections for Large Bluff Bodies in Wind Tunnels," *Advances in Road Vehicles Aerodynamics*, BHRA Fluid Engineering, 1973.

5 McKeon, R. J., and Melbourne, W. H., "Wind Tunnel Blockage Effects and Drag on Bluff Bodies in a Rough Boundary Layer," *Proc. of the Third Int. Conf. on Wind Effects on Buildings and Structures*, Tokyo, 1971, pp. 263-272.

6 Modi, V. J., and El-Sherbiny, S., "On the Wall Confinement Effects in Industrial Aerodynamics Studies," *Int. Symp. Vibration Problems in Industry*, Keswick, England, Paper No. 116, 1973.

7 Farell, C., et al., "Effect of Wind-Tunnel Walls on the Flow Past Circular Cylinders and Cooling Tower Models," ASME JOURNAL OF FLUIDS ENGINEERING, Sept. 1977, pp. 470-479.

8 Pankhurst, R. C., and Holder, D. W., "*Wind-Tunnel Technique*," Pitman, 1968, Chapter 8.

9 Achenbach, E., "Experiments on the Flow Past Spheres at Very High Reynolds Numbers," *J. Fluid Mech.*, Vol. 54, Part 3, 1972, pp. 565-575.

10 Achenbach, E., "The Effects of Surface Roughness and Tunnel Blockage on the Flow Past Spheres," *J. Fluid Mech.*, Vol. 65, Part 1, 1974, pp. 113-125.

11 Calvert, J. R., "Some Experiments on the Flow Over a Sphere," *Aeronautical Journal*, Apr. 1972, pp. 248-250.

12 Fage, A., "Experiments on a Sphere at Critical Reynolds Numbers," *ARC* R & M 1766, 1937.

13 Hoerner, S., "*Aerodynamic Drag*," Published by the Author, 1951, pp. 22-23.

14 Pope, A., and Harper, J. J., "*Low-Speed Wind Tunnel Testing*," Wiley, 1966, Chapter 6.

J. A. C. Humphrey

S. Li

Department of Mechanical Engineering,
University of California,
Berkeley, Calif. 94720

Tilting, Stretching, Pairing and Collapse of Vortex Structures in Confined Counter-Current Flow

Visualization observations are reported for the time evolving vortex structure at the interface of a counter-current channel flow. The results are primarily qualitative in nature, but show clearly the evolution of a two-dimensional saddle-point flow into a complex, three-dimensional, periodic vortex-pairing process. Generation, pairing and collapse of the flow structure at the free interface is attributed to tilting and stretching of transverse vorticity by the main flow in the longitudinal direction. It is suggested that the present flow configuration may prove of use for investigating mixing in chemically reacting flows due to entraining vortex motions.

Introduction

In the course of an experiment originally intended for establishing the in situ growth and pairing of coherent vortex structures of the type first observed by Brown and Roshko [1] we have discovered various two- and three-dimensional flow phenomena of a rather unusual type. While the new observations also correspond to the periodic generation and pairing of vortex structures, as will be shown, they are quite distinct in nature and without precedent in the open literature. In particular, upon pairing, the vortical structures in the flow become unstable and collapse. Collapse of the structures is characterized by an intense local mixing of the flow which everywhere else is streamlined. Although the complex flow reported here is not yet fully understood, its potential for visualizing and helping to understand mixing (with or without chemical reaction) as a consequence of vortex pairing warrants a description and discussion of some interesting observations made to date.

Flow System

The flow system is illustrated in Fig. 1 and shows two constant head tanks from which water at room temperature was delivered to the counter-flowing test section. The flow entering each symmetrical channel section was passed through two perforated plates and a screen to remove large scale swirl and inhomogeneities. It then continued through a 4:1 converging passage prior to entering a straight duct of 3.81 by 5.08 cm^2 rectangular cross-section. A continuous, smooth, splitter plate 8.90 cm in length kept the symmetrical flows separate until the 7.62 cm long free-interface portion of the test section was reached. It was at this station that the observations reported here were made.

Flow meters were placed far upstream and downstream of the entrance and exit stations to the test section and permitted the determination of mass flow rates to within ± 5 percent. Flow rates were preset by means of needle valves while synchronized solenoid valves were used to simultaneously start and stop the respective channel flows. The solenoid valves remained fully open during the course of an experiment. Flow patterns were visualized by dissolving methylene blue in one of the channel flows or by means of a dilute acid/(excess) base reaction with thymol blue initially present in the acid stream. The latter technique is tri-color and allows visualization of the chemically reacting interface. Possible buoyancy-driven motions due to the presence of the chemical species required for visualization were completely negligible in the flow. For the Reynolds number range reported here, $370 < Re < 1000$, visualization also showed that the two channel flows were laminar; $Re = WV/\nu$ where $W = 3.81$ cm is the channel width and V is the mass average velocity in one of the channels. Results are given here for the

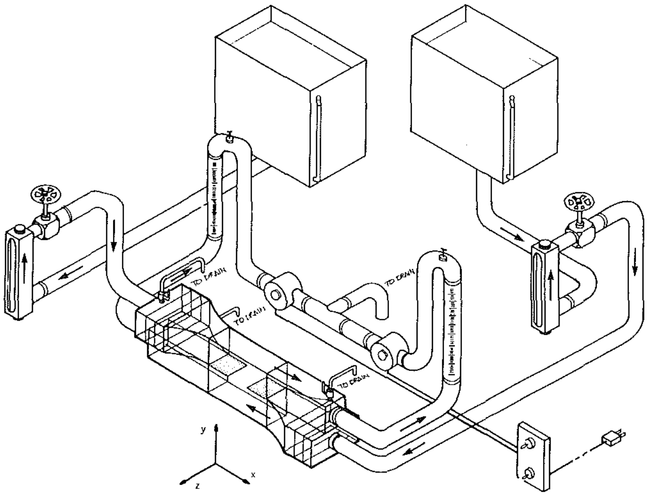

Fig. 1 Confined counter-current flow system and definition or coordinates

---

Contributed by the Fluids Engineering Division of THE AMERICAN SOCIETY OF MECHANICAL ENGINEERS and presented at the Winter Annual Meeting, Chicago, Ill., November 17-21, 1980. Paper No. 80-WA/FE-11. Manuscript received by the Fluids Engineering Division, December 17, 1979.

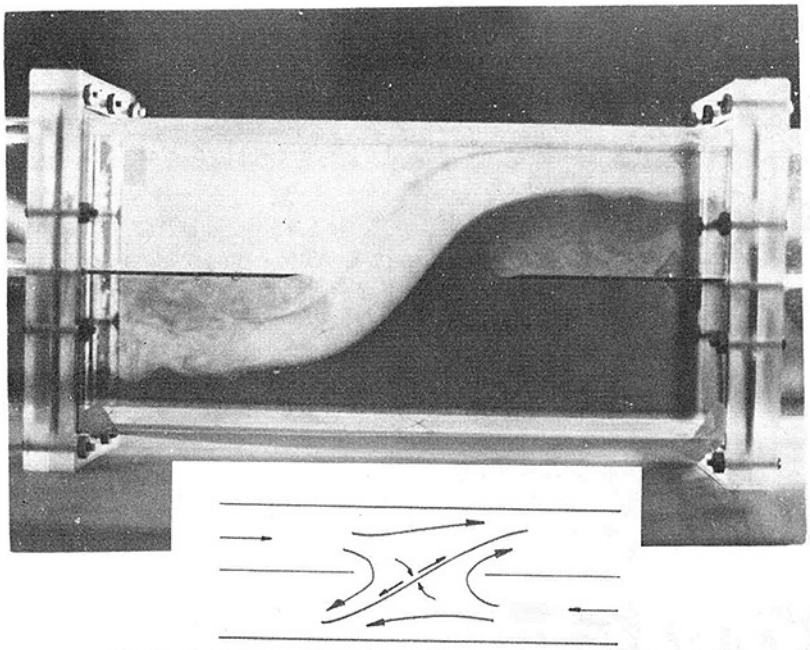

Fig. 2 Typical two-dimensional flow a few seconds after starting motion from rest showing saddle-point structure initially present in this flow. Top flow is from left and bottom flow is from right.

case of equal channel flow rates entering and leaving the test section. Unequal flow rate observations did not differ fundamentally from the results presented.

Results and Discussion

A typical side view of the flow field a few seconds after starting the motion from rest is given in Fig. 2. The figure shows respectively bifurcating channel flows impinging at a saddle point on the tilted interface delineating the two channel streams. Bifurcation of the flows is due to the transverse pressure gradients imposed by the main (longitudinal) motions. An important consequence of bifurcation is the removal by convection from the saddle point region on the tilted interface of essentially all span-wise vorticity (ω_z) initially generated at the splitter plate.

Whereas the motion just described is essentially two-dimensional, it is soon followed by a spectacular three-dimensional phenomenon as shown in the sequences of Figs. 3 and 4. These figures show side and top wall views respectively of the behavior of two vortices which are sequentially created, amplified, paired and collapsed along a tilted interface. Collapse of the paired vortex structures is characterized by a short period of intense local mixing at much smaller scales. The mixed flow is convected away from the interface region by the main streams and the two- to three-dimensional flow sequence repeats again.

Early experiments showed that evolution from the two-dimensional flow to the three-dimensional flow was erratic; in the sense that both the time required for vortex generation and pairing, and the sense of vortex rotation, were irregular and dependent on the flow-rate settings for the respective streams. Three possibilities were observed for the sense of rotation of the two vortices, corresponding to: (*a*) clockwise co-rotating vortices; (*b*) counter-clockwise co-rotating vortices; (*c*) counter-rotating vortices. Thus, upon pairing and collapse the sense of rotation of the new vortex pair was any of the three possibilities listed above, as dictated by preponderant instabilities in the flow.

By skewing the inlet flows to the respective converging channel sections the vortex pairing phenomenon was rendered periodic and reproducible. Skewing of the flow in the channel sections was accomplished by masking with tape 20 percent of the open area of the first perforated plate in each section (at one end of the plate; opposite ends in each section). Thus, counter-clockwise co-rotating vortices were generated in this study as shown in Fig. 4. For the above conditions vortex pairing periodicity was a function of Reynolds number as shown in Fig. 5. With more than 50 percent of plate areas masked the flow behavior reverted to erratic and unpredictable. Vortex pairing frrequency did not appear to be sensitive to the amount of area masked for values less than 50 percent.

A pair of stable counter-rotating vortices could only be generated by removing the masking tape from the perforated plate in one channel section and masking both ends of the perforated plate in the other. For equal mass flow rates the higher inertia of the constricted stream determined the sense of vortex rotation.

Longitudinal vorticity (ω_x) was observed to be negligible in the straight channel sections preceding the free interface. Because flow bifurcation also removes spanwise vorticity (ω_z) from the free interface, an explanation for the generation and growth of the two vortices must be given in terms of the transverse (ω_y) component of vorticity. For purposes of further discussion, Fig. 6 provides a simplified but helpful representation of the three-dimensional tilted interface flow region. Due to the asymmetry induced in the incoming velocity profiles, tranverse vorticity is distributed unevenly along the width of each channel flow. While this component of vorticity is weaker in the low velocity region of each flow moving towards the free interface than it is in the high velocity region, ω_y associated with the low velocity is extended over most of the width of the test section. Tilting and subsequent stretching (amplification) of transverse vorticity along the inclined interface (giving a component of vorticity in the longitudinal direction, *x*) arises mainly as a consequence of the gradient $\partial U_x/\partial y$ in the product ω_y $(\partial U_x/\partial y)$ in the longitudinal component vorticity equation. Contributions to ω_x due to ω_x $(\partial U_x/\partial x)$ and ω_z $(\partial U_x/\partial z)$ are small because ω_x and ω_z are initially negligible in the flow approaching the free interface. The transverse gradient of longitudinal velocity, $\partial U_x/\partial y$, approaching the free interface, is larger in the low

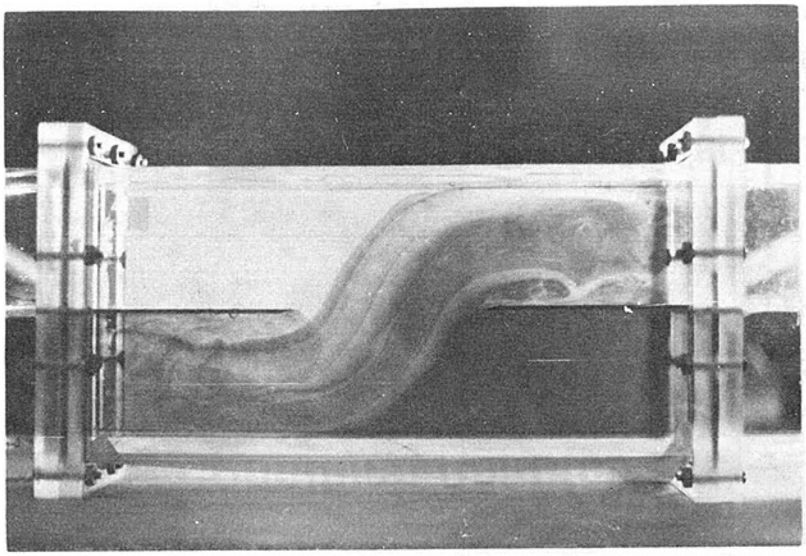

Fig. 3(*a*)

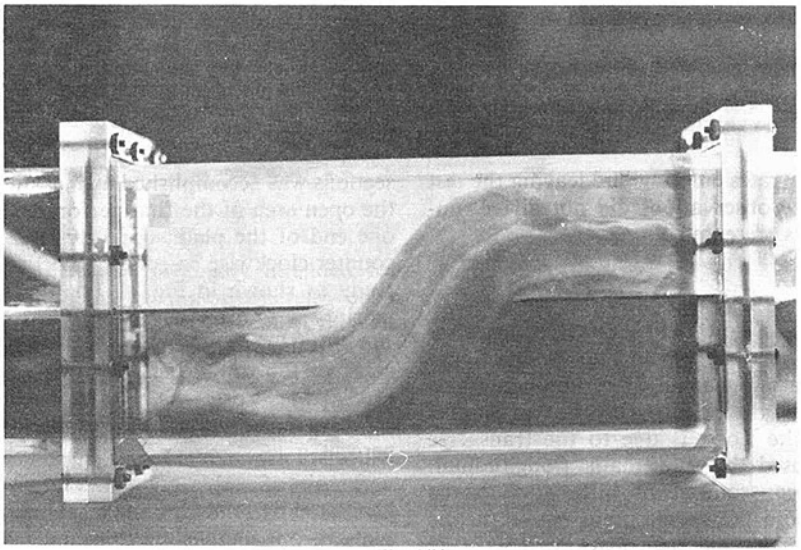

Fig. 3(*b*)

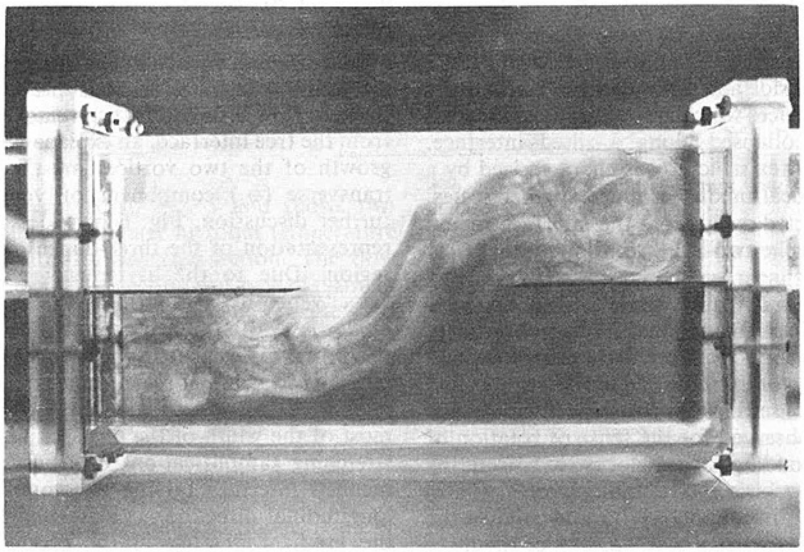

Fig. 3(*c*)

Fig. 3 Consecutive (*a*, *b*, *c*) side views of vortex pairing process at intervals of 10 s, Re = 500. Top flow is from left and bottom flow is from right.

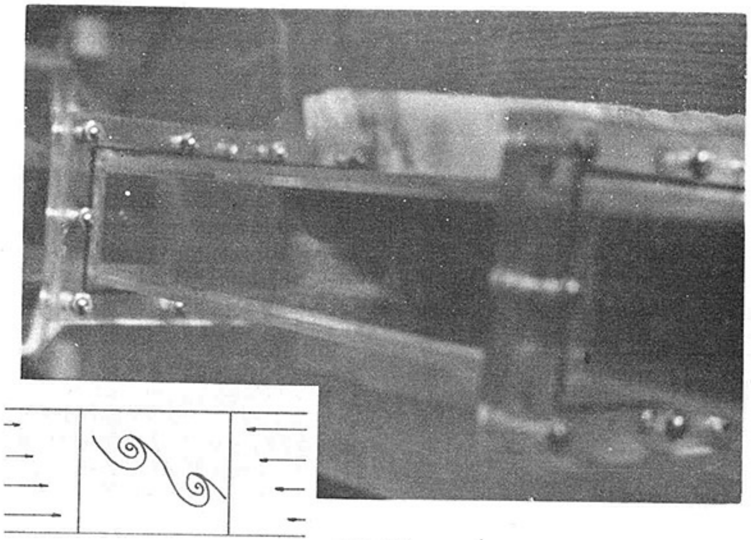

Fig. 4(*a*)

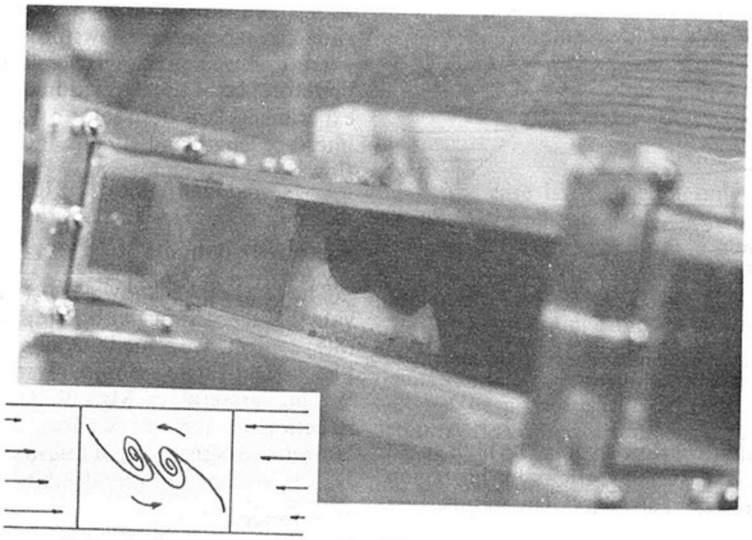

Fig. 4(*b*)

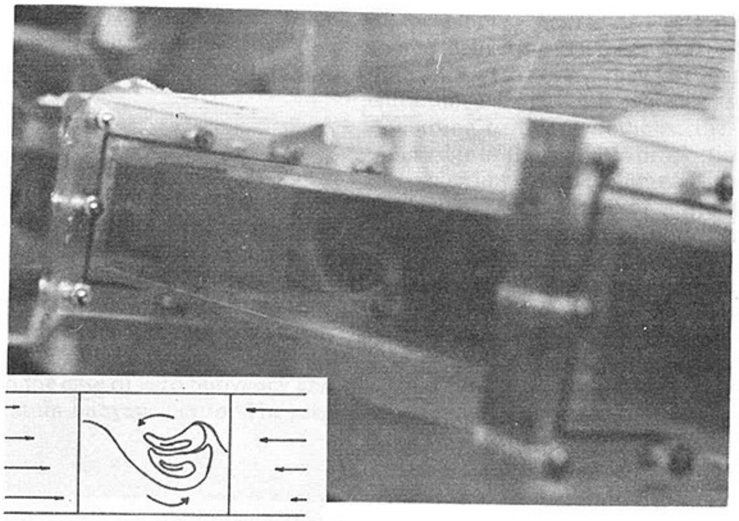

Fig. 4(*c*)

Fig. 4 Consecutive (*a*, *b*, *c*) top views of vortex pairing process at intervals of 10 s, Re = 500. Sense of vortex rotation is counterclockwise due to imposed skewing of inlet velocity profiles.

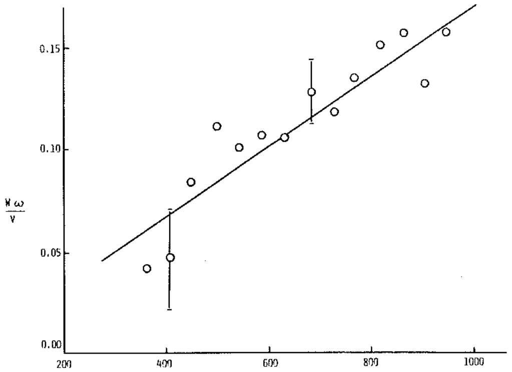

Fig. 5 Pairing frequency of vortex structures as a function of Reynolds number

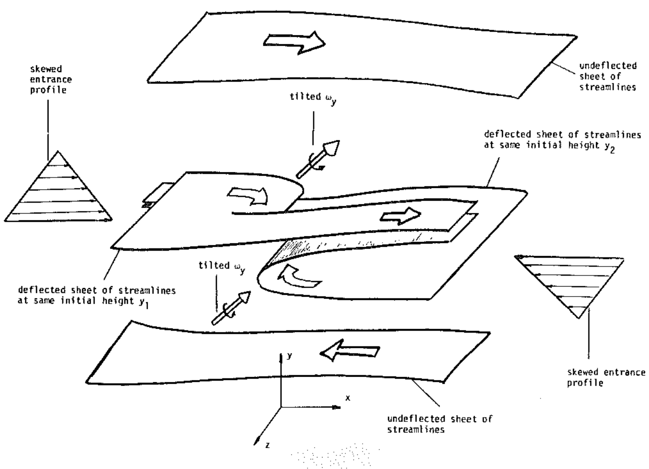

Fig. 6 Simplified schematic of streamline surfaces in the vicinity of and away from the tilted interface. Relative positions of vortex structures indicated by ω_y.

speed region of incoming channel flow than in the high speed region.[1] As a consequence, transverse vorticity in this region of the free interface is titled more strongly. This results in a weaker, but more widespread, pair of vortex tubes dominating the flow. The strain field around the stagnation point is responsible for the reorientation of the side walls' vertical (y) vorticity along the direction of maximum strain and for its intensification. Vortex pairing occurs when the two vortices (with vorticity of the same sign) are brought close together, possibly by the strain field. While the periodic character of the flow is not yet understood, the chaotic low Reynolds number motion ensuing collapse eventually reverts to a streamlined motion to reproduce the events just described.

Conclusions

An unusual fluid motion has been qualitatively described which evolves from a two-dimensional saddle point flow into the strongly three-dimensional periodic pairing process of two vortex tubes. It would appear that the growth, pairing and subsequent collapse of these structures is due mainly to tilting and stretching of transverse vorticity in the flow. To our knowledge this type of fluid motion has not been observed before.

An attractive feature of the experiment is the relative ease with which vortex pairing phenomena could be investigated in situ. The experiment shows promise for allowing the study of vortex-induced mixing in chemically reacting flows and could, therefore, be of use in relation to combustion studies. Further experiments are desirable to examine the influence of free interface length and viscous and buoyant stratification in this flow.

Acknowledgments

The authors acknowledge with gratitude, frequent and valuable discussions with Professor G. Corcos. Funding for this project was made available by the Department of Mechanical Engineering, University of California, Berkeley. We are grateful to Mr. W. Gandola for the precise construction of the test section. Thanks are due to Miss J. Harmon for the typing of this manuscript.

Reference

1 Brown, G., and Roshko, A., "On Density Effects and Large Structure in Turbulent Mixing Layers," *J. Fluid Mech.*, Vol. 64, 1971, pp. 775-816.

---

[1] Ignoring boundary layer and wake effects due to termination of the splitter plate.

W. F. Phillips
Associate Professor,
Department of Mechanical Engineering,
Utah State University,
Logan, Utah 84322

The Effect of Froude Number on Entrainment in Two-Dimensional Line Plumes

Theoretical results are presented which predict the entrainment coefficient in a forced plume as a function of the local Froude number. The model does not require any external specification of the velocity and temperature profiles. The Froude number for any plume, in a motionless isothermal ambient, approaches a universal constant, at a large distance above the source. However, it is shown here that the development length for the Froude number, in plumes with high discharge Froude number, is of the order of a few hundred times the discharge width.

Introduction

The mathematical modeling of jets and plumes has been of interest for many decades. Many papers have been written which deal with the modeling of jets and plumes generated from sources which deliver a steady flux of mass, momentum and buoyancy. Excellent reviews of this work have been presented by Briggs [1], Hirst [2], and Davis and Shirazi [3]. The models which have been developed can be divided into two classes, those models which are derived from a differential formulation and those models which are obtained using an integral formulation.

The differential models are based on the original work of Tollmien [4], Schlichting [5], and Schmidt [6]. Models of this type are obtained from solutions to the appropriate boundary layer equations. This system of partial differential equations provides a formulation for determining the axial velocity, V_x, the transverse velocity, V_y, the temperature, T, and the concentration, ρ, as a function of the axial distance above the source, x, and the transverse distance from the axis, y. These equations are made more mathematically tractable through a similarity transformation in powers of x. For example, the axial velocity is written as

$$V_x(x,y) = x^n u(y/x^m), \qquad (1)$$

where the exponents n and m are chosen to make the boundary layer equations separable. There are two major drawbacks to the models which are obtained using this transformation. First of all, the transformation is singular at $x = 0$. This means that the models are only valid for large x, unless the source is a virtual point source with zero mass flux. Secondly, this transformation produces separable equations for only two specific values of Froude number. These two Froude numbers correspond to the case of zero buoyancy and the case of equilibrium momentum-buoyancy ratio. The zero buoyancy case is of interest only for isothermal jets. The equilibrium momentum-buoyancy ratio only develops at large x. Near the origin, the Froude number is controlled by the source. As the flow moves away from the source, the momentum and buoyancy are changed through interactions with the surroundings and the Froude number approaches its equilibrium value. Thus, plume models which are based on the method of Tollmien [4], Schlichting [5], and Schmidt [6], will not be accurate near a finite source which delivers an arbitrary flux of mass, momentum and buoyancy.

In order to avoid these limitations, approximate integral models have been developed. These models are based on the initial work of Taylor [7], Priestley and Ball [8] and Morton, et al. [9]. They are often referred to as Gaussian models. Such models do not require mass, momentum, and energy to be conserved at every point within the plume. They only require these quantities to be conserved on an average over the width of the plume. Models of this type can be used for a finite source delivering a steady flux of mass, momentum, and buoyancy. However, they are based on a very simplified entrainment hypothesis which was proposed by Taylor [7]. According to this hypothesis, the transverse velocity at the outer edge of the plume is proportional to the axial velocity on the centerline of the plume. It was originally assumed by Taylor [7], that the ratio of entrainment velocity to centerline velocity is independent of both the plume velocity and temperature. With this entrainment hypothesis, the fundamental moments of the continuity, momentum, and energy equations can be satisfied. More recently, Fox [10] has shown that the ratio of entrainment velocity to centerline velocity is a function of the local Froude number. Fox found that a linear relationship, between this ratio and the inverse square of the Froude number, would satisfy the first moment of the momentum equation as well as all the fundamental moments. All models of this type require an external specification of the velocity and temperature profiles. Usually Gaussian profiles are assumed.

In the present paper, the differential boundary layer equations are used to develop a plume model which can be used for a finite source which discharges an arbitrary flux of

---

Contributed by the Fluids Engineering Division and presented at the Joint Applied Mechanics, Fluids Engineering, and Bioengineering Conference, Boulder, Colo., June 22-24, 1981, of THE AMERICAN SOCIETY OF MECHANICAL ENGINEERS. Manuscript received by the Fluids Engineering Division, August 28, 1980. Paper No. 81-FE-6.

mass, momentum and buoyancy. From this model, a relationship for the plume entrainment is derived. The model does not require any external specification of the velocity and temperature profiles, as does the integral model of Fox [10]. The present model predicts the entrainment coefficient as a function of the local Froude number. However, the relationship is somewhat different from that of Fox [10].

Two-Dimensional Line Plumes

Consider a two-dimensional Cartesian plume rising vertically through a motionless isothermal ambient. Let x be the vertical coordinate measured above the position of the source and y be the horizontal coordinate measured outward from the centerline of the plume. The fluid velocity in the x-direction will be denoted as V_x, the velocity in the y-direction will be V_y and the buoyancy will be given the symbol ϕ. The buoyancy can be expressed in terms of temperature, $\phi(x,y) = \beta g[T(x,y) - T_\infty]$, where β is the coefficient of thermal expansion, g is the acceleration of gravity, T is the plume temperature, and T_∞ is the ambient temperature. Here we shall consider the case where the plume is composed of the ambient fluid and a trace concentration of one foreign species. The concentration of this foreign species will be referred to as ρ. Additional foreign species can be handled in an indentical manner.

Using the boundary layer approximation and the Boussinesq approximation, the conservation of mass, momentum, energy, and species yield the well known formulations

$$\frac{\partial V_x}{\partial x} + \frac{\partial V_y}{\partial y} = 0, \tag{2}$$

$$\nu \frac{\partial^2 V_x}{\partial y^2} - V_x \frac{\partial V_x}{\partial x} - V_y \frac{\partial V_x}{\partial y} + \phi = 0, \tag{3}$$

$$\frac{\nu}{\mathrm{Pr}} \frac{\partial^2 \phi}{\partial y^2} - V_x \frac{\partial \phi}{\partial x} - V_y \frac{\partial \phi}{\partial y} = 0, \tag{4}$$

$$\frac{\nu}{Sc} \frac{\partial^2 \rho}{\partial y^2} - V_x \frac{\partial \rho}{\partial x} - V_y \frac{\partial \rho}{\partial y} = 0, \tag{5}$$

This formulation can be used for either laminar or turbulent flow. If the flow is laminar, ν, Pr, and Sc are, respectively, the kinematic viscosity, Prandtl number, and Schmidt number for the fluid. If the flow is turbulent, these three parameters are the virtual kinematic viscosity, the turbulent Prandtl number, and the turbulent Schmidt number, respectively. This formulation and the underlying assumptions have been adequately discussed in the literature and will not be discussed here.

The y boundary conditions for this system of equations are

$$V_y(x,0) = 0, \tag{6}$$

$$\frac{\partial V_x}{\partial y}(x,0) = 0, \tag{7}$$

$$V_x(x,\infty) = 0, \tag{8}$$

$$\frac{\partial \phi}{\partial y}(x,0) = 0, \tag{9}$$

$$\phi(x,\infty) = 0, \tag{10}$$

$$\frac{\partial \rho}{\partial y}(x,0) = 0, \tag{11}$$

$$\rho(x,\infty) = 0. \tag{12}$$

For convenience, we now define the one-dimensional variables

$$Q(x) = 2\int_0^\infty V_x(x,y)\,dy, \tag{13}$$

$$W(x) = Q^2(x)/2\int_0^\infty V_x^{\,2}(x,y)\,dy, \tag{14}$$

$$B(x) = [2/W(x)]\int_0^\infty \phi(x,y)\,dy, \tag{15}$$

$$C(x) = [2/W(x)]\int_0^\infty \rho(x,y)\,dy. \tag{16}$$

It is also convenient to define a stream function, $\psi(x,y)$, which satisfies the relations

$$V_x = \frac{\partial \psi}{\partial y}, \tag{17}$$

$$V_y = -\frac{\partial \psi}{\partial x}. \tag{18}$$

Previous solutions to the formulation given by equations (2) - (12) have been based on the similarity transformation

$$\psi(x,y) = x^n f(y/x^m). \tag{19}$$

This transformation leads to the limitations which were discussed in the introduction. Here we shall use a more general similarity transformation,

$$\psi(x,y) = Q(x)\,f(\zeta), \tag{20}$$

Nomenclature

B = buoyancy integral (equation (15))
C = concentration integral (equation (16))
E = turbulent entrainment coefficient
F = dimensionless stream function (equation (54))
Fr = Froude number
f = dimensionless stream function (equation (20))
G = dimensionless buoyancy (equation (55))
g = acceleration of gravity
H = dimensionless concentration (equation (56))
I = integral (equation (59))
J = integral (equation (58))
K = integral (equation (71))
Pr = Prandtl number
Q = flux integral (equation (13))
Re = Reynolds number
Sc = Schmidt number
T = temperature
V = velocity
W = width integral (equation (14))
x = axial coordinate
y = transverse coordinate
β = thermal expansion coefficient
γ = dimensionless number (equation (45))
ϵ = experimental constant
ζ = dimensionless coordinate (equation (23))
θ = dimensionless buoyancy (equation (21))
λ = laminar entrainment coefficient
ν = kinematic viscosity
ξ = dimensionless coordinate (equation (57))
ρ = concentration
ϕ = buoyancy
ψ = steam function
ω = dimensionless concentration (equation (22))

$$\phi(x,y) = B(x)\,\theta(\zeta), \tag{21}$$

$$\rho(x,y) = C(x)\,\omega(\zeta), \tag{22}$$

$$\zeta(x,y) = y/W(x). \tag{23}$$

From equations (17) and (18), it can be seen that any function $\psi(x,y)$ will satisfy equation (2). Rewriting equations (3) - (12) in terms of the stream function and using equations (2) - (23) we have

$$\begin{aligned} f''' + \frac{W}{\nu}\frac{dQ}{dx}(ff'' - f'^2) + \\ \frac{Q}{\nu}\frac{dW}{dx}f'^2 + \frac{BW^3}{\nu Q}\theta = 0, \end{aligned} \tag{24}$$

$$\theta'' - \frac{\mathrm{Pr}\,WQ}{\nu B}\frac{dB}{dx}f'\theta + \frac{\mathrm{Pr}\,W}{\nu}\frac{dQ}{dx}f\theta' = 0, \tag{25}$$

$$\omega'' - \frac{\mathrm{Sc}\,WQ}{\nu C}\frac{dC}{dx}f'\omega + \frac{\mathrm{Sc}\,W}{\nu}\frac{dQ}{dx}f\omega' = 0, \tag{26}$$

$$f(0) = 0, \tag{27}$$

$$f''(0) = 0, \tag{28}$$

$$f'(\infty) = 0, \tag{29}$$

$$\theta'(0) = 0, \tag{30}$$

$$\theta(\infty) = 0, \tag{31}$$

$$\omega'(0) = 0, \tag{32}$$

$$\omega(\infty) = 0. \tag{33}$$

Here the prime indicates differentiation with respect to ζ. From equations (13)-(16), we also must have

$$\int_0^\infty f'\,d\zeta = \mathrm{f}(\infty) = 1/2, \tag{34}$$

$$\int_0^\infty f'^2\,d\zeta = 1/2, \tag{35}$$

$$\int_0^\infty \theta\,d\zeta = 1/2, \tag{36}$$

$$\int_0^\infty \omega\,d\zeta = 1/2. \tag{37}$$

An entrainment parameter, λ, is now defined such that

$$\frac{dQ}{dx} = \frac{\lambda\nu}{W}. \tag{38}$$

Also, integrating equations (24)-(26) with respect to ζ from zero to infinity and applying equations (27)-(37), we have

$$\frac{d}{dx}\left(\frac{Q^2}{W}\right) = WB, \tag{39}$$

$$\frac{d}{dx}(QB) = 0, \tag{40}$$

$$\frac{d}{dx}(QC) = 0, \tag{41}$$

If λ were a known function of Q, W, B, and C, equations (38)-(41) could be solved, with the appropriate boundary conditions, to determine these four functions of x.

Using equations (38) - (41) in equations (24) - (26), we get

$$f''' + \lambda(ff'' + f'^2) + \gamma(\theta - f'^2) = 0, \tag{42}$$

$$\theta'' + \mathrm{Pr}\lambda(f\theta' + f'\theta) = 0, \tag{43}$$

$$\omega'' + \mathrm{Sc}\lambda(f\omega' + f'\omega) = 0, \tag{44}$$

where

$$\gamma = \frac{BW^3}{\nu Q}. \tag{45}$$

For the purpose of evaluating the velocity, temperature and concentration profiles, the assumption of local similarity will be used so the parameters λ and γ can be treated as constants. If these parameters are found to be truly constant, the resulting solution will be exact.

Equations (42)-(44) make up a seventh order system which includes one unknown parameters, λ. Thus the solution to this system can, at most, satisfy eight constraints. However, physics seems to have provided eleven constraints, equations (27) - (37). Fortunately, these are not all independent. The eight independent constraints which are to be used with equations (42)-(44) are

$$f(0) = 0, \tag{46}$$

$$f''(0) = 0, \tag{47}$$

$$f'(\infty) = 0, \tag{48}$$

$$f(\infty) = 1/2, \tag{49}$$

$$\theta'(0) = 0, \tag{50}$$

$$\omega'(0) = 0, \tag{51}$$

$$\int_0^\infty \omega\,d\zeta = 1/2, \tag{52}$$

$$\int_0^\infty f'^2\,d\zeta = 1/2. \tag{53}$$

Equation (31) can be obtained from equations (43), (46), (49), and (50). Equation (33) can be obtained from equations (44), (46), (49), and (51). Also, equation (36) can be obtained from equations (42), (46), (47), (48), and (53). Thus, these equations have been omitted.

To make this formulation somewhat simpler, let

$$F(\xi) = \frac{J}{G(0)}f(\zeta), \tag{54}$$

$$G(\xi) = \left(\frac{J}{G(0)}\right)^4 \frac{1}{\lambda^2}\theta(\zeta), \tag{55}$$

$$H(\xi) = \frac{JIH(0)}{\lambda G(0)}\omega(\zeta), \tag{56}$$

$$\xi = \frac{\lambda G(0)}{J}\zeta, \tag{57}$$

where

$$J = 2\int_0^\infty F'\,d\xi = 2F(\infty), \tag{58}$$

$$\mathrm{I} = 2\int_0^\infty H\,d\xi. \tag{59}$$

Using equations (54)-(57) in equations (42)-(44), we have

$$F''' + FF'' + F'^2 + (\gamma/\lambda)(G - F'^2) = 0, \tag{60}$$

$$G'' + \mathrm{Pr}(FG' + F'G) = 0, \tag{61}$$

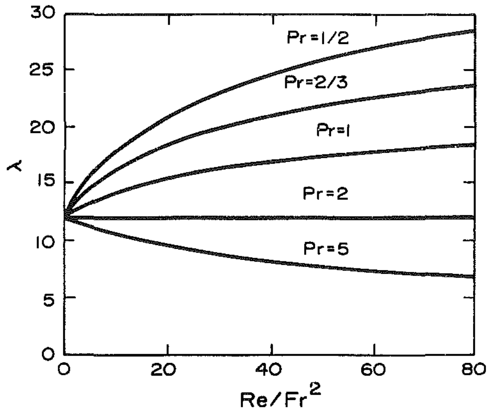

Fig. 1 The laminar entrainment coefficient

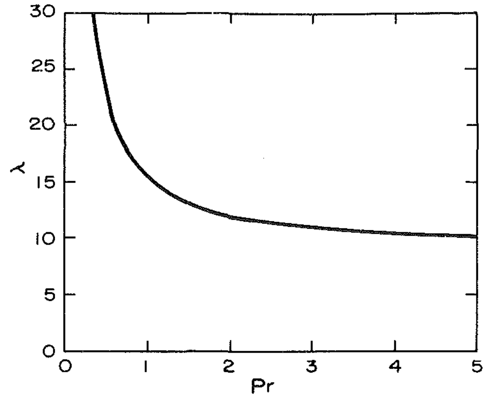

Fig. 2 The equilibrium laminar entrainment coefficient

$$H'' + \mathrm{Sc}(FH' + F'H) = 0. \tag{62}$$

Here the prime indicates differentiation with respect to ξ. Applying the same change of variables to equations (46)-(53) gives

$$F(0) = 0, \tag{63}$$

$$F''(0) = 0, \tag{64}$$

$$F'(\infty) = 0, \tag{65}$$

$$G(0) = 1, \tag{66}$$

$$G'(0) = 0, \tag{67}$$

$$H'(0) = 0, \tag{68}$$

$$H(0) = 1, \tag{69}$$

$$\lambda = J^3/K, \tag{70}$$

where

$$K = 2\int_0^\infty F'^2 d\xi. \tag{71}$$

Equations (60)-(62) can be solved for $F(\xi)$, $G(\xi)$, and $H(\xi)$ using equations (63)-(69) as boundary conditions. Equation (70) can then be used to determine the unknown entrainment parameter, λ. The x-dependent functions, $Q(x)$, $W(x)$, $B(x)$, and $C(x)$, are then obtained from equations (38)-(41) and the appropriate initial conditions. The velocity, temperature and concentration distributions can now be determined by combining equations (17) and (20) - (23) with equations (54)-(57) and (70). This gives

$$V_x(x,y) = \frac{JQ}{KW} F'\left(\frac{J^2 y}{KW}\right), \tag{72}$$

$$T(x,y) = \frac{J^2 B}{K^2 \beta g} G\left(\frac{J^2 y}{KW}\right) + T_\infty, \tag{73}$$

$$\rho(x,y) = \frac{J^2 C}{KI} H\left(\frac{J^2 y}{KW}\right). \tag{74}$$

Laminar Flow

In most practical applications, jets and plumes become turbulent. However, for conceptual continuity, laminar flow will be considered briefly.

For laminar flow ν is the kinematic viscosity, which can be considered constant. The characteristic dimension for the plume is W, the characteristic velocity is Q/W and the characteristic buoyancy is B. The local Reynolds number for the flow is $\mathrm{Re} = Q/\nu$ and the local Froude number is $\mathrm{Fr} = Q/B^{1/2}W^{3/2}$. Thus, for laminar flow, the dimensionless parameter γ is the local Reynolds number divided by the local Froude number squared,

$$\gamma = \mathrm{Re}/\mathrm{Fr}^2. \tag{75}$$

Equations (60)-(70) can be solved numerically to give λ as a function of the Reynolds number, the Froude number and the Prandtl number. This relationship is shown in Fig. 1.

It can be shown, by combining equation (45) with equations (38)-(40), that

$$\frac{d\gamma}{dx} = \frac{\nu}{WQ}\gamma(4\lambda - 3\gamma). \tag{76}$$

From equation (76) and the results shown in Fig. 1, it can be seen that neither γ nor λ will change with x if $\gamma = 0$ or $\gamma = 4\lambda/3$.

The case $\gamma = 0$ is the isothermal jet. Under this condition, $\lambda = 12$. From equations (38) and (39), we obtain the solution for isothermal jets,

$$Q(x) = Q_0[(36\nu/Q_0)(M_0 x/Q_0{}^2) + 1]^{1/3}, \tag{77}$$

$$W(x) = Q_0{}^2/M_0[36\nu/Q_0)(M_0 x/Q_0{}^2) + 1]^{2/3}, \tag{78}$$

where Q_0 and M_0 are, respectively, the initial kinematic mass and momentum flux of the jet. It should be noted that, for the case of a virtual point source, $Q_0 = 0$, this solution agrees with the exact solution of Schlichting [5].

The case $\gamma = 4\lambda/3$ is what will be called the equilibrium plume. This corresponds to the equilibrium value of $\mathrm{Re}/\mathrm{Fr}^2$, which develops in a laminar plume at large distances from the source. Under this condition λ is a function only of Prandtl number, as shown in Fig. 2. From equations (38)-(40) we obtain the solution for equilibrium plumes,

$$Q(x) = Q_0[(5\lambda\nu/3Q_0)(M_0 x/Q_0{}^2) + 1]^{3/5}, \tag{79}$$

$$W(x) = Q_0{}^2/M_0[(5\lambda\nu/3Q_0)(M_0 x/Q_0{}^2) + 1]^{2/5}, \tag{80}$$

$$B(x) = B_0[(5\lambda\nu/3Q_0)(M_0 x/Q_0{}^2) + 1]^{-3/5}, \tag{81}$$

where B_0 is the initial buoyancy of the plume. It should be emphasized that this solution is not valid near the source, except for the special case where, at the source, the Froude number is such that $\gamma = 4\lambda/3$ or, in terms of the source momentum flux, $M_0 = (3B_0Q_0^5/4\lambda\nu)^{1/3}$. It should also be noted that, for $Q_0 = 0$ and Q_0B_0 nonzero, this solution reduces to the virtual source solution which can be obtained following the method presented by Schmidt [6].

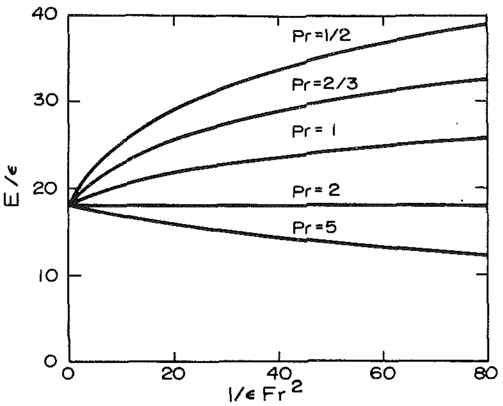

Fig. 3 The turbulent entrainment coefficient

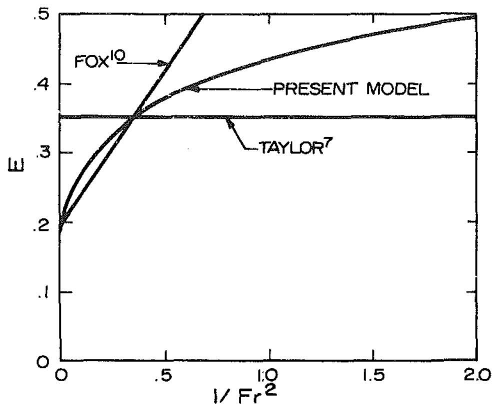

Fig. 4 The turbulent entrainment coefficient for Pr = 1/2 and ϵ = 0.01086

Turbulent Flow

For turbulent flow, ν is the virtual kinematic viscosity. From the mixing length theory of Prandtl [11], the virtual kinematic viscosity is proportional to the product of the centerline velocity and the characteristic transverse dimension, W. Thus, using equation (72), we have

$$\nu = \epsilon J Q F'(0)/K, \tag{82}$$

where ϵ is a dimensionless constant which must be determined experimentally.

Using equation (82) in equation (45) results in

$$\gamma = \frac{K}{\epsilon J F'(0)} \frac{1}{\mathrm{Fr}^2}, \tag{83}$$

where

$$\mathrm{Fr}^2 = Q^2/(BW^3). \tag{84}$$

Using equations (70) and (82) in equation (38), we obtain the turbulent entrainment equation,

$$\frac{dQ}{dx} = \frac{EQ}{W}, \tag{85}$$

where E is the turbulent entrainment coefficient, defined as

$$E = \epsilon J^4 F'(0)/K^2 \tag{86}$$

Combining equations (70), (83), and (86), it can be shown that

$$\gamma/\lambda = 1/(E\mathrm{Fr}^2) \tag{87}$$

Using this in equation (60), we have

$$F''' + FF'' + F'^2 + [1/(E\mathrm{Fr}^2)]\,(G - F'^2) = 0. \tag{88}$$

Equations (61)-(69) can be applied directly to turbulent flow, if we let Pr be the turbulent Prandtl number and Sc be the turbulent Schmidt number. Using equation (88) with equations (61)-(69), we can determine $F(\xi)$, $G(\xi)$, and $H(\xi)$. Equation (86) can then be used to determine the turbulent entrainment coefficient, E. Thus, it can be seen that the turbulent entrainment coefficient is a function of the dimensionless number, ϵ, the turbulent Prandtl number, and the Froude number. Both ϵ and the turbulent Prandtl number are constants. However, the Froude number varies with the local ratio of momentum to buoyancy. Figure 3 shows how the turbulent entrainment coefficient depends on ϵ, Pr, and Fr. From this figure, it can be seen that the entrainment coefficient is a universal constant only if the turbulent Prandtl number is 2. The experimental results of Reichardt [12] and the vorticity transport theory of Taylor [13] indicate that the turbulent Prandtl number is 1/2. Thus, it appears that the turbulent entrainment coefficient is not independent of Froude numbers as hypothesized by Taylor [7], but instead a function of local Froude number, as suggested by Fox [10]. The empirical constant ϵ was determined experimentally by Reichardt [14], who found that ϵ = 0.01086. Using this value and a turbulent Prandtl number of 1/2, the relationship between turbulent entrainment coefficient and local Froude number is shown in Figure 4. For comparison, the entrainment models proposed by Taylor [7] and Fox [10] are also shown.

It can be shown, by combining equations (84) and (85) with equations (39) and (40), that

$$\frac{d}{dx}\left(\frac{1}{\mathrm{Fr}^2}\right) = \frac{3}{W\mathrm{Fr}^2}\left(E - \frac{1}{\mathrm{Fr}^2}\right). \tag{89}$$

Because the entrainment coefficient is a function only of the Froude number, this equation shows that both the Froude number and the entrainment coefficient are independent of x if Fr = ∞ or Fr = $1/E^{1/2}$.

The condition Fr = ∞ corresponds to the isothermal jet. In this case, the turbulent entrainment coefficient is $E = 18\ \epsilon$. Using equations (39)-(41) and (85) we obtain the solution for turbulent isothermal jets,

$$Q(x) = Q_0(2EM_0x/Q_0{}^2 + 1)^{1/2}, \tag{90}$$

$$W(x) = Q_0{}^2/M_0(2EM_0x/Q_0{}^2 + 1), \tag{91}$$

$$C(x) = C_0(2EM_0x/Q_0{}^2 + 1)^{-1/2}, \tag{92}$$

where Q_0 and M_0 are, respectively, the initial kinematic mass and momentum flux and C_0 is the initial concentration. For the case of a virtual source, this agrees with the solution of Tollmien [4]. Using equation (88) with equations (63)-(72), we obtain the classical velocity distribution for isothermal jets.

$$\frac{V_x W}{Q} = (3/2)[1 - \tanh^2(3y/W)]. \tag{93}$$

The condition Fr = $1/E^{1/2}$ is the Froude number which develops in a turbulent plume at a large distance from the source. With the turbulent Prandtl number equal one half, this equilibrium Froude number is Fr = $0.1759/\epsilon^{1/2}$. Thus, the equilibrium entrainment coefficient is $E = 32.30\ \epsilon$, which is nearly eighty percent larger than the entrainment coefficient for the isothermal jet. Using equations (39)-(41) and (85), we obtain the solution for the turbulent equilirium plume,

$$Q(x) = Q_0(EM_0x/Q_0{}^2 + 1), \tag{94}$$

$$W(x) = Q_0{}^2/M_0(EM_0x/Q_0{}^2 + 1), \tag{95}$$

$$B(x) = B_0(EM_0x/Q_0{}^2 + 1)^{-1}, \tag{96}$$

$$C(x) = C_0(EM_0x/Q_0{}^2 + 1)^{-1}, \tag{97}$$

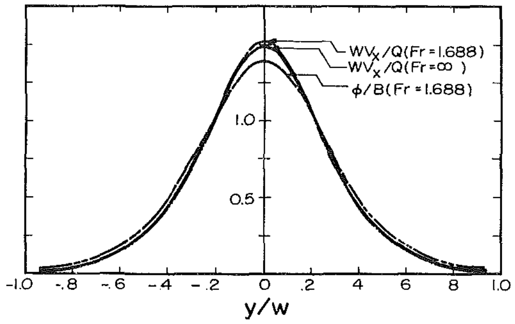

Fig. 5 The velocity and temperature profiles

where B_0 is the initial buoyancy of the plume. This solution is, of course, not valid near the source, except for the special case where the Froude number at the source is Fr = $1/E^{1/2}$ = 1.688. For the case of a virtual source, this solution agrees with that of Schmidt [6]. For Fr = $1/E^{1/2}$ and Pr = 1/2, equations (61)-(72) and (88) do not readily yield a closed form solution for the velocity, temperature and concentration profiles. However, these profiles can easily be determined numerically. Figure 5 shows the velocity and temperature profiles for an equilibrium plume. For comparison, the velocity profile for an isothermal jet, as predicted by equation (93), is also shown. It should be noted that, even though the buoyancy had a very large effect on the entrainment coefficient, it's effect on the velocity profile is rather small.

If the Froude number at the source is neither infinity nor 1.688, then both the Froude number and the entrainment coefficient will vary with distance above the source. Under these conditions, the integral variables, Q, W, B, and C, can be computed numerically. Consider the general case where the kinematic mass and momentum flux at the source are Q_0 and M_0 while the buoyancy and concentration at the source are B_0 and C_0. From equations (39)-(41) and (85), we obtain the dimensionless formulation,

$$\frac{dq}{d\eta} = \frac{Eq}{w}, \tag{98}$$

$$\frac{d}{d\eta}(q^2/w) = \frac{wb}{F_0{}^2}, \tag{99}$$

$$\frac{d}{d\eta}(qb) = 0, \tag{100}$$

$$\frac{d}{d\eta}(qc) = 0, \tag{101}$$

where $q = Q/Q_0$, $w = M_0 W/Q_0{}^2$, $b = B/B_0$, $c = C/C_0$, $\eta = M_0 x/Q_0{}^2$ and F_0 is the Froude number at the source, $F_0{}^2 = M_0{}^3/B_0 Q_0{}^4$. The dimensionless boundary conditions are

$$q(0) = w(0) = b(0) = c(0) = 1. \tag{102}$$

The solution to this system of equations for the case $F_0 = 20$, is shown in Figs. 6 and 7. In obtaining this solution, the relationship between entrainment coefficient and local Froude number, which is shown in Fig. 4, was used.

Discussion

The widely used entrainment hypothesis of Taylor [7] is based on the assumption that the turbulent entrainment coefficient for plumes is independent of Froude number. The moment solution of Fox [10] suggests that the entrainment coefficient is a linear function of the inverse square of the Froude number. The differential analysis presented here gives a nonlinear relationship between entrainment coefficient and the inverse square of the Froude number. The Froude number for any plume tends toward a universal constant, at large distances above the source. Thus, all three models should give the same entrainment, except in some development region near the source. The length of this development region is obviously of some importance.

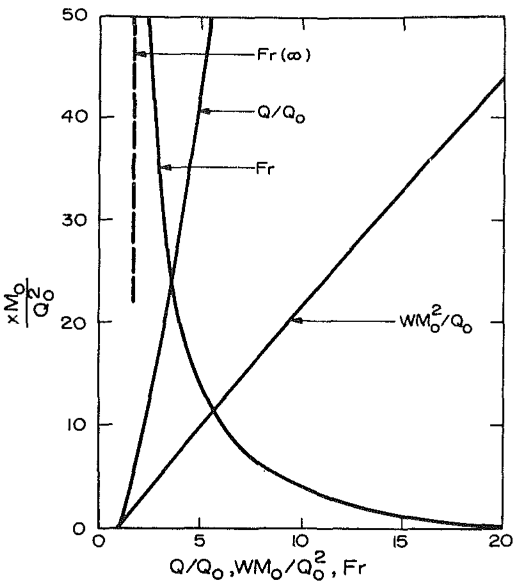

Fig. 6 The integral variables *Q*, *W*, and Fr

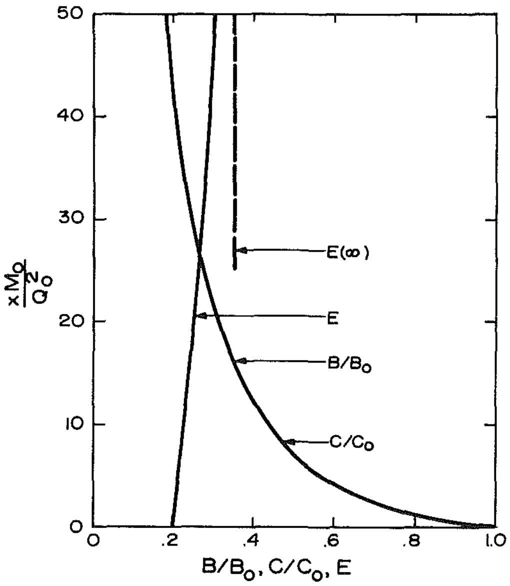

Fig. 7 The integral variables *B*, *C*, and *E*

From Figs. 6 and 7, it can be seen that the Froude number and the entrainment coefficient approach their equilibrium values rather slowly. With a discharge Froude number of 20, the local Froude number is still 45 percent above the equilibrium value at $\eta = 50$. The discrepancy is still 15 percent at $\eta = 100$. It was found that the local Froude number did not come within one percent of the equilibrium Froude number until about $\eta = 400$. Clearly, the length of this development zone depends on the magnitude of the discharge Froude number. However, it can be stated in general that, for plumes with high discharge Froude number, the development length for the Froude number is of the order of a few hundred times the discharge width. For most applications, a development zone of this length cannot be ignored. Furthermore, in this development zone, a knowledge of how the entrainment coefficient depends on Froude number is essential. This relationship is predicted by the theoretical model presented here. Experimental verification of this relationship is needed.

References

1 Briggs, G. A., "Plume Rise," NTIS No. TID-25075 (Oak Ridge National Laboratory, Oak Ridge, 1969).

2 Hirst, E. A., "Analysis of Round, Turbulent, Buoyant Jets Discharged to Flowing Stratified Ambients," Report ORNL-4685 (Oak Ridge National Laboratory, Oak Ridge, 1971).

3 Davis, L. R., and Shirazi, M. A., "A Review of Thermal Plume Modeling," in *Proceedings Sixth International Heat Transfer Conference* (Hemisphere, Washington, 1978), p. 109.

4 Tollmien, W., "Berechnung Turbulenter Ausbreitungsvorgange," *ZAMM,* Vol. 6, 1926, p. 468.

5 Schlichting, H., "Laminare Strahlausbreitung," *ZAMM,* Vol. 13, 1933, p. 260.

6 Schmidt, W., "Turbulence Ausbreitung eines Stromes Erhitter Luft," *ZAMM,* Vol. 21, 1941, pp. 265 and 271.

7 Taylor, G. I., "Dynamics of a Mass of Hot Gas Rising in Air," USAEC Report MDDC-919 LADC-276 (Los Alamos Scientific Laboratory, Los Alamos, 1945).

8 Priestley, C. H. B., and Ball, F. K., "Continuous Convection from an Isolated Source of Heat," *Quart. J. Roy. Meterol. Soc. 81,* Vol. 144, 1955.

9 Morton, B. R., Taylor, G. I., and Turner, J. S., "Turbulent Gravitational Convection from Maintained and Instantaneous Sources," *Proc. Roy. Soc. London A,* Vol. 234, No. 1, 1956.

10 Fox, D. G., "Forced Plumes in a Stratified Fluid," *J. Geophys. Res.,* Vol. 75, 1970, p. 6818.

11 Prandtl, L., "Bemerkungen zur Theorie der freien Turbulenz," *ZAMM,* Vol. 22, 1942, p. 241.

12 Reichardt, H., "Impuls-und Warmeaustansch in freier Turbulenz," *ZAMM,* Vol. 24, 1944, p. 168.

13 Taylor, G. I., "The Transport of Vorticity and Heat through Fluids in Turbulent Motion," *Proc. Roy. Soc. London A,* Vol. 135, 1932, p. 685.

14 Reichardt, H. "GesetzmaBigkeiten der freien Turbulenz," *VDI-Forschungsheft,* 1942, p. 414.

R. V. Westphal

J. K. Eaton

J. P. Johnston

Stanford University,
Stanford, Calif.
Mem. ASME

A New Probe for Measurement of Velocity and Wall Shear Stress in Unsteady, Reversing Flow

Separated turbulent flows exhibit instantaneous reversals of flow direction which make measurement of the velocity field extremely difficult. A three-wire heat-tracer technique has been employed to measure streamwise velocity of a low-speed air flow very near a smooth, solid wall; the wall shear stress is calculated using a similarity hypothesis. Initial results presented show the evolution of average wall shear stress and rms fluctuation intensity of wall shear stress in a reattaching 2-D flow downstream of a backward-facing step.

Introduction

Many real flows of engineering interest contain regions of highly turbulent flow which exhibit instantaneous reversals of flow direction, even though the flow field is nominally steady overall. Examples include the turbulent separated flow over airfoils at high angle of attack and internal flows through sudden expansions. There is much to be learned about turbulent separated flows, and research is needed to provide insight into the complex transport characteristics of these highly turbulent flows. In particular, there is today only a poor understanding of how surface-heat-transfer rates are related to the rapidly fluctuating flows close to separation and reattachment points.

We have been studying turbulent flow through a sudden expansion in a duct (Fig. 1), in order to advance basic understanding of separated and reattaching flows [1, 2]. Previous work in our laboratory has investigated the effects of separating boundary layer state and Reynolds number on mean reattachment length. Recovery of the reattached shear layer downstream of reattachment has been characterized and details of the mean velocity and turbulence profiles obtained. This work convinced us that measurements very near the wall are necessary to a complete understanding of the reattachment process. For example, measurement of the wall shear stress in the reattachment region would allow unambiguous definition of the mean reattachment point – usually defined for two-dimensional flow as a point of zero-average wall shear stress. Also, it seems evident that the fluctuations of the flow field close to reattachment must be responsible for the high values of surface heat flux observed in this zone [3].

We have developed a device to measure instantaneous fluid speed and direction very close to a smooth, solid wall. For our application, the probe is calibrated to yield instantaneous magnitude and direction of the streamwise wall shear stress in a two-dimensional, low-speed air flow downstream of a backward-facing step. We know of no other instrument suitable for measurement of fluctuating velocity in the very near-wall region of a reversing flow [4, 5]. Most analog instruments (e.g., heat or mass-transfer analogy), pressure measurement techniques (e.g., Preston tube), or hot-wire arrays cannot be used in the presence of a rapidly reversing flow. Laser-Doppler anemometers are expensive and difficult to use very near a wall in most wind tunnel facilities. The two-spot laser system shows some promise for use in making near-wall measurements but is as yet undeveloped. Thus the present device fills a gap in current instrumentation technology. Below we discuss its development and present results obtained in a reattaching flow on the flat wall downstream of a backward-facing step (Fig. 1).

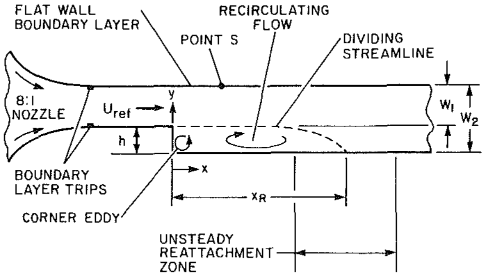

Fig. 1 Backward-facing step test section, $h = 0.05$ m $W_1/W_2 = 0.6$

Pulsed-Wall-Probe Design and Development

Background. The concept for the pulsed-wall probe evolved from the pulsed-wire anemometer of Bradbury [6], an instrument developed to measure streamwise velocity in highly turbulent flows. The pulsed-wire probe measures the instantaneous velocity by measuring the time of flight of a heated tracer of fluid. It employs an array of three parallel wires to generate and detect a small volume of heated air. The center ("heater") wire is pulsed with a short-duration (about 5 μs), high-amplitude pulse of current in order to produce a tracer of heated fluid at its surface. The two outside wires

---

Contributed by the Fluids Engineering Division of THE AMERICAN SOCIETY OF MECHANICAL ENGINEERS and presented at the Winter Annual Meeting, Chicago, Ill., November 16-21, 1980. Manuscript received by the Fluids Engineering Division, August 18, 1980.

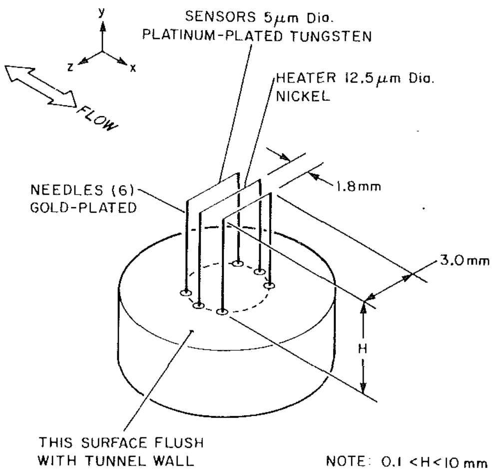

Fig. 2 Pulsed wall probe schematic

("sensors") are operated as resistance-temperature transducers in a bridge configuration. When the time derivative of sensor-wire temperature exceeds a preset value (the "trigger level"), control circuitry stops the counter and notes which sensor was triggered. Then the counter-elapsed time (the "time of flight") and a signal to tell which wire was triggered are both displayed on the instrument panel and, more importantly, made available at a computer interface port.

Figure 2 shows the geometry of the present probe. Note that H, the distance of the plane of the wire array from the wall surface, may be varied by means of a micrometer traverse. This geometry is appropriate for use only where streamlines are nearly parallel to the wall, since a substantial vertical (v) velocity component will cause the tracer to miss the sensor wire. Since this condition is satisfied only very near the wall for our reattaching flow, no velocity profiles are reported here. For the measurements shown below, $H \cong 0.2$ mm, although the current probe design provides for $0.1 \text{ mm} \leq H \leq 10 \text{ mm}$.

We elected to use the same instrument-control electronics developed by Bradbury, which are now manufactured by Malvern Instruments. These electronics provide adjustments for heat-pulse amplitude, sensor-wire current, and independent trigger-level control for each sensor wire. The pulsed-wire concept has one undesirable feature: the pulsing circuitry causes an inductive spike in the sensor circuitry. To prevent this spike from giving a false indication of time of flight, a delay circuit is used in the Malvern electronics, to prevent any trigger until after the inductive spike has disappeared. This delay time is about 280 μs, and it sets a lower limit on the allowable time of flight, giving an upper limit on velocity for the current probe of about 8 m/s. The absolute upper limit on measurable time of flight is about 40 ms; however, for the particular pulse-amplitude and trigger settings we used, the effective maximum detectable time of flight is about 8 ms. As the result of both of these limits, the probe can be calibrated to measure streamwise velocity u in the range $-8 \text{ m/s} < u < 8 \text{ m/s}$, with a region of poor resolution (a "hole") in the response for $-0.3 \text{ m/s} < u < 0.3$ m/s. If the velocity being measured is within the hole there is a high probability that it will be interpreted as a zero velocity.

Some comments are needed concerning interpretation of time-of-flight data. We consider a single sample of time of flight, T, to represent (through a calibration function) the *instantaneous* value of u at the heater wire's geometric center. This is true only if (i) the fluid-dynamic time scales of interest are long compared to T, and (ii) length scales of interest in the spanwise and streamwise directions are large compared to the effective probe dimensions in those directions. We feel both conditions are well satisfied for our measurements near reattachment in the backward-facing step flow, but in other cases these criteria may not be met. If conditions (i) and (ii) are not satisfied, then T represents a time and space-averaged velocity sample and must be interpreted with caution.

Further, we have assumed that, if H is small enough, the instantaneous streamwise velocity may be used to infer the instantaneous streamwise component of wall-shearing stress:

$$\tau_w = f(u) \quad \text{for } H \text{ "small"} \tag{1}$$

This is equivalent to asserting that the velocity profile remains similar (at least very close to the wall) and scales on the wall shear stress even in a highly turbulent, reversing flow. For "normal," nonreversing, turbulent boundary layers this assumption is similar to the observation that

$$U^+ = Y^+ \quad \text{for } Y^+ \leq 5 \tag{2}$$

A better evaluation of this assumption will be possible through associated research now progressing in our laboratory.

Calibration. Ideally, the relation between measured time of flight and velocity would simply be $U = d/T$. However, the effects of thermal diffusion and the operation of the control electronics distort this relation enough so that the two sensor wires must be individually calibrated. As was done by Bradbury [6], we assumed a calibration relationship of the form

$$u = A/T + B/T^2 \tag{3}$$

and determined A and B to give the "best fit" to calibration

Nomenclature

A,B = calibration constants
C_f = skin friction coefficient: $C_f \triangleq \tau_w/1/2\rho U_{\text{ref}}^2$
d = spacing between heater and sensor wires, m
h = step height, m
H = distance of wire array from the wall surface, m
Re_θ = Reynolds no. based on θ, $\text{Re}_\theta \triangleq \frac{U\infty\theta}{\nu}$
T = time of flight, s
u,v,w = velocity components in x, y, z directions, respectively, m/s
u_τ = friction velocity: $u_\tau \triangleq \sqrt{\tau_w/\rho}$, m/s
U_∞ = core or free-stream velocity, m/s
U^+ = inner-layer velocity: $U^+ \triangleq \frac{\bar{u}}{u_\tau}$
U_{ref} = nominal backstep channel inlet velocity, m/s
W_1 = backstep channel inlet width, m
W_2 = backstep channel downstream width, m
x,y,z = stream, gradient, and spanwise coordinate directions, respectively, m
Y^+ = inner-layer distance: $Y^+ \triangleq \frac{yu_\tau}{\nu}$
γ_P = percent downstream flow in a thin layer of fluid adjacent to the wall
θ = momentum thickness, m
ν = kinematic viscosity, m^2/s
ρ = fluid density, kg/m^3
τ_w = wall shear stress in streamwise (x) direction, N/m^2
– = overbar; denotes time-averaged quantity
′ = prime; denotes rms fluctuation intensity

data. A table of a dozen or so values of u versus T is obtained in a very steady parallel flow, and the reference velocity is measured with a stagnation probe and a wall-static tap. To obtain a reliable measure of reference velocity, one is obliged to perform this calibration outside wall layers which in our flow required $H \geq 5$ mm.

Alternatively, if velocity measurements are not to be made, a direct calibration for wall shear stress may be performed *at fixed H* in a nonreversing turbulent boundary layer. Equation (2) implies

$$\tau_w = \mu u/H \quad \text{for} \quad Hu_\tau/\nu \leq 5 \tag{4}$$

so we anticipated the relationship between τ_w and T to be

$$\tau_w = A/T + B/T^2 \tag{5}$$

This calibration is implemented by compiling a *distribution* of values of T for each of a dozen or so values of $\bar{\tau}_w$ at fixed H. The fully developed, two-dimensional, turbulent channel flow apparatus of Hussain and Reynolds [7] provided an accurately known average wall shear stress for calibration purposes. The distribution of T is needed at each value of $\bar{\tau}_w$, because the channel flow is turbulent and moderate rms fluctuations of wall shear stress are expected [4]. Fitting the *average* value of T to the *average* wall shear stress $\bar{\tau}_w$ is not appropriate for even moderate rms intensity fluctuations, due to the nonlinear relation between wall shear stress and time of flight, shown in equation (5). We have devised a simple scheme for correcting this "nonlinear averaging error" appropriate for the level of fluctuation present. It provides a 2 percent correction to the constants A and B for our calibration conditions.

A third way to calibrate the probe would be to devise a flow field of accurately known velocity profile; a two-dimensional, fully developed, laminar channel provides such a flow situation. In this case the calibration could be performed with fixed or variable H, either in terms of the known velocity or known velocity gradient at the wall. The very small geometric scale of a laminar flow facility for this purpose makes dimensional tolerances very stringent, but we have built a channel for these purposes. The laminar flow calibration is desirable to minimize uncertainty in the reference velocity or wall shear stress (especially at low speed), to provide the flexibility of fixed or variable H, and to obviate the correction for "nonlinear-averaging error" required when using the turbulent channel flow. Measurements show that the same calibration function for wall shear stress results whether the probe is calibrated in the laminar or the turbulent channel flow.

The calibration function was implemented in real time using a microcomputer. The sampling rate was about 5 Hz; enough data were processed and stored to compute average velocity or wall shear stress, the rms fluctuation intensity, and the probability distributions. Generally, 2400 samples were taken to obtain wall shear-stress data in the region of recirculating flow. Spectral data were not obtained due to the low sampling frequency. Incidentally, we view the microcomputer as essential to successful application of any pulsed-wire technique.

Development Work. Initial development work confirmed the feasibility of the design. The heat tracer could be unambiguously detected for the range of flow velocity 0.3-8 m/s, and "noise" produced by the turbulent flow past the sensor wires did not trigger the control circuitry. To obtain a good calibration fit (within 0.1 m/s over the range 0.3-8 m/s), each of the two sensor wires was calibrated individually; but, having done this, the measured wall shear stress was found to be insensitive to probe orientation. The calibration was checked periodically for drift and was always found to repeat to about a percent; drift such as that often experienced by hot wires and films should not be a significant problem for the pulsed wire so long as reasonable precautions are taken to remove dust and lint from the flowing gas.

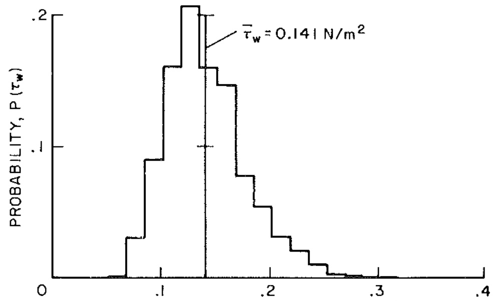

(*a*) **Pulsed wall probe, two-dimensional air flow**

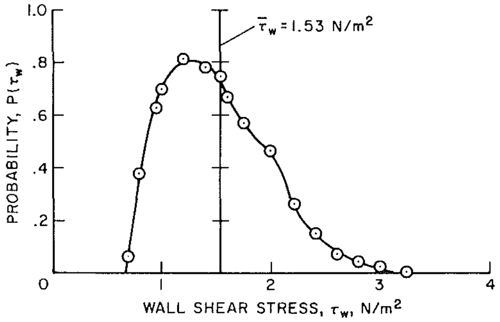

(*b*) **Film gage, open channel water flow from reference [5], Fig. 6(*a*)**

Fig. 3 Wall shear stress probability density functions for fully-developed turbulent channel flow

The next phase of development was to compare the pulsed-wall probe results to those from other measurement techniques. One such test was to compare results obtained in the reattaching flow to those from a thermal tuft [8], a simple device for determination of instantaneous flow direction in a very thin layer of fluid at the wall. The thermal tuft gives a continuous output which can be averaged to yield the fraction of time that the flow very near the wall is in a particular direction; γ_p denotes the fraction of downstream flow. Thermal tuft γ_p results (from the backstep of Fig. 1 with $U_{\text{ref}} = 11.2$ m/s) were compared to the fraction of downstream samples obtained by the pulsed-wall probe, used in the same location to measure wall shear stress ($H = 0.2$ mm). Measurements of γ_p from both probes agreed within a few percent throughout the entire region of reattachment where $0.02 \leq \gamma_p \leq 1.0$.

The pulsed-wall probe was also tested in the "normal" turbulent boundary layer which exists downstream of point S (Fig. 1) along the opposite wall of our test apparatus. At point S, the boundary layer has been growing in a very mild favorable pressure gradient and is about 10 mm thick, and $\text{Re}_\theta = 850$ for our test conditions. A stagnation probe of 0.7 mm outside dia was used with a wall static tap to traverse the boundary layer. The velocity profiles fit the log law of the wall, and a Clauser plot gave the average wall shear stress values. The values of $\bar{\tau}_w$ obtained agreed with those measured by the pulsed-wall probe within two percent.

Sandborn [5] has reported probability distributions of the wall shear stress for several nonreversing turbulent boundary layers. The notable feature of these distributions is the long "tail" toward higher values of shear stress; the result is that the average wall shear stress is higher than the most probable value. Probability distributions of the wall shear stress from the fully developed turbulent channel flow [7] show similar shapes as those reported in reference [5]. Figure 3 contrasts

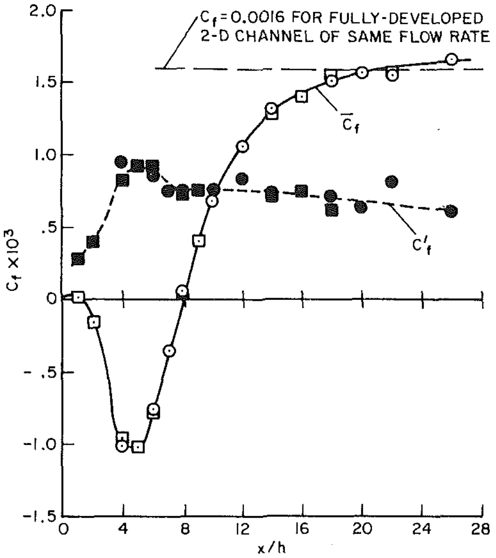

Fig. 4 Skin friction in backward-facing step. Circles and squares are from two different runs.

typical results from the pulsed-wall probe to those reported by Sandborn for fully developed flow; qualitative agreement is demonstrated. It would be most interesting to directly compare results from a heat transfer device such as that of Sandborn to the pulsed-wall probe for measuring average and fluctuating wall shear stress in nonreversing turbulent boundary layers.

Results in Recirculating Flow

A complete set of data using the pulsed-wall probe along the step wall of the backward-facing step tunnel at one upstream reference velocity (U_{ref} = 11.2 m/s) has been obtained. The average and rms fluctuation intensity of wall shear stress in the reattachment zone are shown in Fig. 4, and a selection of probability distributions for these data are shown in Fig. 5. Several characteristics are notable. First, the average shear stress attains a large negative value in the backflow region, where $3 < x/h < 6$. This was surprising to us, since several fairly successful zonal prediction methods developed at Stanford for separated flows in diffusers use $C_f \simeq 0$ within much of the separation "bubble" [1, 9].

Second, the rms intensity of shear stress fluctuation exhibits a maximum value in the reattachment zone and decays slowly thereafter. The result is in general agreement with the observations of Kim [1]: recovery of the reattached shear layer is generally quite slow. The very high values of the shear stress fluctuations near reattachment are consistent with the high heat flux observed by other investigators in this zone [3].

Third, the probability distributions of wall shear stress (Fig. 5) evolve in an important way. Downstream of reattachment the distributions are skewed toward more positive shear stress values, much as they are for normal turbulent boundary layers (Fig. 3). However, as the mean reattachment point is approached from downstream, these distributions rapidly become symmetric and remain nearly symmetric throughout the region of recirculating flow. Figure 6 summarizes these results and shows that, at the streamwise location of 50 percent downstream flow, the average wall shear stress vanishes:

$$\gamma_p = 0.5 \quad \text{for } \bar{\tau}_w = 0 \qquad (6)$$

suggesting that the thermal tuft may actually be used to measure the mean reattachment length [2]. This hypothesis for use of the thermal tuft has, in the past, been questioned.

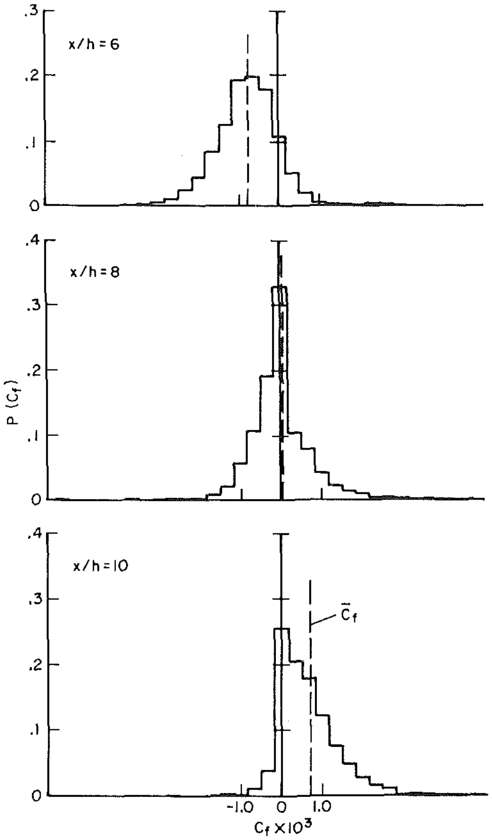

Fig. 5 Normalized probability density functions near reattachment in the backward-facing step at three streamwise locations along the step wall.

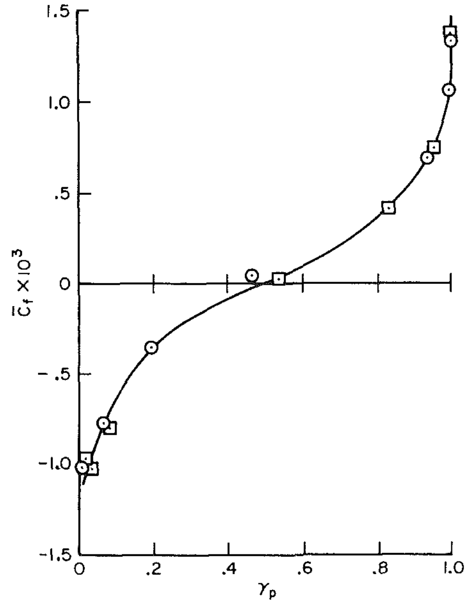

Fig. 6 Average skin friction coefficient versus downstream flow fraction in the region of reversing flow, $4 \le x/h \le 14$. Symbols as in Fig. 4.

Conclusions

The viability of a new pulsed-wall probe for determining average and fluctuating components of streamwise velocity very near a smooth wall in a recirculating air flow has been demonstrated. Preliminary development work has been completed, and it shows that the pulsed-wall probe gives results which generally agree with other instruments when used in nonreversing flow. Development work continues to prove the technique further, to evaluate uncertainties in different measuring situations, and to develop more accurate calibration procedures. The assumptions required to relate the probe output to wall shear stress will be evaluated by interpretation of new flow-visualization studies of the near-wall flow structure now being undertaken in our laboratory.[1]

Initial results presented here show the evolution of average and fluctuating wall shear stress downstream of a backward-facing step for one inlet Reynolds number. Surprisingly high values of negative average wall shear stress were found within the recirculating region, and high values of the rms fluctuation of wall shear stress are noted near reattachment. The results may ultimately be helpful in understanding surface heat transfer characteristics of recirculating flows.

Acknowledgments

The work described above has been supported by grant NSF-CME-78-02248-A1 from the National Science Foundation.

References

1 Kim, J., Kline, S. J., and Johnston, J. P., "Investigation of Separation and Reattachment of a Turbulent Shear Layer: Flow Over a Backward-Facing Step," MD-37, Apr. 1978, Thermosciences Div., Dept. of Mech. Engrg., Stanford University.

2 Eaton, J. K., Johnston, J. P., and Jeans, A. H., "Measurements in a Reattaching Turbulent Shear Layer," *Proceedings of the Second Symposium on Turbulent Shear Flows*, London, 1979.

3 Ota, T., and Kon, N., "Heat Transfer in the Separated and Reattached Flow on a Blunt Flat Plate," ASME *Journal of Heat Transfer*, Vol. 96 1974, pp. 459–462.

4 Simpson, R. L., "Summary of the Colloquium on Turbulent Flow Separation, January 18-19, 1979," Project SQUID Report SMU-3-PU, Purdue University, 1979.

5 Sandborn, V. A., "Evaluation of the Time-Dependent Surface Shear Stress in Turbulent Flows," ASME 79-WA/FE-17, 1979 ASME Winter Annual Meeting.

6 Bradbury, L. J. S., and Castro, I. P., "A Pulsed-Wire Technique for Velocity Measurements in Highly Turbulent Flow," *Journal of Fluid Mechanics*, Vol. 49, 1971, pp. 657–691.

7 Hussain, A. K. M. F., and Reynolds, W. C., "Measurements in a Fully Developed Turbulent Channel Flow," ASME JOURNAL OF FLUIDS ENGINEERING, Vol. 97, Dec. 1975, pp. 568–579.

8 Eaton, J. K., Jeans, A. H., Ashjaee, J., and Johnston, J. P., "A Wall-Flow-Direction Probe for Use in Separating and Reattaching Flows," ASME JOURNAL OF FLUIDS ENGINEERING, Vol. 101, Sept. 1975, pp. 364–366.

9 Bardina, J., Lyrio, A., Kline, S. J., Ferziger, J. H., and Johnston, J. P., "A Prediction Method for Planar Diffuser Flows" (1980, unpublished).

10 Kline, S. J., and McClintock, F. A., "Describing Uncertainty in Single-Sample Experiments," *Mechanical Engineering*, Jan. 1953.

APPENDIX

Uncertainties in Primary Data

Uncertainties in the reported average data of this paper were estimated by the method of Kline and McClintock [10] at 20:1 odds, as follows:

$\bar{\tau}_w = 0.141\ \mathrm{N/m^2}: \pm 0.005\ \mathrm{N/m^2}$, Fig. 3(*a*).

$\bar{C}_f$: ± 0.0001, Figs. 4, 5, 6.

x/h: ± 0.05, Fig. 4.

γ_p: ± 0.02, Fig. 6.

These estimates include possible fixed errors and, for the case of C_f measurements, our estimate of the uncertainty involved in using a near-wall similarity assumption for the flow studied.

---

[1] Work in progress by S. J. Kline and S. W. Pronchick.

Journal of Fluids Engineering Discussion

The Third Two-Dimensional Problem of Three Dimensional Blade Systems of Hydraulic Machines[1]

T. Katsanis. The problem considered in this paper is interesting and the authors have developed a new method of solution. The main point of this discussion is to point out previous solutions of this problem. Reference [1] presents an analysis method and includes a FORTRAN computer program for the solution of this problem for a very general turbomachine blade row. The solution in [1] is obtained by the numerical integration of velocity gradient ordinary differential equations in two different directions on a surface approximately orthogonal to the flow passage. The method used in [1] is based on previous work going back to 1949 [2]. Other references are [3]-[5]. Early work was limited to axial turbomachines, however there is no limitation of this type in the latest work.

Additional References

1 Katsanis, Theodore, "FORTRAN Program for Quasi-Three Dimensional Calculation of Surface Velocities and Choking Flow for Turbomachine Blade Rows," NASA TN D-6177, 1971.

2 Huppert, M. C., and MacGregor, Charles, "Comparison Between Predicted and Observed Performance of Gas-Turbine Stator Blade Designed for Free-Vortex Flow," NACA TN 1810, 1949.

3 Hamrick, Joseph T., Ginsburg, Ambrose, and Osborn, Walter M., "Method of Analysis for Compressible Flow Through Mixed-Flow Centrifugal Impellers of Arbitrary Design," NACA TR 1082, 1952.

4 Stewart, Warner L., Wong, Robert Y., and Evans, David G., "Design and Experimental Investigation of Transonic Turbine with Slight Negative Reaction Across Rotor Hub," NACA RM E53L29a, 1954.

5 Stewart, Warner L., Whitney, Warren J., and Schum, Harold J., "Three-Dimensional Flow Considerations in the Design of Turbines," Paper No. 59-Hyd-1, ASME, 1959.

---

[1] By P. K. Agarwal and G. V. Viktorov, published in the March, 1981, issue of the JOURNAL OF FLUIDS ENGINEERING, Vol. 103, No. 1, pp. 33-51.

Journal of Fluids Engineering

Book Reviews

Small and Micro Hydroelectric Plants, edited by Robert Noyes, Noyes Data Corp., Park Ridge, NJ, 1980. Price: $42.

REVIEWED BY FRANK M. WHITE

This book is essentially a clothbound grouping of the contents of four 1979 government reports and thus at its present list price is not really a bargain, being infinitely more expensive than the original material. But the original reports were not widely distributed—the reviewer possesses none of them, for example—so their compilation into a sturdy book creates a very useful item for hydropower engineering groups and libraries.

The book is thoroughly practical throughout and could be used by a consulting engineer to design an industrial plant or by a homeowner to construct a backyard facility. It makes an excellent practical companion to the recent ASME WAM'80 Symposium Volume No. G00180, *Small Hydro-Power Fluid Machinery*, edited by D. R. Webb and D. N. Papadakis.

The term "small" hydropower means a capacity of less than 15 megawatts or a dam height of less than 20 meters, while "micro" hydropower means less than 100 kilowatts. Both aspects are very well treated in this book.

Part I, entitled Resource Potential for Small Scale Hydropower, is taken from a 1979 U.S. Army Corps of Engineers report and documents the hydropower potential for the entire United States in 24 fact-filled pages.

Part II, Feasibility of Small Scale Hydroelectric Power Generation, is a 324-page Corps of Engineers report, written by D. W. Davis and co-workers. It is a comprehensive guide to the field and should be in the library of every prospective hydropower engineer. Its six chapters treat introductory technical and planning details, economic and financial analysis, hydrologic studies, existing facility integrity, electromechanical features, and civil and sitework features. It has a nice glossary of terms and many references.

Part III, Equipment for Small Scale Hydroelectric Power Plants, is a 43-page paper by W. W. Wayne Jr. presented to a 1979 DOE symposium. It briefly describes available equipment: packaged Francis and propeller units, bulb units, cross-flow turbines, and STRAFLO axial turbines. Included in the paper are some cost estimates, plus very nice drawings and photos.

Finally, Part IV describes Micro Hydropower, from a 1979 report to DOE by Ron Alward and co-workers from the National Center for Appropriate Technology in Butte, Montana. Its 62 pages are aimed directly at domestic individual users, with clear prose and excellent drawings. Along with technical, economic, and construction details, it includes a list of microequipment manufacturers, consulting engineers, and do-it-yourself booklets, with critical annotations.

Although apparently photocopied directly from the original reports, reproduction of this book is excellent throughout. At the list price it costs 9.2¢ a page, but is probably worth it for any engineer seriously pursuing small scale hydropower.

Fluid Power With Applications,
Anthony Esposito,
Prentice-Hall, 1980, 452 pages, Price: $18.95

REVIEWED BY KENNETH R. HALLIDAY

The stated purpose of this text is to provide an introduction to fluid power systems and their application in industry. Emphasis is placed on describing fluid power components and showing how they can be integrated into useful functional loops. Within that context this is a very good book.

The first five chapters discuss the physics of fluid systems. Useful equations are presented, without derivation, as required. Topics covered include fluid properties, energy methods and pipe flow.

The next three chapters describe fluid pumps, actuators and control devices. The operation of these devices is very clearly described by a well written thorough narrative and excellent illustrations. The remainder of the book, five chapters, covers hydraulic and pneumatic circuit design, fluid logic, electronic controls and safety of construction.

The major strength of this book, in comparison to other introductory texts, is the clarity with which the components and processes are described. Each device is shown in a cutaway illustration, and numerous line drawings are presented showing various aspects of its operation. The figures are discussed in detail in the narrative. Sizing, power and dynamic calculations are presented both in the narrative and in numerous examples to help the student perform the actual processes of system design and component selection. Questions and numerical problems are provided at the end of each chapter.

The chapter on fluid control is also very good. The basic fluidic logic and sensory components are presented and a number of useful circuits are described in detail. The treatment of electro-hydraulic servo systems, on the other hand, is very sparse. This is perhaps the only real weakness in this otherwise fine text.

In summary, this is a well written introduction to fluid power. It is detailed enough to stand alone as an introduction to the field while at the same time maintaining a comfortable readability.

Viscous Flow Drag Reduction, edited by Gary R. Hough, Progress in Astronautics and Aeronautics, Vol. 72, AIAA, 1290 Avenue of the Americas, New York, NY 10104. Price: $45.

REVIEWED BY FRANK M. WHITE

For people interested in drag reduction, this book is a joy. Actually, it isn't really a book, being a printed proceedings of 24 papers given at a Symposium on Viscous Drag Reduction held in Dallas on Nov. 5–6, 1979. But the papers are of high quality and cover a wide variety of drag reduction techniques. Previous similar proceedings—*Viscous Drag Reduction*, edited by C. S. Wells (1969), and the 1975 and 1977 *Drag Reduction* volumes published by BHRA—were primarily devoted to the dissolved polymer additive technique. Polymer additives take up only a fraction of the present book.

At first I thought the word "viscous" in the title was a redundancy. After all, D'Alembert's paradox pretty well guarantees that inviscid drag reduction is not a topic of intense study. But in fact the term means skin friction drag reduction, which is the principal focus of the book. There are only a few papers concerned with form or pressure drag reduction, and none are directly related to wave drag reduction.

The book is divided into seven chapters along specific drag reduction methods: laminar boundary layers, turbulent flows, nonplanar geometries, blowing and suction, compliant surfaces, and two chapters on polymer additives. Each chapter is introduced with overview remarks by noted experts.

Chapter I on laminar flows has three papers dealing with environmental disturbances, three-dimensional boundary layer stability, and the effect of an elastico-viscous film. The three papers in Chap. II on turbulent flows discuss a regenerative mechanism in turbulent bursting, the generation rate of turbulent patches, and possible drag reduction by injection and electrostatic precipitation of particles.

Chapter III on nonplanar geometries discusses passive turbulence control with four papers on eddy break-up methods: plates normal to the wall (two papers), wavy boundaries, and longitudinal grooves or riblets. The V-groove riblets decrease friction drag up to 7% but also increase form drag so there is no net gain. Chapter IV on blowing and suction emphasizes delay of transition by boundary layer stabilization and "active diffusion" which allows the flow to reach the trailing edge without separation. The four papers treat various shape and transpiration designs for both subsonic and transonic airfoils.

Chapters V and VI present seven papers on polymer additives. Topics discussed are vortex ring/wall interactions, near-wall turbulence structure, bursting dynamics, polymer concentration profiles on an axisymmetric body, pressure reduction near slit injection regions, flow-induced stretching of macromolecules, and the effect of molecular parameters on the drag reduction ability of polymers.

The seventh and final chapter, on compliant surfaces, has one paper reporting numerical modeling of laminar and turbulent flow over wavy boundaries, and two papers giving experimental data on drag and surface deformation in flow over various flexible boundaries. The experiments show little or no drag reduction, lending further discouraging evidence that the original exciting results reported by M. O. Kramer in 1960 cannot be achieved in a practical design.

The reviewer was disappointed to find no mention of another mechanism presently receiving intense study: drag reduction by wall cooling of gases or wall heating of liquids. I will look forward to another volume in this excellent series of AIAA monographs.

Reproduction of the book is of high quality throughout. Unlike most printed proceedings, which use author-prepared mattes, this book is set in uniform type. The figures, however, are author-prepared but look quite good. The book is highly recommended as a reference work.